

DEVELOPMENT OF AN ADVANCED AUTOMATED NONDESTRUCTIVE
EVALUATION SYSTEM FOR INVESTIGATION OF CONCRETE STRUCTURES AND
VALIDATION OF CONCRETE NDE INSTRUMENTS

By

JORDAN D. NELSON

A THESIS PRESENTED TO THE GRADUATE SCHOOL
OF THE UNIVERSITY OF FLORIDA IN PARTIAL FULFILLMENT
OF THE REQUIREMENTS FOR THE DEGREE OF
MASTER OF ENGINEERING

UNIVERSITY OF FLORIDA

2013

© 2013 Jordan D. Nelson

To Marc Ansley, who showed a high school kid what it meant to be an engineer; and to my family who has always shown me the love and support I needed most of all.

ACKNOWLEDGMENTS

I would like to thank each member of my supervisory committee for their support and guidance throughout the development of this work, particularly Dr. Christopher Ferraro. His extensive experience in the field and invaluable support on both a professional and personal level have made this project far more than words on paper. My esteem of him as both a mentor and a friend cannot be overstated.

Drs. Peter Ifju and Bhavani Sankar have been invaluable in successfully helping me succeed as a cross-discipline engineering student. Their guidance has allowed me to pursue a mechanical engineering degree while working on a civil engineering oriented research project, successfully planting me in a niche in which I wish to continue my engineering career.

Dr. Daniel Algernon has been a tremendous resource to this research effort and his work in the earlier phases of this project laid the foundation upon which this thesis is built. I am very grateful for his continued involvement.

My sincerest gratitude goes to all the dedicated personnel at the FDOT State Materials Office, particularly Messrs. Mike Bergin, Richard DeLorenzo, and Pat Carlton, whose support of this project has truly allowed it to flourish.

Acknowledgment is due also to Mr. Sam Fallaha and the staff of the FDOT M.H. Ansley Structures Research Center whose assistance allowed the first field deployment of the Department's newest NDE asset to be a resounding success.

Last, but certainly not least, thanks are due to my dear friend and love Ms. Rebecca Gabay for her support and understanding during my research and writing efforts.

TABLE OF CONTENTS

	<u>page</u>
ACKNOWLEDGMENTS.....	4
LIST OF TABLES	9
LIST OF FIGURES.....	10
ABSTRACT	18
CHAPTER	
1 INTRODUCTION	19
Research Motivation	19
Organization of Thesis	20
2 BACKGROUND	23
NDE Methods Considered in this Research.....	23
Surface Methods	23
Visual inspection.....	23
Surface measurement.....	27
Eddy Current Methods	29
Acoustic Methods	33
Introduction	33
Impact-echo method	34
Ultrasonic pulse velocity method.....	38
Shear wave ultrasound method	40
Ground Penetrating Radar	43
Related NDE Research: Materials-Oriented NDE.....	46
Elastic Property Estimation.....	46
Introduction	46
Elastic properties of concrete using ultrasonic pulse velocity	47
Early age elastic properties of concrete using shear wave ultrasound.....	48
Durability and Degradation of Concrete	49
Introduction	49
Permeability of bridge decks using ultrasonic pulse velocity.....	50
Nondestructive evaluation of sulfate attack.....	51
Nondestructive evaluation of alkali-silica reaction.....	55
Related NDE Research: Structural NDE.....	56
Geometry and Locating Applications	56
Introduction	56
Applications of ground-penetrating radar for pavement thickness measurements	57
Comparison of multiple NDE methods for slab thickness measurement....	59

Detection of Flaws	61
Introduction	61
Comparison of NDE methods for concrete bridge deck evaluation.....	61
Nondestructive evaluation of post-tensioning systems	63
Damage Assessment	67
Introduction	67
Nondestructive evaluation of fire damage.....	67
Nondestructive evaluation of impact damage to concrete bridge piers	69
Related NDE Research: Automation in NDE	71
Introduction.....	71
Federal Institute for Materials Research and Testing (BAM) Berlin, Germany	72
Florida Department of Transportation State Materials Office (FDOT SMO) Gainesville, Florida.....	73
3 DEVELOPMENT STRATEGY	75
Project Starting Point	75
Design Goals	78
Expanding the Capabilities of the FDOT NDE Validation Facility	78
Hardware Improvement.....	79
Integration of Additional NDE Instruments.....	79
Redesign of Software	80
Construction of Additional NDE Evaluation Blocks.....	80
Field Deployment	80
4 IMPROVEMENT OF INSTRUMENT AND SCANNER CONNECTIVITY	82
Approach	82
NDE Instrument Mounting System.....	83
Establishing a Communication Standard	86
Modification to Scanners	87
Modification to Instruments.....	90
5 INCORPORATION OF NEW INSTRUMENTS	94
Approach	94
Ground Penetrating Radar and Parallel Instrument Operation	95
Laser Profilometer	98
Surface Condition Surveyor	101
6 DEVELOPMENT OF THE ANTARES SYSTEM	106
ANTARES and the Concept of Accessible Automated NDE	106
Introduction.....	106
Approach.....	106
ANTARES SVW Operating Software	107
Introduction.....	107

Approach	108
Software Tiers	109
Introduction	109
Low-level I/O subroutines	109
Hardware handling subVIs	113
Task-handling subVIs	114
Human/data interface VIs.....	118
Interface Design	124
Introduction	124
Splash Screen.....	124
Configuration Settings Screen	125
Main Interface	127
Grid Generation Wizard	128
File I/O.....	129
Introduction	129
ANTARES Configuration File (*.ANTCFG).....	130
ANTARES Grid File (*.ANTGRD).....	131
ANTARES Data File (*.ANTDAT).....	131
ANTARES Processing Software	133
Introduction.....	133
Approach.....	134
Covermeter processing	135
Laser profilometer processing	138
GPR processing	141
Shear wave ultrasound processing	144
System Summary	148
7 LABORATORY EVALUATION BLOCK CONSTRUCTION.....	150
Introduction	150
Asymmetric Internal PT Duct Block	150
Design	150
Construction	154
Data Collection	155
Initial NDE scans.....	156
Post-grouting NDE scans.....	160
Void and Flaw Detection Block	162
Design	162
Construction	165
Defects and formwork	165
Concrete placement.....	167
Data Collection	172
Laser profilometer	172
GPR	174
Shear wave ultrasound	177

8 FIELD DEPLOYMENT AND SYSTEM EVALUATION	183
Introduction	183
Deployment Site	184
Transportation of the System.....	186
Deployment Results.....	189
9 CONCLUDING REMARKS	197
APPENDIX	
A SELECTED PROGRAMMING EXCERPTS.....	198
B SELECTED CAD DRAWINGS.....	209
LIST OF REFERENCES	219
BIOGRAPHICAL SKETCH.....	223

LIST OF TABLES

<u>Table</u>	<u>page</u>
6-1 A-Scan data output formats for *.ANTDAT file format.	133

LIST OF FIGURES

<u>Figure</u>		<u>page</u>
1-1	Spalling of concrete due to insufficient cover and poor consolidation.....	20
2-1	Cracking due to stress, plastic shrinkage cracking, curling, and alkali-silica reaction.....	24
2-2	Examples of surface defects.....	24
2-3	National Instruments Smart Camera mounted behind the wheel of the Heavy Vehicle Simulator at the FDOT State Materials Office.....	25
2-4	Single-point distance measurement using a laser distance sensor	28
2-6	A common covermeter with digital display and handheld instrument head	30
2-7	Example of the effect of orientation on covermeter measurement.....	32
2-8	Finite element simulation of an impact on a plate-like structure showing the three types of induced stress wave	33
2-9	Modern impact-echo system with hardened steel ball impactors.....	35
2-10	Test setup for measuring P-Wave velocity using impact-echo (ASTM C-1383) .	36
2-11	Test setup for measuring concrete plate thickness using impact-echo (ASTM C-1383)	36
2-12	Time domain and frequency domain data collected from an impact-echo test of a 250mm thick concrete plate.....	37
2-13	Operating principle of a piezoelectric pulse wave ultrasound transducer	39
2-14	Test setup for standard UPV test in direct transmission mode	40
2-15	Operating principle of a shear wave ultrasound transducer.....	41
2-16	Modern shear wave ultrasound instrument showing 24 transducer array and schematic of wave reflections.....	42
2-17	Modern handheld GPR unit with built-in color line display.....	45
2-18	Schematic of Voigt's experiment illustrating the usefulness of the shear wave technique in determining viscoelastic properties of cement paste	49
2-19	Yaman's test apparatus and results showing a large UPV difference between field and laboratory concrete	51

2-20	SEM Microstructure images of a concrete sample subject to negligible, moderate, and severe sulfate attack.....	52
2-21	Test block and testing locations for Boyd's experiments	53
2-22	Wave velocity results from lime water immersed and sulfate solution immersed concrete blocks.....	54
2-23	Results of Sargolzahi's research using UPV to detect ASR	56
2-24	Data taken in Virginia by Al-Qadi and Lahouar.....	58
2-25	Concrete slab in Berlin used by Beutel and other researchers	60
2-26	Results from Van Buren Road Bridge NDE study overlaid with defect map.	62
2-27	Typical tendon locations	64
2-28	Layers of corrosion protection in a typical post-tensioning tendon	65
2-29	Ultrasonic echo results from Krause's research using a similar instrument and scanning device to that used in this thesis.....	66
2-30	UPV results of a fire damaged concrete panel	69
2-31	Collapse of the southbound main span of the Sunshine Skyway Bridge	70
2-32	Impact block and UPV tomograph after barge impact	71
2-33	Horizontal and vertical scanning systems developed at BAM for use on concrete structures	72
2-34	Scanning system and software used by Algernon	74
3-1	CAD drawing of as-built scanner systems mounted to block clamping frame	75
3-2	Instrument and scanner connection scheme of the Phase I FDOT automated NDE system.....	76
3-3	Phase I scanner operating software based in multiple subroutines and windows, leading to an overly complicated interface	78
4-1	Covermeter mounted on the Phase I scanner system showing exposed and entangled data and power cables and the susceptibility of the instrument to collision during operation.....	83
4-2	CAD drawing excerpt and 3D render of new instrument carrier design	84

4-3	Completed instrument carrier as mounted to the Y-axis linear drive on Scanner 1	85
4-4	Instrument installation process	85
4-5	Scanner control box components in fiberglass enclosure.....	88
4-6	Electrical and data connection panel mounted to instrument head on Scanner 1	89
4-7	Proceq Profometer® 5+ covermeter modified for use with the scanner systems	91
4-8	Covermeter assembled on palette and packed in watertight instrument case	91
4-9	Germann Instruments EyeCON™ adapted to palette system	92
4-10	Germann Instruments EyeCON™ assembled on palette and ready for installation onto automated scanner	93
5-1	GSSI SIR3000™ system with 2.6GHz antennae to be integrated with automated scanning system	95
5-2	GPR antennae mount with limit switch for FCC compliance.....	96
5-3	Byte stream representation of ODSL8™ distance measurement	98
5-4	LabVIEW™ VI which reads and parses the 2-byte serial stream from the Leuze ODSL8™ laser distance sensor.....	99
5-5	Laser profilometer system mounted on palette system and placed in watertight instrument case.....	100
5-6	Laser profilometer mounted on scanner instrument head	100
5-7	SCS instrument adapted to standard aluminum mounting bracket and packed in watertight case.....	102
5-8	Startup subroutine of SCS run-time application.....	103
5-9	SCS placard design with origin and direction markers	104
5-10	SCS instrument mounted to Scanner 1 with ring light illuminating an orienting and calibration placard	105
5-11	Threshold image of SCS placard origin marker demonstrating ability to digitize orientation and origin marker and calibration grid.....	105
6-1	FDOT ANTARES logo designed by the research team	107

6-2	Basic tiered architecture of the ANTARES SVW LabVIEW™ application	109
6-3	Parsing structure of CML Command SubVI.....	111
6-4	Command section of pneumatic instrument head command subroutine	112
6-5	Pneumatic instrument head query subroutine with integral error handling	112
6-6	Code snippet of Ultrasound A-Scan SubVI.....	113
6-7	Portion of Scanner Movement VI with low-level SubVIs visible	114
6-8	Code snippet of Native Instrument A-Scan SubVI.....	114
6-9	Code section of Autoscan VI	116
6-10	Independent loops on main program used to call Autoscan VI.....	116
6-11	Emergency Stop VI with integrated reset dialog box	117
6-12	Initialization phase of main interface.....	119
6-13	Human interface loop of ANTARES SVW	120
6-14	Clean-up phase of the main VI	120
6-15	The first four sequences of the Splash Screen VI.....	121
6-16	Main loop of Configuration Settings Screen displaying the export *ANTCFG file case	122
6-17	Grid Generation Wizard main loop with state machine architecture	123
6-18	ANTARES SVW splash screen with loading bar and feedback to operator.....	124
6-19	Configuration Settings Screen on Scanner Configuration tab	126
6-20	Configuration Settings Screen modifying a native instrument's default port and scanning operation settings	126
6-21	Main interface of ANTARES SVW during a shear wave ultrasound scan.....	127
6-22	Grid Generation Wizard on one of the final steps to completion of a functional grid	129
6-23	Grid configuration cluster as it appears in the Grid Generation Wizard	131
6-24	Excerpt of an ANTARES Data File (*ANTDAT) showing generic file format and standard header information.....	132

6-25	Welcome panel of ANTARES Processing Suite	135
6-26	Code snippet for covermeter and laser data realization V.	136
6-27	Example of a 2D intensity plot covermeter data visualization in the ANTARES Processing Suite.....	137
6-28	Example of a 3D scatter plot covermeter data visualization in the ANTARES Processing Suite.....	138
6-29	Example of a 2D laser profilometer data visualization of a rough experimental bridge deck.....	139
6-30	3D render of laser profilometer data a rough bridge deck surface.....	140
6-31	GSSI binary data file (*.DZT) importing VI used to interpret GPR data for the ANTARES Processing Suite.....	141
6-32	Fly-through C-Scan GPR display showing a layer of dense rebar in a test specimen	143
6-33	Tomograph display of GPR data showing a dense rebar mat in the YZ plane. Two layers of rebar running transverse to the display are visible as a series of white hyperbolic traces on the pink background	144
6-34	Ultrasound processing pane with trimming and filtering options enabled	145
6-35	Ultrasound C-Scan of a dense rebar mat at a depth of 54mm with Original, Absolute, and Hilbert data transforms	146
6-36	3D ultrasound scatter plot of a densely reinforced concrete structure	147
6-37	Tomograph display of reinforced specimen with rebar mat and back side of specimen visible	148
6-38	Instruments and signal connection scheme for the new ANTARES system....	149
7-1	Grouting of middle ducts of Asymmetric Internal PT Duct Block.....	152
7-2	3D render of Asymmetric Internal PT Duct Block design.....	152
7-3	Design for Asymmetric Internal PT Duct Block	153
7-4	Formwork under construction within the scanner frames	154
7-5	Completed block immediately after formwork removal	155
7-6	Manually performed GPR scans illustrating the effect of air voids in plastic internal PT ducts on GPR reflections.....	156

7-7	View of ultrasound data of dry PT ducts in the XY plane.....	157
7-8	View of the Asymmetric Internal PT Duct Block shear wave ultrasound data in the XZ plane	158
7-9	Ultrasound scan of deep cover (153mm) side of block showing indistinguishable wave reflections from all four ducts	159
7-10	Ultrasound XZ plane tomograph of Asymmetric Internal PT Block after <i>in situ</i> grouting of duct 1.....	161
7-11	GPR trace of Ducts 1-4 showing radar scattering in Ducts 2 and 4 due to duct/water/grout interface refractory effects	162
7-12	3D render of Void and Flaw Detection Block showing relative location of intentional defects.....	164
7-13	Drawing for Void and Flaw Detection Block.....	164
7-14	Pervious concrete prisms suspended along the middle plane of the formwork for the ANTARES Void and Flaw Detection Block	166
7-15	Three rebar pieces including the two moving specimens in Void and Flaw Detection Block formwork.....	167
7-16	Consolidating the Void and Flaw Detection Block with an internal vibrator	169
7-17	Levelling the Void and Flaw Detection block with a wooden board screed.....	169
7-18	Installing the surface-visible pervious concrete prism in the Void and Flaw Detection Block.....	170
7-19	Installing the surface-visible, wet-sieved concrete simulated honeycombing into the Void and Flaw Detection block.....	170
7-20	ANTARES Void and Flaw Detection Block installed in scanner frame with surface defects visible	171
7-21	Unfiltered 3D trace of defected block surface	172
7-22	Laser C-Scan image of defected block surface with cracks and honeycombing visible	173
7-23	3D laser trace of block surface viewed from defected end in YZ plane	173
7-24	Laser C-Scan of B-side of block revealing a smooth—but not flat with respect to the scanner—concrete surface.....	174

7-25	GPR C-Scan image of rebar in Void and Flaw Detection block at a depth of 105mm	176
7-26	XZ Plane GPR tomograph of the Void and Flaw Detection block	176
7-27	GPR C-Scan image of Void and Flaw Detection block	177
7-28	Initial ultrasound data processing for Void and Flaw Detection Block.....	178
7-29	Ultrasound C-Scan image with no secondary processing at a depth of 90mm.	179
7-30	Ultrasound C-Scan image of Void and Flaw Detection Block at a depth of 120mm showing damage from depth-moving rebar, lack of rebar reflection due to earlier reflection from simulated entrapped air, and minor concrete disturbance due to length-moving rebar	180
7-31	Hilbert transform C-Scan ultrasound image of Void and Flaw Detection Block at 120mm depth.....	181
7-32	Ultrasound C-Scan “shadow” image of the back surface of the Void and Flaw Detection Block.....	182
8-1	Prefabricated bridge deck panels are lowered onto concrete girders during an Accelerated Bridge Construction (ABC) operation.....	184
8-2	Location of the test element behind the FDOT M. H. Ansley Structures Research Center in Tallahassee, Fl	186
8-3	ANTARES Scanner 1 fastened to an open frame flatbed trailer outside of the FDOT State Materials Office in Gainesville, Fl.	187
8-4	Laboratory block clamping frame with ANTARES Scanner 1 removed for field transport	187
8-5	ANTARES system in operation at the Ansley center, performing a laser profilometer scan of the first location on the ABC test element	188
8-6	ANTARES scan locations on the ABC test element	189
8-7	Laser profile of the ABC test element surface at location 1	190
8-8	Surface of bridge deck at location 1 as profiled by the laser scan	191
8-9	Ultrasound C-Scan image at ABC Location 1	192
8-10	Ultrasound C-Scan of location 2 showing severe delamination and stronger backwall reflection of adjacent bridge deck due to lack of contact with foundation.....	193

8-11	GPR C-Scan image at a depth of 120mm showing dense reinforcement on either side of the keyway joint.....	194
8-12	GPR B-Scan image of antennae path over the area of suspected severe delamination	195
8-13	Drilled core specimens from ABC Element Location 1 showing boundaries of regions with grout delamination.....	196
8-14	Drilled core of Location 1 in an area predicted by ANTARES to have a proper grout interface.....	196
A-1	Covermeter Single Point Acquisition VI.	199
A-2	Laser Single Point Acquisition VI.....	200
A-3	Ultrasound Single Point Acquisition VI.	201
A-4	SCS Startup VI Sequence 0.	201
A-5	SCS Startup VI Sequence 1 (main loop).	202
A-6	SCS Image Stream VI.	203
A-7	CML Command VI.	204
A-8	CML Query VI.....	205
A-9	Pneumatic Head Command VI.	206
A-10	Pneumatic Head Query VI.	206
A-11	*.ANTDAT File Creation VI.	207
A-12	*.ANTDAT File Append VI.	208

Abstract of Thesis Presented to the Graduate School
of the University of Florida in Partial Fulfillment of the
Requirements for the Degree of Master of Engineering

DEVELOPMENT OF AN ADVANCED AUTOMATED NONDESTRUCTIVE
EVALUATION SYSTEM FOR INVESTIGATION OF CONCRETE STRUCTURES AND
VALIDATION OF CONCRETE NDE INSTRUMENTS

By

Jordan D. Nelson

December 2013

Chair: Peter Ifju

Cochair: Christopher Ferraro

Major: Mechanical Engineering

Nondestructive evaluation (NDE) of concrete has historically been a niche discipline within civil engineering and a process carried out by an individual operator in the field to evaluate the extent of known or suspected flaws within a concrete structure. NDE techniques such as Ground Penetrating Radar, Ultrasound, and Eddy Current methods depend heavily on the expertise and diligence of the operator to maintain accuracy and are prone to producing sparse, subjective data. In recent years the Florida Department of Transportation (FDOT) has called for NDE techniques to be applied in an automated manner to produce denser, more precise, and more defensible data suitable for structural evaluation and quality control in a variety of applications. This body of work chronicles the development of such a system for use by FDOT: a precision automated scanning system coupled with state-of-the-art NDE instruments, standardized laboratory evaluation specimens, and purpose-built operation and data processing software that together comprise the FDOT Automated Non Destructive Testing for Applied Research and Evaluation of Structures (ANTARES) system.

CHAPTER 1 INTRODUCTION

Research Motivation

Non-destructive evaluation (NDE) of concrete structures is not a recent application of engineering science, but historically its application has been limited due to a number of difficulties including modeling the behavior of an inhomogeneous, time dependent material such as concrete. Additionally, NDE techniques are most frequently performed manually by trained technicians whose method of application and interpretation will invariably affect the quality of the reported data. For these reasons, NDE methods such as eddy current methods, ultrasound, and ground-penetrating radar (GPR) are typically called upon by governing agencies only rarely, and only to identify the extent of known defects or defects suspected to be present.

Concrete NDE techniques have shown the potential to reliably identify many forms of structural deficiency including poor material quality, poor consolidation, insufficient cover (thickness of protective concrete layer over reinforcing steel), and subsurface cracking and delamination due to damage such as that shown in Figure 1-1. The application of such methods for quality control purposes, however, requires spatially dense, exhaustive data collection performed in an irrefutable manner suitable for holding construction agencies responsible for the product they produce.



Figure 1-1. Spalling of concrete due to insufficient cover (left) and poor consolidation (right). Both deficiencies could have been detected using NDE methods shortly after construction (Photos courtesy of Pioneer Masonry Restoration Company) [1].

The Florida Department of Transportation (FDOT) has recently decided to invest in advanced NDE technology research to attempt to overcome the traditional limitations in NDE for structural quality control and quality assessment. The subsequent chapters of this work chronicle the development of such a system: an automated structural scanning system capable of interfacing with many common NDE instruments to produce spatially dense, repeatable, easily interpreted data from multiple methods suitable for laboratory system verification and field deployment for structural evaluation.

Organization of Thesis

This thesis can be thought of as a narrative following the development of a complex electromechanical system and supporting battery of software, hardware, and ancillary projects suitable to verify the proficiency of the system in accomplishing its intended function. It would be incomplete, however, to dispense such a narrative without providing the necessary technical background explaining the operating principles of the NDE instruments themselves and their potential applications as well as briefly

discussing the background research into advanced NDE methods in the State of Florida that led to the research discussed herein. The chapters devoted to the development of the scanning system will follow a roughly chronological order with some liberties taken for organizational flow.

Chapter 2 focuses on the requisite background knowledge to fully comprehend the development of the NDE scanning system. Included is a history of NDE research performed by FDOT, the sponsoring agency of this research. Additionally, a detailed description of each NDE method employed by the scanning system including data acquisition and interpretation practices based on material modeling is provided.

Chapter 3 describes the development strategy and goals of the research which comprises the framework of this thesis as planned before initiation of the research effort.

Chapter 4 discusses initial improvements to the inherited automated scanning system and their role in producing a more effective, more versatile, and more accessible system suitable for laboratory and field use.

Chapter 5 is devoted to discussion of new NDE instruments to be included in the system, their relative strengths and weaknesses, and the methods by which they were employed.

Chapter 6 chronicles the development of the software packages used to operate the scanning system and associated NDE instruments and process the data produced by the system into a form suitable for interpretation by the operator and owning agency alike. This effort represented by far the largest investment of time into the development of the system.

Chapter 7 emphasizes the design, construction, and subsequent non-destructive evaluation of a pair of concrete blocks intended to simulate a number of structural defects likely to be found in real-world concrete structures. This effort is a direct continuation of earlier research discussed in Chapter 2, but demonstrates the improved usability and data processing capabilities of the system.

Chapter 8 reviews a field trial of the system and addresses the viability of automated NDE as applied to reinforced concrete structures currently in use.

Chapter 9 closes with a summary of the results of this research as well as recommendations for continued research and development by FDOT and other agencies.

CHAPTER 2 BACKGROUND

NDE Methods Considered in this Research

The list of NDE methods that have successfully been applied to concrete structures is incredibly long and is growing every day. For this reason, instead of presenting an exhaustive review of a large collection of methods, this chapter investigates in depth only those few methods used specifically with the automated system and a few older methods that illustrate how the method of interest is utilized. While one of the main goals of the development of the automated system was to create a system capable of expansion to include new NDE instruments, a review of a myriad of potential instruments to be included in future research is not necessary for comprehension of this work.

Surface Methods

Visual inspection

Perhaps the most versatile and frequently employed method of non-destructively evaluating the quality of concrete in place is to simply direct a trained eye at the exposed surface [2]. For many deterioration mechanisms of concrete, the degradation of the material occurs on the surface and works its way inward. These include very common material wear mechanisms such as sulfate attack, surface wear, and erosion due to scour, freeze-thaw, etc. Inspection methods for such modes of deterioration are well established and standardized by certification agencies around the world and are demonstrated in Figures 2-1 and 2-2.

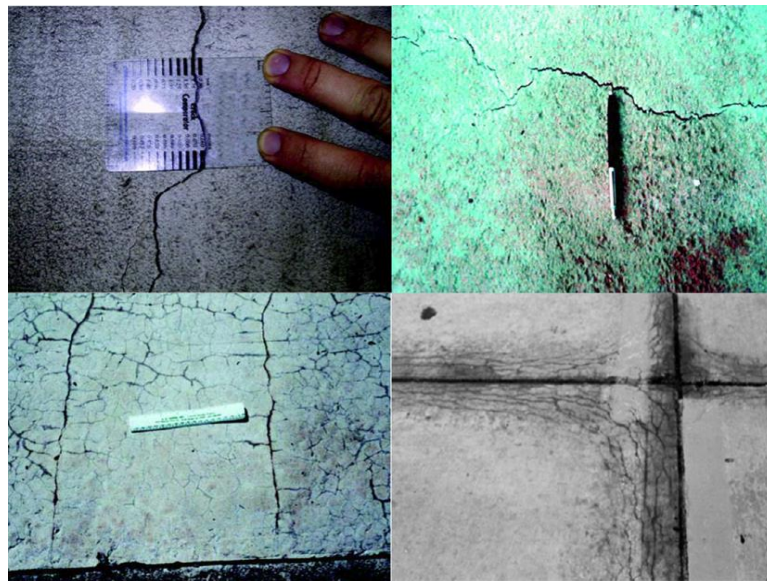


Figure 2-1. Clockwise from top-left: cracking due to stress, plastic shrinkage cracking, curling, and alkali-silica reaction (Photos courtesy of American Concrete Institute) [3].

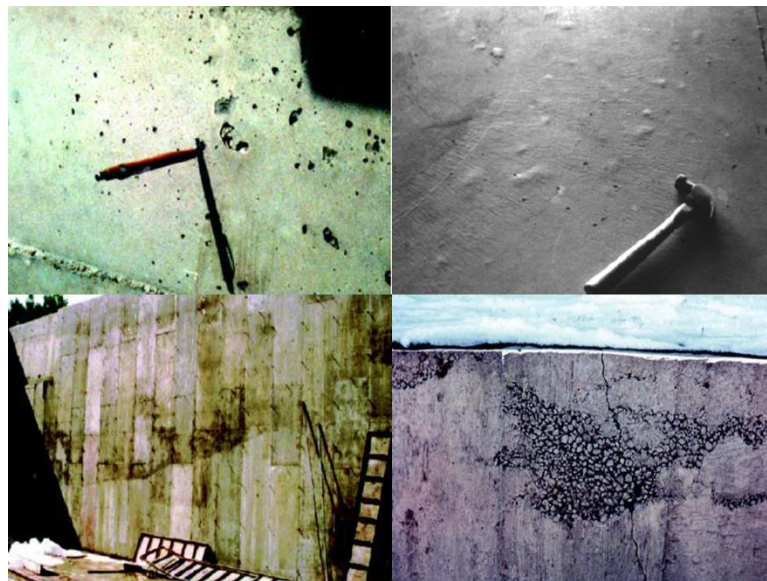


Figure 2-2. Examples of surface defects. Clockwise from top-left: bugholes, blistering, honeycombing, cold joint line (Photos courtesy of American Concrete Institute) [3].

While a certified concrete inspector can quickly and accurately judge the condition of a concrete surface, automating the process using a high resolution digital camera and sophisticated image processing algorithms offers an interesting potential to

increase the precision and repeatability of the process. The FDOT State Materials Office has applied such a technique to their Heavy Vehicle Simulator shown in Figure 2-3. This equipment is used in the Accelerated Pavement Testing program to detect cracks generated on a pavement surface during operation of the machine. Using a similar camera and software arrangement on structural concrete, one could detect small surface voids ("bugholes"), cracks, honeycombing, and surface deterioration due to sulfate attack, alkali-silica reaction, and erosion.

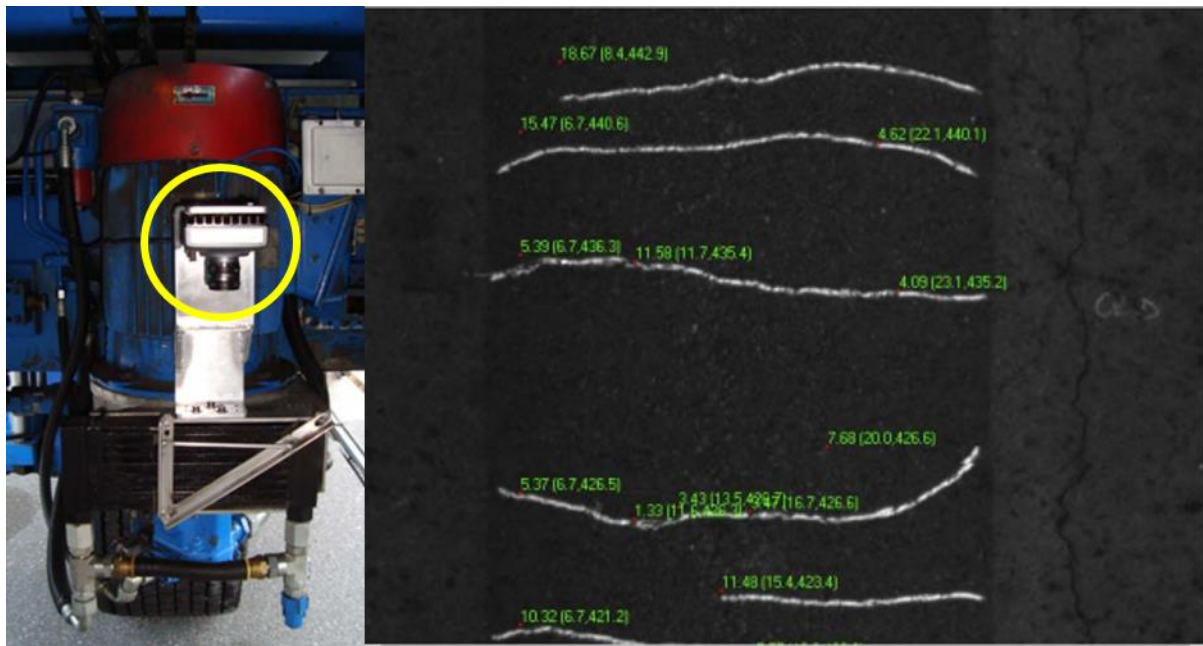


Figure 2-3. National Instruments Smart Camera mounted behind the wheel of the Heavy Vehicle Simulator at the FDOT State Materials Office. The software automatically detects and measures large cracks in the wake of the loading wheel (Photo courtesy of FDOT State Materials Office) [4].

Image processing is often a difficult task to automate due to, among other things, the overall density of the data. In the eye of a computer, a digital image is nothing more than a two dimensional array of squares of varying colors. While measuring the color and position of a particular pixel is not particularly difficult for a modern computer, consider that modern high resolution cameras measure anywhere from 10 to 20

Megapixels (up to 20 million data points) per frame where each pixel can have up to 64 bits ($2^{64}=1.845 \times 10^{19}$) of color level. When a typical computer is assigned to process repeated frames stitched together in the case of a long composite image, the demands on the computer's processing and memory architecture may rapidly become too much to handle. Fortunately for the purposes of concrete surface inspection, a grayscale camera of relatively low resolution is usually sufficient and allows a survey of a much larger area before requiring extremely high computer performance.

Conceptually, processing the images generated by the camera system for these purposes is relatively simple. Using a repeatable light source and tuning the camera at the time of testing, an operator can establish a minimum light level for a "good" concrete surface. Recessions in the surface due to cracks and voids will appear in the data processing algorithms as darker pixels, which can be identified and counted if they fall below the established light threshold. Variation in ambient light, reflective areas, and surface markings left intentionally may cause a false flaw detection in a simple algorithm such as this, so more advanced detection techniques also establish minimum sizes and establish boundaries on shapes using edge detection algorithms when defining a defect.

Performing planar measurements with a single camera system is fairly simple. Using a pre-printed grid where easily distinguished lines are set a known distance apart, a software package can be assigned a calibration factor where a designated number of pixels in its two dimensional field of view corresponds to a known distance. This calibration loses accuracy when applied surfaces that are not planar with respect to the camera's lens as a single camera can only perceive two dimensions. Three dimensional

measurements are possible with two or more cameras that share a field of view from different viewing angles, however this capability is outside of the scope of this research and was not investigated.

Surface measurement

Precision measurements of the contours of a structural concrete surface are rarely performed as critical concrete surfaces are usually formed by precise reusable forms such as in a precast yard. In the case of some cast-in-place structural pieces such as bridge decks, however, the shape and roughness of the finished surface can have an impact in the overall performance of the element in terms of the contour and friction characteristics of roadway. Perhaps even more importantly, large cast structures formed in-place have a tendency to bulge in areas of insufficient formwork support which may completely change the dimensions and center of gravity of the structure.

Modern surface contour measurements over large areas are typically performed using laser distance sensors mounted to a known reference point. Most reflection-based laser sensors use a laser source mounted a known distance from an optical sensor to create a laser light path that can be modeled as a right triangle. Using simple trigonometry, a single-point laser distance sensor can rapidly measure distance from the camera aperture to the concrete surface as demonstrated in Figure 2-4.

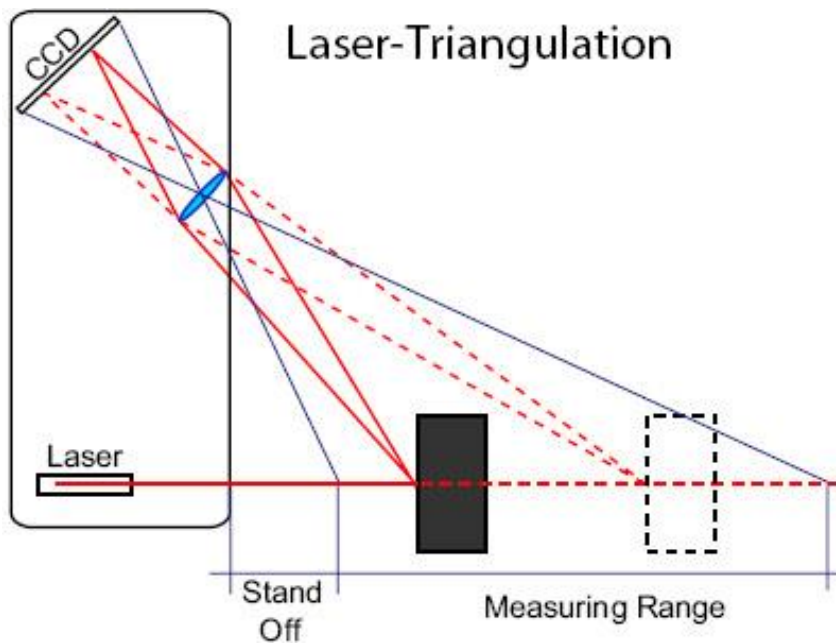


Figure 2-4. Single-point distance measurement using a laser distance sensor [5].

A three dimensional contour can be created from a two dimensional scanning system with a single point laser measurement system. To cover larger distances and make measurements at highway speed, pavement surface measurements typically achieve a three-dimensional contour using an array of laser sensors or a laser line projection system mounted to a survey vehicle. Fugro Company's Automatic Road Analyzer (ARAN) system, shown in Figure 2-5, uses such a system in conjunction with several other instruments to evaluate pavement surfaces at high speed and is an example of an entire class of survey vehicles built with technology such as this.



Figure 2-5. Rear-mounted laser surface contour system on Automatic Road Analyzer (ARAN) system (Photo courtesy of Fugro Roadware) [6].

Eddy Current Methods

Eddy current methods are a popular subset of a larger class of magnetism-based NDE methods used in reinforced concrete. The technique is based upon the tendency of long ferromagnetic rods to emanate a magnetic field when small electric currents are induced due to a nearby moving magnetic field. The effect is described by Faraday's laws for mutual inductance.

The eddy current method is commercially available in a simplified device referred to as a covermeter, a relatively inexpensive and accessible instrument typically used to

accurately locate and determine the size of reinforcing steel within a concrete surface.

An example of a common covermeter device is shown in Figure 2-6.



Figure 2-6. A common covermeter with digital display and handheld instrument head (Photo courtesy Proceq USA) [7].

Locating and sizing reinforcing bars (rebar) in concrete is important both for verification of construction practices as well as locating obstruction to drilling and cutting operations when portions of a structure are to be removed, such as coring and slab removal operation. Additionally, covermeters are extensively used to verify the cover (depth from surface) of reinforcing steel, a parameter with minimum values specified in concrete design guides which has a profound impact on the durability of a structure. Reinforced concrete structures with insufficient cover are documented to experience rapid corrosion of the reinforcing steel, resulting in premature failure of the structure.

Covermeters induce a time-varying magnetic field in the concrete near the handheld instrument head by passing an alternating current source through an excitation coil. Concrete, having a high magnetic reluctance, will resist the transmission

of this field and limit the magnetic flux registered by a second sensing coil. When the instrument head is sufficiently close to ferromagnetic reinforcement, the low magnetic reluctance of the nearby steel bar will yield a much higher flux registered by the instrument [8].

One of the main disadvantages of eddy current methods is that the method is insensitive to non-magnetic features within the concrete surface. Water pockets, air voids, organic contaminants, and non-ferromagnetic reinforcement do not exhibit the induced eddy current phenomenon required for covermeter operation. This disadvantage can actually become a major advantage to an inspector when this technique is combined with another method that is sensitive to, for example, density changes as in acoustic methods where steel, air, water, etc. are all resolved within the structure but are difficult to tell apart from one another. If the data from a covermeter and an ultrasound array were overlaid, it would be very apparent to the operator which features were ferromagnetic (e.g. steel rebar) and which were some other nonmagnetic material.

It is important to note that covermeters are extremely effective at resolving cylindrical ferromagnetic rods of infinite length in shallow cover situations where the excitation and sensing coils are both centered over the centerline of the rod. In situations where steel features have a non-circular cross section, short lengths, are in deep cover (dependent upon the sensor head used), or are oriented perpendicular to the instrument head of a common cover meter begins to lose accuracy. Previous research has quantified this effect very well with the particular covermeter used in this research, as illustrated in Figure 2-7 [9].

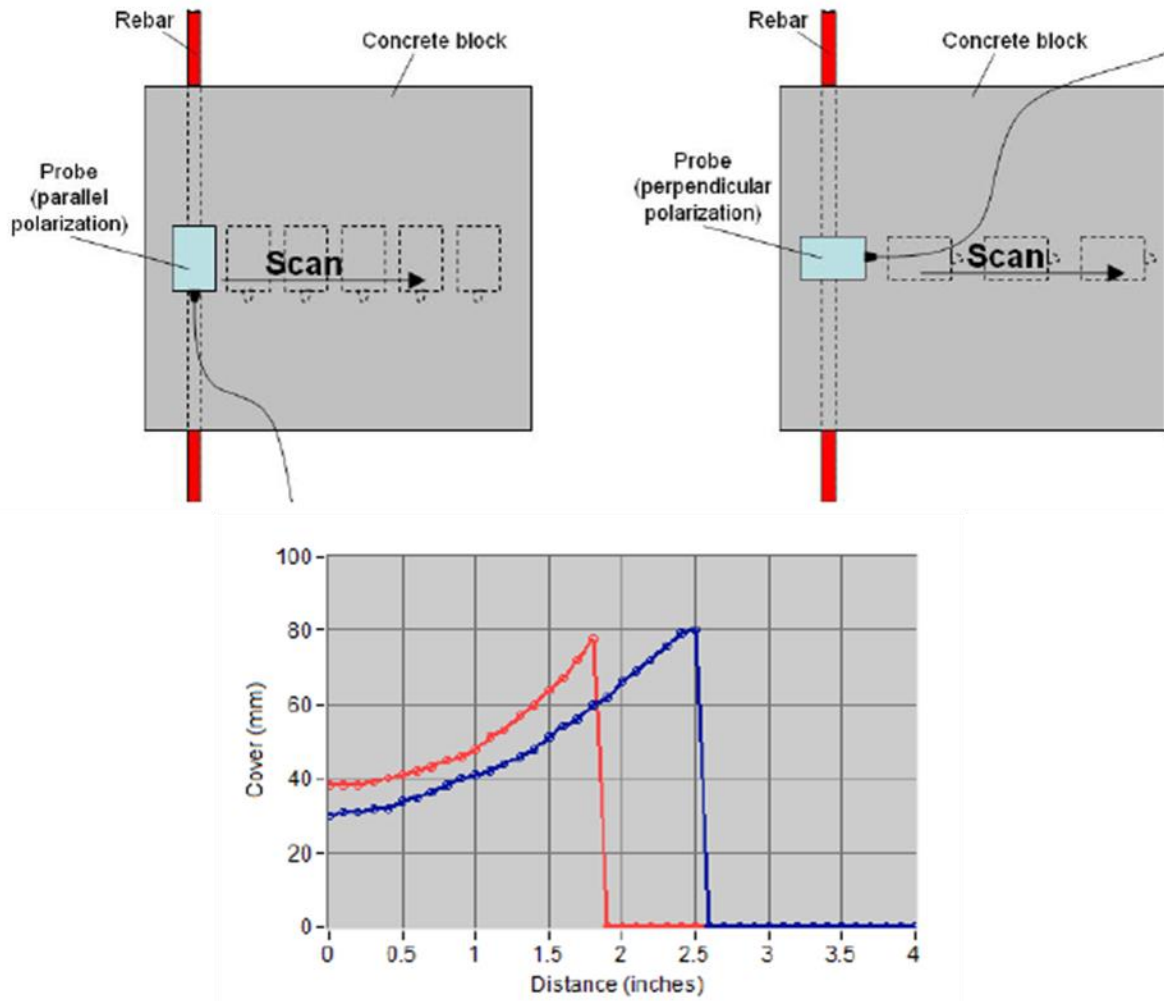


Figure 2-7. Example of the effect of orientation on covermeter measurement. These line scans were performed on the same specimen with the instrument head parallel (blue) and perpendicular (red) to the rebar [9].

Despite the obvious limitations of eddy current methods and the covermeter in particular, the method was included in this body of work primarily to complement the other included methods and to include a method that is well known, well understood, and commonly used manually in the field.

Acoustic Methods

Introduction

“Acoustic methods” is a moniker encompassing an entire range of methods based on the measurement of stress wave propagation in a material. For the purposes of this work, we will consider only ultrasonic methods in depth with a few ancillary methods that help explain them. The research described herein utilizes shear wave ultrasound as its acoustic method, so this technique will be discussed in detail. To better understand the mechanism behind shear wave ultrasound method, the earlier impact-echo and ultrasonic pulse velocity methods are discussed.

All acoustic methods are based on the detection of one or more of three distinct stress wave types which propagate through a material when a stress event is induced on the surface or within the continuum of a material as shown in Figure 2-8. The pulse wave, or P-Wave corresponds to a normal stress event, the shear wave, or S-Wave corresponds to shear stress, and the surface, Rayleigh, or R-Wave corresponds to the disturbance propagating along an impacted free surface [10].

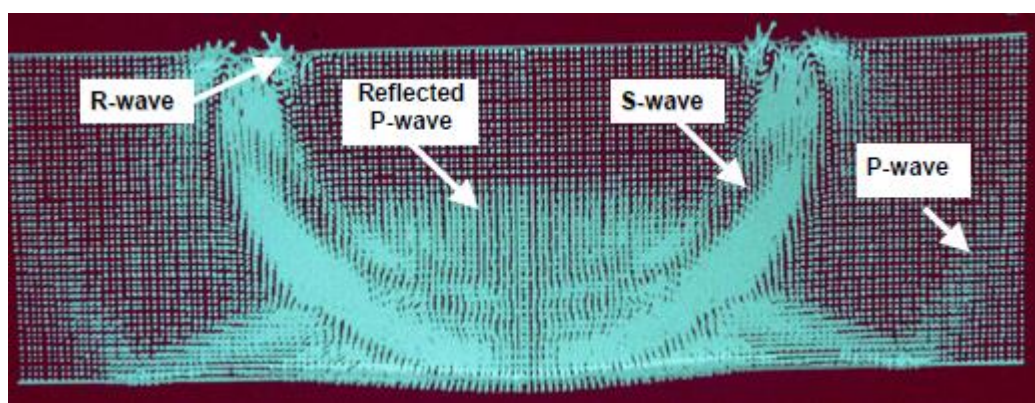


Figure 2-8. Finite element simulation of an impact on a plate-like structure showing the three types of induced stress wave [11].

For an infinite, isotropic, perfectly elastic solid the wave velocities for each of the three wave types (C_p , C_s , and C_r for P, S, and R wave respectively) is described in terms of the modulus of elasticity E, shear modulus G, Poisson's ratio v, and density ρ as follows [12].

$$C_p = \sqrt{\frac{E(1-v)}{\rho(1+v)(1-2v)}} \quad (\text{Equation 2.1})$$

$$C_s = \sqrt{\frac{G}{\rho}} = \sqrt{\frac{E}{\rho 2(1+v)}} \quad (\text{Equation 2.2})$$

$$\frac{C_r}{C_s} \approx \frac{0.87 + 1.12v}{1+v} \quad (\text{Equation 2.3})$$

Some acoustic methods simply use a measurement of the time of flight of a stress wave in order to determine the wave velocity. Wave velocity can be used to estimate the elastic properties of the material using the above equations or determine if the material has been damaged or has significantly degraded. Other methods will register a complete waveform of reflected waves to better determine if flaws or defects exist in the material's thickness. The two techniques and the principles required to employ them are discussed in the section for the method to which they pertain.

Impact-echo method

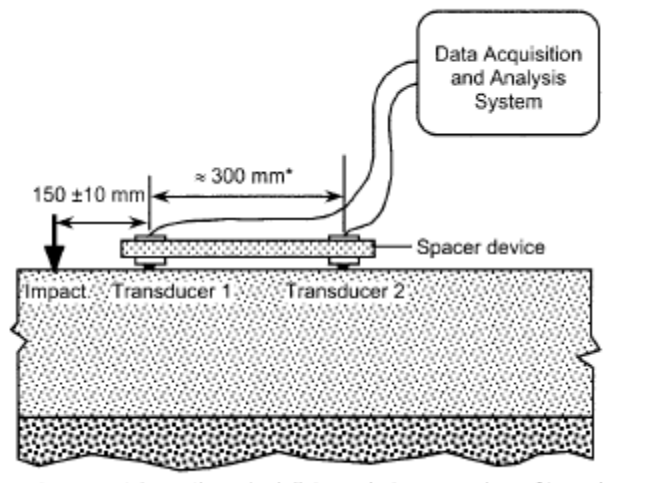
The impact-echo method is based on monitoring the minute movements of the surface of a concrete specimen using a sensitive accelerometer following a short duration point impact. The method was borne out of a technique called hammer-sounding in which an operator would tap on the surface using a hammer and listen for a low-frequency rattling sound indicative of near-surface voids in the concrete specimen. While the operating principle of the modern impact-echo method is essentially the same

as hammer-sounding, computer based data acquisition is used to replace the trained human ear to interpret the frequency (pitch) of the returned acoustic wave and more consistent impacts are generated using specialized manual or electromechanical impactors.



Figure 2-9. Modern impact-echo system with hardened steel ball impactors (Photo courtesy of NDT James Instruments) [13].

In practice, the impact-echo method is used by first creating a short duration point impact on the concrete surface using a falling or spring loaded spherical ball made of hardened steel or an electric solenoid striker. In a P-Wave velocity measurement, two transducers mounted a known distance apart on a spacer record the surface wave as it passes under their contact point allowing a simple distance-by-time calculation for wave velocity. The P-Wave is distinguished from the slower-traveling R-Wave by using the shortest recorded time delay between wave peaks, usually performed in software automatically [14].



*Measure to nearest 1 mm the actual distance between centers of transducers

Figure 2-10. Test setup for measuring P-Wave velocity using impact-echo (ASTM C-1383) [14].

In a depth measurement or flaw detection analysis, a single transducer located near the impact point is used to record the P-Wave as it reflects from the back of the specimen to the impacted surface repeatedly for several reflections. This waveform is often processed using fast Fourier transform (FFT) or other suitable technique to take the data from time domain to frequency domain.

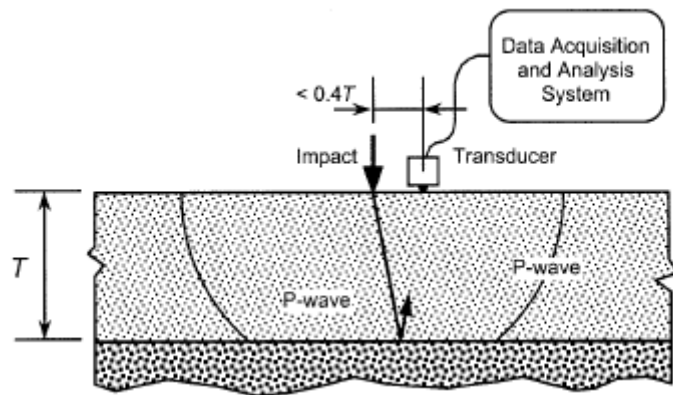


Figure 2-11. Test setup for measuring concrete plate thickness using impact-echo (ASTM C-1383) [14].

Once the collected data is processed into frequency domain, a single dominant peak is exhibited in the power spectrum.

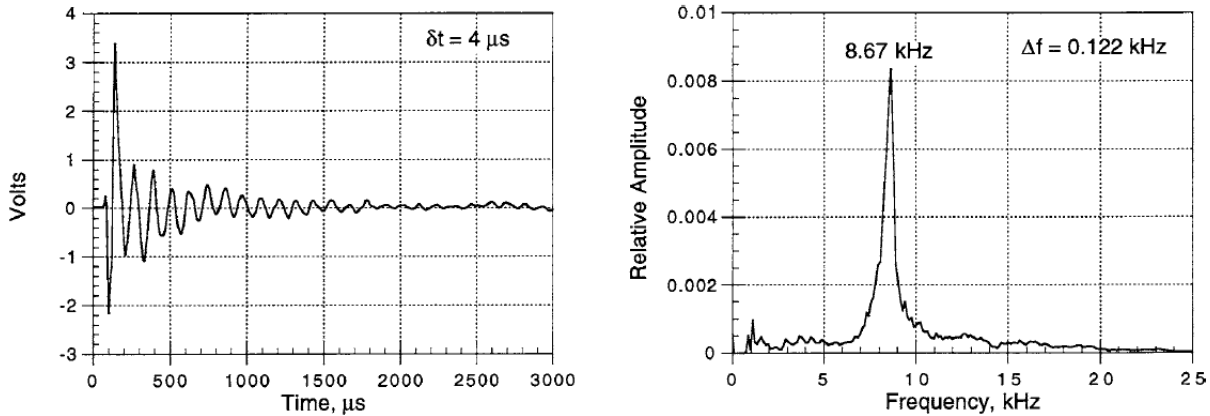


Figure 2-12. Time domain (left) and frequency domain (right) data collected from an impact-echo test of a 250mm thick concrete plate. Note the single dominant peak in the power spectrum [14].

The frequency of this dominant peak corresponds to the frequency of the P-Wave as it bounces from the impacted surface to the point of original reflection. The distance from the reflected point to the impacted surface can be calculated from the pulse wave velocity C_p and the calculated dominant frequency f as follows [10].

$$T = \frac{C_p}{2f} \quad (\text{Equation 2.4})$$

In situations where an air void, water pocket, area of poor consolidation, delamination, or other discontinuity exists between the transducer and the back wall of the concrete plate, two distinct situations may occur.

1. In the case of a **small aspect ratio defect**, the stress wave will travel **around the defect** and the calculated thickness of the concrete plate will be **larger** than expected
2. In the case of a **large planar defect**, the stress wave will **reflect off the defect** and the calculated thickness of the concrete plate will be **smaller** than expected

Flaw detection using impact-echo is unreliable when defects are very small, non-planar with respect to the transducer, or hidden behind another interface such as another anomaly or reinforcing steel in an effect known as “masking”. It also unreliable to use the impact-echo method in “compact” specimen geometries where wave reflections from the sides of the specimen may cause modes of vibration other than the desired plate-like vibration mode to become dominant [10].

Ultrasonic pulse velocity method

Ultrasonic pulse velocity (UPV) methods applied to concrete structures were borne out of related techniques applied to metals and other homogeneous materials. By coupling a high frequency piezoelectric oscillator to the surface of a specimen, collimated stress waves are driven into the material to either be received on the other side of the material in direct transmission mode as shown in Figure 2-14 or received on the same side a short distance away in pulse-echo mode. The velocity of these pulse waves is well described by the equation listed in the preceding section and the fast, repeated manner by which the pulses are created and received lends itself to making many measurements averaged over a short time span to yield much more accurate data than is obtained from a single pulse. Additionally, the generated waves are far more collimated than those originating from a point impact and the wave fronts do diverge greatly from the intended path, reducing the effect of compact specimen geometry on wave reflection.

UPV methods as applied to concrete generally operate at much lower frequencies than their metals testing counterparts as standard high frequency oscillating transducers fail to overcome the scattering effect caused by the many paste and aggregate interfaces and pores present in concrete to create repeatable stress waves.

The operating principle of the transducer is, however, identical: a piezoelectric crystal within a housing is used to drive a hard contact surface into the concrete surface. The air gap between the UPV transducer and the concrete surface must be filled with a thin layer of acoustic couplant in the form of a gel or grease in order to ensure complete transfer of the stress wave . The transducer is driven by an electric function generator in transmit mode and the impact of the transducer on the concrete surface generates a series of collimated longitudinal stress waves. The stress waves are received using an identical transducer whose piezoelectric crystal is connected to a data acquisition system which records the voltage generated by the movement of the transducer. The time of flight of the wave pulses is calculated and averaged and the ultrasonic pulse velocity is determined by dividing the measured transit distance by the calculated transit time.

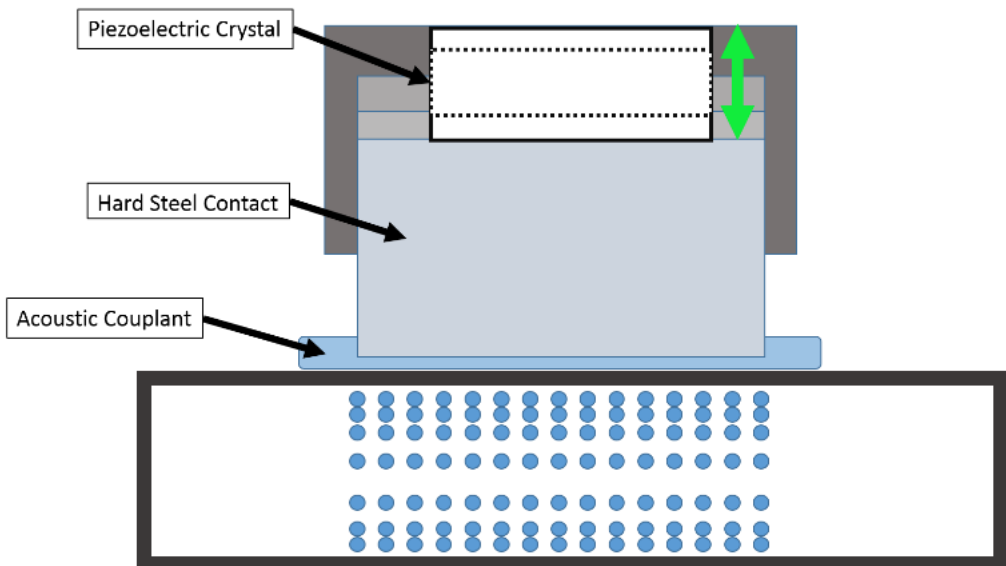


Figure 2-13. Operating principle of a piezoelectric pulse wave ultrasound transducer.
Note the longitudinal stress wave and corresponding particle motion.

The receiving transducer may be located on the opposite side of a planar specimen from the transmitting transducer in a technique known as direct transmission

or located on another surface in a technique known as indirect transmission. Due to the difficulties in measuring an accurate transit distance and ensuring constant material properties along the wave path in indirect transmission mode, ASTM C597 currently only allows direct transmission to be used to determine the ultrasonic pulse velocity of a concrete specimen. More recent research and improved practices have shown that in certain circumstances indirect measurements are valid and statistically similar to direct measurements, and it is possible that this method may one day be approved by standardized testing organizations [15].

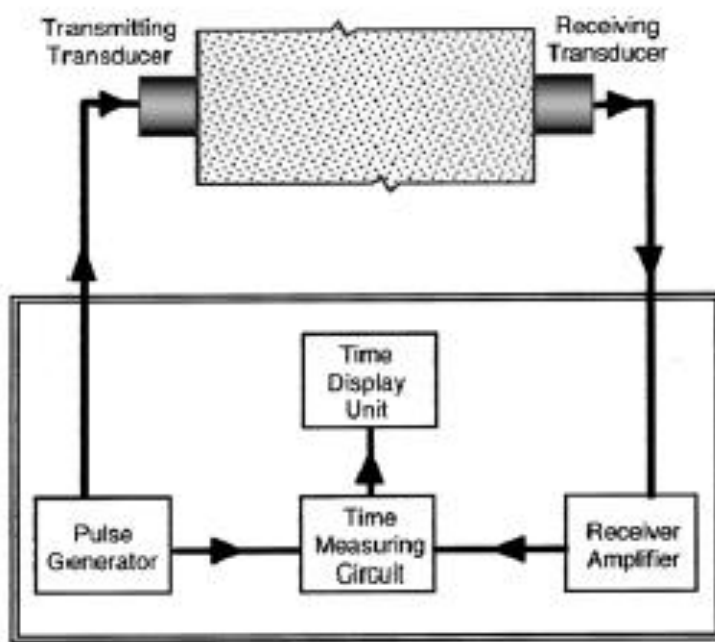


Figure 2-14. Test setup for standard UPV test in direct transmission mode [16].

Shear wave ultrasound method

Shear wave ultrasound is a relatively new technique designed to overcome many of the limitations carried by standard pulse wave ultrasound when applied to concrete. The mechanism by which stress waves are induced on the concrete surface is fundamentally different from ultrasonic pulse: shear wave ultrasound transducers use a

piezoelectric oscillator whose principal axis is oriented parallel with the concrete surface to slide the transducer contact point along the surfaces instead of drive it into the surface. In the case of both transducers, the piezoelectric crystal can be used to either drive the transducer and generate stress waves by driving the crystal with an alternating electric current or receive the stress wave by measuring the current generated by the crystal as the transducer receives a stress wave. In this way, a sophisticated control system can take advantage of a relatively small number of transducers arranged in an array to both generate and receive stress waves at many different points using the same transducers.

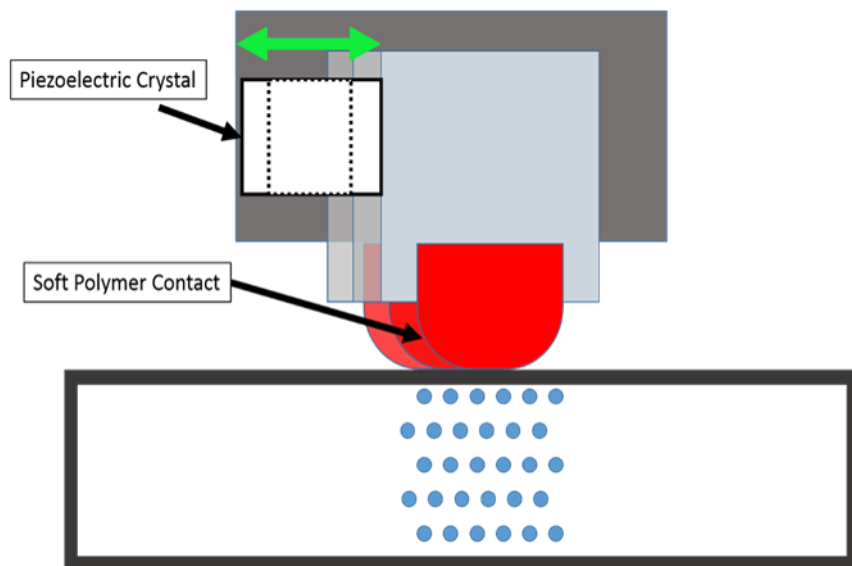


Figure 2-15. Operating principle of a shear wave ultrasound transducer. Note the piezoelectric crystal is mounted transverse to the transducer and particle motion follows this direction.

The operating mechanism of shear wave ultrasound allows the transducer to be designed in such a way where a stress wave can be reliably generated and transmitted through a soft polymer tipped transducer without the use of acoustic couplant. This simple advantage over standard UPV testing is not only more convenient when the

technique is applied in manual testing, but allows the technique to be much more easily automated as an ancillary system to manage application of couplant and verification that sufficient couplant was used for a reliable measurement is not required. This is the primary reason why this technique was chosen for use in this body of research and UPV was excluded.

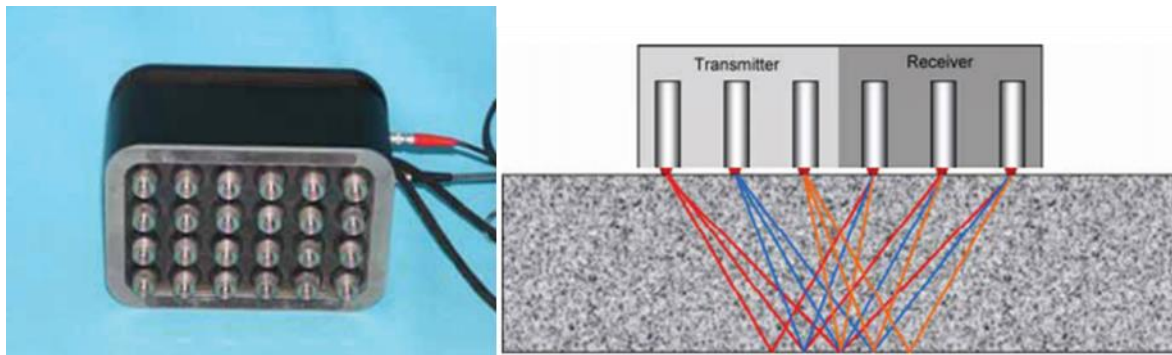


Figure 2-16. Modern shear wave ultrasound instrument showing 24 transducer array (left) and schematic of wave reflections (right) (Photo courtesy of Germanm Instruments) [17].

A return signal using the shear wave ultrasound technique depends on successful transmission and reception of S-Waves, which leads to a few properties of interest for the concrete inspector. S-Waves travel significantly slower than P-Waves and with less energy, so they tend to reflect off of small defects and delaminations easily. While this means the technique is very sensitive, it also exacerbates the masking effect discussed in the Impact-Echo Method section. The technique is also far more sensitive than pulse wave to fluid pockets within a solid since liquids and gases cannot transmit shear stress and, as a result, much stronger wave reflections are observed. This makes the technique ideal for locating honeycombing, bleed water pockets, and similar defects.

A shear wave ultrasound array typically produces a single waveform showing a composite of the reflected shear waves as received by the instrument head. This waveform can be thought of as a single-point representation of the thickness of the concrete specimen and is referred to as an “A-Scan.” When waveforms are collected iteratively over a line, an array of waveforms can be assembled to generate a two dimensional intensity plot. This two dimensional representation of a line of data through the thickness of the specimen is referred to as a “B-Scan.” Finally, if repeated B-Scans are assembled together to form a three dimensional intensity array, the operator can view the specimen top-down and investigate each received data layer of the specimen or generate a three dimensional render of the interior of the specimen. This complicated data assembly is referred to as a “C-Scan.” Production of these data renders as well as all signal processing used in creating useful, quality data from shear wave ultrasonic array is discussed in Chapter 6.

Ground Penetrating Radar

Ground Penetrating Radar (GPR) is a somewhat nascent method in the world of concrete NDE. Geological surveyors have been employing GPR for decades to detect sinkholes, utilities, and other anomalies hidden below ground but these applications utilize large, low frequency antennae that would not resolve any fine, near surface details as required in structural concrete NDE. As smaller, higher frequency GPR antennae have emerged into the market, concrete inspectors have embraced the technology and the technique is quickly becoming one of the most popular NDE methods for structural concrete.

GPR is based on the principle of reflection of electromagnetic waves off of interfaces within the structure. As with any wave reflection technique, an (approximate)

impulse of energy is generated upon the structure and allowed to propagate through it. Reflected waves are generated on boundaries where step changes in the velocity with which the wave may propagate occur and recorded upon their return using a receiving transducer.

The velocity of an electromagnetic wave in any material is described by the material's dielectric permittivity (ϵ) and magnetic susceptibility (μ). Using Maxwell's equations, the velocity takes the following form.

$$v = \frac{1}{\sqrt{(\epsilon_r \epsilon_0 \mu_r \mu_0)}} \quad \begin{aligned} \epsilon_r &= \text{Permittivity ratio } \left(\frac{\epsilon}{\epsilon_0} \right) \\ \epsilon_0 &= \text{Permittivity of Free Space } \left(8.85 \times 10^{-12} \frac{\text{A}^2 \text{s}^2}{\text{Nm}^2} \right) \\ \mu_r &= \text{Magnetic susceptibility ratio } \left(\frac{\mu}{\mu_0} \right) \\ \mu_0 &= \text{Mag. susceptibility of Free Space } \left(4\pi \times 10^{-7} \frac{\text{N}}{\text{A}^2} \right) \end{aligned} \quad (\text{Equation 2.5})$$

In free space, the permittivity and magnetic susceptibility ratios are exactly equal to unity. Which yields the following calculation for the speed of light in a vacuum.

$$v = c = \frac{1}{\sqrt{\epsilon_0 \mu_0}} = \boxed{2.998 \times 10^8 \frac{\text{m}}{\text{s}}} \quad (\text{Equation 2.6})$$

For nonmagnetic materials, the magnetic susceptibility ratio can be assumed equal to unity. Equation 2.1 then reduces to the following relation.

$$v = \frac{1}{\sqrt{(\epsilon_r \epsilon_0 \mu_0)}} = \boxed{\frac{c}{\sqrt{\epsilon_r}}} \quad (\text{Equation 2.7})$$

This relation effectively shows that the GPR method is sensitive to abrupt changes in dielectric permittivity [18].

An extremely large change in dielectric permittivity, such as a radar wave propagating through concrete incident upon a water pocket would cause a

correspondingly large portion of the wave to be reflected back towards the source. This reflection is what is recorded and measured by a GPR data acquisition system.

Knowing the speed of the wave in concrete, one could measure the time of flight of the reflected wave from the source, multiply by the velocity, and yield the distance the wave traveled: twice the distance from the source to the water pocket.

Modern GPR equipment performs this single point measurement thousands of times per second to yield highly dense, accurate data and generate a complete depth plot of the structure. Connected to a rolling cart with built-in position encoder such as the device shown in Figure 2-17, this equipment has the capability of producing long, detailed line scans (B-Scans) of a concrete structure in great detail with an easily interpreted data display.



Figure 2-17. Modern handheld GPR unit with built-in color line display (Photo courtesy of Geophysical Survey Systems, Inc.) [19].

Despite the popularity and flexibility of modern GPR technology, the method still has some limitations. First and foremost, as with any wave-reflection method GPR is sensitive to the masking effect. In the case of GPR, this is most commonly seen as a

case where an air or water pocket is masked by rebar; the GPR reflection display is consistent with a normal rebar reflection and the defect is undetected. Additionally, a GPR antenna is sensitive to the manner in which it is coupled to the concrete surface. Since the electromagnetic wave must first cross an air barrier before reaching the concrete surface, the impulse wave is often attenuated before ever reaching the surface and all defects within the structure are effectively masked. This effect is exacerbated in so-called “air coupled” systems commonly used in pavement survey vehicles in which a relatively large gap is placed between the antennae and the surface and higher energy radar waves are used to compensate. Finally, free moisture in concrete serves to make the previous two limitations even worse by increasing its dielectric permittivity, leading to a situation where the surface of the concrete itself becomes an effective mask for all targets in the structure in the case of young or highly saturated concretes [20].

Related NDE Research: Materials-Oriented NDE

Elastic Property Estimation

Introduction

One of the most common applications of concrete NDE—and indeed one of the earliest requirements of the technology—is to estimate useful measurements of material properties normally acquired from more destructive or labor intensive tests. From a concrete mix design standpoint, two of the most useful and desirable material properties to measure from hardened concrete are the compressive strength (f'_c) and the static modulus of elasticity (E). These two measurements are usually made from destructive tests performed on concrete cylinders or cores according to ASTM C-39 Standard Test Method for Compressive Strength of Concrete and ASTM C-469 Standard Test Method for Static Modulus of Elasticity and Poisson’s Ratio of Concrete. A common situation

faced by concrete engineers and testing professionals is a need to estimate the compressive strength or elastic modulus of a quantity of concrete already in place and in use where companion specimens are not available for traditional testing. For example, if a section of Interstate highway is temporarily closed and heavy traffic needs to be detoured over older infrastructure that may or may not meet the strength required to support heavy trucks, depending on the age of the structure compressive strength and modulus data may not be available. The options available to engineering authorities in this situation are limited and essentially boil down to two main options: temporarily remove the structure from service in order to obtain core specimens to test traditionally or estimate the desired properties quickly and unobtrusively using a non-destructive evaluation method.

Elastic properties of concrete using ultrasonic pulse velocity

Acoustic methods are popular for estimating elastic properties since the speed of a stress wave in an isotropic elastic material is described analytically by its elastic properties as shown in the Introduction of the Acoustic Methods section. A cornerstone of research to this end was completed in 1990 by Sandor Popovics [21]. Carefully fabricated concrete specimens were subjected by Popovics and his assistants to UPV testing from several different transducer frequencies. The elastic moduli and densities of concrete were calculated from the UPV results and used to estimate compressive strength. The tendency of the measurements to be affected by material inhomogeneity, directional preference, and internal stress was addressed in detail. The results were clear: while an accurate determination of the speed of a P-Wave or S-Wave in concrete can be used to estimate the elastic or shear modulus with a high degree of reliability, estimating concrete strength is not as straightforward. While there is a correlation

between ultrasonic pulse velocity and compressive strength, it varies between concrete mixes due to varying material properties and overall material behavior. Attempting to estimate the strength of a particular concrete mix using an estimated elastic modulus and an empirical correlation without first establishing a calibration data set for the mix proved to be highly unreliable [21].

Early age elastic properties of concrete using shear wave ultrasound

A decade and a half after the groundbreaking research by Popovics, Dr.-Ing Thomas Voigt of the University of Leipzig employed shear wave ultrasound reflection in a novel approach to evaluating the elastic properties of very early age cementitious specimens [22]. In response to demand from the construction industry to better evaluate the quality of in place concrete days or even hours after placement, Dr. Voigt addressed the feasibility of using shear wave reflections to monitor the set of cementitious materials as their complex viscoelastic modulus becomes increasingly solid-like. Shear waves were passed through a Poly[methyl methacrylate] (PMMA) buffer into an early age mortar specimen as shown in Figure 2-18 and the reflections were recorded to determine the energy lost. The loss in wave energy is directly correlated to the viscous portion of the material's modulus, and as such a lower loss in energy is readily correlated to the completeness of set of the cementitious material [22].



Figure 2-18. Schematic of Voigt's experiment illustrating the usefulness of the shear wave technique in determining viscoelastic properties of cement paste [22].

While the research discussed in this thesis is concerned primarily with later age structures, the effect of early age material properties on the behavior of the shear wave ultrasound technique cannot be ignored as the automated system will inevitably be applied in the future to early age structures as a quality control measure.

Durability and Degradation of Concrete

Introduction

General degradation of concrete, whether due to natural environmental weathering action, chemical reaction, or traumatic damage, has a profound impact on the performance of reinforced concrete structures, pavements and indeed any practical application of concrete as a primary material. Degradation of concrete in steel reinforced concrete structures is especially harmful as increased concrete permeability leads to an increase in chloride ion infiltration paths. Once an increase in permeability, either locally or globally in the structure, is sufficiently severe corrosion of the reinforcing steel within the structure will initiate and inevitably lead to a structural failure if left unmitigated.

Durability is a term which describes the ability of concrete to withstand environmental degradation and prevent infiltration of corrosive agents to the reinforcing steel contained within a structure. While the definition of a “durable” concrete product and a “less durable” concrete product is somewhat subjective and depends heavily on the environment in which the concrete is placed, the characteristics of a durable concrete are low permeability, good chemical and biological compatibility with the environment, ability to resist freeze-thaw degradation if applicable, resistance to bleed during placement, and good resistance to wear [23].

While standardized tests exist for estimating permeability and wear resistance of concrete, non-destructive evaluation techniques are frequently requested to more rapidly detect significant loss in concrete durability due to weathering, cracking, alkali-silica reaction (ASR), sulfate attack, fire damage, and other common sources of catastrophic concrete failure. This subset of concrete NDE continues to be the subject of research efforts across the scientific community.

Permeability of bridge decks using ultrasonic pulse velocity

In a Michigan DOT funded study, I.O. Yaman and a research team attempted to better describe concrete permeability in bridge decks using the UPV method [24]. Yaman compared UPV measurements of a bridge deck to UPV measurements of a standard, ideally cured cylinder specimen in a manner similar to an established test metric known as Paste Quality Loss (PQL). PQL uses a porosity probe known as a Figg’s apparatus to compare the permeability of field-placed concrete with ideally fabricated concrete to determine to what degree the past is compromised. This metric establishes the later age porosity—and as a result the later age durability—of a concrete placement.

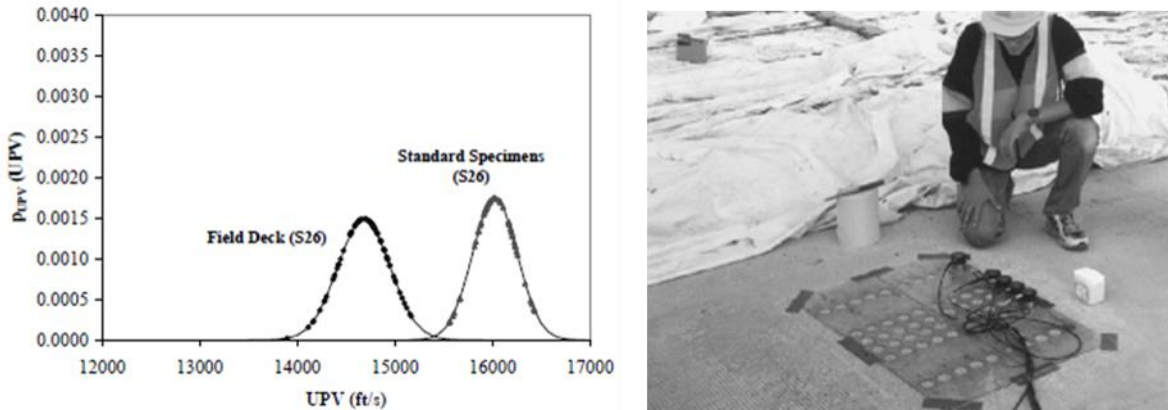


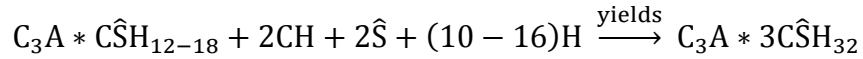
Figure 2-19: Yaman's test apparatus and results showing a large UPV difference between field and laboratory concrete. This difference is attributed to Paste Quality Loss (PQL) [24].

Yaman employed an array of UPV transducers to generate a statistical model of the pulse velocity of a bridge deck placed in the field. When compared to the pulse velocity of standard specimens taken in the laboratory, there was a significant difference in the average UPV reading that correlated closely with the PQL value calculated using the standard method. This correlation was also shown valid in areas of known defects such as poor compaction. In addition to establishing the basis of UPV as what could be a valid permeability test method for concrete bridge decks, Yaman showed the superiority of the method versus the Figg's apparatus in terms of speed. The UPV based measurement took roughly half as long as a measurement using the Figg's apparatus, a speed increase that could likely be improved if purpose-built UPV systems were fabricated [24].

Nondestructive evaluation of sulfate attack

Sulfate attack in concrete is a mechanism by which environmental conditions promote the formation of ettringite ($C_3A * 3C\hat{S}H_{32}$) crystals in concrete from the reaction

of monosulfates ($C_3A * C\hat{S}H_{12-18}$) within the hydrated cement paste and sulfate (\hat{S}) within the environment according to the following chemical reaction.



The ettringite crystals, possessing a larger volume than their precursors, cause expansion within concrete and result in highly destructive microstructural cracking. The effect is mitigated using low water-cement ratio concrete to reduce permeability and cement which resists the formation of ettringite by containing lower quantities of tricalcium aluminate (C_3A) [25].

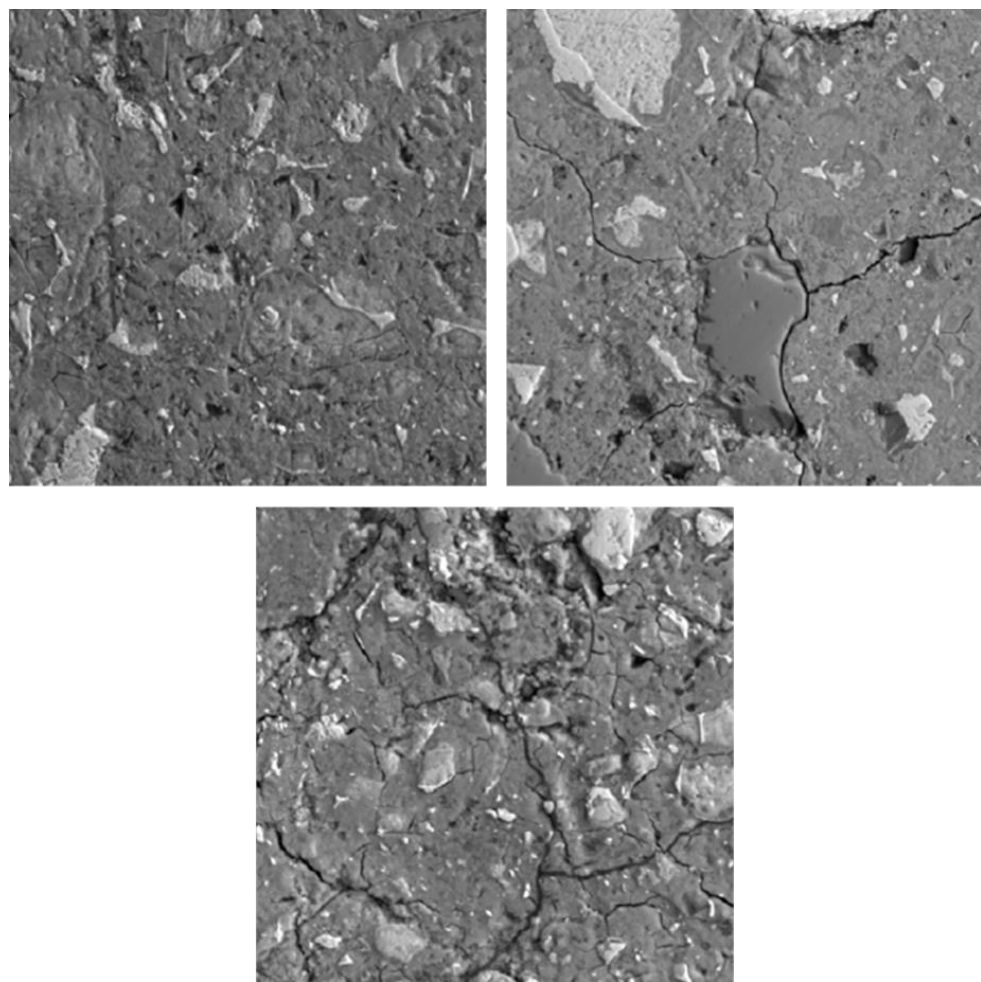


Figure 2-20. SEM Microstructure images of a concrete sample subject to negligible (top-left), moderate (top-right), and severe (bottom) sulfate attack [25].

Microstructural cracking causes a reduction in stress wave velocity since the discontinuities within the material inhibit the transmission of the wave. This effect is well established and techniques such as UPV have been used successfully with concrete cylinders submerged in a sulfate solution. Boyd et al. sought to apply the same method to more realistic situations of sulfate attack involving large concrete blocks partially submerged in a sulfate solution. In this manner, the region of the block not submerged in the solution but subject to its effects due to absorption could be investigated.

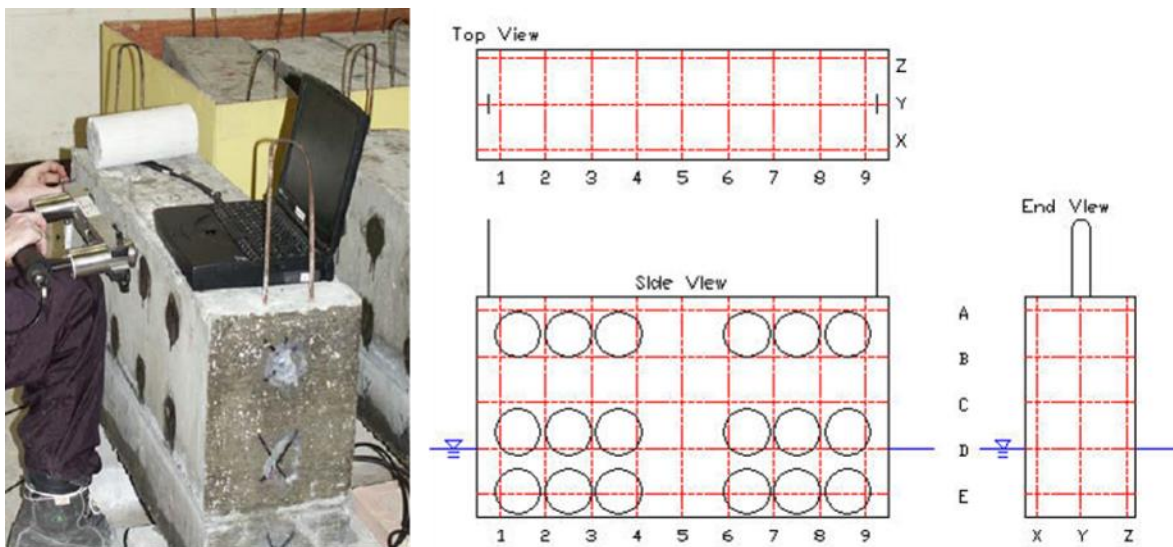


Figure 2-21: Test block and testing locations for Boyd's experiments. Note the water line and the relative location of top, middle, and bottom test levels (Photo courtesy of C. Ferraro) [25].

Concrete blocks partially submerged in a sulfate solution were tested in parallel with identical panels partially submerged in lime water as a control. The blocks were tested in a grid using surface impact-echo and direct UPV techniques as well as other non-destructive methods. The results for the NDE methods were compared with destructive data from compressive strength, static elastic modulus, and pressure tension tests collected from cores of the blocks.

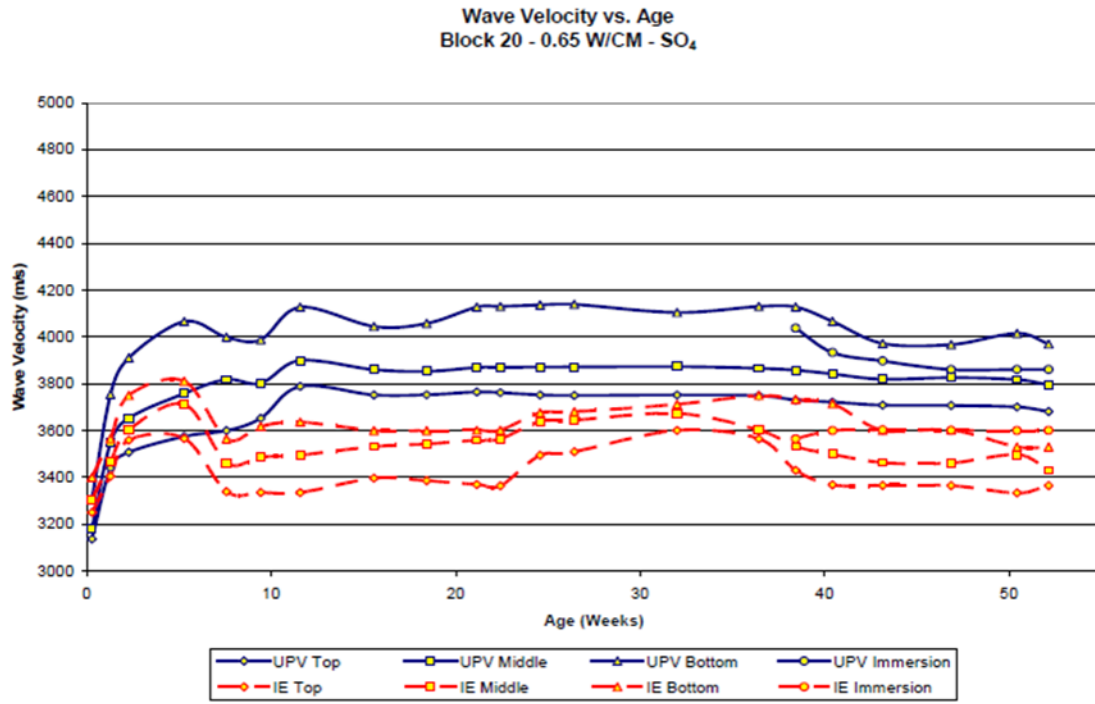
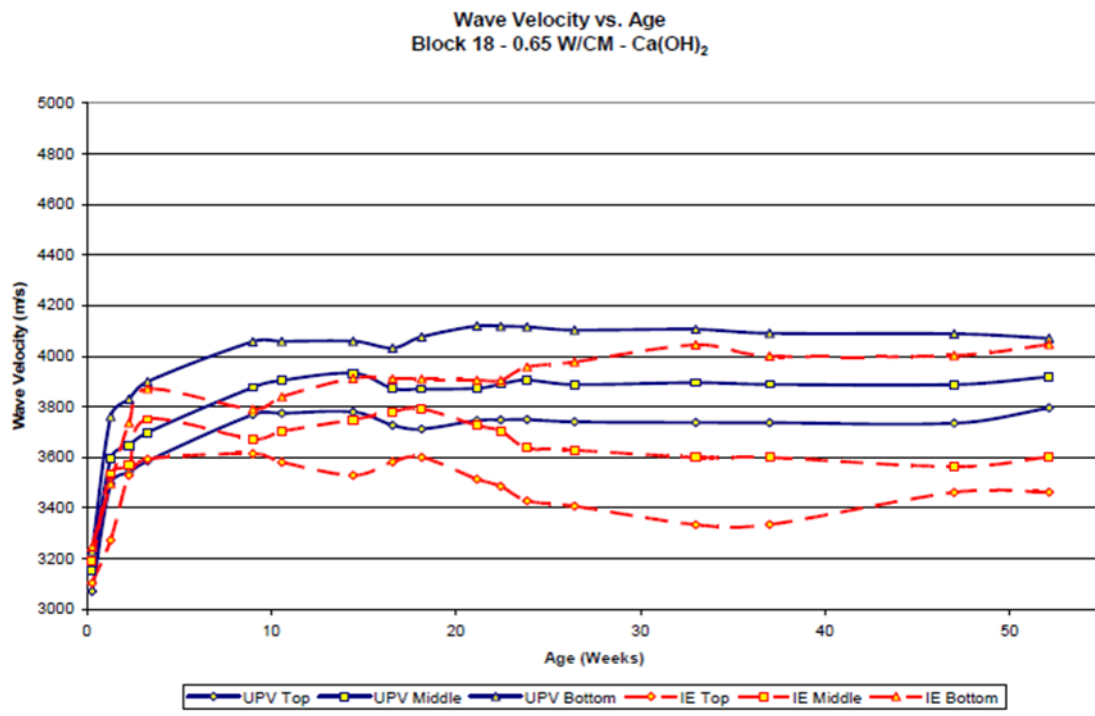


Figure 2-22. Wave velocity results from lime water immersed (top) and sulfate solution immersed (bottom) concrete blocks. Note the decay in wave velocity for the sulfate exposed block [25].

Boyd's experiment contained several interesting results of note to the research contained in this thesis. First and most obvious, there was a notable difference in the wave velocity between the top, middle, and bottom testing locations on the concrete block even in the control blocks. This can be attributed to compaction and segregation during casting of the blocks as well as differential curing. This result is a major reason why the majority of laboratory blocks used in this thesis were cast horizontally. Secondly, a rise in wave velocity as the concrete fully hydrates is noted, remaining constant in the case of the lime water saturated panels. The blocks exposed to sulfate solution, however, showed a decrease in wave velocity at later ages with a more dramatic decrease farther down the block. This result suggests the sulfate attack mechanism verified by SEM images and other data [25].

Nondestructive evaluation of alkali-silica reaction

In order to evaluate the effectiveness of several non-destructive test methods to detect the presence of alkali-silica reaction (ASR) in concrete, Maryam Sargolzahi et al. engaged in a series of laboratory trials applying NDE methods on cylinders fabricated from ASR reactive and nonreactive materials [26]. Prisms were also cast from the batches to be tested in accordance with Canadian standard CSA A23.2-14A, a measurement of expansion used to quantify the presence of ASR.

In addition to a mechanical test of the specimen compressive strength and elastic modulus, Sargolzahi performed the following non-destructive tests in an attempt to quantify the severity of ASR

- UPV
- Dynamic modulus of elasticity
- Nonlinear frequency shift and harmonic generation
- Petrographic examination

Of particular interest to this thesis is the investigation using UPV as wave velocity can be easily gleaned from the shear wave ultrasonic array in a manner analogous to the indirect UPV method. While Sargolzahi noted that UPV did correlate well to ASR expansion by showing a reduction in wave velocity due to the increase in void fraction within the specimen, the research showed that the technique is not particularly sensitive when compared with other methods [26].

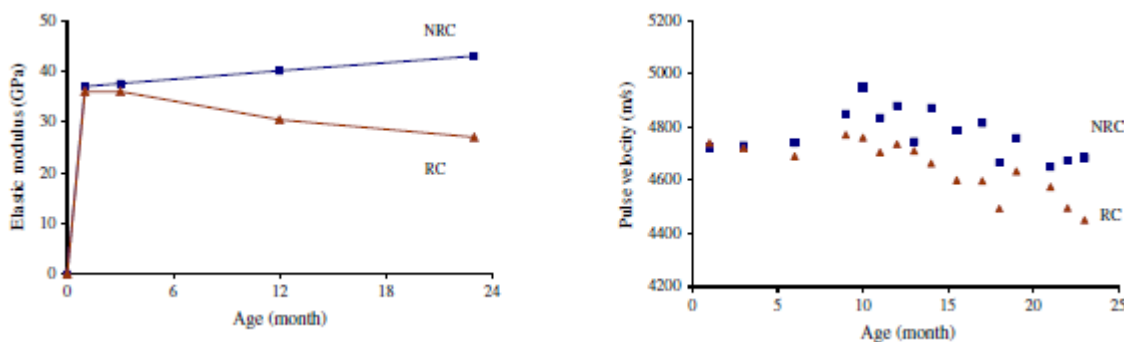


Figure 2-23. Results of Sargolzahi's research using UPV to detect ASR. Data in blue is from nonreactive specimens while orange is ASR reactive. The static elastic modulus test (left) showed excellent sensitivity compared to UPV (right) [26].

The results of Sargolzahi's research dissuaded the research team involved in this thesis from investigating ASR using the automated system at this time. With the recent success of chemical tests for ASR using dye indicators, a better approach may be to use a chemical method coupled with vision acquisition to automate early age detection of ASR in future research.

Related NDE Research: Structural NDE

Geometry and Locating Applications

Introduction

One of the most basic requirements of NDE as applied to concrete structures is to verify the structure was built per design. This verification often involves simply

checking the geometries of the finished structure to ensure formwork was installed accurately and reinforced sufficiently to prevent bulging. In many cases, however, portions of the structure are inaccessible and a reliable measurement cannot be made. This includes situations such as concrete pavements, foundations, and headwalls. NDE methods are frequently called upon to reliably perform these thickness measurements. Perhaps even more frequently, NDE methods are used to verify the placement of reinforcement *within* the concrete structure in a method known by the generic term as locating. The applicability and effectiveness of NDE methods used in the body of this research for these purposes will be investigated.

Applications of ground-penetrating radar for pavement thickness measurements

Since ground-penetrating radar has recently become popular for structural concrete applications, most research into thickness measurements using GPR originates from a desire to rapidly measure pavement thickness. Pavement thickness measurements do, however, present an interesting problem as the desire is usually to measure a single layer of the composite pavement and the individual layers frequently do not have very disparate dielectric constants. Given these challenges and the extreme speed and accuracy demands of the pavement industry, such applications of GPR are worthwhile to consider as an automated GPR system to measure structural concrete element thickness is developed.

While Al-Qadi and Lahouar focused their research primarily on hot-mix asphalt (HMA) pavements, their methods for interpreting GPR data to determine pavement thickness are certainly valid for concrete. In the course of their research, Al-Qadi and Lahouar showed that their GPR measurements for the thickness of an HMA layer taken using a high speed, air-coupled GPR system closely followed the actual layer thickness.

Their method for showing this involved scanning a special test road in Virginia which has multiple copper plates placed under the HMA layer on top of the base layer. The copper plates show up exceptionally well on GPR and can be taken as a “true” reflection when attempting to distinguish reflections between pavement layers [20].

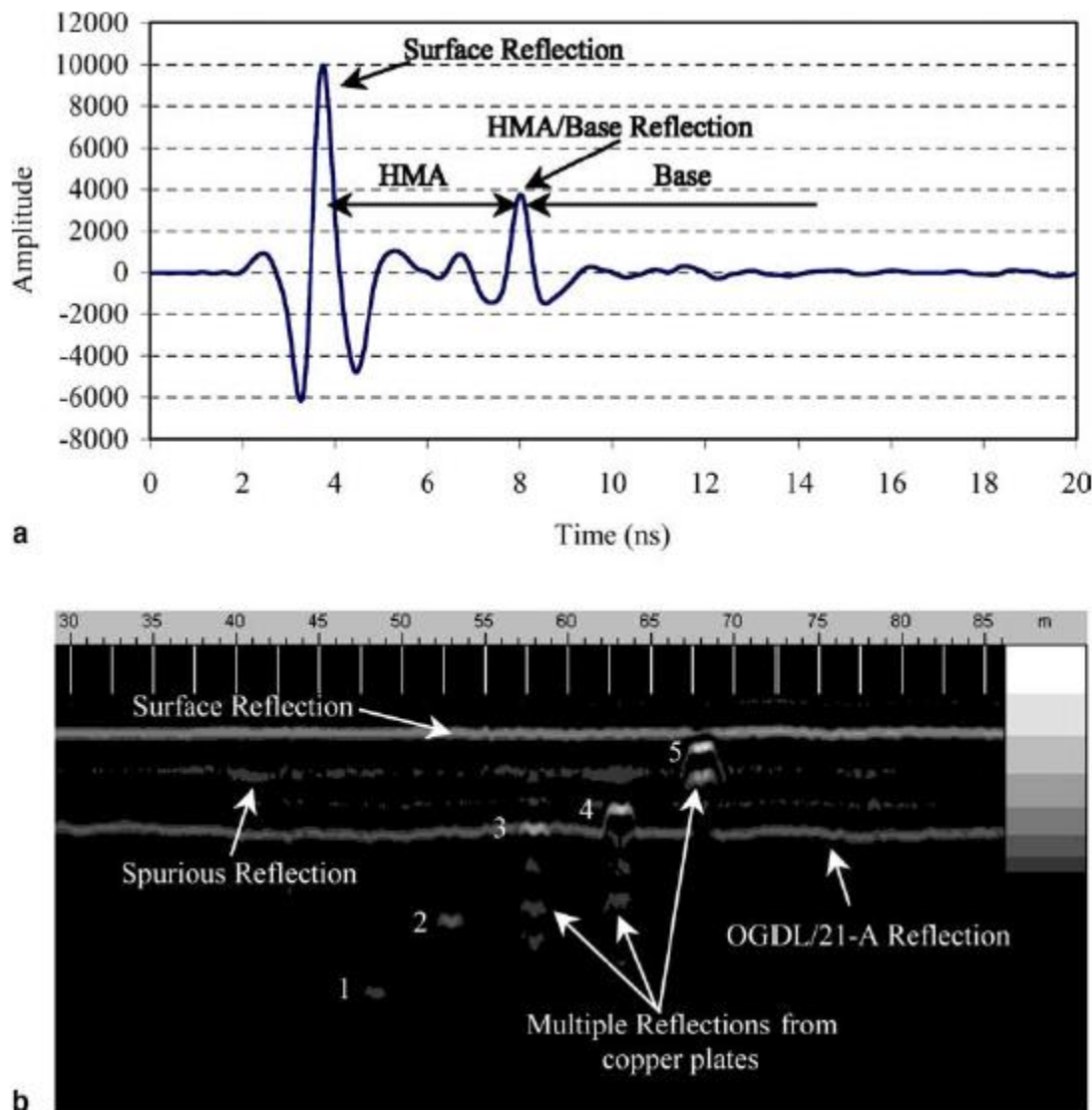


Figure 2-24. Data taken in Virginia by Al-Qadi and Lahouar. Note the clear reflections from the embedded copper plates [20].

A number of important details are to be noted from this GPR research. First, the processing techniques are readily applied to the GPR processing algorithms to be developed herein. Secondly, the idea of using a metal plate to create a known reflection using GPR could be readily applied to measuring the thickness of concrete elements. In situations where the back side of an element is accessible, a metallic plate could be adhered to the concrete surface and quickly found using GPR on the other side for an accurate thickness measurement.

Comparison of multiple NDE methods for slab thickness measurement

Validation of NDE methods for their various applications is an important function of many research entities. To this end, Ralf Beutel and his research group used a specially design concrete specimen in Berlin, Germany consisting of realistic but well documented intentional defects to evaluate the abilities of several different impact-echo, ultrasound, and GPR methods [27]. Their primary intent was to certify the instruments for quality control purposes in detecting slab thicknesses, locating reinforcement, and detecting delaminations, contaminants, and other flaws. Of particular importance to the research contained in this thesis was the comparison of acoustic and radar techniques for reinforcement locating and geometry measurement purposes.

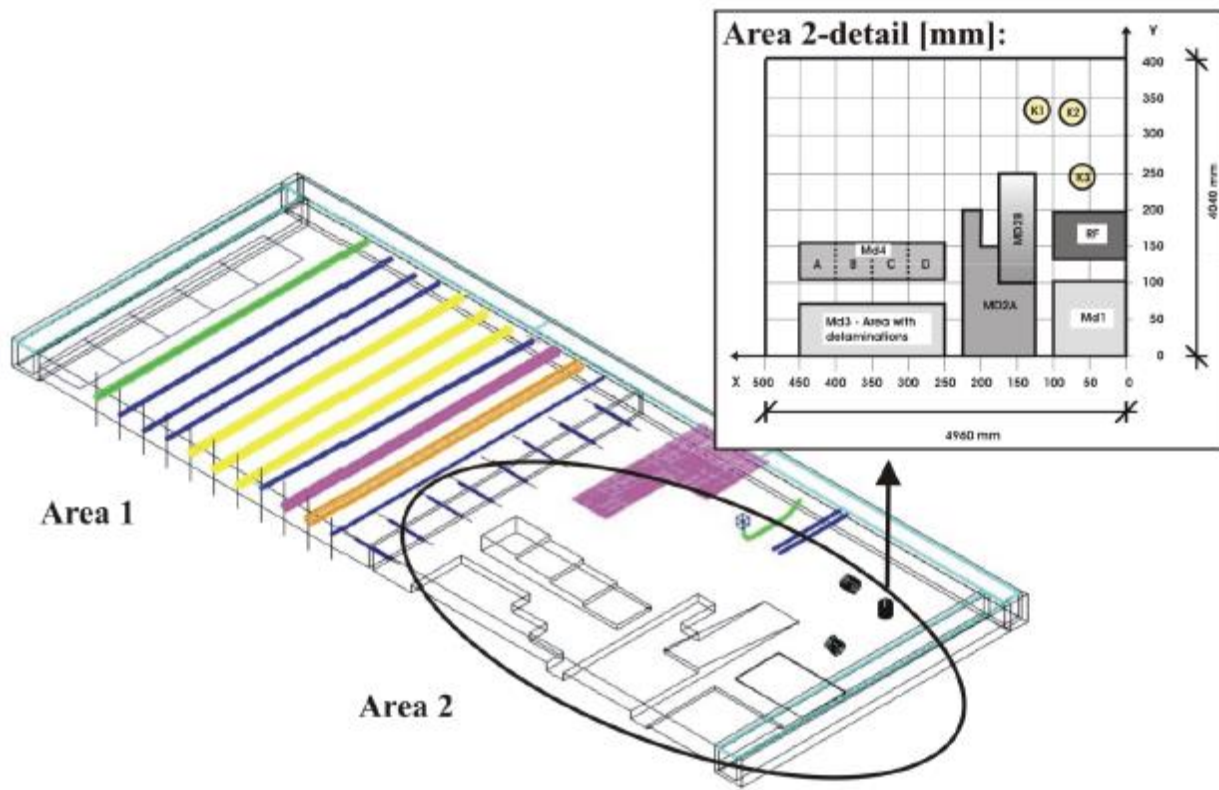


Figure 2-25. Concrete slab in Berlin used by Beutel and other researchers. The block consists of known defects, reinforcement locations, and dimensions, including sudden changes in geometry [27].

The research conducted by Beutel established confidence in all the techniques used in the study and proved the reliability of appropriate acoustic and radar techniques to measure concrete thickness and locate rebar and post-tensioning ducts [27].

Beutel's comparative research established several sound practices and a significant amount of confidence in the NDE instruments used in this research. His exhaustive study of a multitude of different methods, including multiple instruments of each individual instrument type, was invaluable for the work discussed in this thesis.

Detection of Flaws

Introduction

Flaws within a concrete structure are both difficult to observe and have the potential to severely compromise the integrity of a structure. A “flaw” within concrete from the perspective of a fabricator or inspector can include any number of things: cracks, air voids due to poor consolidation, water pockets due to bleed, contaminants such as construction debris, waste, organics, etc. NDE methods are usually called upon to evaluate the extent of a known flaw, such as measuring the depth of a crack in a bridge pier. Most of the research discussed in this section will be motivated as such, however once automation is considered it is necessary to address NDE methods in a quality control capacity, detecting unknown flaws within a structure before they become apparent.

Comparison of NDE methods for concrete bridge deck evaluation

In order to provide a comprehensive comparison of several popular NDE techniques for use on concrete bridge decks, Scott et al. engaged in a study of four NDE methods used on the Van Buren Road Bridge over Quantico Creek, Virginia. Scott and other researchers employed chain dragging, impact-echo, and two forms of GPR to evaluate the condition of an aging bridge deck and compare the test results with cores taken from the structure [28]. The data was overlaid with a map of the known defect areas and used to compare the effectiveness of the NDE methods.

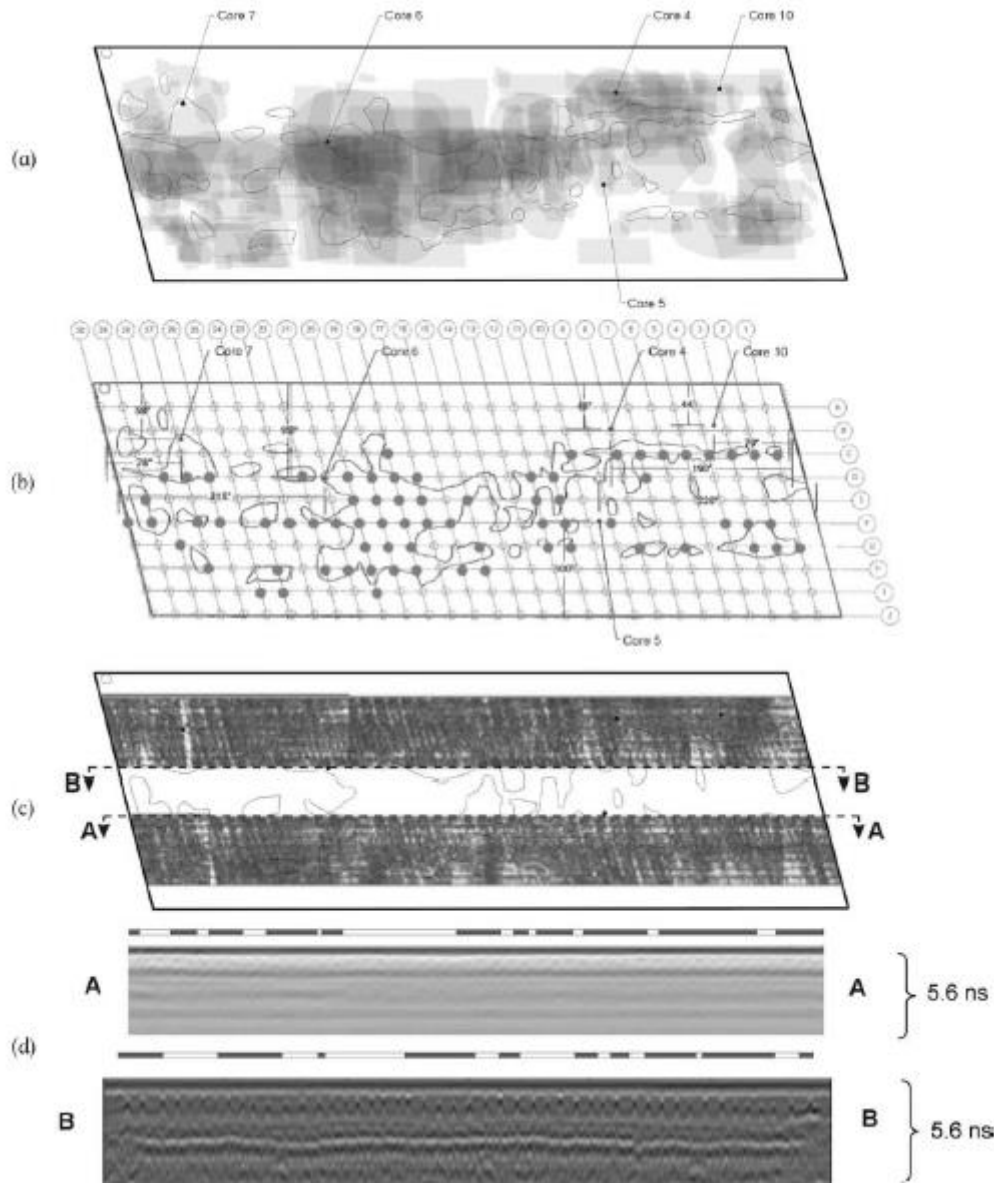


Figure 2-26. Results from Van Buren Road Bridge NDE study overlaid with defect map.
 (a) Chain-dragging with suspect areas shaded (b) Impact-echo with dark spot suspect locations and (c) GPR scans with section AA from proprietary HERMES system and section BB from GSSI system similar to the one used in this thesis [28].

The major cause of distress in the Van Buren Road Bridge is delamination of the concrete layer from the rebar mat nearest the surface of the bridge deck. This is a common mode of failure for concrete bridge decks and is usually fairly easy to detect

using acoustic methods, especially when a scanning system is used to increase data point density.

The most important information to glean from this particular study is the reliability of impact-echo, and indeed any acoustic method, in detecting planar air voids within a thin plate-like structure of reinforced concrete. Indeed the map provided by Scott showed very close correlation between suspect areas detected with impact-echo and the contours developed by taking cores. By contrast, GPR is fast and effective and characterizing large areas of a bridge deck very rapidly, but must be carefully analyzed and is prone to missing smaller defects [28].

Mr. Scott's study was especially useful in the course of this thesis as one of the main applications for an automated NDE scanning system for FDOT would be evaluation of aging bridge decks. The study suggests a combination of GPR to rapidly detect areas of significant damage where applicable followed by a slower, methodical application of acoustic echo for precise detection of air voids. A major conclusion of the study—that acoustic methods are extremely effective in evaluating aging bridge decks subject to delamination but highly limited by their speed of application—is addressed within this thesis.

Nondestructive evaluation of post-tensioning systems

Recently, demand has been placed on the NDE community in the United States to develop advanced methods for evaluating post-tensioning ducts in segmentally constructed structures. Post-tensioning is used to assemble pre-cast reinforced concrete segments into a functioning structure and can consist of high strength threaded rods or long, steel, multi-wire strands passed through adjacent segments and tensioned. Between the two methods, multi-wire strands are usually selected for long

structures such as segmental bridges due to their relatively easy installation procedure, a manufacturing procedure that allows very long development lengths, and comparatively low cost.

Multiple strands are combined to form a single tendon, contained either internally in ducts embedded in the concrete structure or externally in ducts spanning the interior space of a segment from one diaphragm to the next. Depending on the design of the segments, multiple strands may be used for each tendon, and multiple tendons may be used in each segment.

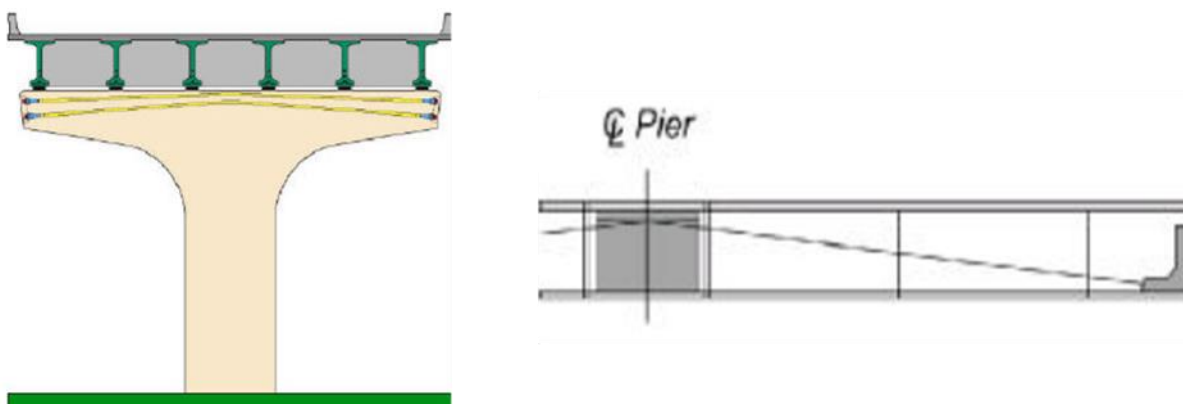


Figure 2-27. Typical tendon locations. Internal tendon ducts in a hammerhead pier (left) and external tendon ducts in a box girder (right) [29].

After installation and tensioning of the tendons, the ducts are filled and pressurized with specialized grout designed to promote load transfer between the tendon and the structure and most importantly protect the mild steel strands from corrosion. The result is a multi-layer protection for the tendon that is usually highly effective in preventing corrosion of the post-tensioning tendon.

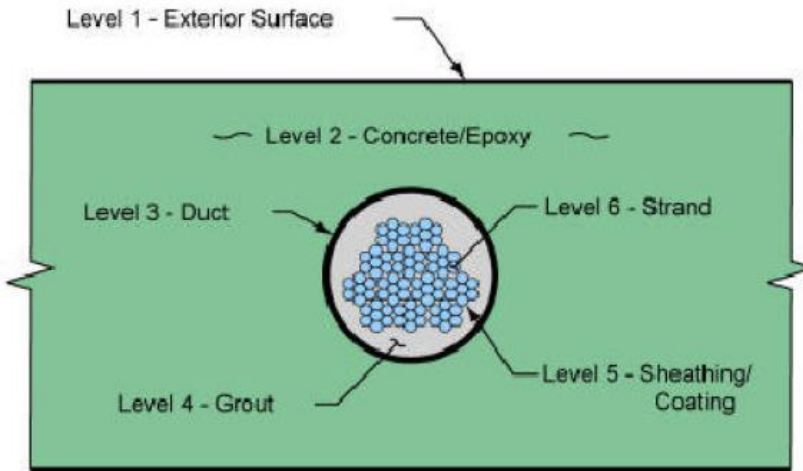


Figure 2-28. Layers of corrosion protection in a typical post-tensioning tendon [29].

Recently, a number of premature failures of post-tensioning tendons has been noted across the United States. Many of these failures were traced back to improper grouting. Void spaces left in the grout within a post-tensioning duct allow infiltration of water and corrosive agents which attack any and all exposed strands, resulting in a catastrophic loss in tension. Left unchecked, this failure will inevitably lead to loss of structural capacity [29].

Martin Krause and other personnel at the German Federal Institute for Materials Research and Testing (BAM) have researched non-destructive methods to investigate grout quality within post-tensioning ducts. Through Krause's research, a comprehensive comparison of radiographic, impact-echo, ultrasonic echo, and radar techniques for evaluating voided internal post-tensioning grout is presented.

Among Krause's important recommendations are the use of GPR for evaluating internal post-tensioning ducts where the ducts are made of plastic and not steel. While steel ducts are common in older structures, current practice in the State of Florida allows only plastic internal ducts.

Additionally, important data processing and interpretation methods are presented for acoustic techniques. Using Synthetic Aperture Focusing Technique (SAFT) and carefully designed data displays, the full-field image developed from ultrasonic echo scanning clearly shows defected areas within the post-tensioning ducts and lends credibility to the technique as a whole [30].

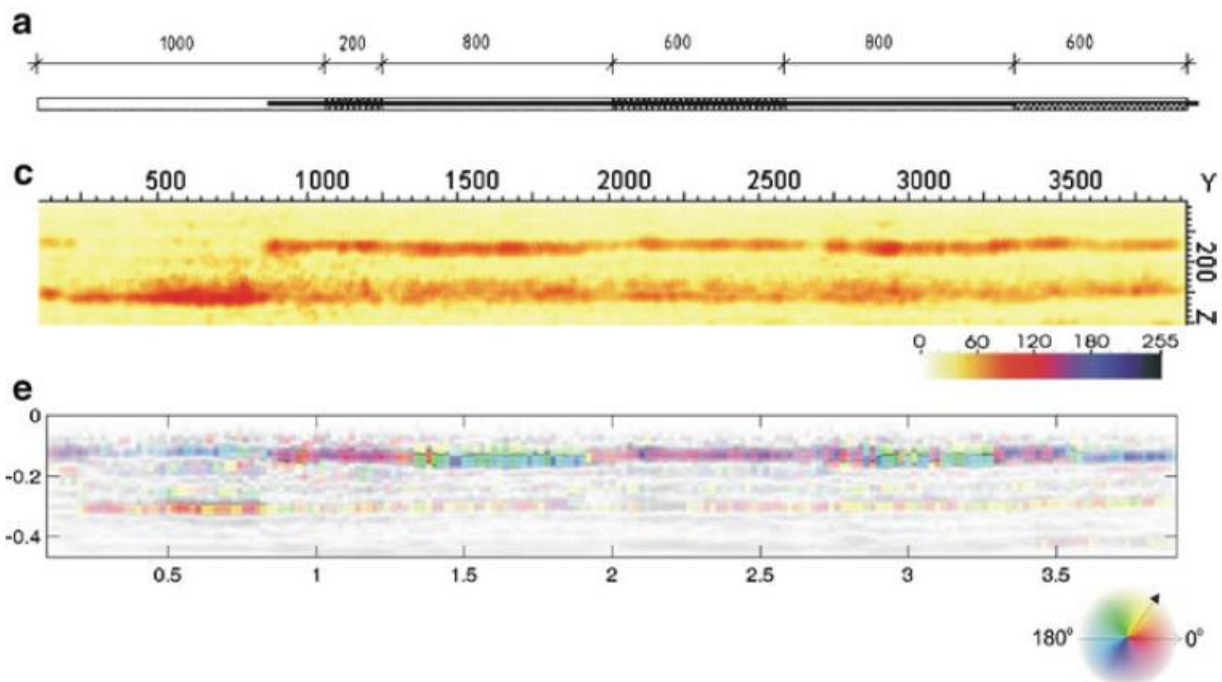


Figure 2-29. Ultrasonic echo results from Krause's research using a similar instrument and scanning device to that used in this thesis. Plan view showing defected areas (top) B-Scan (middle) and phase-displayed B-Scan (bottom) [30].

Ultrasonic echo is the principal method used in evaluation of post-tensioning ducts in this thesis with GPR used a supplementary method. The research performed by Krause and the rest of the concrete NDE scientists at BAM is considered the foundation for the work performed herein.

Damage Assessment

Introduction

In the case of catastrophic damage to an in-service structure by act of man or act of God, engineers are called upon to rapidly and accurately assess the condition of the structure and dictate repair or replacement procedures. Historically, the tools available to these individuals have been highly limited. Practices exist for conservative visual inspection of structures damaged by natural disaster, impact, and thermal events, however a common application of NDE technology and a major area of NDE research is to quantitatively evaluate the extent of damage to an in-place structure to better recommend appropriate repair procedures. This application of an automated NDE system for use in the State of Florida cannot be ignored.

Nondestructive evaluation of fire damage

While an inherently fire-resistant material, concrete exposed to sufficiently high temperature for long periods of time exhibits a number of unfavorable property changes. If concrete is well hydrated and relatively impermeable, temperatures higher than the boiling point of the free water within its microstructure may result in superficial spalling as the vapor pockets expand beyond the strength of the concrete surface. Sustained material temperatures above 300°C will result in interlayer and some chemically combined water being driven off. Microstructural cracks will also be observed above this temperature as differences in the thermal properties of the constituent materials results in crack initiation at the interfaces and a significant loss of strength and elastic modulus. Decomposition of calcium silicate hydrates (C-S-H) begins at around 500°C and ends around 900°C resulting in an unrecoverable loss of strength in the paste [8].

Frequently in the event of fire damage to a structure, only small portions may need to be repaired or replaced due to the very low thermal conductivity of concrete. NDE methods are frequently used to evaluate the extent of thermal damage to better reduce the cost associated with repairing a fire damaged concrete structure. In the early 2000s, Matteo Colombo and Roberto Felicetti of the Politecnico di Milano in Milano, Italy engaged in a research program to evaluate the effectiveness of multiple NDE methods to rapidly evaluate the extent of thermal damage sustained by concrete structures. To test the NDE instruments, in depth analyses were conducted on laboratory specimens as well as two full-scale structures subjected to fire damage.

Among their many contributions, Colombo and Felicetti established correlations between uniformly heated specimens and several NDE parameters including UPV reading and digital image colorimetry. Indirect UPV was found to be extremely sensitive, though time consuming to apply and difficult to apply to anything but flat surfaces. Loss in ultrasonic pulse velocity within a structure is also directly correlated to a loss in elastic modulus, therefore no calibration data for the particular concrete mix is necessary when this technique is applied appropriately to evaluate fire damage. Digital image colorimetry also showed great promise for rapid evaluation of concrete with well characterized constituent materials [31].

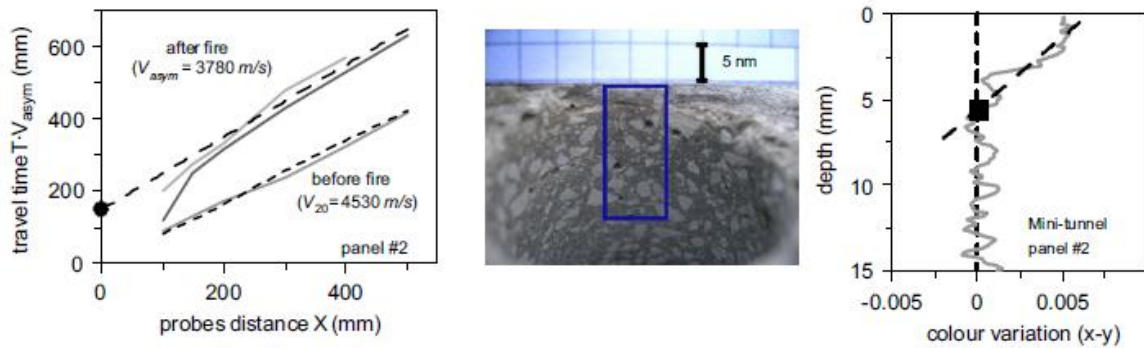


Figure 2-30. UPV results of a fire damaged concrete panel (left). Color variation in a section of a small core with a fire damaged surface (right) [31].

For the purposes of the work contained in this thesis, the research performed by Colombo and Felicetti established a new application for the automated system. Ultrasonic pulse velocity may be readily derived from data taken using a shear wave ultrasonic echo array and the included vision system can be rapidly adapted to perform colorimetry calculations. While neither application is within the scope of this project, it is a logical future application to be promoted.

Nondestructive evaluation of impact damage to concrete bridge piers

The removal of a functionally obsolete bridge in Apalachicola, Florida provided researchers with a unique opportunity to study the behavior of a concrete bridge pier when impacted by a barge or other large vessel. Such a mode of damage had not been previously studied, but was the cause of the tragic collapse of the Sunshine Skyway Bridge spanning Tampa Bay, Florida in May of 1980. The freighter M.S. *Summit Venture* veered off course in poor weather and struck Pier 2S, sending the main southbound span into the Bay and 35 people to their death. A photo of this tragic accident is shown in Figure 2-31.



Figure 2-31. Collapse of the southbound main span of the Sunshine Skyway Bridge. Thirty-six motorists fell into Tampa Bay, only one survived (Photo courtesy of St. Petersburg Times) [32].

In the Barge Impact Study, a partially-laden barge was driven at low speed into heavily reinforced, load instrumented impact blocks mounted to the targeted piers. The structural research authorities involved in the study monitored the deformation of the blocks using various instruments and high speed cameras to refine models intended for use in developing more impact-resistant bridge piers in the future.

In parallel with the structural data gathering teams, Christopher Ferraro and other material researchers performed ultrasonic pulse velocity tests on the impact blocks before and after barge impact. Using a dense grid of UPV readings, Ferraro constructed a three-dimensional tomograph of the impact blocks illustrating the change in ultrasonic pulse velocity correlating to the areas of damage experienced by the block [2].

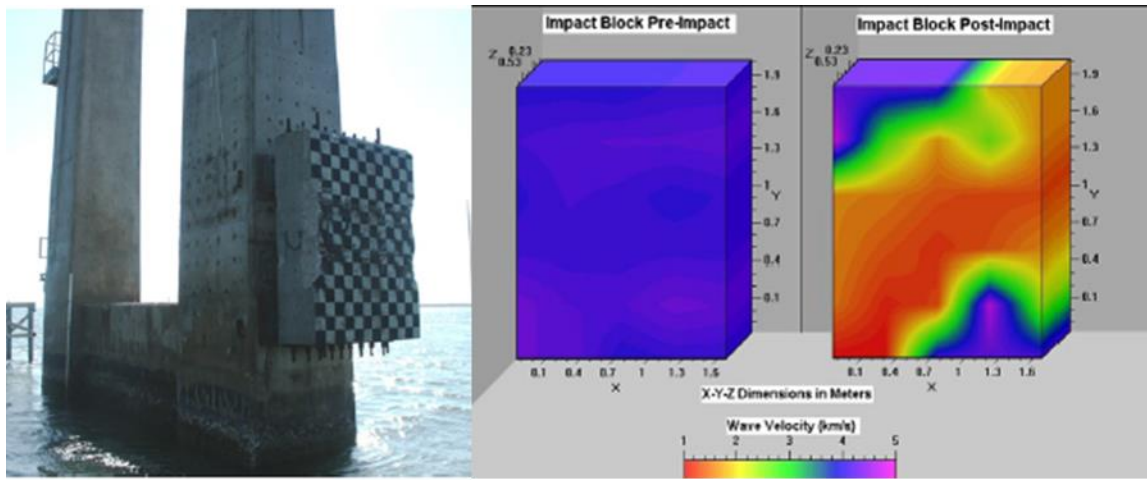


Figure 2-32. Impact block (left) and UPV tomograph (right) after barge impact. While the severely damaged area of the block was clear, the tomograph gave indications of sustained damage far from the impact on the block as well as the pier upon which it was attached (Photo courtesy of C. Ferraro) [2].

Perhaps the most important information gleaned from Ferraro's research is the requirement of highly dense measurement grids when using ultrasonic tomography to generate a clear snapshot of the damage sustained by a structure. While most inspectors would have thought it prudent to take a few UPV readings on and around the impact block to verify the level of damage to the structure, a full tomographic characterization of the structure better defines the extent of damage and is far more valuable to assessing the need of repair or replacement in the event of catastrophic impact.

Related NDE Research: Automation in NDE

Introduction

A common trait amongst NDE research considered to this point is the need for dense, repeatable data grids to produce reliable data. Most NDE researchers would agree that there is simply no replacement for more data, especially when trying to detect small defects in an area of heavy reinforcement. The need for automation in

structural concrete NDE is obvious, and several institutions have invested heavily in developing automated NDE systems capable of producing very dense scan areas. This section will acknowledge the two most influential sources for this work, though many other organizations are actively contributing to the development of automated concrete NDE.

Federal Institute for Materials Research and Testing (BAM) Berlin, Germany

One of the first organizations to act on the need for automation in concrete NDE, the Federal Institute for Materials Research and Testing (BAM) in Berlin, Germany has spent years developing a multitude of different NDE scanning systems. Under the leadership of Herbert Wiggenhauser, BAM Division VIII.2 has developed vertical and horizontal two-dimensional scanning systems with pneumatic instrument application devices. With sophisticated data acquisition, revolutionary data processing and data fusion techniques, and the ability to use shear wave ultrasound, impact-echo, GPR, and a multitude of other instruments, BAM remains at the cutting edge of automated NDE research. [33]

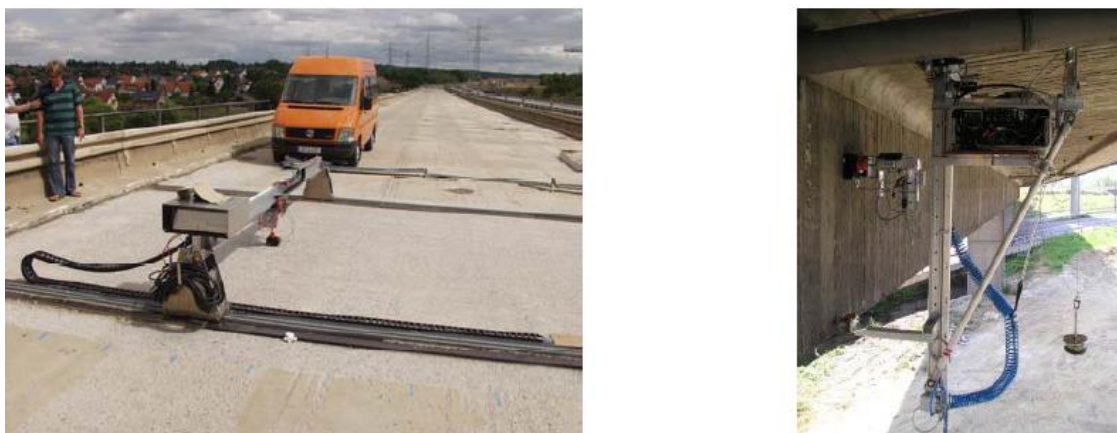


Figure 2-33. Horizontal (left) and vertical (right) scanning systems developed at BAM for use on concrete structures (Photo courtesy of BAM) [33].

The research and development performed at BAM and the cooperation between their organization, the Florida Department of Transportation, and the University of Florida have led directly to the developments contained in this Thesis. Indeed, the basis of the scanning system used in this work comes from designs generated at BAM.

**Florida Department of Transportation State Materials Office (FDOT SMO)
Gainesville, Florida**

Following in the groundbreaking research by BAM, the Florida Department of Transportation State Materials Office (FDOT SMO) in Gainesville, Florida requested a research program in the early 2000s to validate NDE equipment used throughout the State. The result was an automated scanning system similar to that used in BAM designed and developed by one of their scientists, Daniel Algernon.

In the course of his post-doctoral research at the University of Florida, Dr. Algernon and his team developed a pair of precision automated scanning systems with pneumatic instrument application devices. The scanning systems were operated remotely using programs developed by Algernon in National Instruments LabVIEW™. The system ultimately operated and collected data from a covermeter, impact-echo, and shear wave ultrasound device and verified the instruments using four laboratory specimen blocks constructed with known features and defects. The result was a “first-stage” NDE validation facility for use by the State of Florida [9].

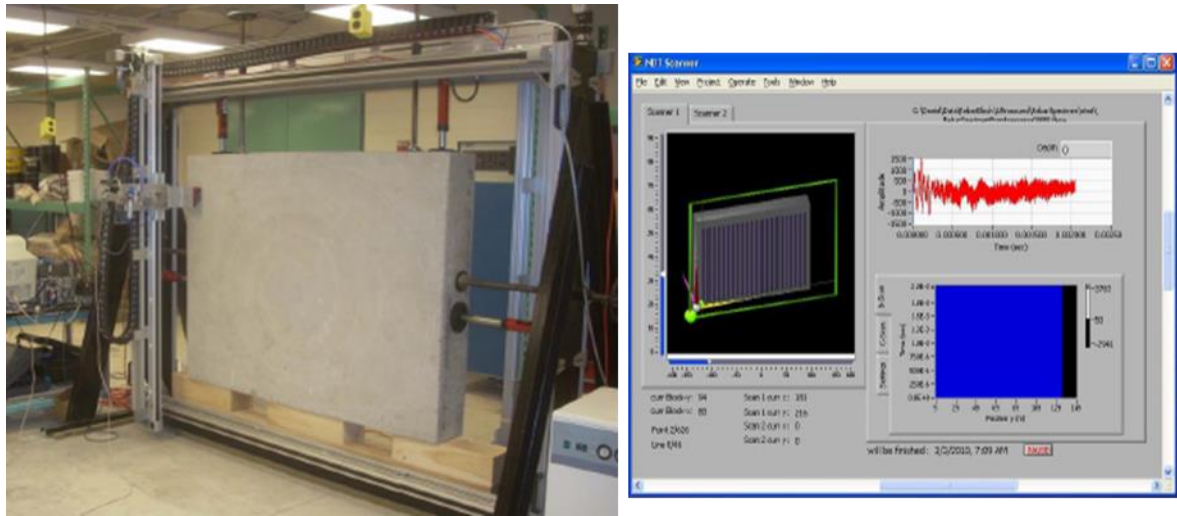


Figure 2-34. Scanning system (left) and software (right) used by Algernon. This system formed the starting point of the research discussed in this thesis (Photo courtesy of D. Algernon) [9].

The work by Algernon, et al. lead directly into the research discussed in this thesis. The first stage facility, referred to subsequently as the Phase I system, developed by Algernon was an excellent starting point for the FDOT SMO as they ventured into automated NDE research. The SMO required improvements to hardware and communication systems of the scanner systems themselves, the incorporation of new instruments, a redesign of the operating software, a suite of improved data processing software, and further research using new laboratory specimens to effectively create a system their personnel could use in the laboratory and field to rapidly take dense, reliable, easily interpreted NDE data. These are the goals the research contained herein sought to achieve.

CHAPTER 3 DEVELOPMENT STRATEGY

Project Starting Point

The scanning system developed in the course of the postdoctoral research by Algernon was left with the Florida Department of Transportation State Materials Office and inherited in this research effort. While the system was very effective for its original purpose, several deficiencies were noted by FDOT that were to be addressed in this phase of automated NDE research.

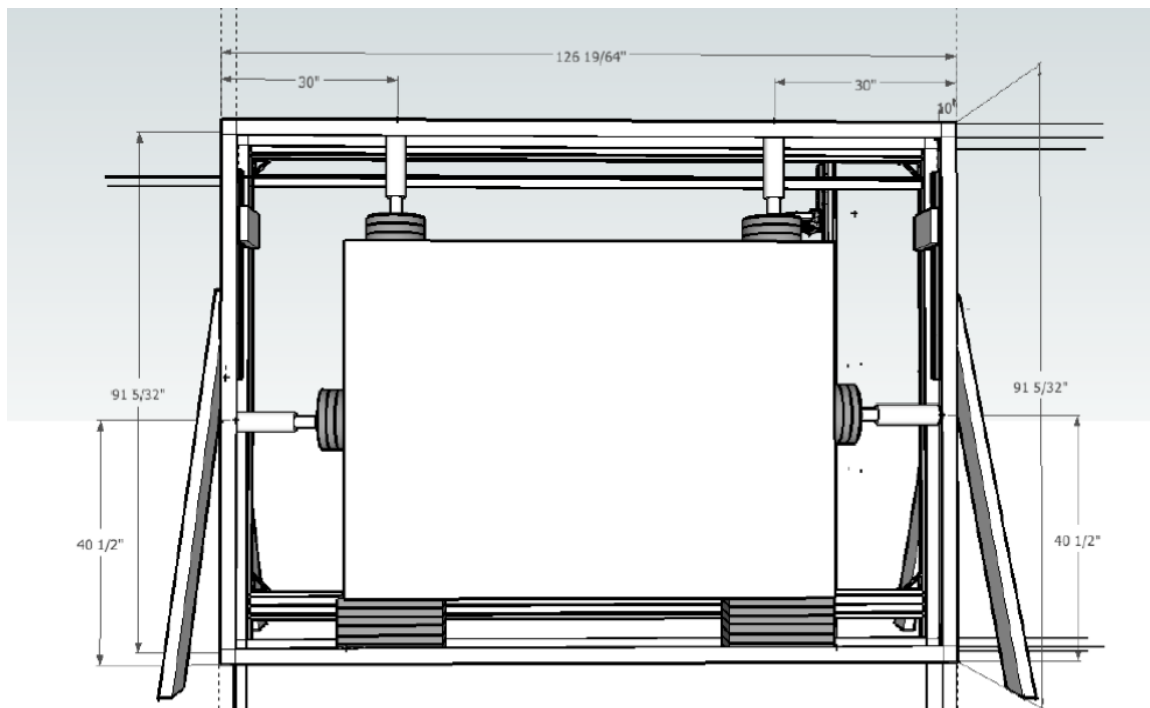


Figure 3-1. CAD drawing of as-built scanner systems mounted to block clamping frame.

The two electric scanning gantry frames, each measuring approximately 3.65 by 2.75 m, were operated by a National Instruments PXI chassis with embedded computer through a combination of serial and analog voltage interfaces. This configuration required a separate serial cable for each of the two stepping motors for each scanner and a custom-built, four conductor cable for each scanner's pneumatic cylinder used to

apply instruments to the concrete specimen surface. These interfaces were unreliable, fragile, difficult to manage, and much more expensive than a single digital interface. Furthermore, since so many data interfaces were needed the scanning systems were unable to be operated at the same time; when switching to a different scanner the operator had to physically disconnect the first scanner's data cables and connect the second. The PXI itself was also a liability as it is a large, expensive, fragile piece of equipment requiring special care and attention to function correctly.

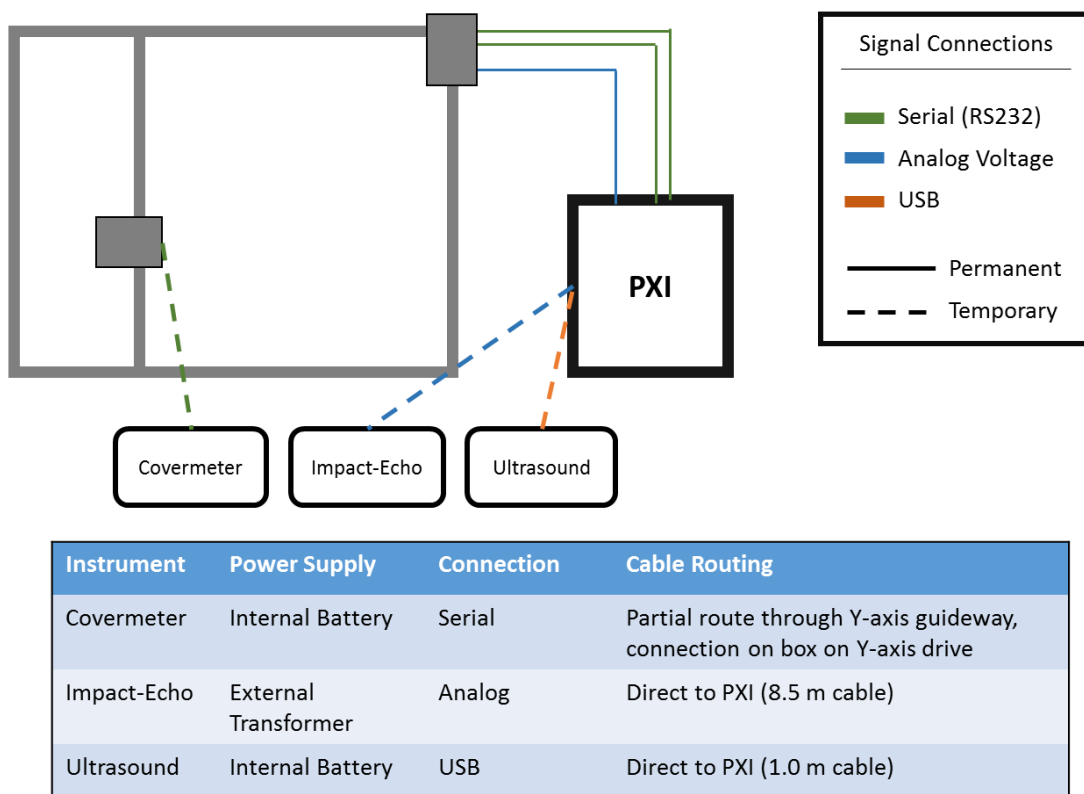


Figure 3-2. Instrument and scanner connection scheme of the Phase I FDOT automated NDE system.

NDE instruments were physically attached to the moving instrument head using an improvised mount consisting of elastic bands and cable ties with their own unique data cables painstakingly routed through the cable guideways on the scanner drives.

The result was a clumsy, time-consuming mounting process that left the instrument open and susceptible to damage from impact, water spray, etc. At best, a serial-based instrument such as the Proceq Covermeter took 20-30 minutes to connect to the scanner, undergo cable routing, and connect to a remote serial port. In the case of the German Instruments EyeCON™ shear wave ultrasound device and the Olson Instruments impact-echo device, the instrument had to be connected directly to the PXI chassis using their own proprietary cables, leading to situations where short cables mandated close placement of the PXI to the scanner and created the potential for dangerous entanglement of cables during operation.

The operating software itself was also identified by FDOT as insufficient for the next phase of automated NDE development. While the software performed well for research purposes, it was far too complex for effective use by technicians and prone to poor behavior when used improperly. The software package also included little room for expansion as new instruments were incorporated into the system.

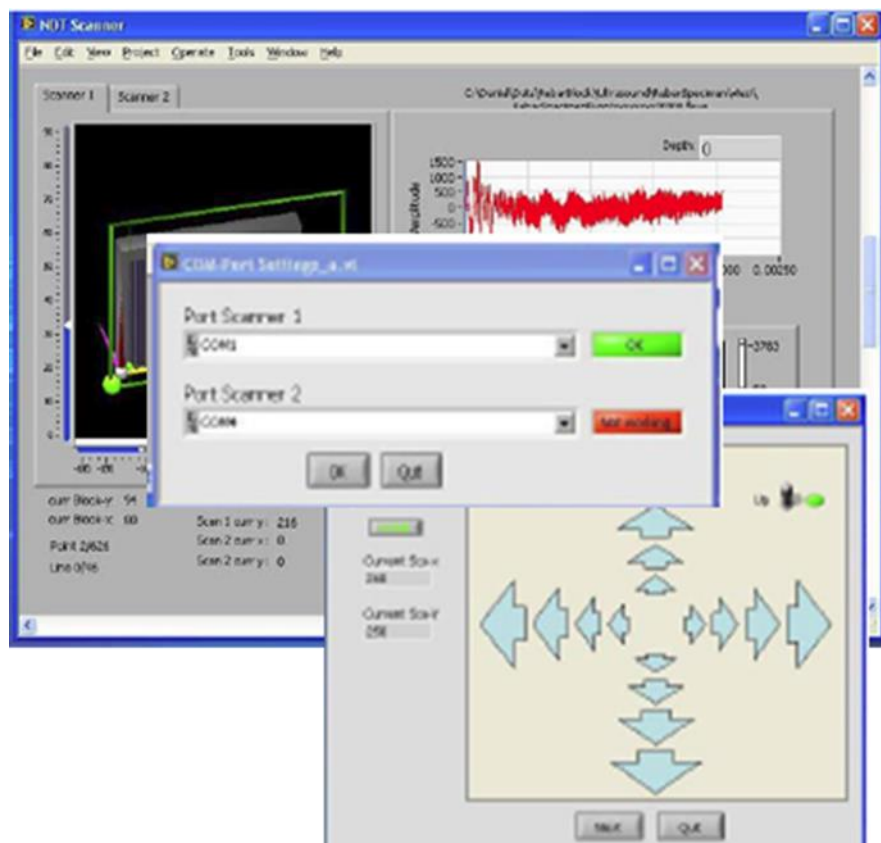


Figure 3-3. Phase I scanner operating software based in multiple subroutines and windows, leading to an overly complicated interface.

Design Goals

Expanding the Capabilities of the FDOT NDE Validation Facility

The FDOT NDE Validation Facility or Phase I system established by the research performed by Algernon, et al. was an excellent first stage facility for the FDOT's foray into automated NDE. A logical next step in development for the FDOT was to expand the capabilities of the Phase I system by generally improving the hardware and software interfaces for better system survivability, integrating additional NDE instruments, rebuilding the system around a more cohesive and advanced software package, designing and constructing new NDE validation blocks, and proving the system as a whole is viable for deployment in the field on real world infrastructure

components. This need for research as expressed by the FDOT was addressed by the research team in the course of this thesis.

Hardware Improvement

FDOT expressed several deliverable goals in the design of this research effort in terms of ruggedizing and simplifying the ways in which the automated scanning system interfaces with the system operating computer. First and foremost, if the scanners were to be successfully used in the field the overly complicated mixed signal interface had to be simplified. The research team addressed this need by proposing an all-digital interface handled through manufactured, off-the-shelf cables. In order to make the connections more robust, the research team proposed signal connections be systematically moved from cheap fragile connectors to washdown-rated sealed connectors. Additionally, improved methods of mounting and protecting the instruments on the scanning system were to be designed and implemented.

Integration of Additional NDE Instruments

While the Phase I automated NDE system included an eddy current covermeter, shear wave ultrasound, and impact-echo system fully integrated with the scanning hardware and software, FDOT recognized the need to include several new instruments with the system to keep up with the rapidly expanding NDE instrument market. The new instruments proposed by the research team were a ground penetrating radar (GPR) system, a laser distance sensor used to profile the specimen surface, and a high resolution camera system with embedded vision processing computer. FDOT was already in possession of the GPR and laser profilometer devices however they were not successfully integrated with the scanning hardware and software in the earlier research phase.

Redesign of Software

The software package originally developed to operate the scanning systems worked extremely well for the first stage research it was designed to fulfill. FDOT requested a more comprehensive, robust, and user-friendly software package for the second phase of their automated NDE research. The research team proposed a new operating software package designed from the ground-up in National Instruments LabVIEW™ to be as user friendly and robust as possible while still allowing expansion in the future. Additionally, the software was to fulfill the need of real-time data visualization while using the scanner as an additional source of feedback for the operator. An additional software package for processing data into two and three dimensional displays was also to be developed as part of this research effort.

Construction of Additional NDE Evaluation Blocks

The NDE Evaluation Blocks produced for FDOT by Algernon, et al. are an invaluable tool to compare NDE systems and methods when applied to controlled, well documented structural features and defects. FDOT wanted to expand upon this capability by producing two additional blocks. The first block would address evaluation of internal polypropylene post-tensioning ducts where potential defects include air voids, water inclusions, and soft grout in the grouted tendon ducts. The second block would be used to evaluate NDE instrument effectiveness in locating cracks, honeycombing, and delamination of reinforcing steel.

Field Deployment

After all the aforementioned improvement to the automated NDE system were implemented successfully, FDOT requested a trial field deployment of the system to evaluate the feasibility of using the system to evaluate the condition of real world

structures *in situ*. The field deployment was to be performed at the discretion of the research team and could be a vertical or horizontal application of a single or both scanning frames. The research team delayed choosing a site and time for deployment until the scanning system was sufficiently complete and FDOT could recommend a site that would offer them a useful set of data for their own research as well as a convenient location to deploy the system.

CHAPTER 4

IMPROVEMENT OF INSTRUMENT AND SCANNER CONNECTIVITY

Approach

At the beginning of this sponsored research project, FDOT made it clear that this new automated NDE system was to be considered satisfactory only if it was able to be deployed in the field to evaluate structures *in situ*. This application warranted a system that was able to withstand the rigors of field deployment while being simple and reliable to set up. In the interest of simplifying the earliest software development efforts while also addressing this end goal, it was decided to simplify and ruggedize the system interfaces as the first step in the development process.

The first phase of this effort was to design and implement an improved instrument mounting system capable of protecting the relatively fragile and valuable NDE instruments once attached to the scanners' instrument heads. This mounting system included provisions for a new universal data and power connection scheme for current and future NDE instruments.

The next phase of the connectivity improvements was to establish a standardized and simplified methodology for communicating with the scanner systems and their attached NDE instruments. This communication standard needed to be simple, rugged, and flexible enough to support current and future NDE instruments and was designed accordingly.

Finally, concurrently with the previous two phases, the entire system was readdressed for field survivability and modified using weather resistant electrical and data connections to ensure reliable operation outside a controlled laboratory environment.

NDE Instrument Mounting System

The original instrument mount of the Phase I system was not only cumbersome but in fact posed hazards to the NDE instruments themselves as shown in Figure 4-1. Conversely, the improved NDE instrument mounting system would not only have to be capable of quickly mounting and protecting the delicate instruments already in use with the automated NDE scanners, it would have to be easily and inexpensively adaptable to new instruments and would have to take advantage of the very limited space available on the scanners' instrument heads.

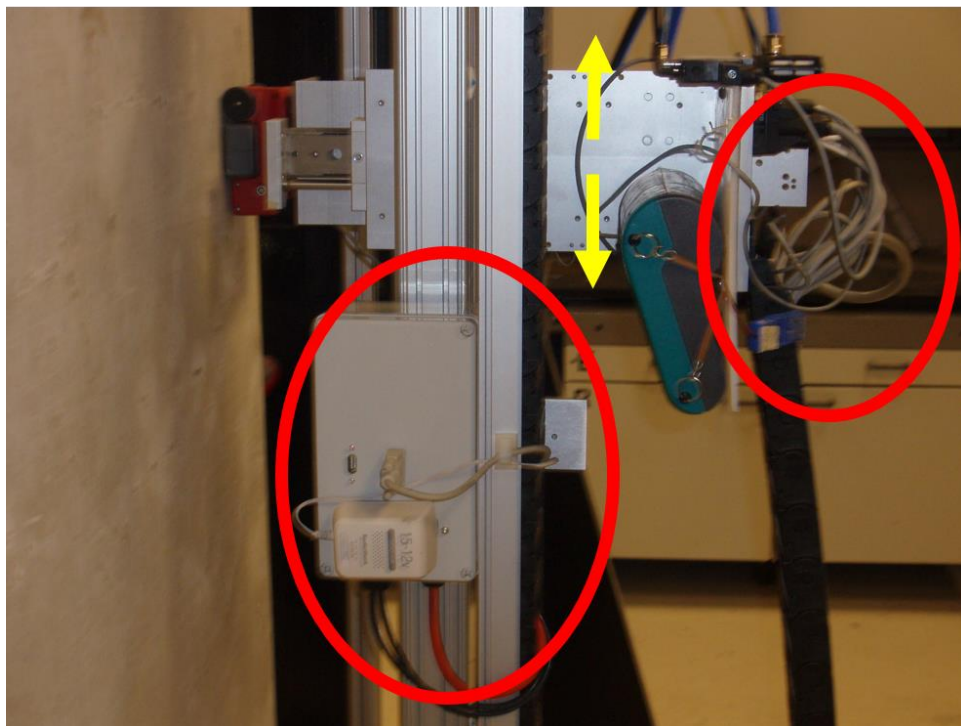


Figure 4-1. Covermeter mounted on the Phase I scanner system showing exposed and entangled data and power cables (circled in red) and the susceptibility of the instrument to collision during operation (Photo by J. Nelson).

A small T-slot extruded aluminum frame polycarbonate enclosure was designed to fit inside the space between the back side of the connector flange on the moving instrument head and the Y-axis linear drive as shown in Figure 4-2 and expounded

upon in Appendix B-1. The NDE instrument and any supporting components to be used were mounted onto a polycarbonate panel which, when inserted into the aluminum frame, formed the rear panel of the instrument enclosure. The exposed end of the enclosure was then closed with an aluminum panel fastened by aluminum thumb screws. This methodology allowed maximum available space for instruments as well as a small level of protection against water and debris infiltration. Additionally, since the dimension of the back panel of the instrument carrier was standardized between the two scanners, a new instrument may be incorporated with the scanner simply by fastening it and any supporting hardware to an inexpensive piece of cut polycarbonate sheet. Similarly, the aluminum right-angle bracket which fastens the instrument sensing head to the pneumatic cylinder is a standardized part which can be fabricated at very low cost.

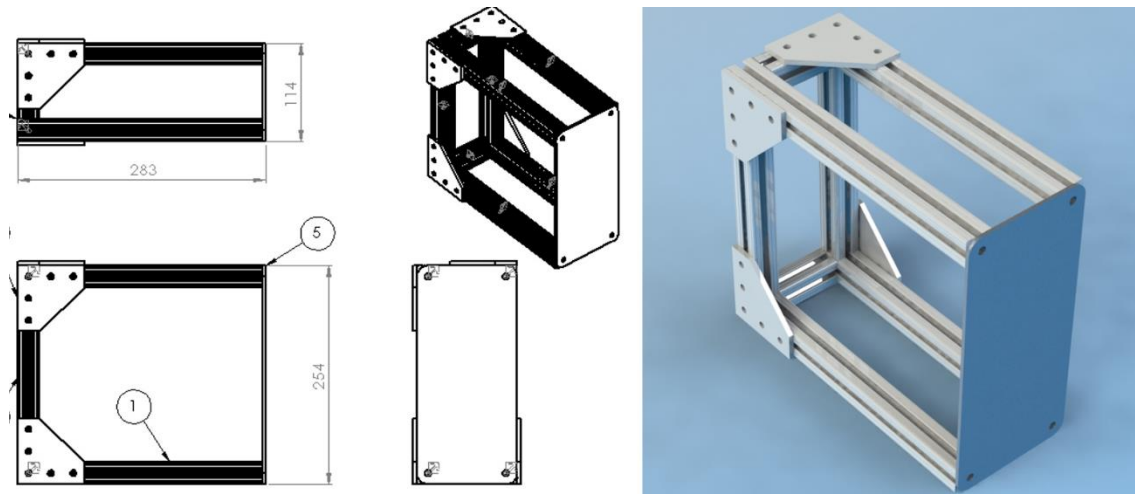


Figure 4-2. CAD drawing excerpt and 3D render of new instrument carrier design.



Figure 4-3. Completed instrument carrier as mounted to the Y-axis linear drive on Scanner 1 (Photo by J. Nelson).

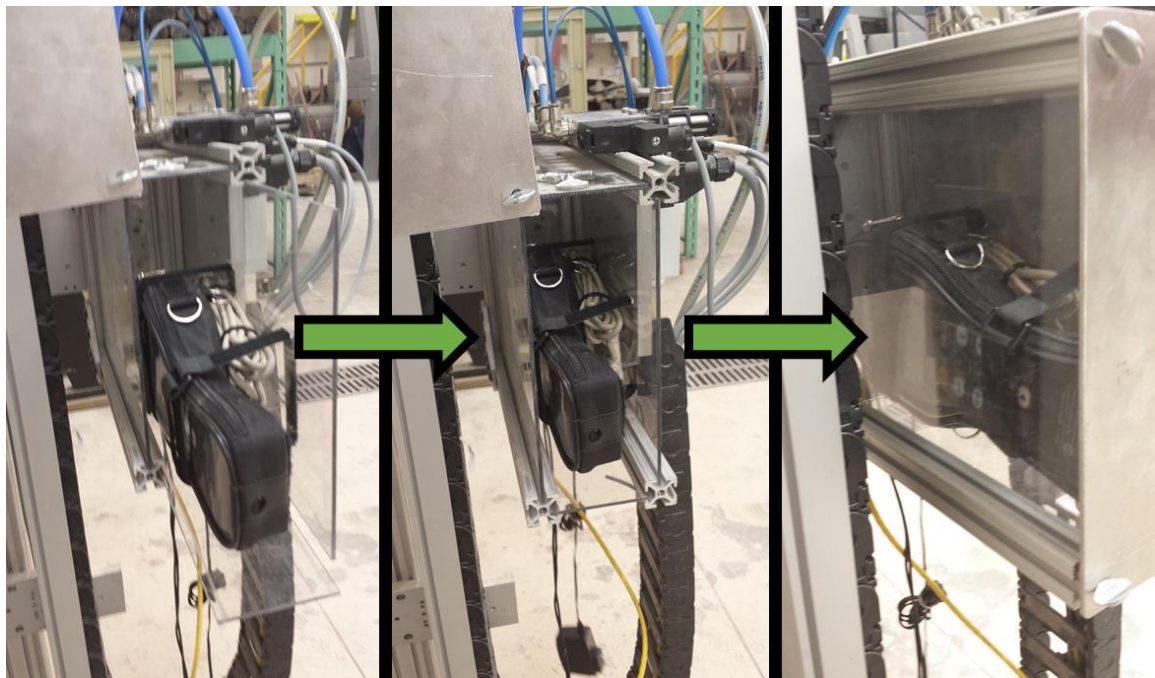


Figure 4-4. Instrument installation process. Note the panel the instrument is mounted on forms the back panel of the polycarbonate enclosure (Photos by J. Nelson).

Establishing a Communication Standard

Given the overly complicated and fragile system in which the PXI chassis was connected to the scanner systems and NDE instruments discussed in the opening section of this chapter, it was decided that the entire communications protocol would have to be redesigned. Furthermore one of the most useful instruments integrated with the scanner systems, the shear wave ultrasound device, was limited by its USB protocol interface to a meager distance of 1.5m from the PXI. For field deployment using the Phase I system in a difficult-to-access position—on a bridge pier for example—there would be no feasible arrangement for the PXI to be sufficiently close to the scanner's operating location to execute a successful ultrasound scan.

In order to extend the operating distance between the operating computer and the scanner system, eliminate signal degradation due to transmitting analog voltages over long cable lengths, and increase the maximum distance from the instrument to the operating computer it was decided to convert both of the scanner systems entirely to a local area network (LAN) based communication standard. A LAN protocol offered a number of advantages over other digital or analog communication schemes:

- An all-digital, lossless, universal communication protocol capable of cable lengths up to 100m (TIA/EIA 568-5-A) without signal extenders; indefinite cable length with signal extenders
- Multiple devices may be connected to a single, inexpensive network hub
- Ruggedized, weather resistant cables and connectors are available off-the-shelf
- Support for data sharing using publisher subscriber protocol (PSP)
- Easy integration with LabVIEW™ developed software
- Standard, inexpensive, readily available manufactured patch cables
- Compatibility with most computers

- Direct compatibility with many available NDE instruments and DAQ devices
- Indirect compatibility with USB, serial, and analog voltage data types using off-the-shelf components

Modification to Scanners

In order to fully implement a LAN protocol, the scanners themselves were first modified for an all-digital interface. Each scanner's X and Y movement is accomplished using serial command operated Cool Muscle™ stepper motors. The stepper motors have onboard serial servers and can be "daisy chain" operated: the Y-axis stepper motor is connected directly to the X-axis motor, which receives serial commands for both motors. The pneumatic cylinder which applies contact-based NDE instruments to the concrete surface was driven by an electromechanical 24V relay which was operated remotely from the PXI's onboard analog output channels. To integrate these systems with the new LAN protocol, a Silex serial device network server was employed to operate the X and Y axis drives and a National Instruments NI-9181 Ethernet cDAQ™ carrier with a NI-9401 8 channel Digital I/O TTL cDAQ™ device was used to remotely operate the pneumatic relay installed on each scanner. Since the low power DAQ device was incapable of driving the high power levels required to drive the electromechanical relay, a simple transistor relay circuit was designed and constructed for each scanner control system. These components, as well as a network hub to interface them all, were installed in washdown-rated fiberglass enclosures and mounted to each scanner in place of the existing electrical junction box as illustrated in Figure 4-5.

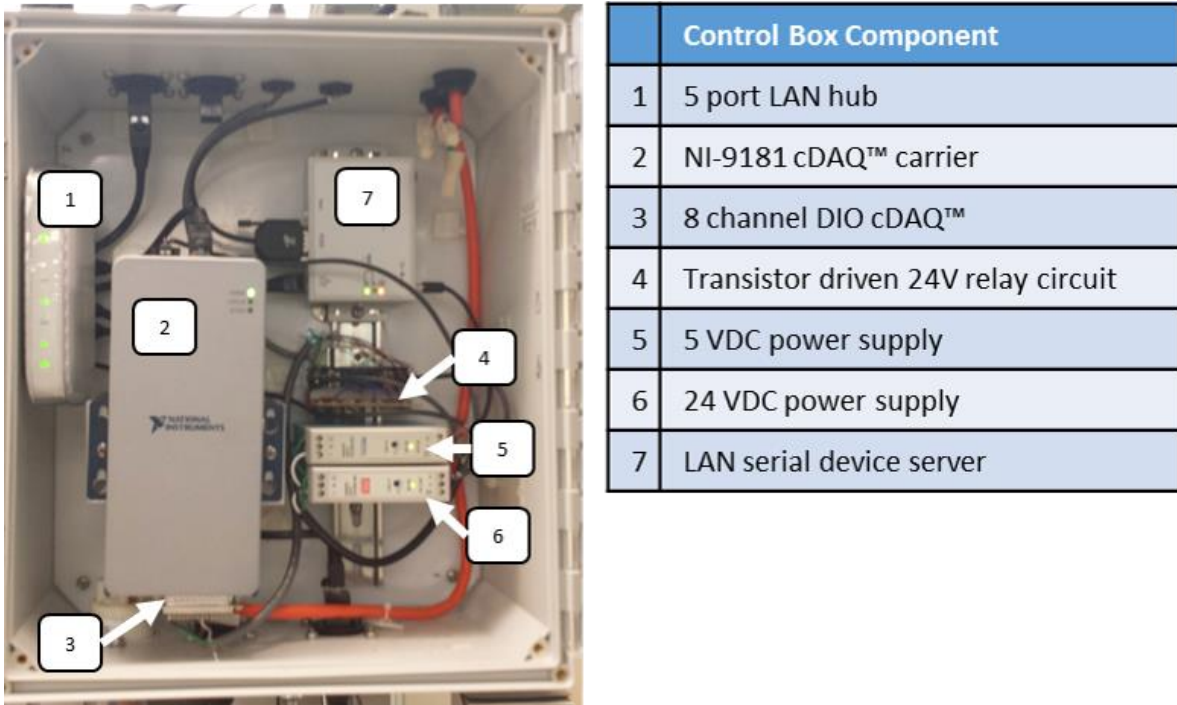


Figure 4-5. Scanner control box components in fiberglass enclosure (Photo by J. Nelson).

To connect NDE instruments to the LAN for each scanner system, a compact watertight ABS enclosure was mounted on each scanner's moving instrument head. Each enclosure was outfitted with one National Electrical Manufacturers Association (NEMA) 5-15R electrical outlet to power each NDE instrument as well as a watertight RJ45 LAN panel connector to establish connectivity between the NDE instrument and the scanner's network hub.

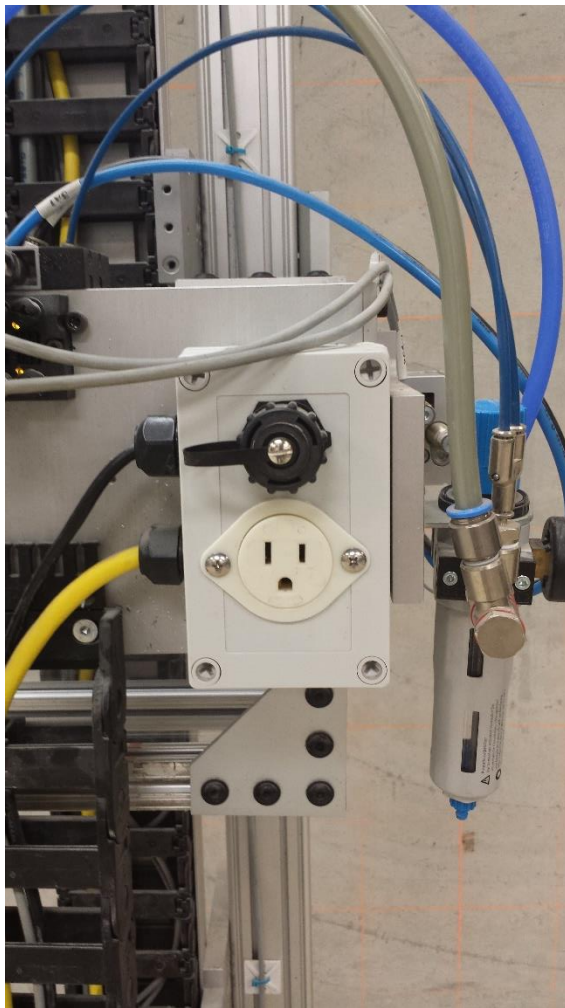


Figure 4-6. Electrical and data connection panel mounted to instrument head on Scanner 1 (Photo by J. Nelson).

With these modifications to the scanner complete, additional benefits were realized. First, both scanner systems could be operated at the same time since they no longer required multiple dedicated serial resources to operate. Secondly, because the two scanners could be connected to each other using independent onboard network hubs, a single Ethernet cable was all that was required to operate both scanners with their own independent instruments from a single computer. Finally, the implementation of the LAN protocol and the all-digital interface had effectively eliminated the need for

the PXI chassis to operate the system. Almost any inexpensive computer could be used in lieu of the more expensive and heavy PXI chassis in watertight case

Modification to Instruments

Once the scanner hardware was fully integrated to the new LAN protocol, the instruments themselves had to be modified to communicate over the new all-digital data communication system. The three instruments in use with the first-stage scanner systems—the covermeter, shear wave ultrasound, and impact-echo devices—communicated over serial, USB, and analog voltage formats respectively.

Through prior discussion with FDOT and based on the recommendations of the research team, it was decided that the impact-echo device could be eliminated from the automated NDE system for this phase of development. In the course of the previous research by Algernon, et al. it was shown that for the sorts of structural defects and characteristics FDOT wished to investigate the impact-echo method offered few advantages over shear wave ultrasound and was not worth the cost associated with converting it into an all-digital device [9]. Since both methods are based on stress waves, they are sensitive to the same sorts of defects, however the shear wave ultrasound instrument offered higher sensitivity, better resolution, faster operation, and easier integration with the scanner system as its data output was already digitized.

The Proceq Profometer®5+ eddy current covermeter originally operated on a 9VDC supply provided by 6 AA batteries and communicated its data using a serial byte stream over an RS232 interface. It was found that the AA battery supply was insufficient to power the device for the duration of a single scan, so the device was modified to accept a low-profile plug in transformer that could be conveniently connected to the ABS enclosure on the scanners' instrument heads. A Silex serial device server was

connected to the covermeter's RS232 port and the instrument and server were mounted on a polycarbonate panel for convenient installation into the instrument carrier as shown in Figure 4-7 and 4-8. The rolling cart sensing head used by the covermeter instrument was mounted to the standard aluminum mounting bracket using a rubber buffer to allow the cart to adapt to uneven concrete surfaces during use.

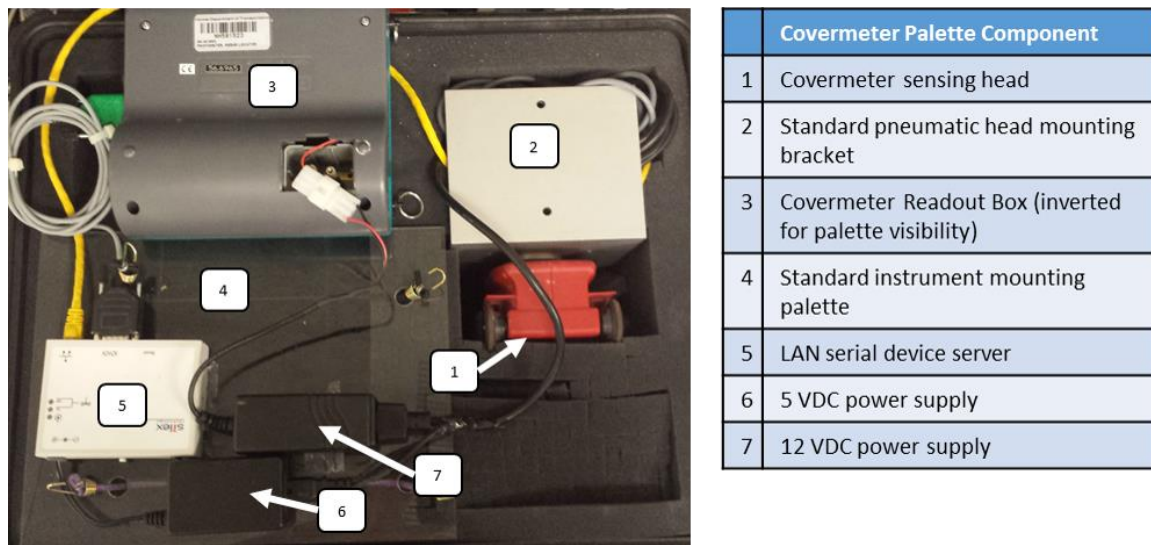


Figure 4-7. Proceq Profometer® 5+ covermeter modified for use with the scanner systems (Photo by J. Nelson).



Figure 4-8. Covermeter assembled on palette and packed in watertight instrument case (Photo by J. Nelson).

The Germann Instruments EyeCON™ shear wave ultrasound device had posed problems in the past when attempting to interface over a Silex USB device server. The device communicates its data as a 2048 element array of 8 bit integers over what is known as *bulk transfer protocol*, a USB transfer mode that until recently has not been supported by USB device servers. Fortunately, shortly before the beginning of this project, Silex launched a new USB device server that supported the transfer mode and allowed the EyeCON™ to communicate over a network, eliminating its previously short cable restriction. The EyeCON™ device retained its original rechargeable internal battery, which was capable of operating the device over multiple area scans before depleting, and was mounted to a polycarbonate panel with its USB device server using removable hook-and-loop ties as shown in Figure 4-9 and 4-10.

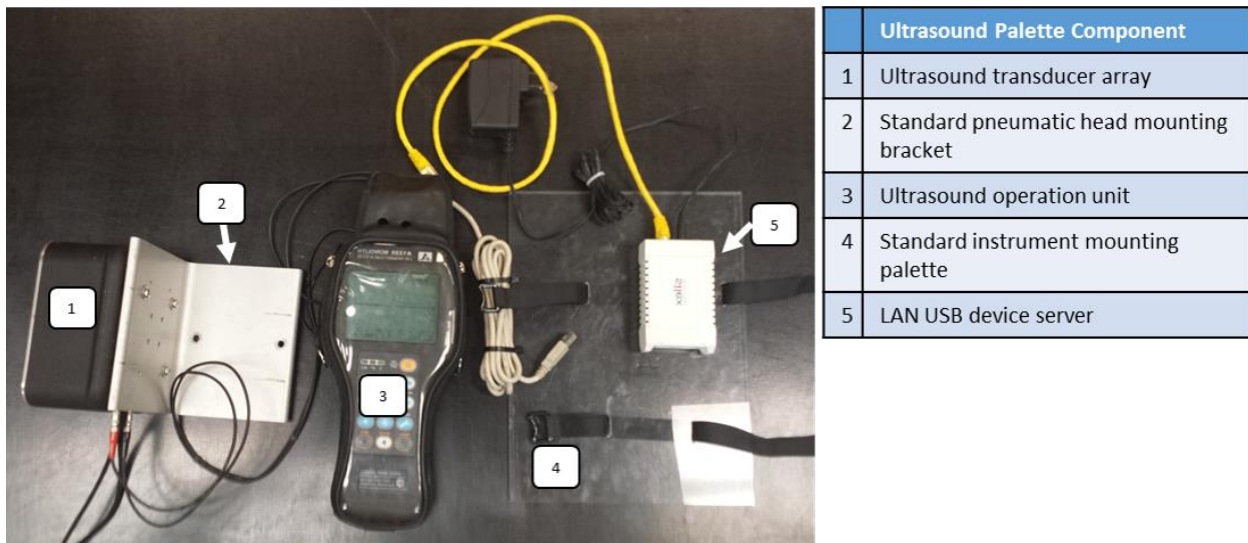


Figure 4-9: Germann Instruments EyeCON™ adapted to palette system. No physical modifications were made to the instrument (Photo by J. Nelson).



Figure 4-10. Germann Instruments EyeCON™ assembled on palette and ready for installation onto automated scanner (Photo by J. Nelson).

Though initially only two instruments were converted to the new LAN protocol, new instruments were added to the system using a similar methodology. Indeed, the LAN protocol is capable of supporting almost any data communication type using servers in the case of digital communication busses and Ethernet DAQ devices in the case of analog devices.

CHAPTER 5

INCORPORATION OF NEW INSTRUMENTS

Approach

With the new instrument mounting and communication protocol established with the NDE instruments from the Phase I system, and at the request of FDOT, three additional instruments were incorporated with the automated NDE scanning system.

Ground penetrating radar (GPR) is a technique that has seen a sharp increase in interest from the structural concrete community in recent years and was the first and arguably most important new method to be addressed. A GPR system was purchased for the Phase I NDE system but never successfully automated due to its bulky supporting equipment, lack of data output, and tight Federal Communications Commission (FCC) restrictions on operation. The research team sought to solve the issues with integrating GPR into the system by creating a new and elegant approach to instrument assimilation that would become an additional method for the automated NDE system to rapidly work with new NDE instruments in the future.

A Leuze ODSL8™ laser distance sensor was also purchased for the first-stage system as a surface profilometer but not successfully integrated due to its somewhat unusual method of signal communication. Since little additional cost was required to integrate this device, it was decided to solve the signal parsing issue and assimilate the device.

Finally, the research team recommended inclusion of a Power PC driven National Instruments NI1742 Smart Camera™ due to its potential for surface investigation. It was decided to integrate the camera and program it to do basic image acquisition and transfer to support future research endeavors.

Ground Penetrating Radar and Parallel Instrument Operation

GPR is one of the most frequently used—and often misused—NDE techniques for structural concrete. GPR has a reputation for being fast, accurate, and intuitive to deploy and operate. The technique is so fast, in fact, that there has been little call to automate its application to structural concrete. Here, the technique was included simply as a compliment to the other instruments incorporated in the automated NDE scanning system and due to the fact that FDOT was already in possession of a GPR system intended to be adapted to the scanning systems.

The GPR system to be adapted was a Geophysical Survey Systems, Inc. (GSSI) SIR3000™ self-contained operation and display unit with a 2.6GHz remote antennae. The antennae came with a detachable rolling cart with integral position encoder as shown in Figure 5-1.



Figure 5-1. GSSI SIR3000™ system with 2.6GHz antennae to be integrated with automated scanning system (Photo by J. Nelson).

The physical size of the GPR system was the first obstacle to its integration with the automated scanning system. The SIR3000™ unit itself was too large and heavy to ride on the scanners' instrument heads and still required management of a thick 6.5m long multiconductor cable and a 15cm x 15cm x 5cm signal conditioner used to interface with the antennae itself. It was decided to allow the signal conditioner to ride loose in the new instrument carrier and leave the SIR3000™ stationary away from the scanner. Routing the custom-built cable through the scanner guideways before every scan was infeasible, so the cable would lie near the cart and be carefully fed and retrieved during scanning.

The antennae and rolling cart were integrated using a specially designed mount that allowed an extension adapter supplied by GSSI to mate the cart to the pneumatic instrument head. A rolling limit switch and self-retracting cord were attached to the GPR antennae mount and designed to replace the remote control handle installed on the GSSI pole extension. The mount is shown in Figure 5-2.

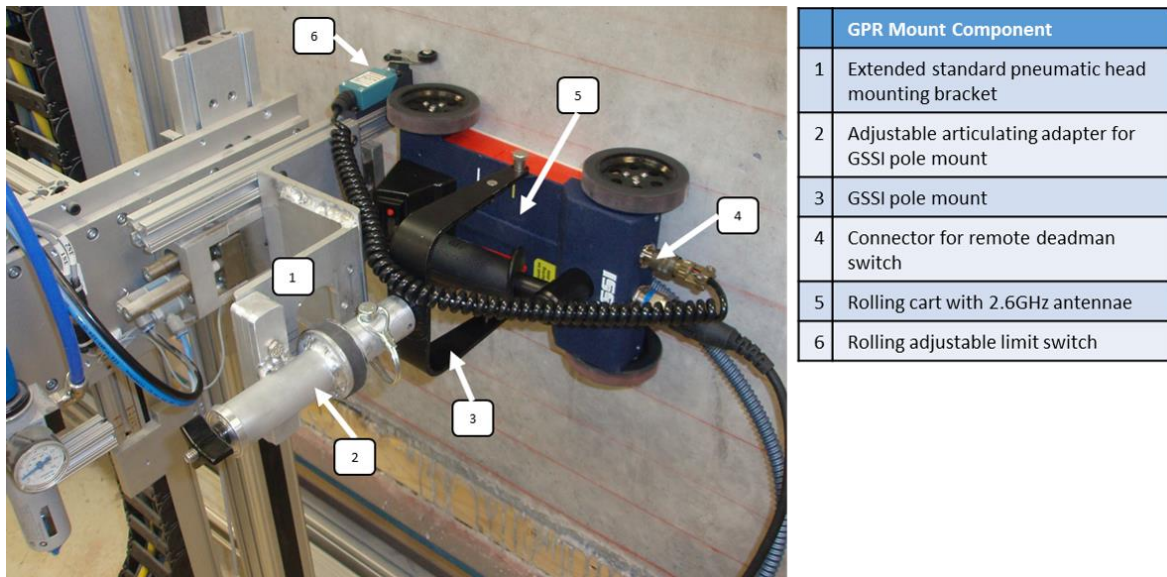


Figure 5-2. GPR antennae mount with limit switch for FCC compliance (Photo by J. Nelson).

FCC regulations require a deadman-type switch to control activation of all GPR antennae due to their ability to interfere with nearby communication systems and potentially harm human tissue. The limit switch was a convenient way to mimic the deadman switch and comply with FCC regulations while not modifying the as-bought GPR system in any way.

The final and most important obstacle to assimilating the GSSI GPR system was retrieving and saving data from the SIR3000™ unit. While the SIR3000™ had multiple interfaces built-in for its embedded PC operating computer, their functions were limited to only low level interfacing operations and manual data transfer. It became clear early in the project that the system simply could not be integrated in the same manner as the previous instruments.

While initially a significant setback to research efforts, the inability to interface the GPR system with the automated scanning software generated an idea to make the system even more flexible and useful. Instead of the software controlling both the scanner systems and the GPR input/output operations, it was decided to allow the software to operate the scanner without ever interfacing with the instrument: to follow a user defined grid in a feed-forward control scheme and output only coordinates and timestamps as its data file output. The data files saved to the SIR3000 unit could then be mapped to the data points generated by the scanner operating software. This methodology was dubbed “parallel operation,” the support of which could allow new and previously incompatible instruments to be rapidly adapted to the automated scanning system. The software support and potential capabilities of this methodology are discussed in Chapter 6.

Laser Profilometer

Incorporation of the laser profilometer, purchased for the Phase I system but never fully integrated, was deemed a side project of this research effort if time permitted. The instrument was revisited shortly before the reprogramming effort was started and determined to be fairly straightforward to integrate and quite useful. The device itself, a Leuze ODSL8™ laser distance sensor, was small in form, robust, and accurate at measuring distances down to +/-0.1mm. The only major difficulty was parsing its data output: a 14 bit measurement carried over a 2-byte stream where the high and low preceding bit represent number position as shown in Figure 5-3. The byte stream was read over serial interface using NI-VISA™ low-level VIs and parsed according to the schematic provided by Leuze USA as shown in Figure 5-4.

Measurement value = 14 Bit

1. Low-Byte (Bit 0=0) 2. High-Byte (Bit 0=1)



Figure 5-3. Byte stream representation of ODSL8™ distance measurement [34].

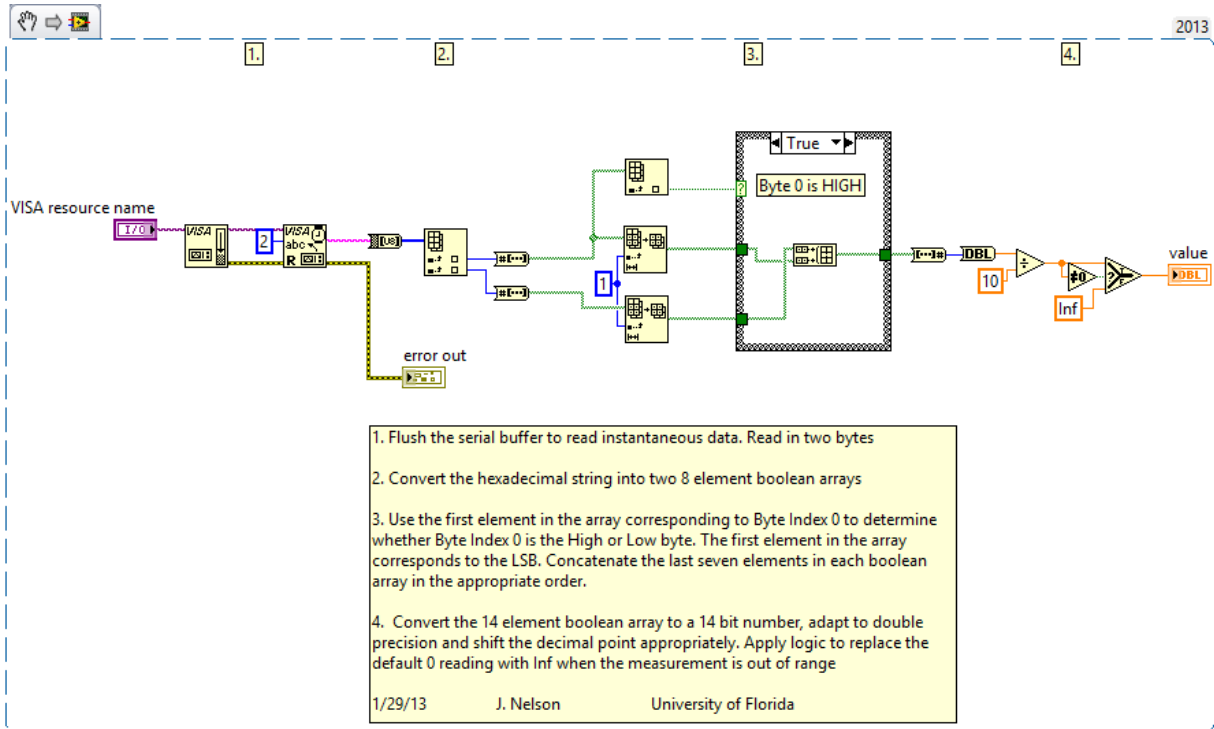


Figure 5-4. LabVIEW™ VI which reads and parses the 2-byte serial stream from the Leuze ODSL8™ laser distance sensor.

Adapting the laser profilometer to the scanner system using the instrument carrier palette system was straightforward due to the low power requirements and small size of the instrument. A small enclosure containing a DC power supply and voltage regulator was designed and constructed to provide the instrument with the requisite 12V to operate and the serial device server mounted on the palette with 5V as shown in Figure 5-5. A cable was constructed to connect the instrument to the serial device server on the palette and the components were assembled and stored in a watertight instrument case until needed.

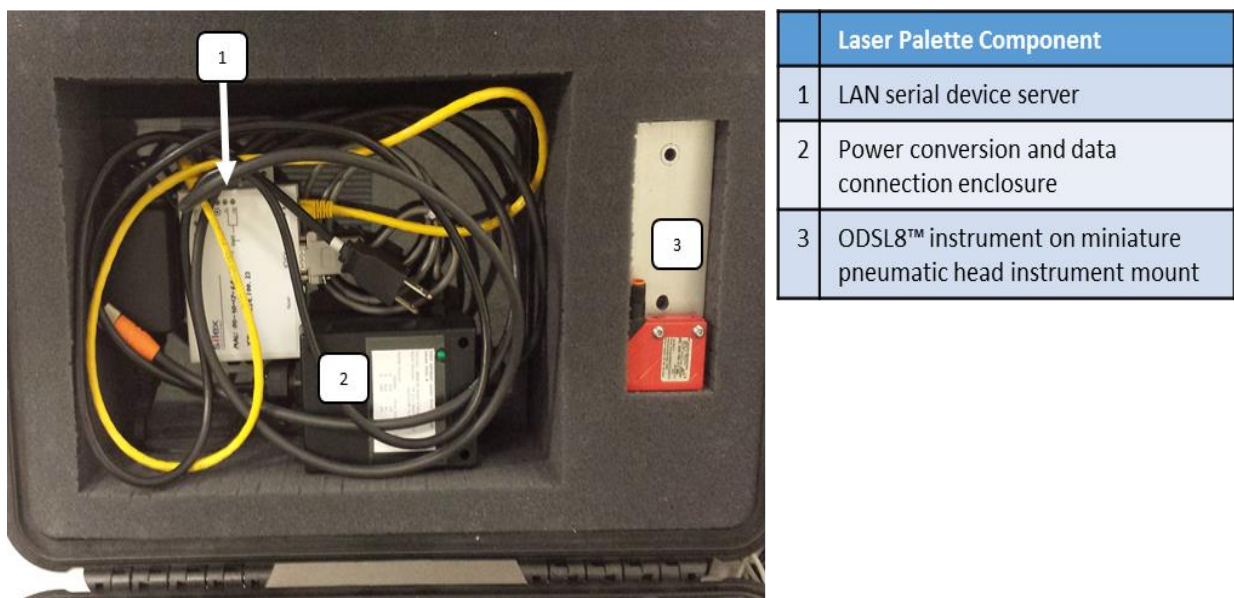


Figure 5-5. Laser profilometer system mounted on palette system and placed in watertight instrument case (Photo by J. Nelson).



Figure 5-6. Laser profilometer mounted on scanner instrument head (Photo by J. Nelson).

Surface Condition Surveyor

The Surface Condition Surveyor (SCS) instrument was an idea borne out of observation of another FDOT SMO program. The Accelerated Pavement Testing program had been using a camera system with LabVIEW™ vision processing support to detect cracks and pavement defects for years [4], and including a similar functionality with this automated NDE system for structural concrete was deemed prudent. A National Instruments NI1742 Smart Camera™ was purchased for the project along with a ring light array that could be driven from the camera itself. The Smart Camera™ platform is essentially a high resolution black-and-white CCD camera coupled to an embedded real-time controller; an architecture which offered a number of advantages for the research team:

- Built-in compatibility with LabVIEW™ Real-Time module and the ability to accept real-time acquisition and data processing algorithms generated in LabVIEW™
- Ability to be programmed, reprogrammed, and readapted to many different needs
- Direct compatibility with the LAN communication architecture using built-in RJ45 ports
- Rugged construction ready for the field
- Small, lightweight form factor

After the instrument was acquired, it was easily adapted to a standard aluminum instrument bracket described in Chapter 4 as shown in Figure 5-7. The camera system itself came with no installed software and was loaded with a custom designed real-time application to allow plug-and-play operation on the scanning systems.

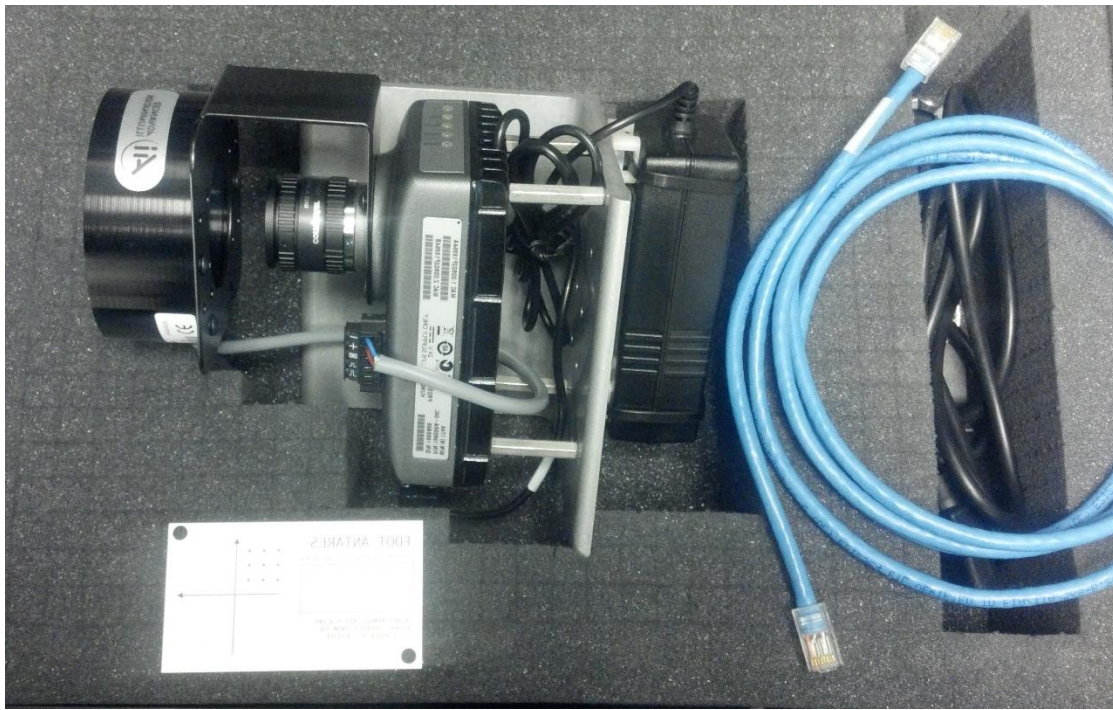


Figure 5-7. SCS instrument adapted to standard aluminum mounting bracket and packed in watertight case (Photo by J. Nelson).

Developing the SCS into a complete and robust tool for detection and measurement of surface flaws was outside the scope of this research, so for the purposes of this project it was decided to simply program the device to capture images at a set rate and push them over the LAN using a network-published shared variable (NPSV) data architecture. This made the program stored on the camera itself as simple as possible and allowed an open-source, unprocessed image to be produced for later processing should future research efforts invest the time in creating vision processing algorithms.

The run-time program was written using the LabVIEW™ Real Time module with support from the LabVIEW™ Vision Acquisition module as shown in Figure 5-8. The VIs that would be used to control the camera acquisition, exposure settings, lighting settings, and operate the ring light array itself were designed to interface with future

control program development using the same NPSV methodology that allowed the image files to be transferred to the control computer over the network. It was decided to transfer and store captured images as flattened data strings despite being far more memory demanding than a binary file so that the output data could be easily interpreted and processed using other software packages and used by other personnel if desired. The completed VIs were published as a real-time application (*.rtexe) and written to the nonvolatile memory of the Smart Camera™ so that the program would execute immediately on power-up of the camera.

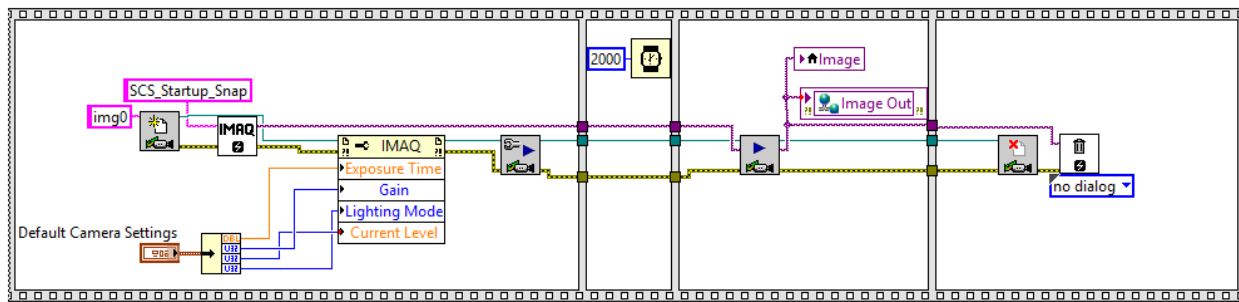


Figure 5-8. Startup subroutine of SCS run-time application. This section of code activates the Smart Camera™ and sets the default exposure time, gain, and lighting settings for the camera. The ring light is illuminated briefly to inform the operator the device is working.

The flexibility of vision-based data acquisition meant that the SCS could, in the future, be used to perform any number of surface evaluation tasks when used to scan structural concrete. The research team recognized one application in particular that could be extremely valuable for field scanning operations: orienting the scanner on a structure.

Historically, attempting to repeat a nondestructive evaluation of a section of a structure—either manually or using an automated scanner—after some time had passed was extremely difficult as intimate knowledge of the previous grid layout and

origin were required. The SCS instrument offered the potential to locate distinguishing marks on a surface and calculate an origin relative to the scanner coordinate system and an angle of rotation. The research team designed etched aluminum placards with an origin marker and a space for an identification label specifically for this purpose. Since the SCS requires a calibration at run time to calculate the size of surface defects (essentially a conversion of pixels to millimeters that changes based on the distance from the camera aperture to the surface), a calibration grid was also included on the SCS placard design shown in Figure 5-9. Future research should include development of vision processing algorithms to fully utilize this significant capability.

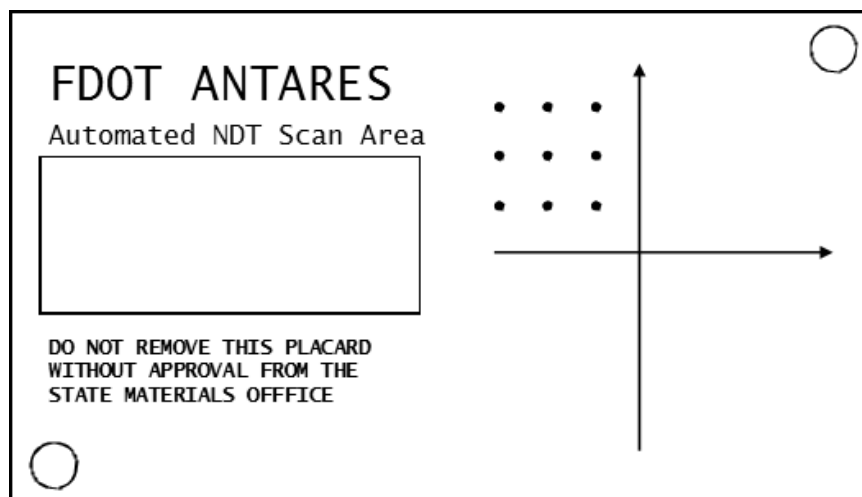


Figure 5-9. SCS placard design with origin and direction markers. The placard is roughly the size of a business card.

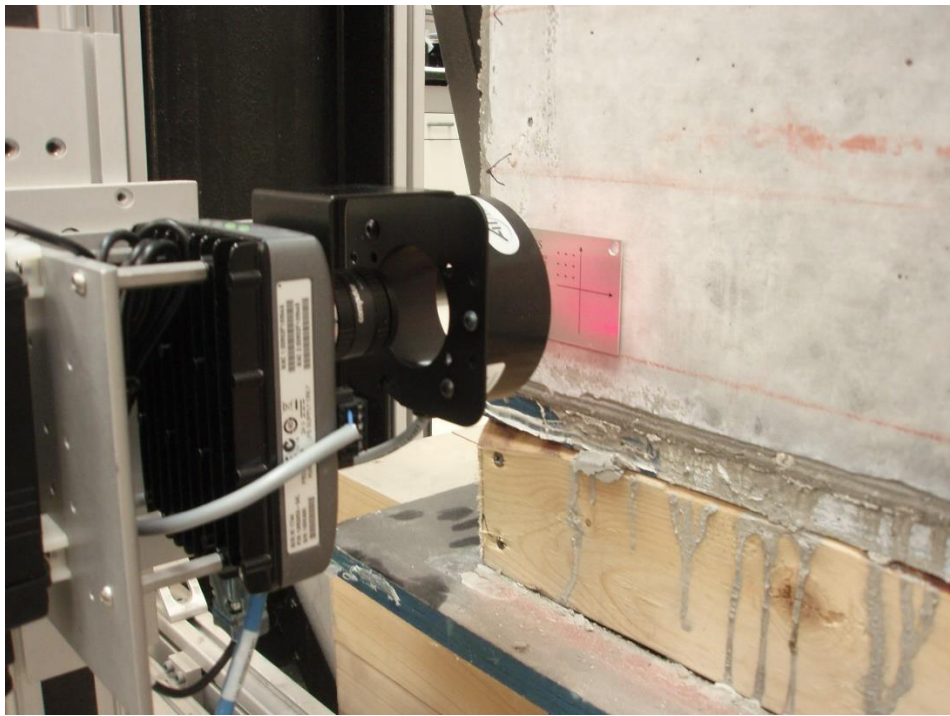


Figure 5-10. SCS instrument mounted to Scanner 1 with ring light illuminating an orienting and calibration placard (Photo by J. Nelson).

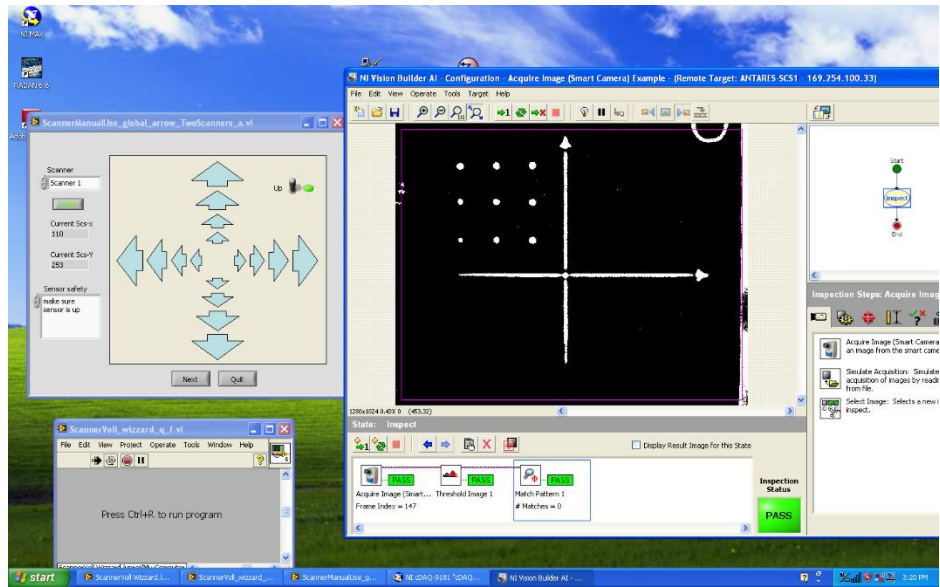


Figure 5-11. Threshold image of SCS placard origin marker demonstrating ability to digitize orientation and origin marker and calibration grid.

CHAPTER 6

DEVELOPMENT OF THE ANTARES SYSTEM

ANTARES and the Concept of Accessible Automated NDE

Introduction

From the beginning of this research effort, one primary goal of this project was to deliver a system to be used by skilled technicians with limited training rather than engineers and research and development teams. The system needed to be dependable, robust, and cohesive with an approachable, well-designed software interface, fault-tolerant programming, and intuitive controls. Until this point, this manuscript has discussed hardware improvements made in service of the goal of creating a more usable system. However, the bulk of the effort invested in the development of this automated system was spent in LabVIEW™ software development creating a simple and robust software package for system control, data acquisition, and data processing.

Approach

To begin the software development effort, an overarching goal of the software architecture was established. In the interest of software unity, the research team decided to begin software development as an entirely new architecture, with no code reused from the Phase I operating software. The automated NDE system—each of the two scanners and all supporting hardware, the laboratory evaluation blocks, and all instruments integrated with the scanner systems—were incorporated under a single program name that would also be applied to the software designed to support the system: Automated Nondestructive Testing for Applied Research and Evaluation of Structures (ANTARES).



Figure 6-1. FDOT ANTARES logo designed by the research team.

The software package was separated into two distinct programs that compartmentalized the programming effort, allowed for future improvements to be programmed in without impacting system capabilities, and minimized the demand on the operating computer. One program was designed for operation of the scanners and instruments, data acquisition and saving, and limited display of incoming data while the other was designed to process the data saved by the operating software into rich, detailed two and three dimensional displays suitable for report generation and structural evaluation.

ANTARES SVW Operating Software

Introduction

As an homage to Dr. Algernon and his original operating software package, ScannerVoll Wizzard (“voll” meaning “full” or “complete” in German), the ANTARES scanner and instrument operating software was named ANTARES ScannerVoll Wizzard or ANTARES SVW for short.

ANTARES SVW was designed from the beginning to have simplified, modular software architecture and an intuitive single-pane interface. One of the most frequent complaints about the Phase I operating software was that it depended far too much on popup windows and multiple screens to the point where it was difficult to discern which

window was active and which was merely open as a subroutine of the active window. Additionally, concerns about safety were raised when unexpected scanner behavior was witnessed and no ability to interrupt an automated scan was included in the Phase I interface. ANTARES SVW was designed to address these two major concerns as well as include significant design changes to increase overall usability of the system.

Approach

To make the ANTARES SVW software easy to troubleshoot and modify, the program was designed around a tiered architecture starting from low-level operating Virtual Instruments (VIs)—LabVIEW™ code sections with graphically programmed subroutines and simplified user interfaces—and moving upwards in complexity until ultimately reaching the master interface VIs. The software architecture will be discussed here in detail and supported by code excerpts found in Appendix A. Noteworthy subroutines and software functions will be discussed, however the complexity of the program as a whole prohibits an in-depth discussion of the code in its entirety.

In order to keep the front panel—the interface visible to the software operator—as clean and simple as possible, the main panel and the limited number of modal popup windows used in the interface were designed around a common theme and operated by event-driven controls that were clearly labeled and identified. Controls that perform the same function across multiple windows are identified consistently and located in the same areas. All of this effort was designed to make operating the ANTARES system highly intuitive.

The most important function of ANTARES SVW is to produce useful NDE data. One improvement ANTARES SVW made over ScannerVoll Wizzard is the use of a common file format for the data output of all instruments. The *.ANTDAT file type was

designed specifically for the ANTARES system and is a universal ASCII file format that can be opened using almost any text-based processing program and easily interpreted by other operators, meaning that other agencies and personnel wishing to utilize data generated by ANTARES SVW can do so using their own processing software if desired.

Software Tiers

Introduction

ANTARES SVW is a relatively complex LabVIEW™ application comprised of over 660 subroutines contained in 135 SubVIs written during the course of this research effort. This program represents over 300 operator hours of programming time closely following a programming hierarchy shown in Figure 6-2.

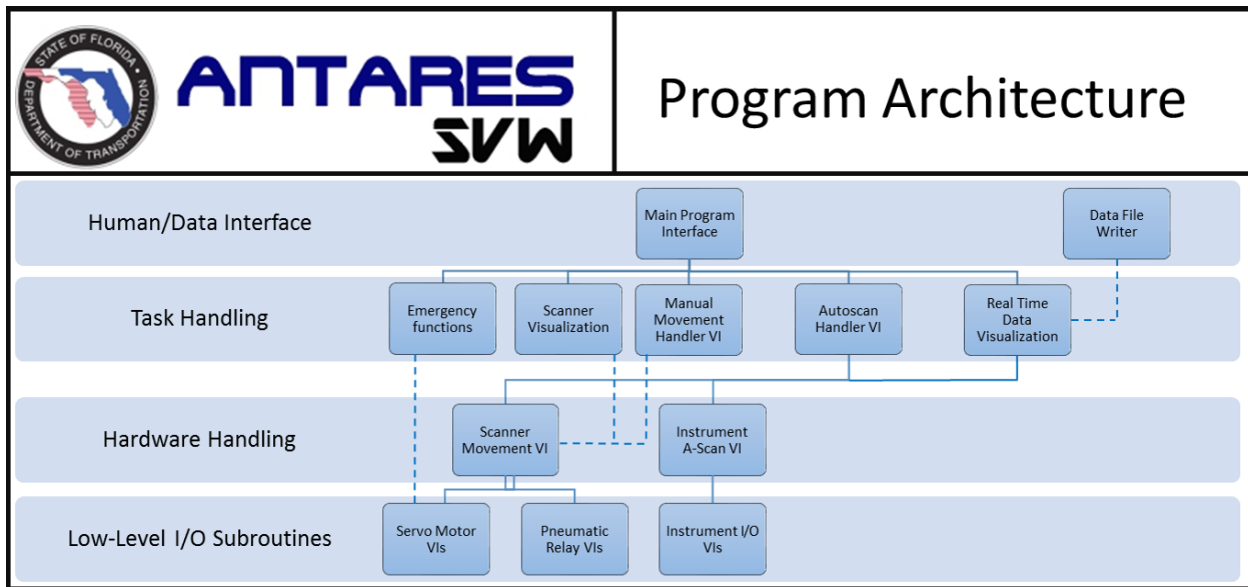


Figure 6-2. Basic tiered architecture of the ANTARES SVW LabVIEW™ application.

Low-level I/O subroutines

The most basic SubVIs included in ANTARES SVW, the low-level I/O subroutines are designed to perform basic command and acquisition functions with the scanner hardware and NDE instruments. They include command and feedback

subroutines for the scanner servo motors and encoders, instrument head pneumatic cylinder relay, and NDE instruments serial, USB, and NPSV interfaces.

The scanner servo motor subroutines operate the servo motors and receive feedback from their onboard encoders by communicating over serial interface using Cool Muscle Language (CML™). The two VIs in this class—CML Command and CML Query—parse a plain text command given by an enumerator control into Cool Muscle Language and write it to the serial port in the case of CML Command, or perform a read-and-parse operation returned as an enumerator indicator in the case of CML Query. These VIs are responsible for operating the servo controls in a limited feedback control scheme, where the movement of the servo motors is controlled in the form of movement “steps” or pulses of the stepper motors and absolute values are stored locally on the operating computer. The movement command is parsed as a text stack including desired motor state in pulses and the velocity and acceleration parameters for the movement step. This text stack is then passed over the network to the scanner’s serial port and interpreted by the onboard controller in the master servo motor. The VI used to accomplish a CML™ motor command is shown in Figure 6-3.

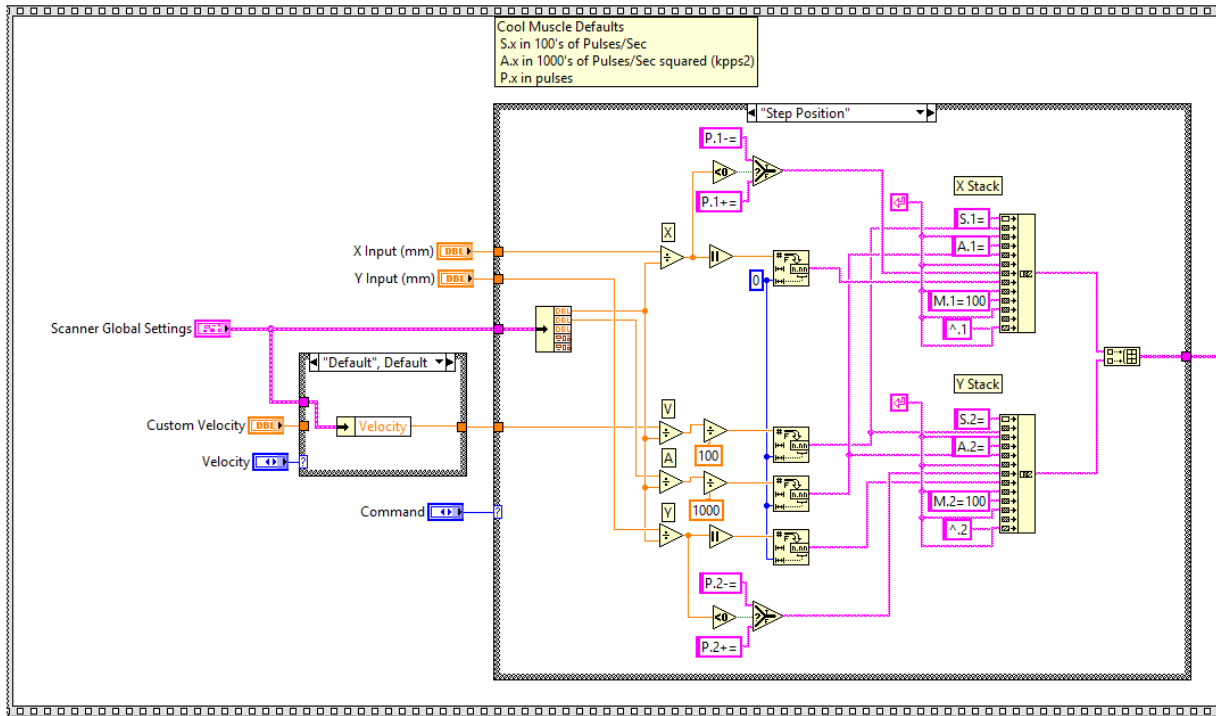


Figure 6-3. Parsing structure of CML Command SubVI.

Command and query functions for the pneumatic cylinder relay were also generated as low-level subroutines. These VIs operated the digital-out ports of the 5V TTL cDAQ™ card to command the pneumatic instrument head to move up or down and read in the status of the instrument head from inductive proximity sensors on the digital-in ports. These subroutines are shown in Figure 6-4 and 6-5 and are available in full form in Appendix A.

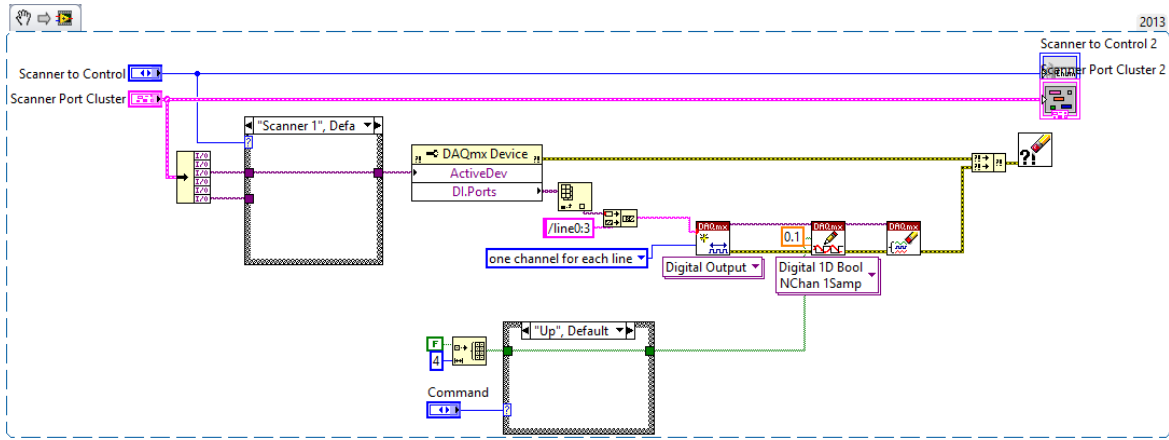


Figure 6-4. Command section of pneumatic instrument head command subroutine.

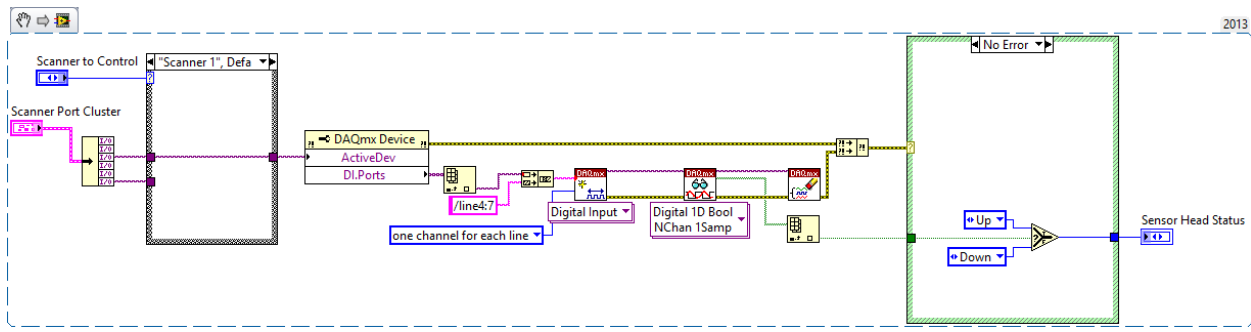


Figure 6-5. Pneumatic instrument head query subroutine with integral error handling.

The SubVIs responsible for interfacing with the NDE instruments and performing low-level command and acquisition functions must be as unique as the instruments themselves. Despite this, incorporating new instruments into the ANTARES SVW system requires only writing of a new low level SubVI, such as the EyeCON™ subroutine shown in Figure 6-6, for that instrument and minor modification to the higher level handling VIs to allow use of the low-level subroutine. This simplicity is owed to the compartmentalized nature of LabVIEW™ and the architecture of the ANTARES SVW program.

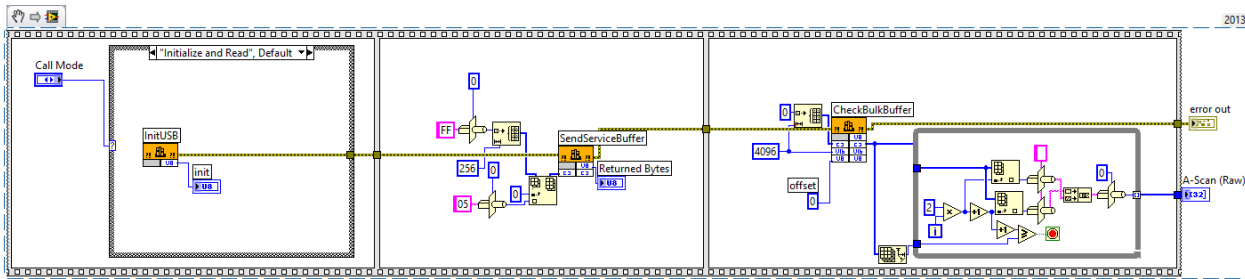


Figure 6-6. Code snippet of Ultrasound A-Scan SubVI, one of four low-level instrument I/O subroutines used with ANTARES SVW.

Hardware handling subVIs

The hardware handling class of SubVIs contains only two SubVIs: the Scanner Movement VI and the Native Instrument A-Scan VI. The former manages all scanner movement including instrument protection by preventing movement outside of accessible scan area, raising the instrument off the surface before moving where applicable, and managing speed and acceleration. This code section is shown in Figure 6-7 and is available in detail in Appendix A.

The A-Scan VI is responsible for polling whichever instrument is connected to the scanner for data and converting that data into a form suitable for display to the operator in the real time data visualization window and saving into the *.ANTDAT data file. This VI is responsible for calling the correct low-level hardware I/O subroutine, handling any errors associated with the read operation, and outputting the instrument data in a standardized format. A section of this code is shown in Figure 6-8.

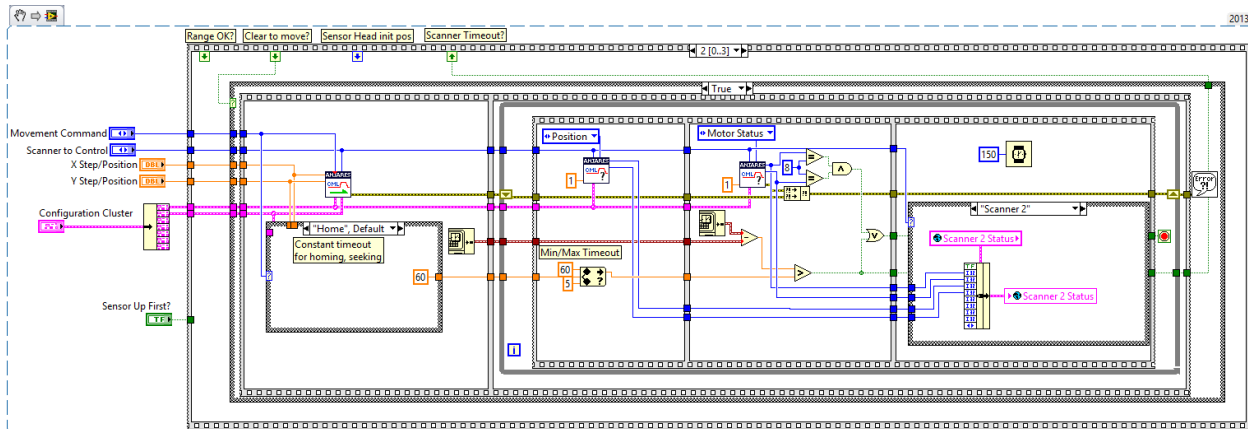


Figure 6-7. Portion of Scanner Movement VI with low-level SubVIs visible as square icons with a blue top border.

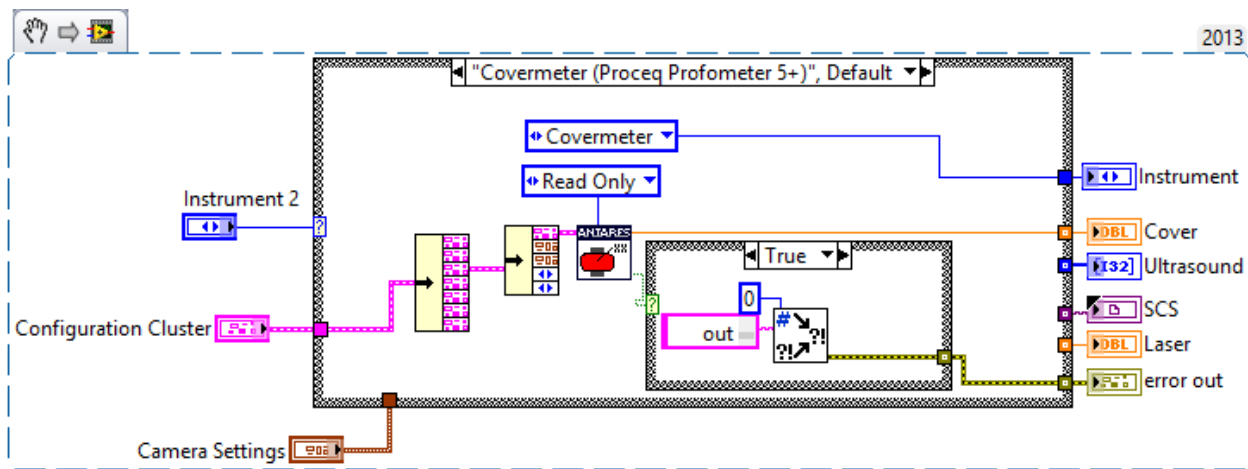


Figure 6-8. Code snippet of Native Instrument A-Scan SubVI.

Task-handling subVIs

The Task-Handling SubVIs are a novel way to handle plain-text commands to the ANTARES system such as “move to location”, “automatically scan the provided grid with the chosen instrument”, “tell me where the scanner is”, or “emergency stop”. They represent the highest programming tier that does not require direct human control. The number of SubVIs in this class is far too great for detailed individual discussion, so only a handful of important VIs are discussed in this chapter.

The Autoscan VI is arguably the most important and complex SubVI in the ANTARES SVW application. This VI is responsible for accepting user-defined scanner grids, instrument settings, and data file paths and performing an entire automated scan. Since the user may decide to pause or interrupt an automated scan at any time, the Autoscan VI must be able to receive commands from the main interface during execution and alter its own function. Since the Autoscan VI is a SubVI, which must fully execute before relinquishing control to the calling VI per LabVIEW™ execution methodology, it was decided to force the Autoscan VI to relinquish control to the Main VI after each step (a single point in a point-by-point scan or an entire line in a line scan) to allow the main interface to update and alter behavior if necessary.

ANTARES SVW introduced the capability to run an NDE scan using a single scanner, both scanners independently and simultaneously, or both scanners dependently following a master/slave protocol in which the slave scanner matches the mirror-image coordinate of the scanner chosen as the master before data is collected. This protocol allows more rapid data collection when run independently and provides for pass-through transmission instrument types to be used when run dependently.

The Autoscan VI makes multiple calls to the Scanner Movement VI, A-Scan VI and various other subroutines at different instances dependent upon grid settings and scan type as shown in Figure 6-9. The VI must be reentrant to allow calls for both scanners when the scanners are operated simultaneously and requires significant computational overhead to do so. This requires ANTARES SVW to be run on a moderate performance computer.

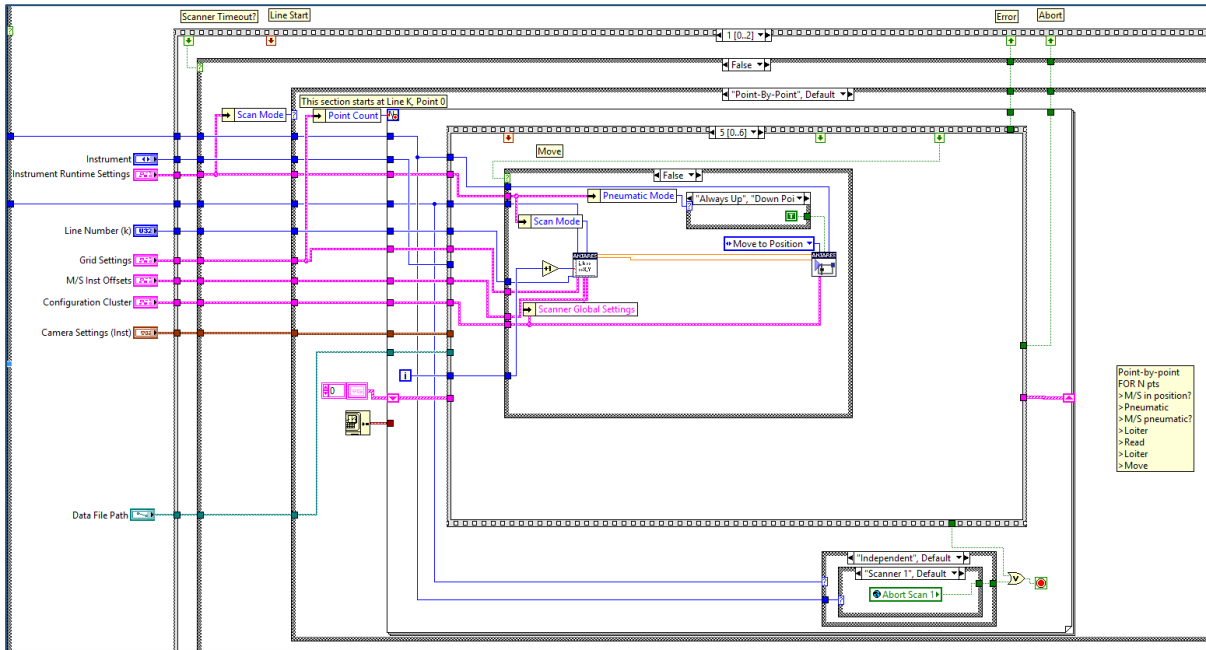


Figure 6-9. Code section of Autoscan VI. The VI is far too large to show in its entirety, but this section shows the structure used to perform a point-by-point scan.

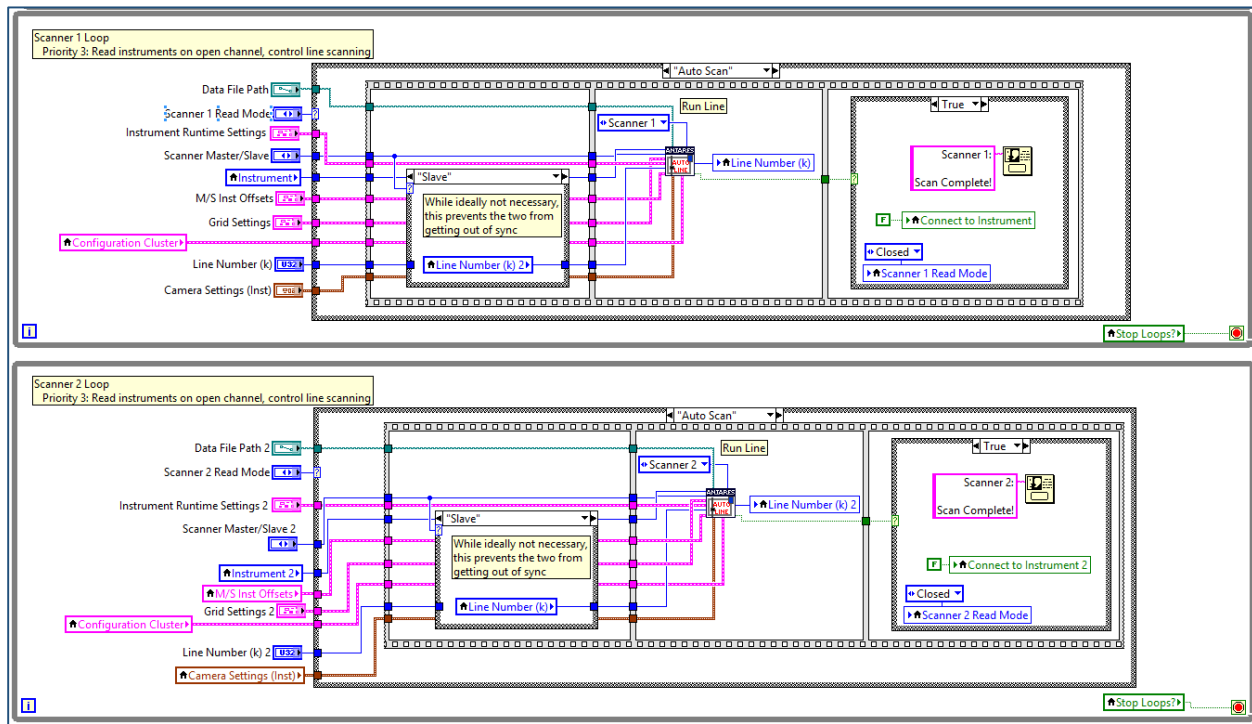


Figure 6-10. Independent loops on main program used to call Autoscan VI.

Another equally important task handling SubVI is the Emergency Stop VI shown in Figure 6-11. This VI is operated in a special priority loop on the main VI and bypasses all other operations. It calls the low-level CML VIs directly and commands all servo motors on all scanners to immediately decelerate at maximum deceleration to zero velocity and remain in place until overridden. There was no provision for an emergency stop of the system in earlier software and unexpected scanner behavior that could potentially damage the sensitive NDE instruments, the scanners themselves, or potentially injure the operator was dealt with by interrupting power to scanners. This method was also dangerous, however, since the scanners are mounted vertically and an interruption in power allows the instrument heads to fall under gravity with very little deceleration from the Y-axis drive motor's back-electromotive force (EMF). The Emergency Stop VI effectively "locks" the scanners in their current location until reset and aborts any active commands to the scanners. The soft buttons are located in convenient areas on the front panel, are large and easy to see, and respond in less than 1ms when clicked.

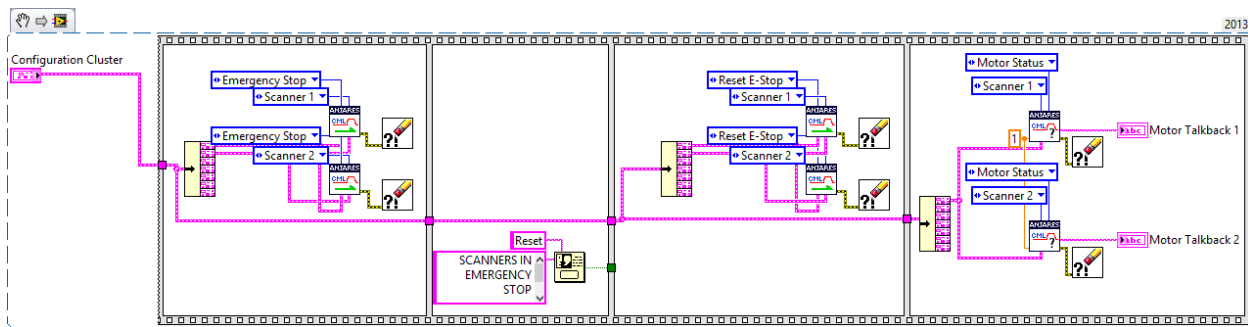


Figure 6-11. Emergency Stop VI with integrated reset dialog box. This VI effectively freezes both ANTARES scanners in place and halts execution of ANTARES SVW until reset.

Human/data interface VIs

These top-level VIs ultimately form the link from human to software or software to data output. While their programming structure is not particularly complex, the ways in which these VIs utilize lower tier subroutines are critical to the overall function of ANTARES SVW. Essentially the human interface VIs can be thought of as event-driven wrappers for the lower tier VIs and the data output VIs can be thought of as a converter of data arrays stored in RAM to formatted ASCII text files.

The human interface VIs are as follows

- Main Interface
- Splash Screen
- Configuration Settings Screen
- Grid Generation Wizard

The Main Interface VI controls all major functions of the scanner system and could in fact be used to operate the entire system from start to finish without ever using another interface. The layout and design of the interface will be discussed later in this chapter, but the architecture of the interface is based in a three-phase sequence where the first sequence initializes the program and loads configuration settings as shown in Figure 6-23, the second phase is a persistent loop allowing operator interaction and automated operation of the scanning systems, and third phase closes any open data ports, relinquishes memory, and terminates the program cleanly.

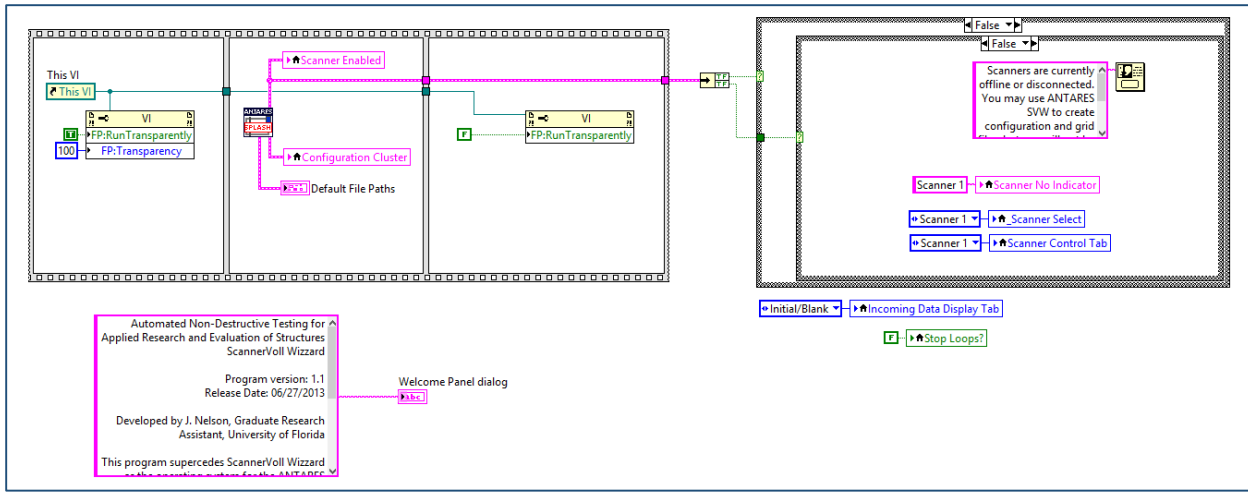


Figure 6-12. Initialization phase of main interface. This subroutine operates the splash screen, loads configuration settings saved on the hard drive, and sets the default state of the interface.

The second phase of the main interface can be thought of as the central program or operating system of the ANTARES system and is shown in Figure 6-13. It consists of four persistent loops

1. Priority Loop: responsible for controlling emergency stop and reset conditions as well as providing the operator with feedback on the scanners' position and activities
2. Human Interface Loop: responsible for accepting commands from the operator and altering the behavior of the system accordingly
3. Scanner 1 Operation Loop: responsible for controlling the operational state of scanner 1—idle, open instrument read, and automated scanning
4. Scanner 2 Operation Loop: responsible for controlling the operational state of scanner 2—idle, open instrument read, and automated scanning

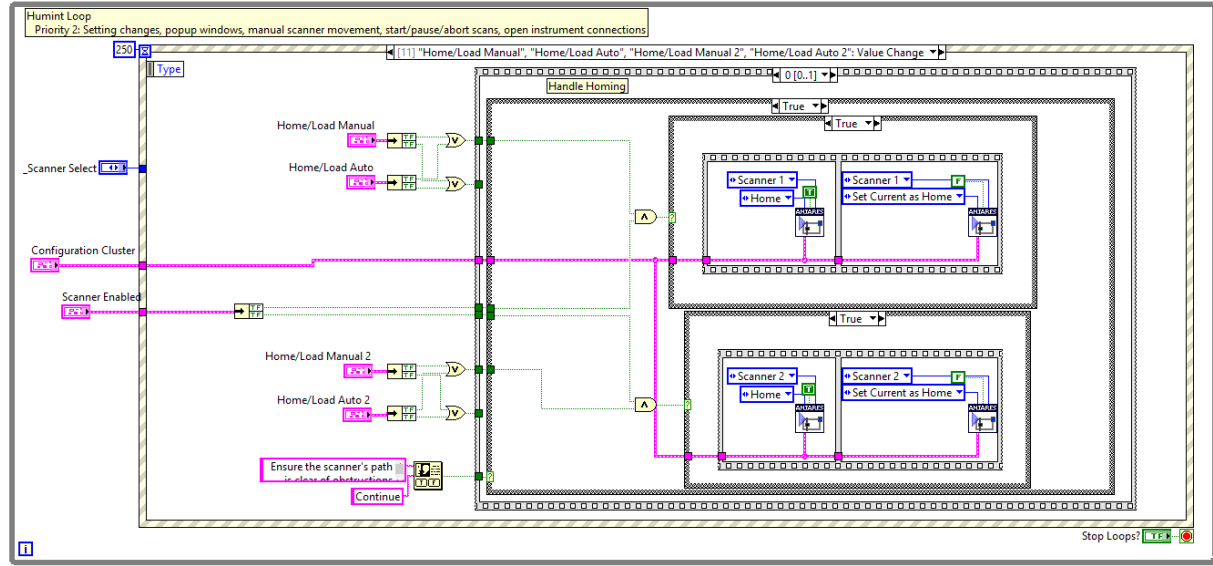


Figure 6-13. Human interface loop of ANTARES SVW.

The final phase of the Main Interface VI closes any existing data port sessions, relinquishing those resources for use by other programs. The code section also operates a clean program termination, ending the program safely and relinquishing the RAM the program has reserved. This code section is shown in Figure 6-14.

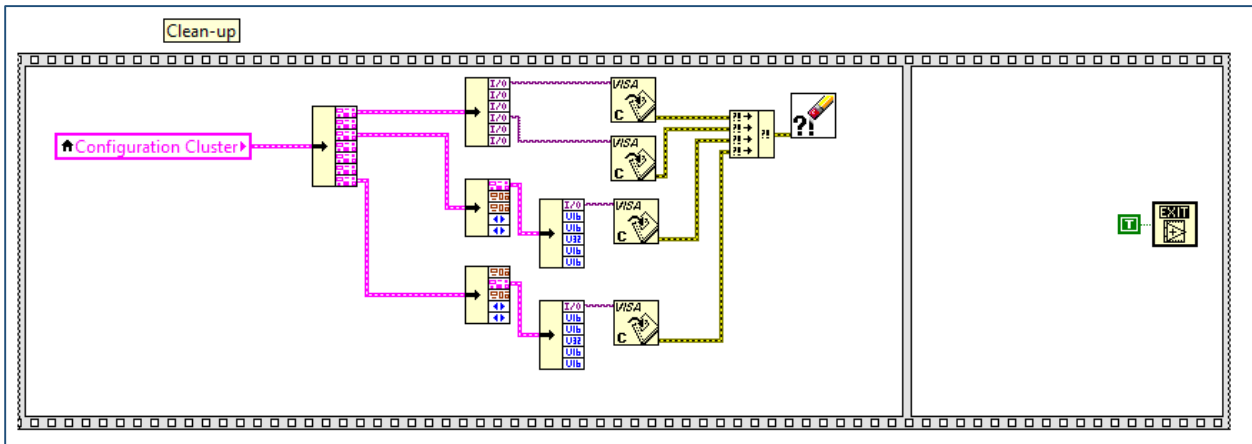


Figure 6-14. Clean-up phase of the main VI. NI-VISA sessions are closed and the program is terminated in a safe, clean manner.

The Splash Screen VI is a piece of interfacial code that performs the vital tasks of initializing communication with the scanner hardware and informing ANTARES SVW of

any hardware faults, missing communication settings, or disconnected scanners. The program itself is an 18 step startup sequence that presets the scanner hardware for use by ANTARES SVW. The program begins by creating default folders for saved grid files (*.ANTGRD), configuration files (*.ANTCFG), and data files (*.ANTDAT) on the computer's hard drive in the current user's document library if they do not exist already. Next the program searches for the last used system configuration file. If the file does not exist, the program launches the Configuration Settings Screen so that the operator may provide the vital system settings necessary to operate the ANTARES system. The remaining steps of the program perform a check and initialization on each scanner's serial port and cDAQ™ and returns the success or failure of each check as a visual cue to the operator as well as a group of settings provided to the main interface that will prevent the operator from using hardware that is either offline or in an error state. The first steps of the Splash Screen VI are shown in Figure 6-15.

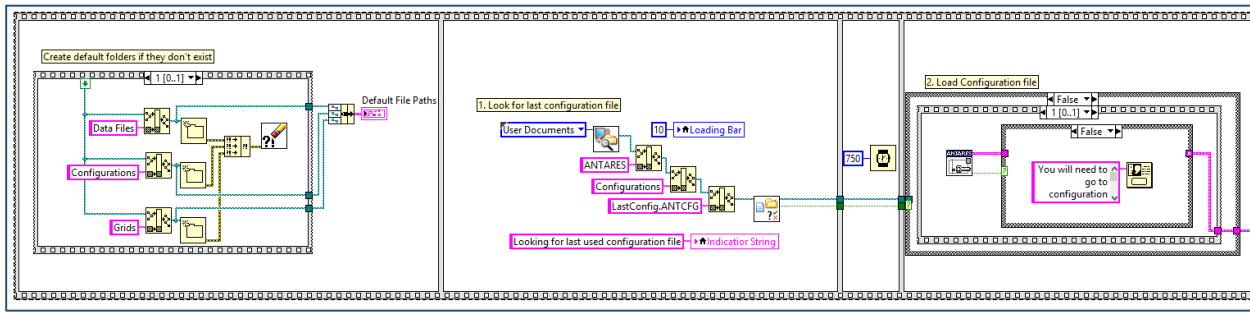


Figure 6-15. The first four sequences of the Splash Screen VI.

The Configuration Settings Screen, shown in Figure 6-16, has the vital task of managing the persistent configuration settings data cluster in ANTARES SVW. This data cluster contains the conversion factor for the servo motors from steps to millimeters, the default velocity and acceleration limits, the scan area limits, the port settings for all native hardware including NDE instruments, servo motors, and each

scanner's cDAQ™, and the default operation mode for each NDE instrument. This program is capable of altering the values listed above, verifying them, writing them to a file, and importing them from a file.

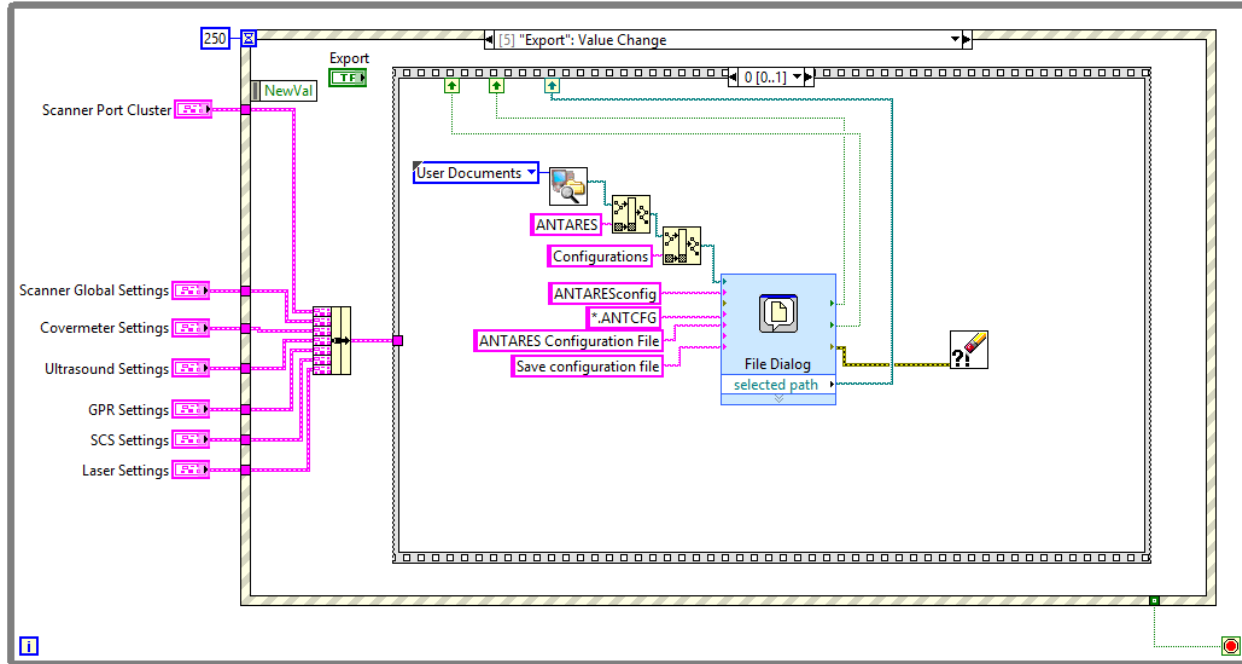


Figure 6-16. Main loop of Configuration Settings Screen displaying the export *ANTCFG file case.

Finally, the Grid Generation Wizard is a supplemental VI to the Main Interface VI which makes creating a grid to be automatically scanned using the ANTARES scanner significantly easier for the operator. An operator can manually complete the grid settings data cluster on the main interface and successfully run an automated scan without using the Grid Generation Wizard, however using the wizard allows the operator to visualize the final size and density of the grid to be scanned.

The Grid Generation Wizard works by allowing the operator to manually move the scanner with the desired NDE instrument attached to the starting point of the grid (the origin), select the orientation of the lines to be scanned (X or Y), move the scanner

to the last point of the first line, move the scanner to the last point of the last line, and provide the desired number of points per line and desired lines in the bracketed scan area. The wizard is intuitive and easy to use and provides detailed feedback to the operator over a text box.

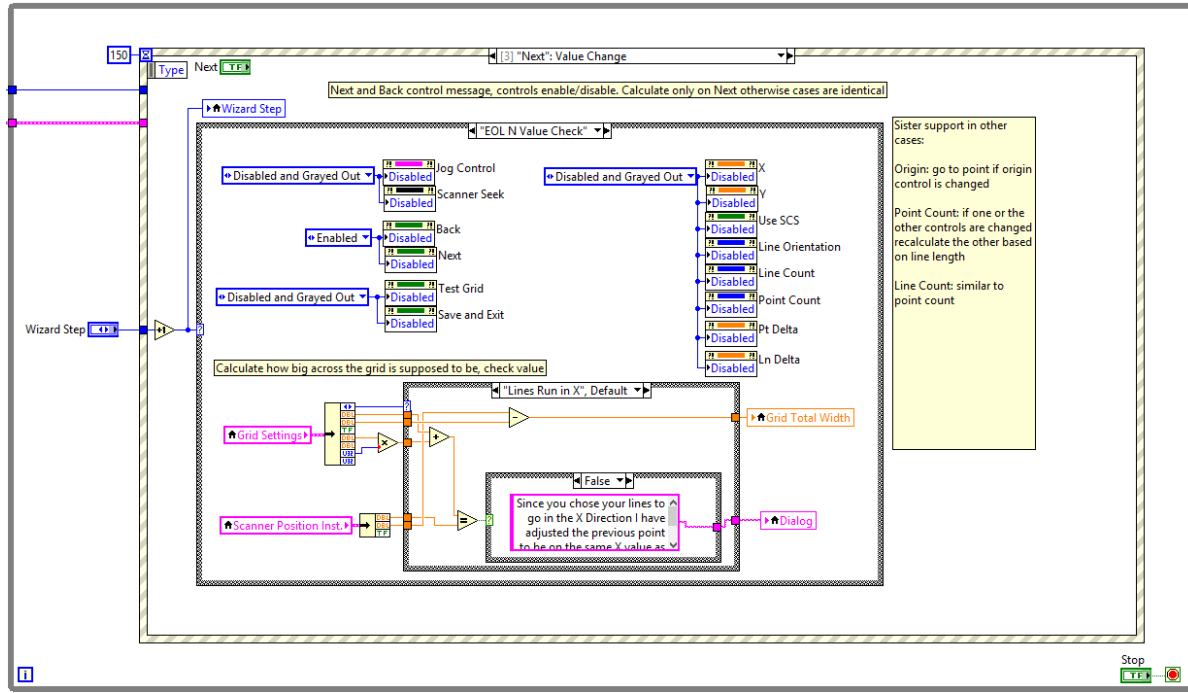


Figure 6-17. Grid Generation Wizard main loop with state machine architecture.

The Grid Generation Wizard VI software architecture is based around a simple state machine—a case-based structure in which the operator's actions change an enumerator control which alters the case (state) of the software. This architecture allows the operator to step through the grid generation process in order, go back one or more steps, and perform each step in different ways as desired. The software also validates the grid setting parameters at each step of the operation so physically impossible grid configurations or grids that may run the instrument into the scanner frame cannot be generated based on invalid user inputs.

Interface Design

Introduction

Interface design is usually secondary to function in software designed by an engineering research team, however to create an intuitive interface for maximum usability significant time and effort was invested in creating a simple, intuitive, cohesive, and attractive interface for the ANTARES SVW software.

This section discusses the design and use of the main software interfaces of ANTARES SVW. The interfaces will be discussed in the order in which the operator is likely to encounter them, in a user's manual style, rather than in order of development, use, or complexity.

Splash Screen

As discussed earlier in this chapter, the Splash Screen VI is an 18 step sequence of events necessary to initialize the ANTARES hardware and software. Each of these steps is completely automatic and requires no operator input. For this reason, it was decided to encase these long but necessary steps in a familiar software structure. The VI was designed as a loading screen as shown in Figure 6-18.

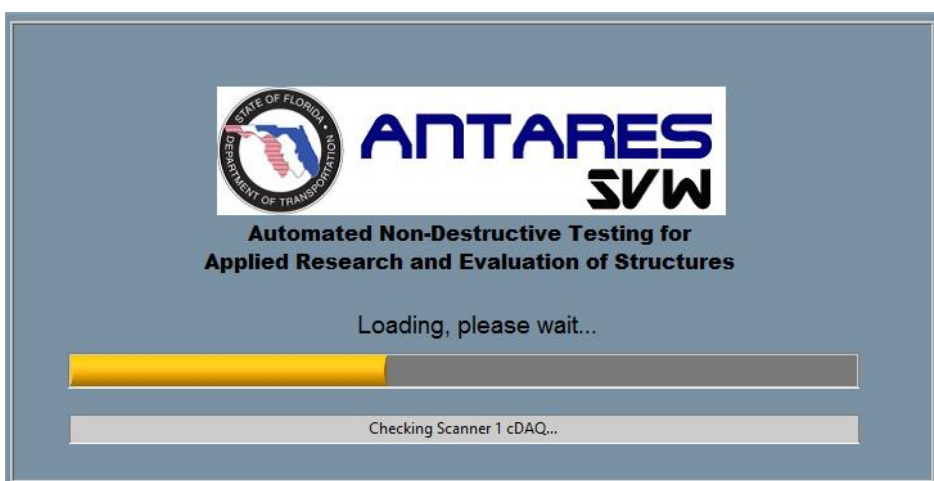


Figure 6-18. ANTARES SVW splash screen with loading bar and feedback to operator.

The loading screen displays the progress of the initialization in a progress bar and provides the operator with text feedback about the procedure including any communication errors and startup issues. One of the most important functions of this screen is to successfully load the configuration settings cluster. If this load is unsuccessful, as usually occurs when ANTARES SVW is launched on a new computer for the first time, the Splash Screen launches the Configuration Settings Screen automatically.

Configuration Settings Screen

The Configuration Settings Screen allows the operator to import, export, and modify the configuration settings cluster for the ANTARES SVW software. The interface with this data cluster is presented as a series of tabs with various numeric and drop-down menu controls. Default settings for the scanners themselves including ports, calibration constants, and default speed and acceleration settings, port settings for each native instrument, and default scan modes for each instrument are generated, altered, loaded, and saved from this panel. One of the most important settings generated in this screen is the COM port and cDAQ™ assignments for each scanner. When these values are changed, the Configuration Settings Screen automatically checks each port and verifies the selection is correct, indicating success or failure with a red or green LED-style indicator as shown in Figure 6-19. Similarly, instrument default settings are changed as shown in Figure 6-20.

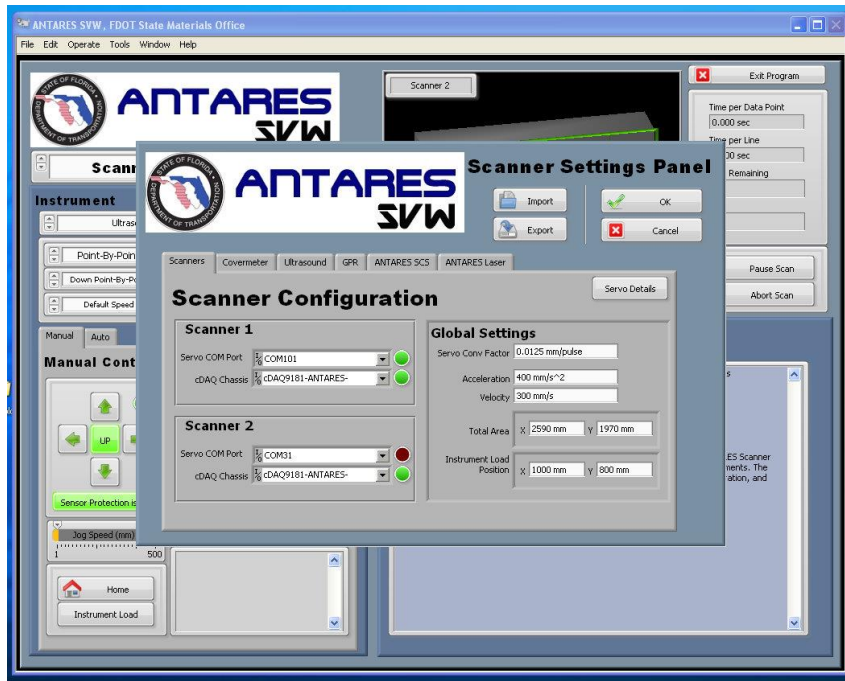


Figure 6-19. Configuration Settings Screen on Scanner Configuration tab.

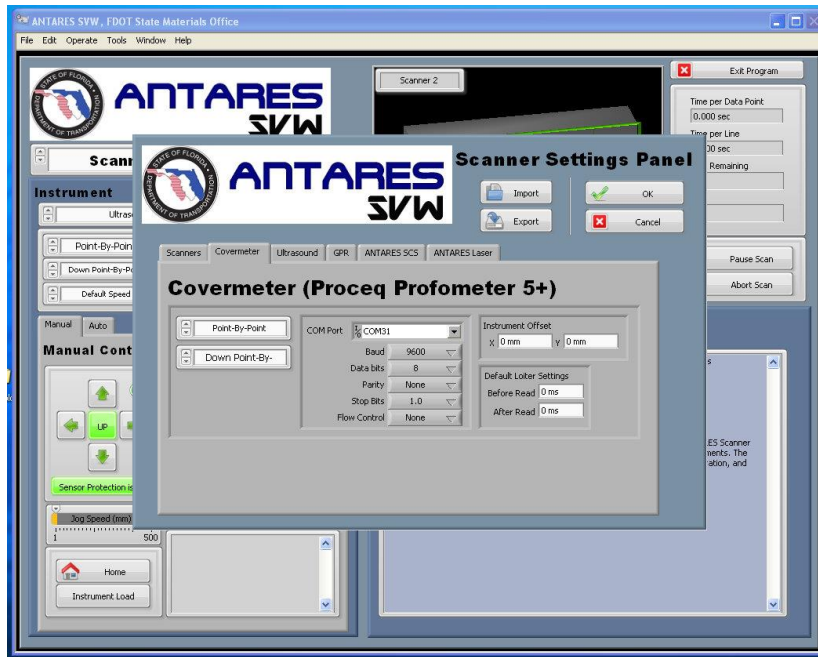


Figure 6-20. Configuration Settings Screen modifying a native instrument's default port and scanning operation settings.

Main Interface

The main interface of ANTARES SVW is designed to provide the operator with complete control over the operation of the ANTARES scanner systems as well as display feedback about the position and instrument head status from scanners themselves and incoming data from the NDE instrument in use during a scan. The interface is designed to be compact, robust, and easy to navigate with clear structure and order as shown in Figure 6-21.

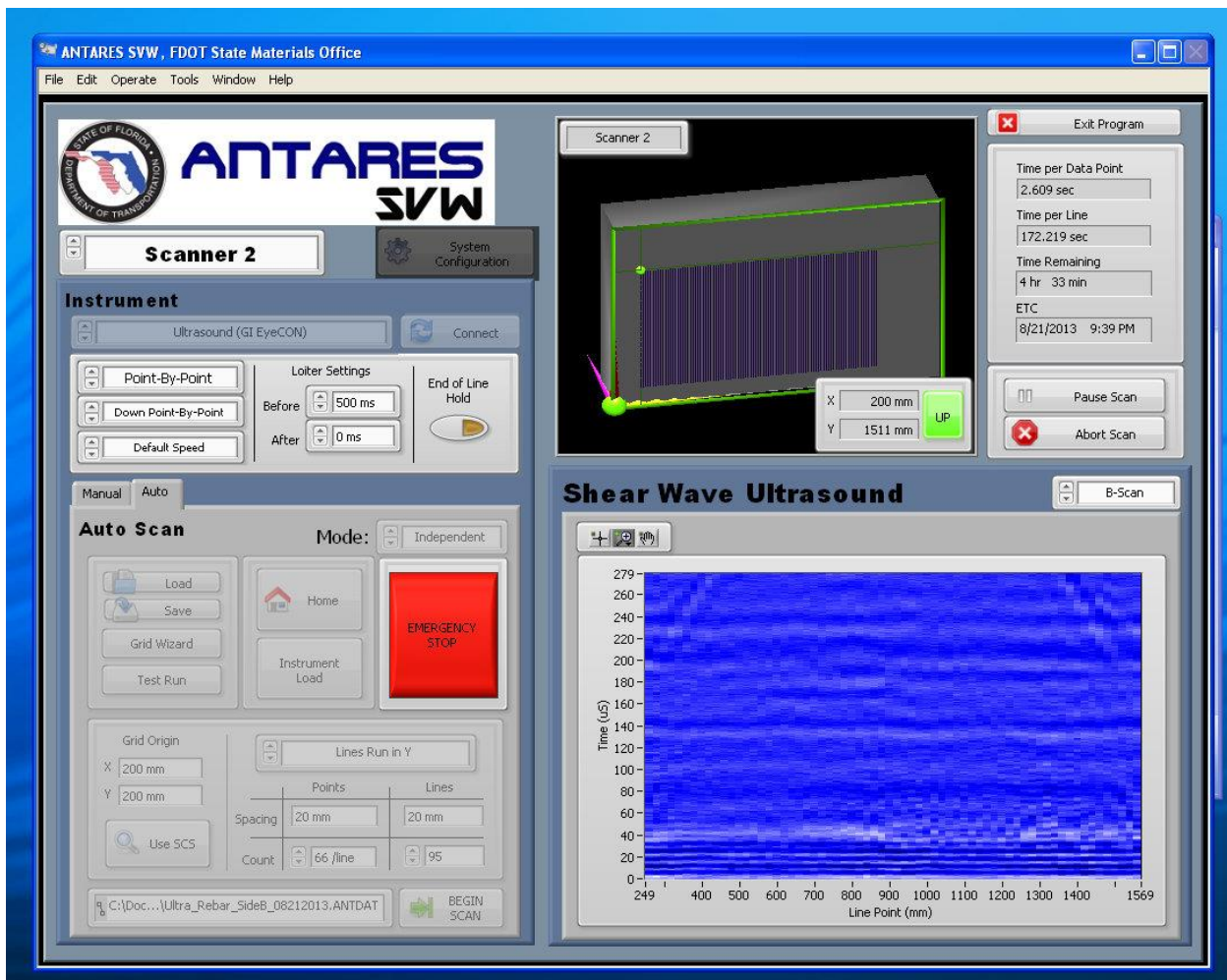


Figure 6-21. Main interface of ANTARES SVW during a shear wave ultrasound scan.

The main interface provides settings and controls necessary to setup the scanners and prepare for an automated scan on the left side of the screen. This

includes a bank of manual scanner movement controls, instrument settings, grid settings, and a control that toggles the settings between the two scanners (if connected successfully). Perhaps most importantly, no matter how the operator configures the software the left side of the main interface always has an emergency stop soft button clearly displayed and enabled any time it is possible for the scanner to be in motion. This applies even when an automatic scan is active, as the Autoscan VI is designed to relinquish control to the Main Interface VI in emergency situations as described earlier in this chapter.

The right side of the screen is devoted to operator feedback and includes a three-dimensional display of the scanner's position in space as well as its coordinates and instrument head up/down status. During an automated scan, incoming instrument data is presented in real time and an information cluster containing the elapsed time of the scan as well as an estimated time to completion (ETC) is presented for the operator's reference. Controls to pause or abort the automated scan are also provided for the operator's convenience.

Grid Generation Wizard

The Grid Generation Wizard VI is accessible from the main program interface as long as the Autoscan VI is not active and an automated scan is not in progress. It is a more convenient and intuitive way to generate a grid for an automated scanning and its mechanics are discussed in detail in the previous section. The wizard's interface itself is a rearranged version of the manual controls and scanner location display in the main interface as shown in Figure 6-22. At the top of the panel a large text box provides the user with contextual instructions for using the wizard as well as buttons to proceed forward or backward in the grid generation process. The text box allows the Grid Wizard

to communicate with the operator in descriptive phrases to aid in navigating the wizard while the soft panel itself is designed to be as simple as possible and to prevent the user from generating poor or unexpected scan grids.



Figure 6-22. Grid Generation Wizard on one of the final steps to completion of a functional grid.

File I/O

Introduction

One of the main features required from the ANTARES SVW software was to comply with State of Florida's Sunshine Law allowing public access to official government communications as well as FDOT's policy of open communication and data

sharing. As a government agency, FDOT was not only amicable but indeed legally bound in many cases to share its research and evaluation data with other agencies. ANTARES was designed to be a research tool not only for FDOT but any agency that wished to collaborate in future research and development efforts.

Since ANTARES SVW was designed to accept and output several different types of files that may be read, interpreted, and modified by third parties, it was required to produce a series of file I/O subroutines that produced and interpreted data in a well-defined and clearly formatted manner. It was decided to build ANTARES SVW around three file types: a master configuration file (*.ANTCFG) that would contain default settings for the scanners and instruments, a grid file (*.ANTGRD) that could be used to save and load the grids upon which ANTARES would perform NDE scans, and an open-source, text-based universal data file (*.ANTDAT) that could be used with all the native instruments and would contain all the information to analyze an NDE scan of a given grid.

ANTARES Configuration File (*.ANTCFG)

The ANTARES Configuration File (*.ANTCFG) is a binary file containing all vital settings necessary to operate the ANTARES system. It is written or loaded manually in the Configuration Settings Screen, loaded automatically in the Splash Screen, and written automatically when altered within operation of the Main Interface. Since the file can be moved and imported, the ANTARES SVW software can be installed and configured on a new PC rapidly and the settings migrated over easily, allowing almost any computer to be quickly adapted to the ANTARES system.

The file is produced by bundling all the settings established on the Configuration Settings Screen into a single data cluster and flattening this data cluster into a big-

endian format binary string. This binary string is written to a file, and interpreted by loading the file and unflattening the string into a configuration settings data cluster.

ANTARES Grid File (*.ANTGRD)

The ANTARES Grid File (*.ANTGRD) is a binary file formed by flattening a grid settings data cluster. The grid settings data cluster contains the coordinates of the grid origin, the orientation of the grid lines, and the point and line count and spacing. ANTARES Grid Files may be written or loaded from the Main Interface in the grid setup section.

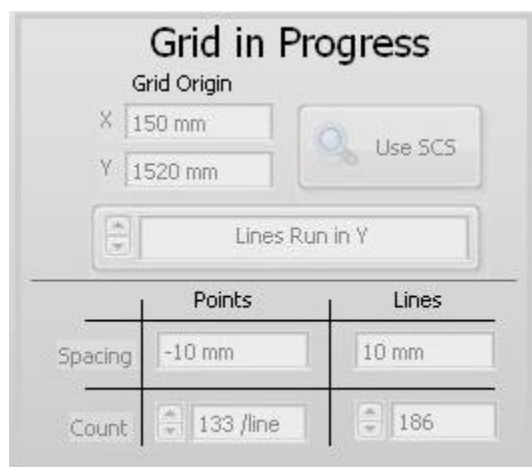


Figure 6-23. Grid configuration cluster as it appears in the Grid Generation Wizard. This data cluster can be written to and read directly from the *.ANTGRD file.

The grid settings data cluster is unique in that it is a complete container of controls for all the numerical and enumerator values necessary to visualize, run, and recreate an automated NDE grid. This makes the cluster ideal for direct flattening to a binary string in the same manner as the configuration settings cluster.

ANTARES Data File (*.ANTDAT)

The ANTARES Data File is a simplification of the multiple file types and formats utilized by the first-stage system software. The Phase I software wrote a unique text file

for each instrument, and separate file for each data point or line of data depending on the instrument. This made the files difficult to interpret and subject to inadvertent separation and loss of individual files.

*.ANTDAT format files contain an entire automated NDE scan and share a common header and data range format. They are text based, tab-delimited files that can be read from any number of available third party programs as well as the ANTARES Processing Software.

ANTARES SVW Data File					
Program Version 1.0b					
Instrument:	ANTARES Laser Profilometer				
Date/Time of creation:	5/30/2013 10:16				
Grid Settings					
Origin X	106				
Origin Y	255				
Line Orientation	X				
Point Spacing	25				
Line Spacing	10				
Point Count	80				
Line Count	74				
Instrument Data					
Time	S-Coord X	S-Coord Y	I-Coord X	I-Coord Y	A-Scan
5/30/2013 10:16	106	255	168	315	86.2

Figure 6-24. Excerpt of an ANTARES Data File (*.ANTDAT) showing generic file format and standard header information.

ANTARES Data Files contain the program version, instrument used, data and time of file creation, and grid settings in the header information. The instrument data section contains a row for each data point with the date and time the data point was

taken, the scanner coordinates, the instrument's coordinates (scanner coordinates plus the instrument's offsets), and A-Scan (single spatial point) data.

The A-Scan data column changes for each instrument as shown in the following table.

Table 6-1. A-Scan data output formats for *.ANTDAT file format.

Instrument	A-Scan Data Type
Covermeter	Cover in mm, 0 digits of precision
Laser Profilometer	Distance in mm, 1 digit of precision
Ultrasound	2048 point 32 bit integer waveform
SCS	Binary image string
GPR/Parallel Instrument	Blank

The universal nature of the ANTARES Data File allows the file format to be expanded easily to new instrument types and new data formats and allows for collaborative processing efforts on data output by the system. Since a data file is generated even in the case of parallel instrument operation, if an NDE scan is performed in parallel mode the data can be mapped to the grid given in the data file by using either the time stamps for each coordinate or by the coordinates themselves if the instrument has its own position encoder (as was the case with the GPR system).

ANTARES Processing Software

Introduction

The capstone piece of software to be developed for the ANTARES system was the software suite for processing the raw data generated by the scanner and attached

NDE instruments into two and three dimensional plots suitable for analysis. The ANTARES Processing Suite would be a simple and accessible platform for processing of NDE data generated by ANTARES to be expanded and modified later as new development efforts were sponsored.

Approach

Compared to ANTARES SVW, the ANTARES Processing Suite would be relatively straightforward to develop. Since no hardware communication and control was involved, the software could be run in a single event-driven structure. Compared to a software loop that continuously executes such as those in ANTARES SVW, an event-driven loop relinquishes a computer's processor threads when idle, greatly reducing hardware demand.

With the basic architecture designed, the framework of the ANTARES Processing Suite was populated using a series of tab controlled panels for each instrument type to be processed. A simple file opening interface was generated to read in *.ANTDAT files for all the native instruments and groups of *.DZT line data files for the GPR system. Each instrument type received customized interfaces with processing and visualization features pertinent to the data to be displayed.

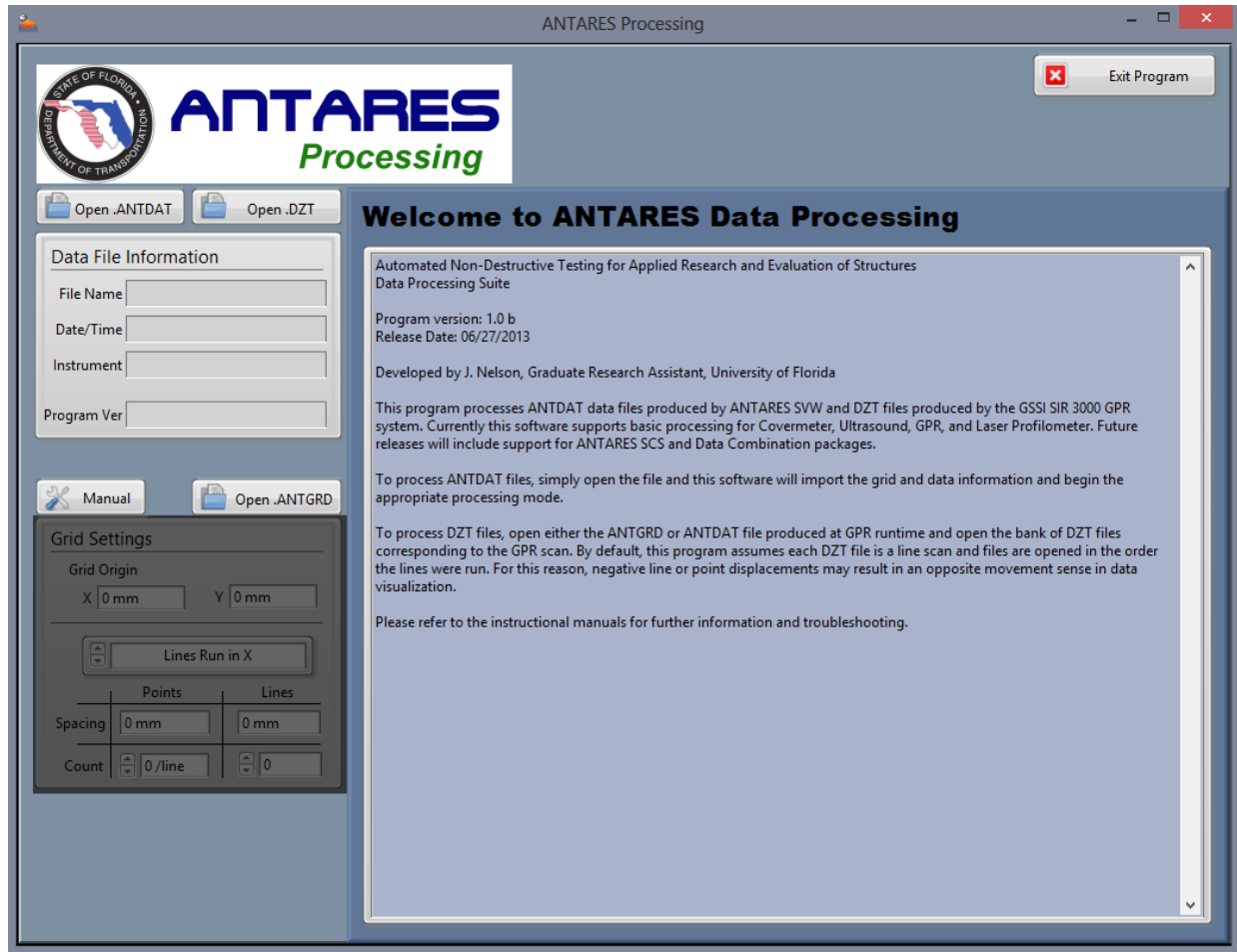


Figure 6-25. Welcome panel of ANTARES Processing Suite.

While designing a software package to output the various processed data sets into formatted report files proved to be impractical, each plot display on the software panel could be exported as a simplified image or data set by right clicking on the plot itself. These images could then be used to generate a report in the program of the user's choice.

Covermeter processing

Processing of covermeter data proved to be relatively straightforward since the data format is scalar in nature. The *.ANTDAT file generated for a covermeter scan contains a table of coordinates for the instrument and the measured cover in millimeters

at that coordinate. The instrument itself performs all necessary calculations and adjustments onboard and reports the measured cover, exactly as a technician using the instrument in the field would use it.

A data realization VI shown in Figure 6-26 was developed to generate a two and three dimensional plot from the provided covermeter data. This VI accepts the values from the instrument coordinates and A-Scan columns of the *.ANTDAT file, the loaded grid settings, and a desired number of points for a moving average smoothing filter (if desired). The VI then generates various data matrices suitable for plot generation using the built-in tools found in LabVIEW™ for three-dimensional scatter plots and two-dimensional intensity plots.

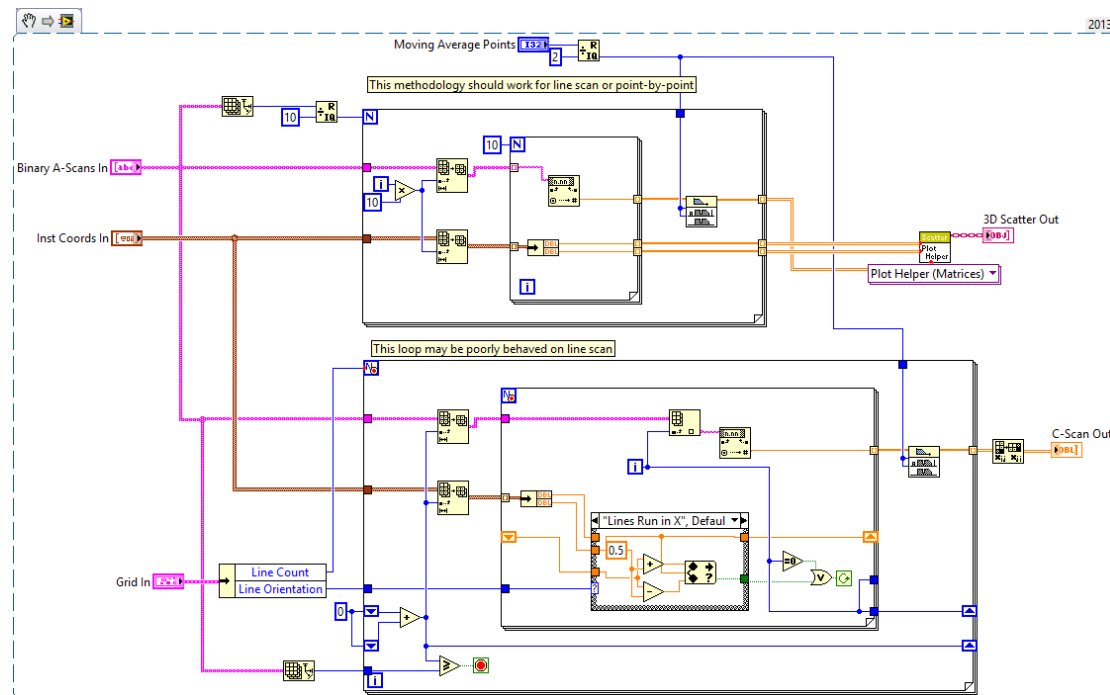


Figure 6-26. Code snippet for covermeter and laser data realization VI.

A two-dimensional display or C-Scan image of covermeter data can be visualized as a top-down view of the scan area with lightly colored pixels representing areas of shallow cover and darker pixels representing areas of deeper cover. Due to the output

format of the covermeter used in this research, when no reinforcement is detected a value of zero is reported, leading to pure white areas on the C-Scan display in areas of infinite cover where one would expect black pixels. This effect is shown in Figure 6-27, where the data display is indexed in point number (X) and line number (Y) format.

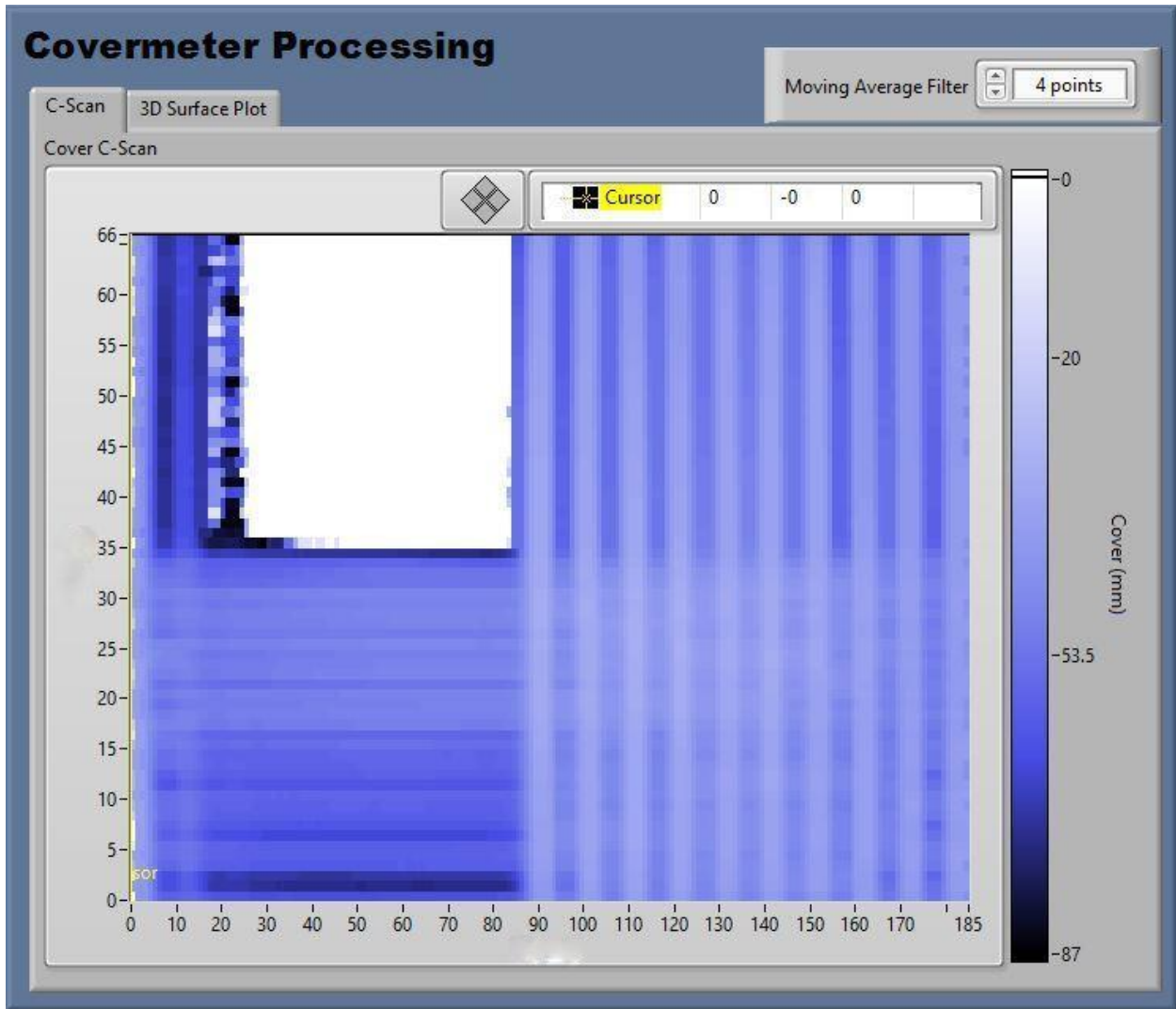


Figure 6-27. Example of a 2D intensity plot covermeter data visualization in the ANTARES Processing Suite.

The three-dimensional plot display shown in Figure 6-28 allows the user to visualize the overall characteristics of the scanned specimen in any desired view orientation. While this is useful for developing a sense of the overall configuration of the

reinforcement within the structure—the two-dimensional intensity plot allows for precise measurements by dragging a special cursor which indicates the X, Y, and Cover values of any point on the plot.

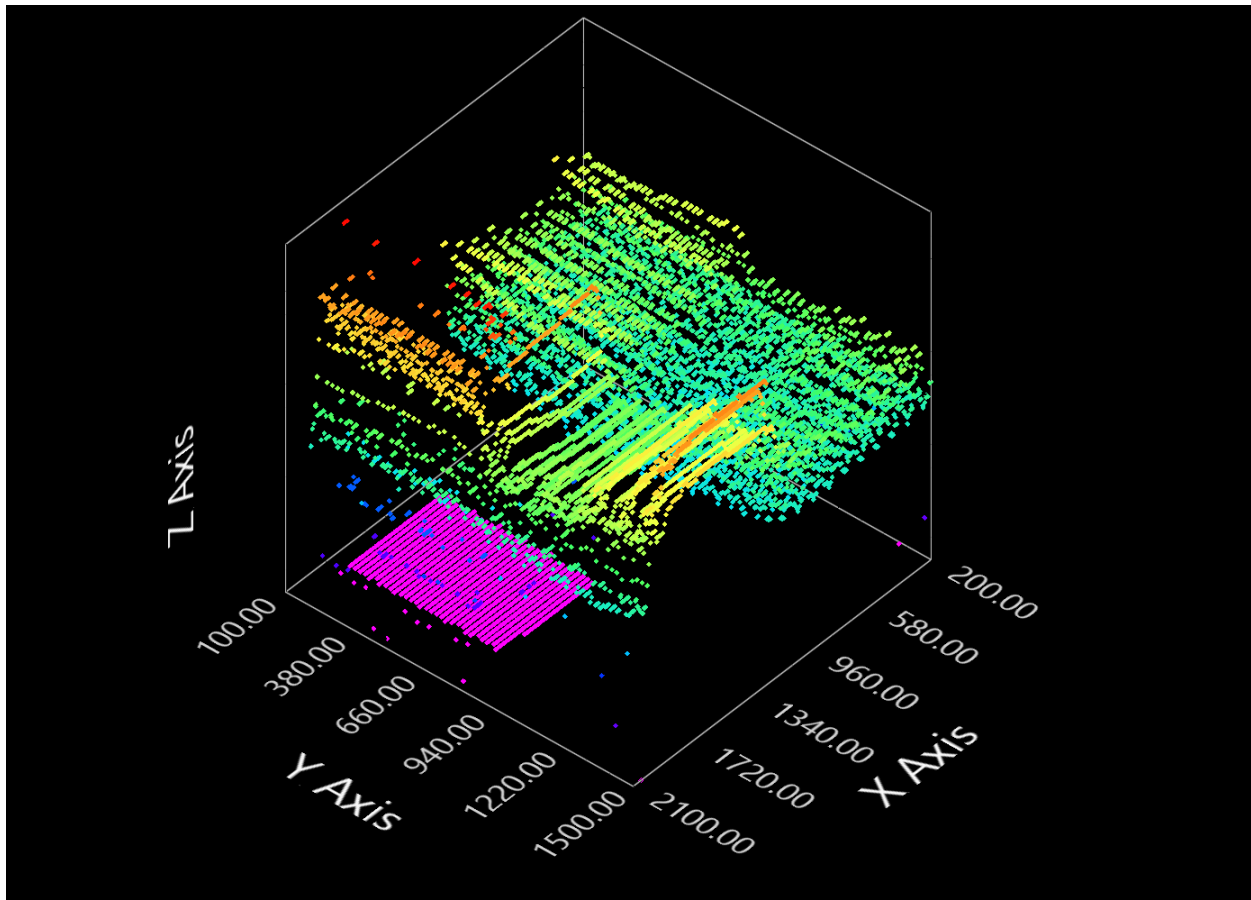


Figure 6-28. Example of a 3D scatter plot covermeter data visualization in the ANTARES Processing Suite.

Laser profilometer processing

Functionally, the processing scheme for the laser profilometer was no different than that of the covermeter. The format of the data is identical—a single numerical data point for each coordinate—however the laser distance measurement affords another decimal of precision, resolving to 0.1mm under ideal conditions. A C-Scan image of a laser profilometer scan of a rough bridge deck is shown in Figure 6-29, where the

difference between the highest (light pixels) and lowest (dark pixels) regions of the display is measured using the cursor to be 15.4 mm.

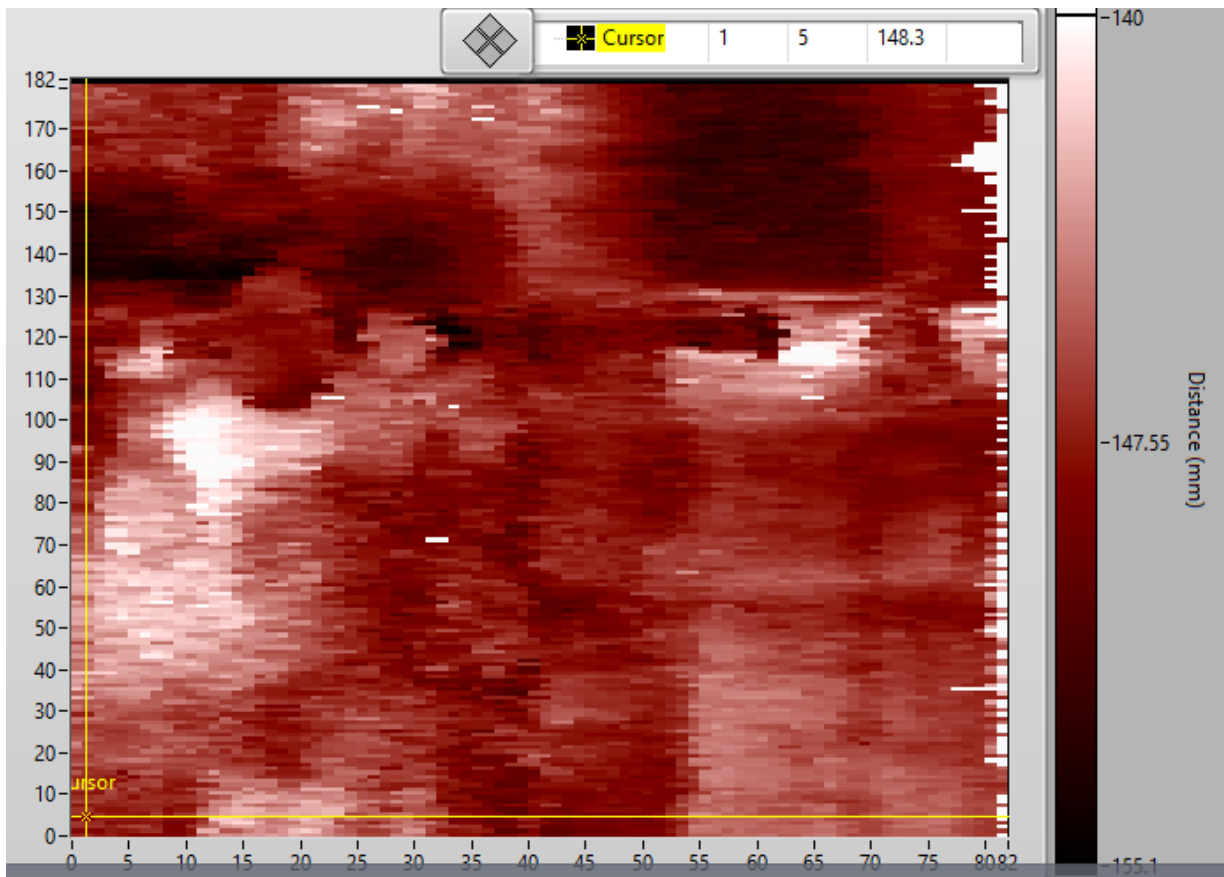


Figure 6-29. Example of a 2D laser profilometer data visualization of a rough experimental bridge deck.

When rendered in three dimensions, laser profilometer data presents the operator with a movable colorized surface representative of the scanned area that can be used to quickly identify overall shape and texture of the specimen surface. A three dimensional display of the rough bridge deck mentioned discussed earlier in this section is provided in Figure 6-30.

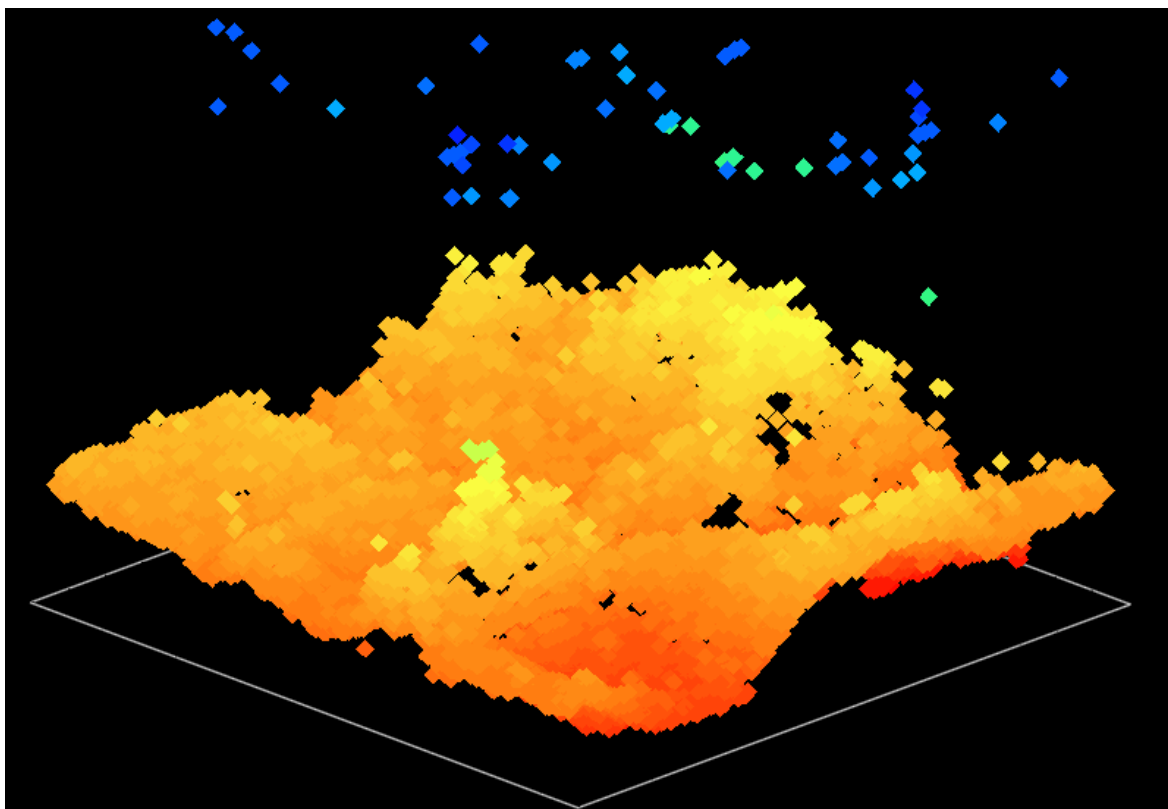


Figure 6-30. 3D render of laser profilometer data a rough bridge deck surface.

The laser profilometer data is usually collected in line-scan mode, meaning the instrument is read continuously at a high rate while the scanner traverses a grid line at a constant velocity. Compared to the point-by-point scan mode used with most other instruments, this operating scheme results in highly dense, far more rapid data collection although the data points may be unevenly spaced and some noise in the data due to vibration in the moving scanner is generated. Additionally, the laser profilometer is prone to scattering when incident on a sharp edge or sudden elevation change, resulting in an erroneous reported value. To overcome these limitations, the laser profilometer data is plotted using the true scanner coordinates at the time of instrument read as given in the *.ANTDAT file and some filtering (usually 4 points) using the provided moving average filter is required.

GPR processing

Almost every major manufacturer of GPR equipment has at some point produced their own data visualization software. These software packages are usually quite powerful and very well refined. Despite the availability of this software, it was decided to include some limited GPR processing ability in the ANTARES Processing Suite.

GPR Processing posed a unique challenge in that the software was required to work with the GSSI standard binary file format (*.DZT) due to the parallel operation nature of the SIR3000™ GPR unit. The GPR processing section of the ANTARES Processing Suite would need to open a group of *.DZT files where each file corresponds to a single line in a scanned grid and map these lines to a grid settings cluster imported from either a *.ANTDAT or *.ANTGRD file.

Fortunately, due to efforts from the US Geological Survey (USGS), GPR manufacturers have agreed to make their binary file formats open-source and USGS have posted these file formats for public use in previous reports [35]. With this file format in hand, a LabVIEW™ VI was developed to open a group of *.DZT files and convert them into a two-dimensional array of unsigned 16-bit integers.

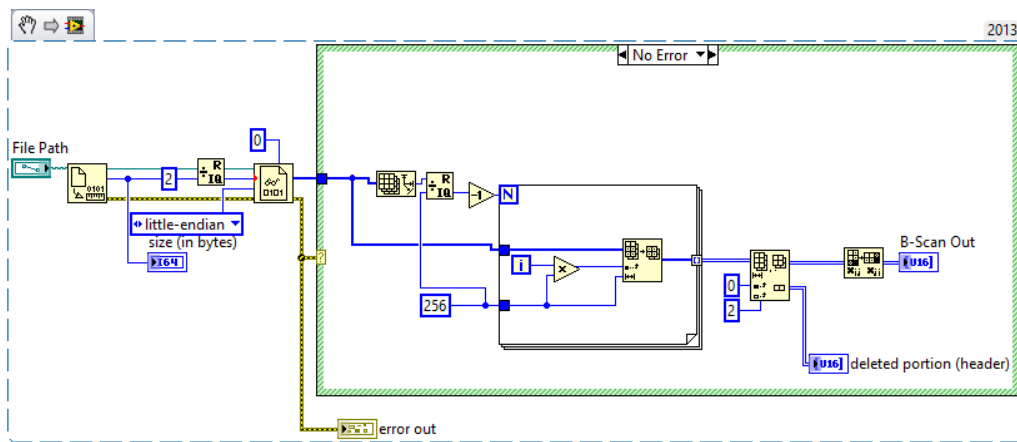


Figure 6-31. GSSI binary data file (*.DZT) importing VI used to interpret GPR data for the ANTARES Processing Suite.

Visualizing the imported GPR data was accomplished by using the grid settings imported from the *.ANTDAT or *.ANTGRD to simply scale the axes of the various plots to match the spacing between the GPR line scans. With this methodology, the two-dimensional GPR data cube could be plotted directly to the intensity plot displays without introducing a mathematical scale to the stored data.

Two distinct intensity plot displays were designed for GPR data visualization: a fly-through C-Scan display and a fly-through Tomograph display. The C-Scan display shows GPR data in the XY plane with the ability to step through the thickness of the scan area using a manual slider control or an automatic fly-through function that played like a video through the plot's thickness as shown in Figure 6-32. The Tomograph display presented in Figure 6-33 allows visibility in the XZ or the YZ plane with the ability to manually step or automatically fly through the dimension not displayed. Depth and distance information is provided from the GSSI instrument using their own calculations for GPR flight time and an integrated position encoder and the data array imported from the *DZT file is already in a scaled format suitable for display.

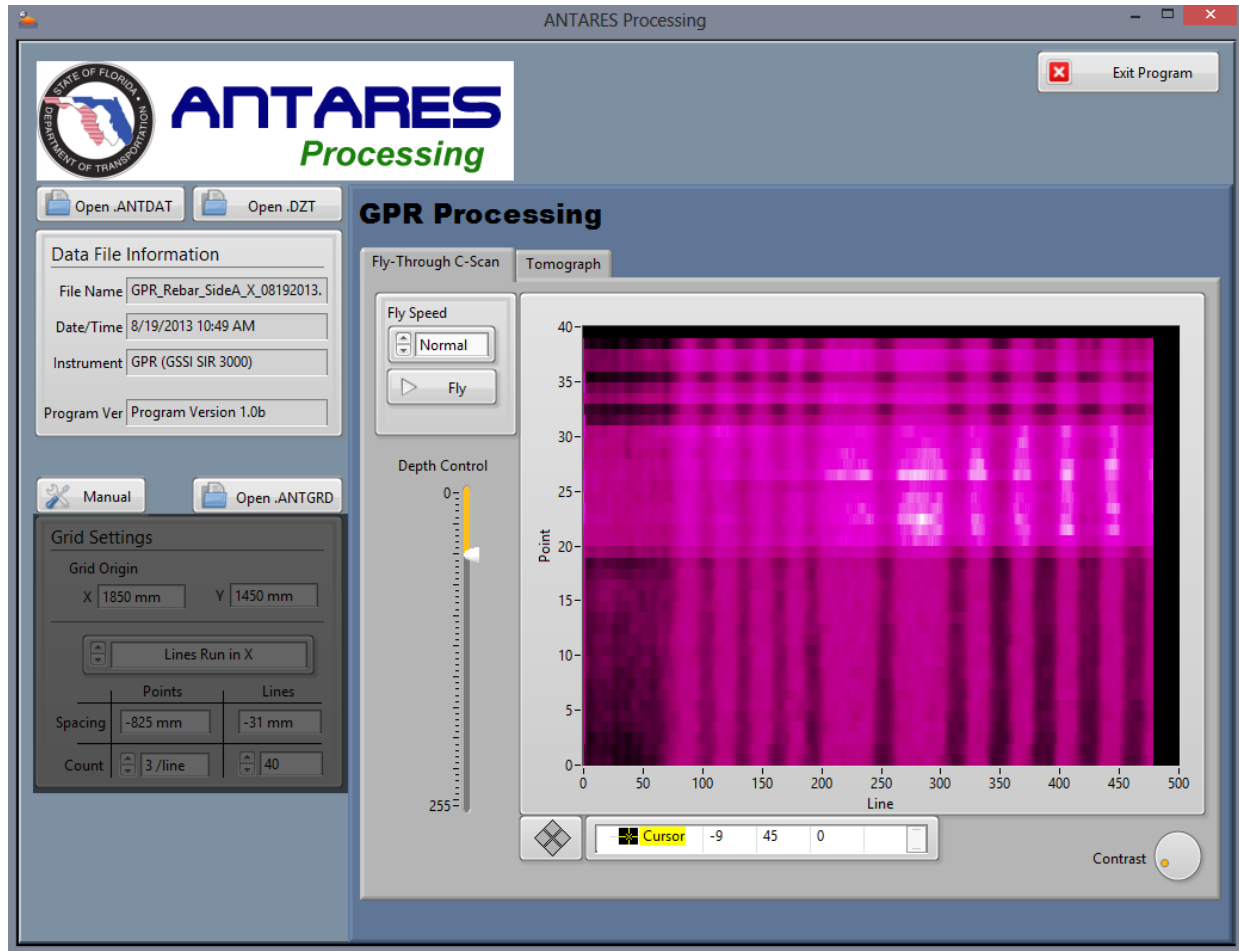


Figure 6-32. Fly-through C-Scan GPR display showing a layer of dense rebar in a test specimen. Depth of the display is controlled using the vertical slider on the left side of the display.

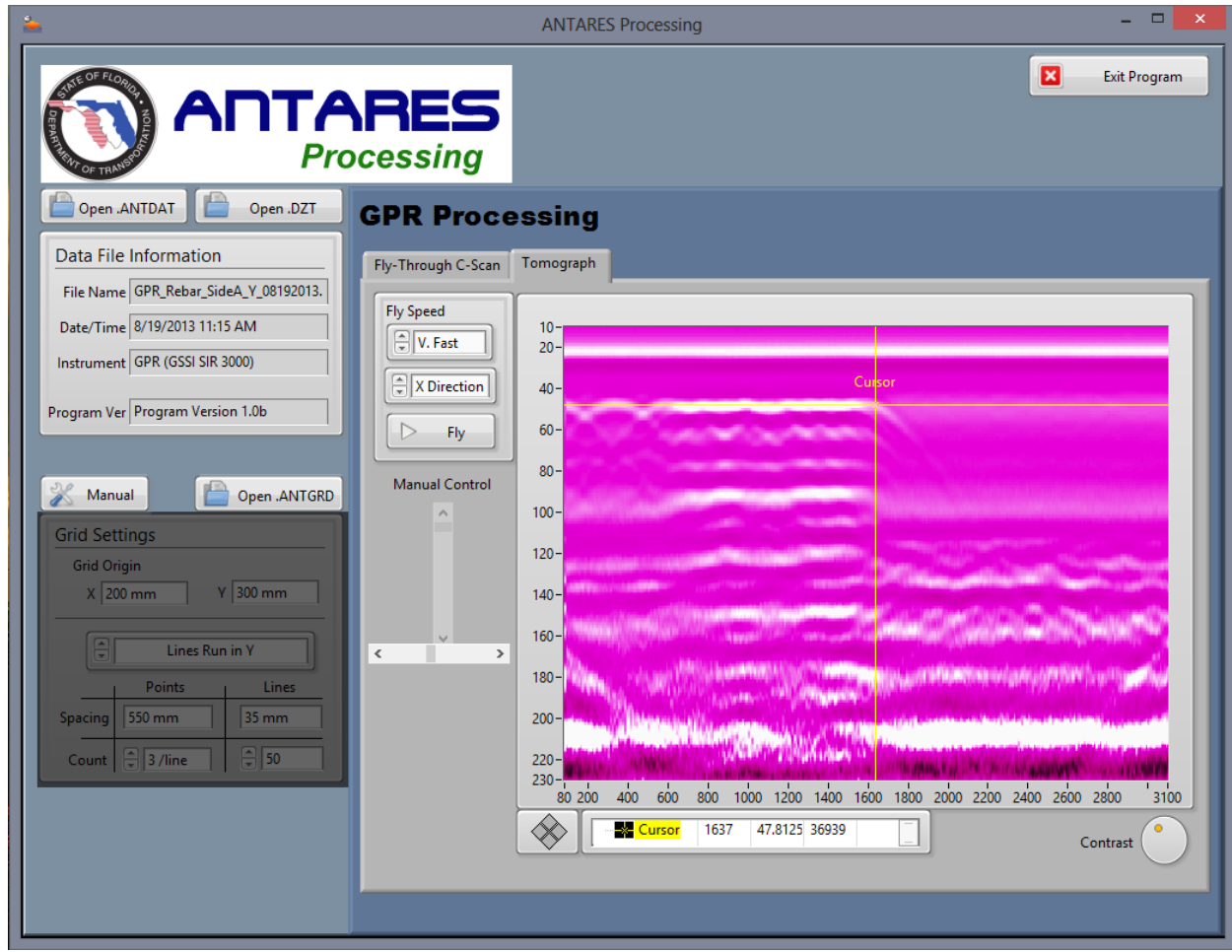


Figure 6-33. Tomograph display of GPR data showing a dense rebar mat in the YZ plane. Two layers of rebar running transverse to the display are visible as a series of white hyperbolic traces on the pink background.

Shear wave ultrasound processing

Shear wave ultrasound data processing offered the most significant contribution, and indeed the most significant challenge, to the successful development of the ANTARES Processing Suite. The 2048 point waveforms generated by the EyeCON™ instrument included significant noise and variation and were often difficult to interpret. Extensive post-processing is required to generate a clear data visualization from the raw ultrasound data. Typical artifacts in a raw ultrasound waveform include

- False reflections near the surface of the specimen due to Rayleigh wave detection by adjacent transducers

- False reflections beyond the specimen thickness due to wave echoes
- Wave reflections from off-axis objects and compact geometries
- High frequency electrical noise

To remove these artifacts, a selectable sequence of filtering steps are available to the processing software operator. First, to trim the false reflections before and after the desired range of depth for the specimen, the operator provides a minimum and maximum depth for the scan area as well as a velocity for the shear wave used to convert the time-domain ultrasound waveforms into depth domain in millimeters. This data is trimmed and passed to a bandpass second order digital Butterworth filter with configurable cutoff frequencies.

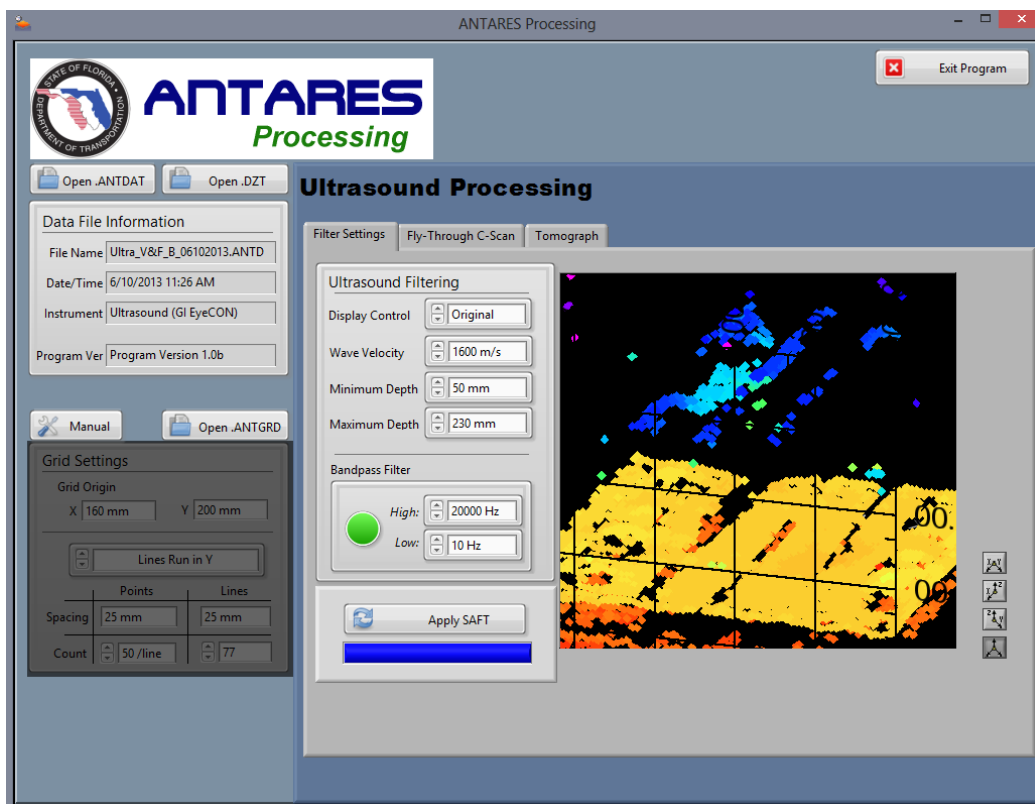


Figure 6-34. Ultrasound processing pane with trimming and filtering options enabled.

The final step in the ultrasound processing VI is to apply a data transform to aid in visualization of the data plots. The selection of a data transform depends on the operator's preference, but three options are available

1. Original: Trimmed, filtered data is presented as calculated
2. Absolute: Waveform amplitude (intensity) is presented as absolute values. This eliminates some confusion in areas where the wave reflection oscillates rapidly and produces alternating light-and-dark layers on the intensity plots
3. Hilbert: Applies a Hilbert transform to each waveform, eliminating superfluous negative frequency content and emphasizing edge detection by creating a display that is more sensitive to change in relative intensities

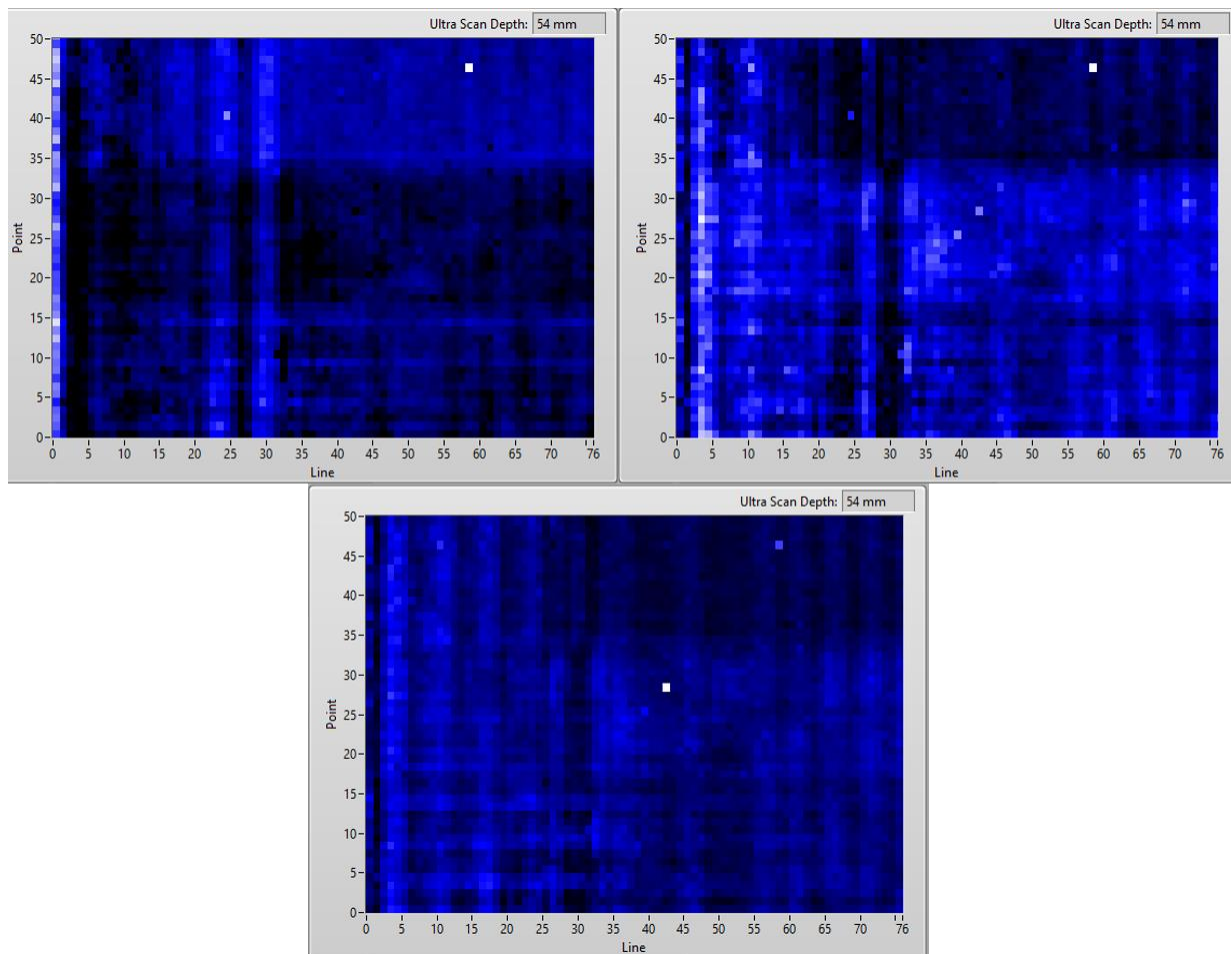


Figure 6-35. Ultrasound C-Scan of a dense rebar mat at a depth of 54mm with Original (top-left), Absolute (top-right), and Hilbert (bottom-middle) data transforms.

After processing, a number of displays for shear wave ultrasound data are available to the operator of the ANTARES Processing Suite. A three-dimensional scatter plot on the filter settings tab visualizes the depth of the maximum intensity of the reflected stress wave. If filtering and trimming are done correctly, this single data point per coordinate should correspond with either the back surface of the scanned specimen or a source of significant reflection within the structure.

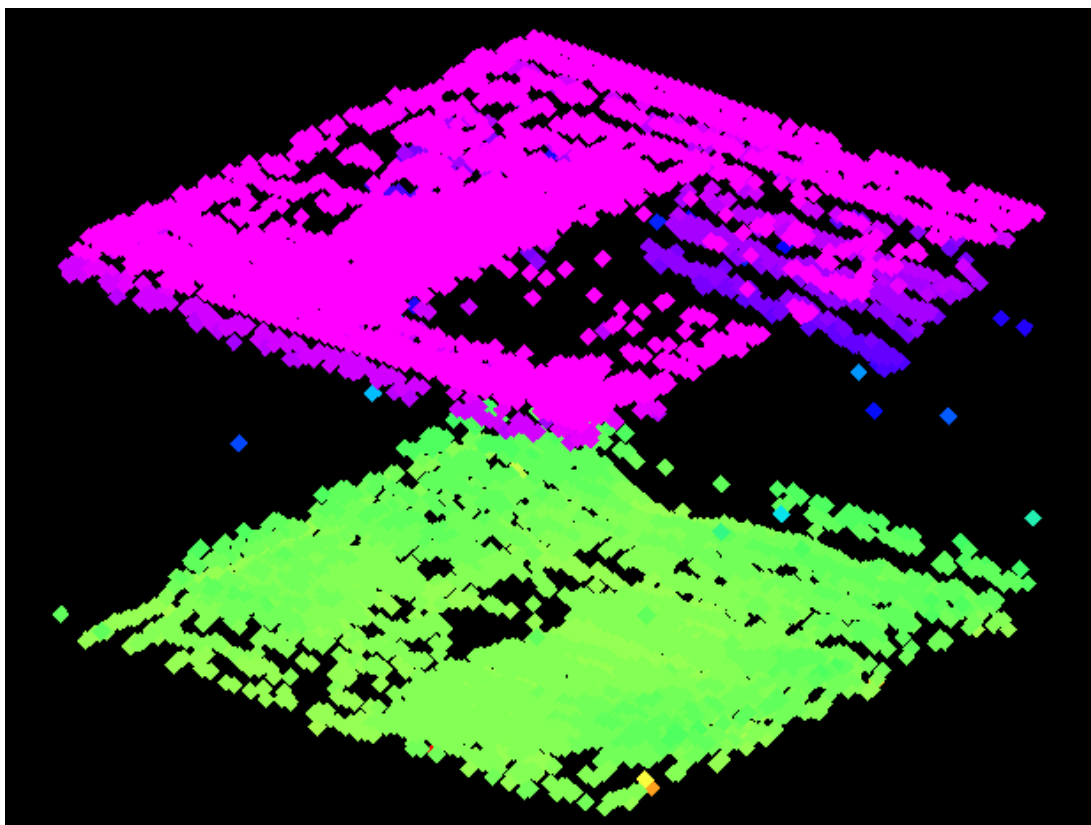


Figure 6-36. 3D ultrasound scatter plot of a densely reinforced concrete structure.

Frequently the scatter plot display is far too cluttered with spurious high reflections to be of sense to the operator. For instances such as these, the Fly-Through C-Scan and Fly-Through Tomograph displays—identical in function to their counterparts in the GPR processing section—are much more useful in visualizing ultrasound data.

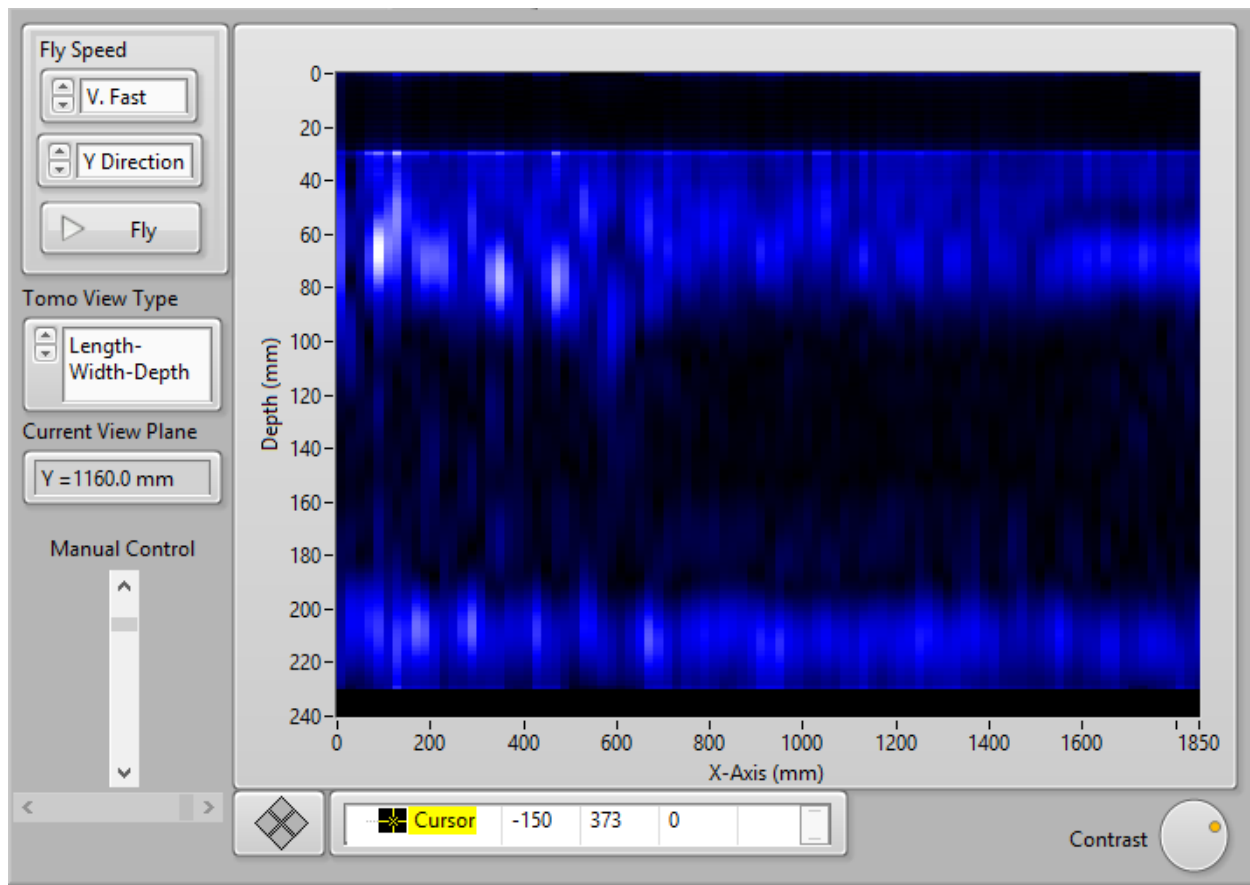


Figure 6-37. Tomograph display of reinforced specimen with rebar mat (top white and light blue) and back side of specimen (bottom light blue) visible.

System Summary

The finalized ANTARES system is a fully integrated expandable system for automated NDE of concrete structures capable of operating five different instruments in a repeatable manner over dense two dimensional grids on a concrete surface. The remainder of this thesis will discuss efforts to prove the viability of the new system and expand its capabilities both in the laboratory and in the field.

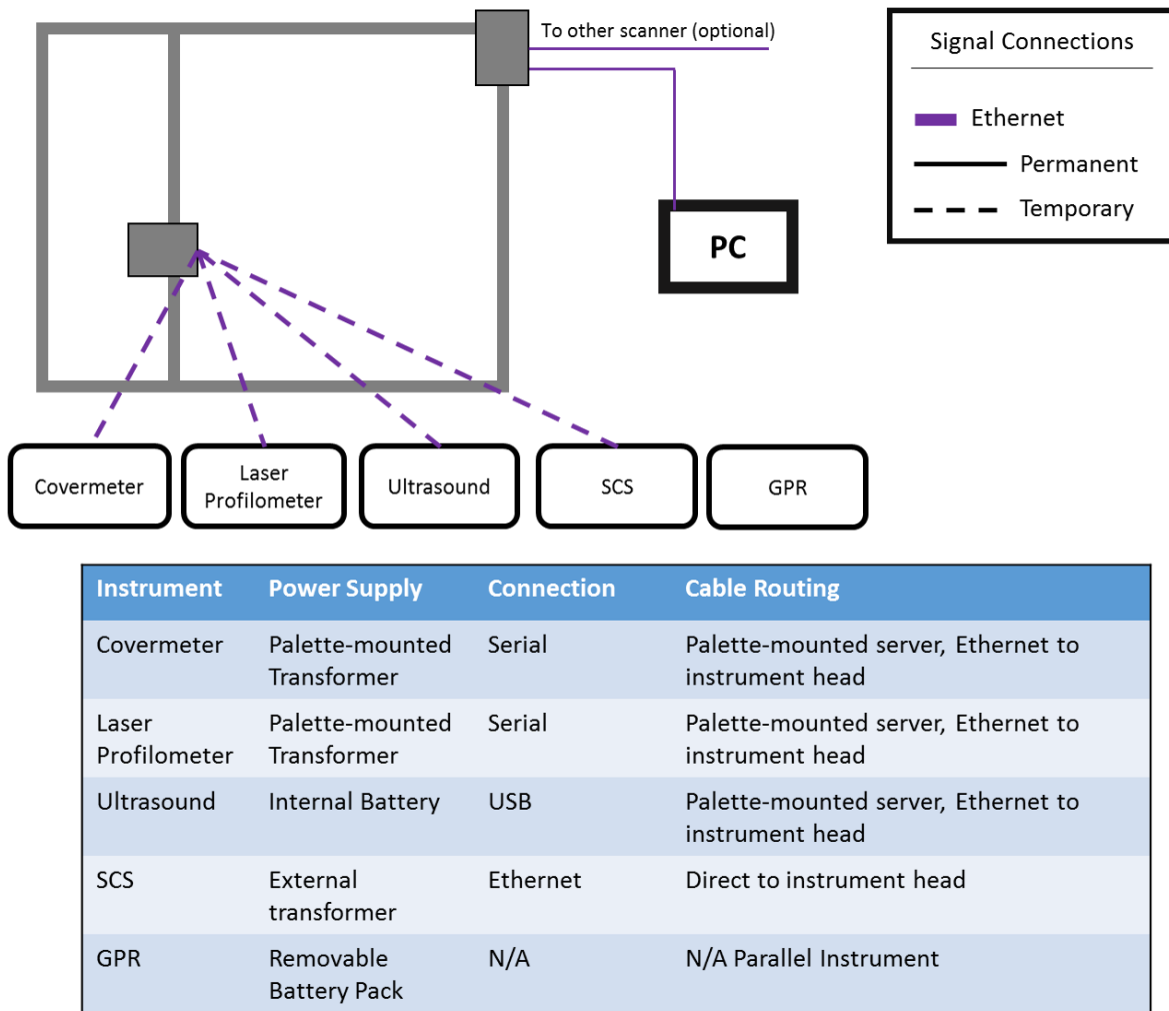


Figure 6-38. Instruments and signal connection scheme for the new ANTARES system.

CHAPTER 7

LABORATORY EVALUATION BLOCK CONSTRUCTION

Introduction

The ANTARES Laboratory Evaluation Blocks represent a tremendous asset to FDOT and any collaborating agencies wishing to test new NDE instruments and techniques to investigate various structural characteristics and defects. The blocks are fabricated with tightly controlled concrete mixes and precisely located features for detection by NDE instruments and supported extensively by laboratory tests for material properties. Blocks may be loaded into a steel clamping frame which also serves as a mount for the two ANTARES scanner systems for simultaneous front and back access or can be scanned using manually operated instruments for comparison with automated techniques. FDOT has already executed several collaborative research contracts with other agencies centered around data collection and comparison with the Laboratory Evaluation Blocks at the time of the writing of this thesis [36] [37].

As a result of this utility and corresponding interests, it was decided that the research team would produce two additional Laboratory Evaluation Blocks in the course of this research effort. The first block would be designed as an improved internal post tensioning duct evaluation block and the second would include some common construction defects including honeycombing, deep cracking, and delamination of reinforcing steel.

Asymmetric Internal PT Duct Block

Design

While the Phase I system produced by Dr. Algernon produced a specimen for evaluating internal post tensioning ducts, it was noted in the conclusion of his research

that the specimen did not perform as expected and included unintentional defects that prevented its use as an effective evaluation specimen for NDE instruments [9].

Furthermore, the original PT duct block was constructed with galvanized steel internal ducts, which are no longer the standard practice in the State of Florida. Currently, all construction agencies using internal post tensioning duct technology in Florida and much of the US are required to use polypropylene or high density polyethylene (HDPE) ducts. Galvanized steel PT ducts are still regularly used for external tendons but are rapidly being phased out in favor of cheaper, easier to handle HDPE ducts.

Design of the new PT duct specimen included four polypropylene internal ducts with a bundle of three seven wire strand elements installed approximately on the center axis of each duct. These ducts would be installed in the concrete mold and held in place with epoxy mortar. Two of the ducts would be inclined on a work surface and partially filled with grout before installation into the concrete mold to create a void space within the duct of linearly increasing cross sectional area as shown in Figure 7-1. The other two ducts would be left empty, with one to be filled completely with grout after concrete placement and the other to remain empty.

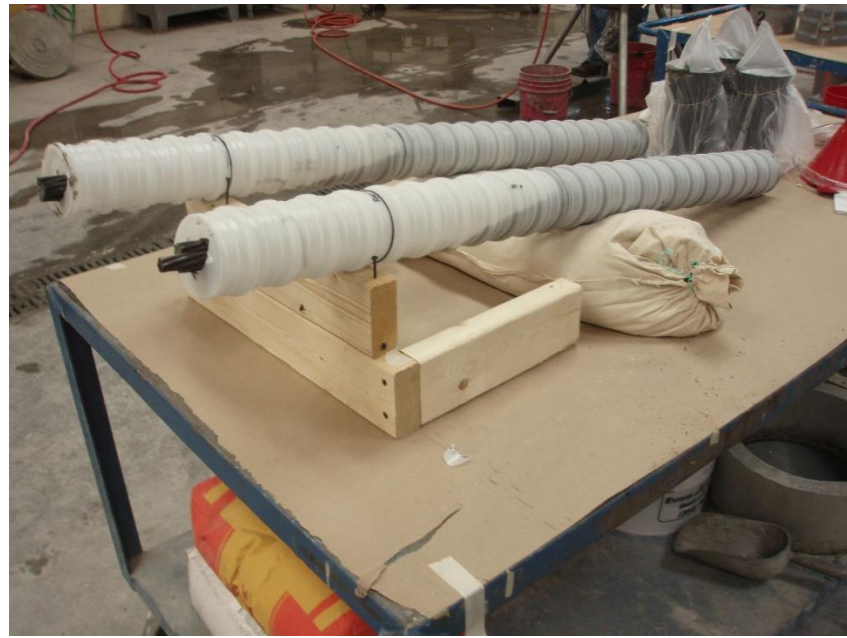


Figure 7-1. Grouting of middle ducts of Asymmetric Internal PT Duct Block. The ducts were filled on an inclined support to produce a varying void space (Photo by J. Nelson).

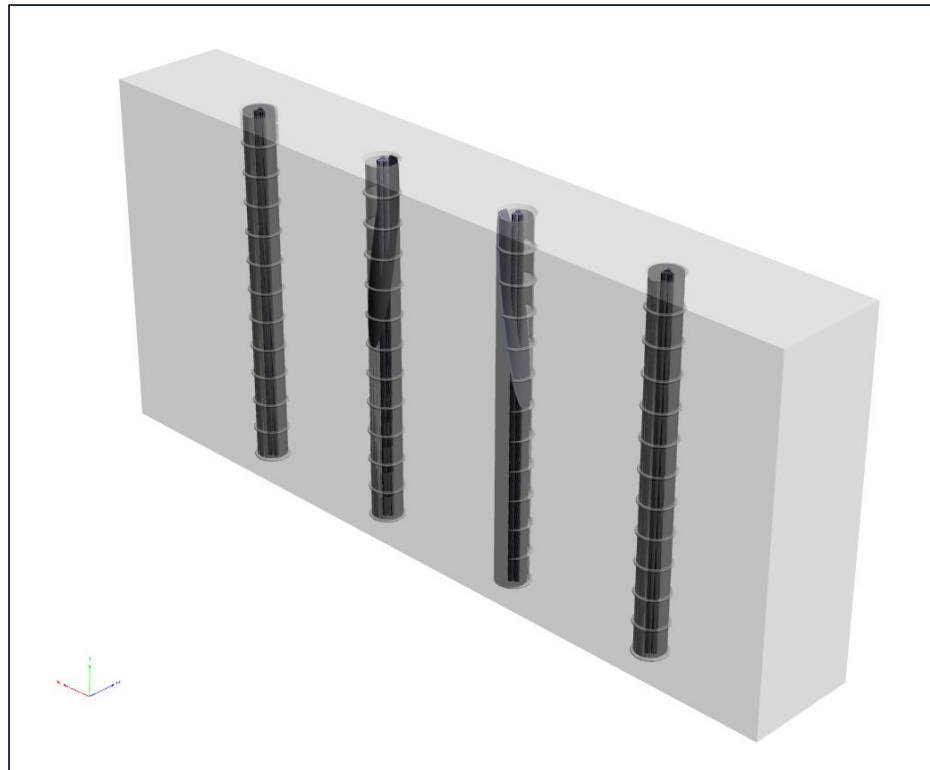


Figure 7-2. 3D render of Asymmetric Internal PT Duct Block design. Note the orientation of the two middle ducts.

It was decided to fabricate the new PT duct block with different overall dimensions than the original evaluation blocks. The block would be approximately 50mm thicker than previous blocks to allow the PT ducts to be offset from the middle plane of the block. This design allowed approximately 63.5mm (2.5") of cover over the ducts on one face of the block and a deeper 152.4mm (6.0") of cover on the other face. The shallower cover represents the minimum cover specified by FDOT design guidelines for durability while the deeper cover is typical of that found in internal PT duct placement in hammerhead piers. To maintain acceptable weight limits for movement with a forklift, the block was also shortened in the Y dimension as shown in Figure 7-3.

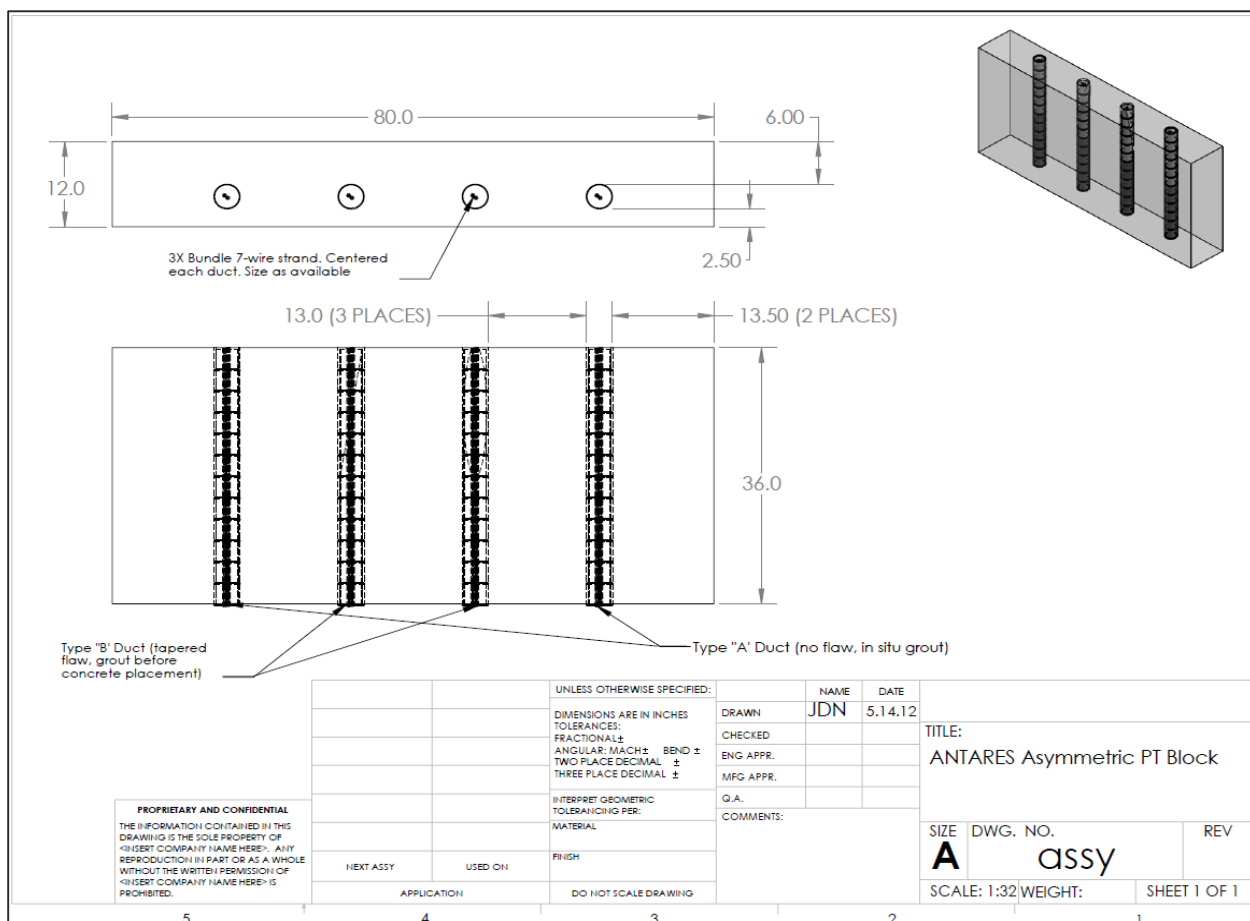


Figure 7-3. Design for Asymmetric Internal PT Duct Block. All dimensions are in Inches. An enlarged view is available in Appendix B.

Construction

Since the new dimensions for this block meant that the reusable formwork constructed for fabrication of the previous NDE evaluation blocks could not be used, it was decided to also attempt a new method of construction. Since it was hypothesized that delaminations were induced in the ducts of the first internal PT duct block when it was stood up and moved from its horizontal mold, this block would be fabricated vertically in-place within the scanner frame as shown in Figure 7-4.

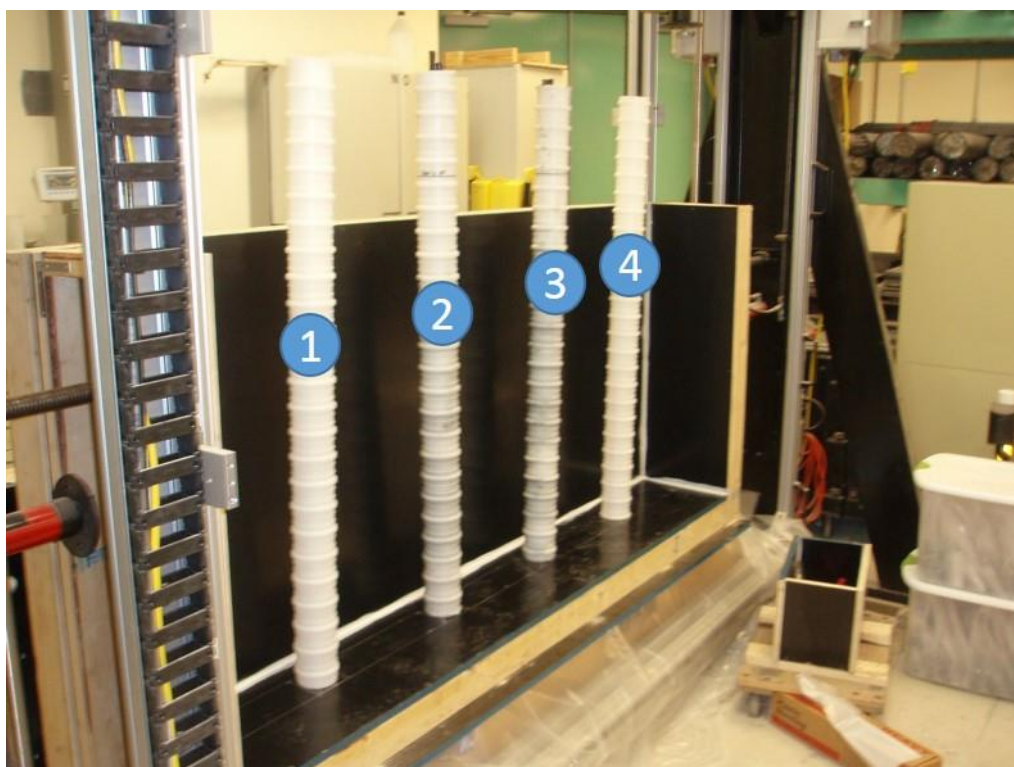


Figure 7-4. Formwork under construction within the scanner frames. Also shown is the small block mold used to make “sister blocks” for wave velocity measurement (Photo by J. Nelson).

After fabrication, the new block was stripped of its formwork and the excess length of PT duct and strand was cut off. Later, PVC screw caps were installed on the ends of the ducts using epoxy mortar and a layer of concrete was placed to smooth the top of the block and seal the PVC caps. The removable caps would allow future users of

the evaluation block to place or remove air, water, or soft grout in the duct void spaces as desired to investigate several different forms of PT duct grout defects.



Figure 7-5. Completed block immediately after formwork removal (Photo by J. Nelson).

Data Collection

The Asymmetric Internal PT Duct Block was fabricated concurrently with the development of ANTARES SVW, so initial NDE scans were as much an evaluation of the instruments and the construction of the block as an evaluation of the performance of the operating software itself. A series of scans were performed emphasizing ultrasound above all other instruments due to its potential to detect defects in grouted ducts. Some data was taken on older software, or even manually before ANTARES SVW was ready.

Initial NDE scans

Before the ANTARES SVW software application was complete, manual GPR scans were made of the block to attempt to discern the difference between air-voided ducts and properly grouted ducts. The data was qualitative in nature but did indicate that modern high frequency GPR was capable of detecting significant air voids in non-metallic post tensioning ducts. As shown in Figure 7-6, the GPR B-Scan plot shows strong double reflections of the ungrouted ducts 1 and 4 at all three scan locations. The partially grouted ducts 2 and 3 show a weaker reflection terminating in a reflection of only the steel strand within the duct as the grout fraction of the duct increases, indicating more wave energy was transmitted through the duct interfaces.

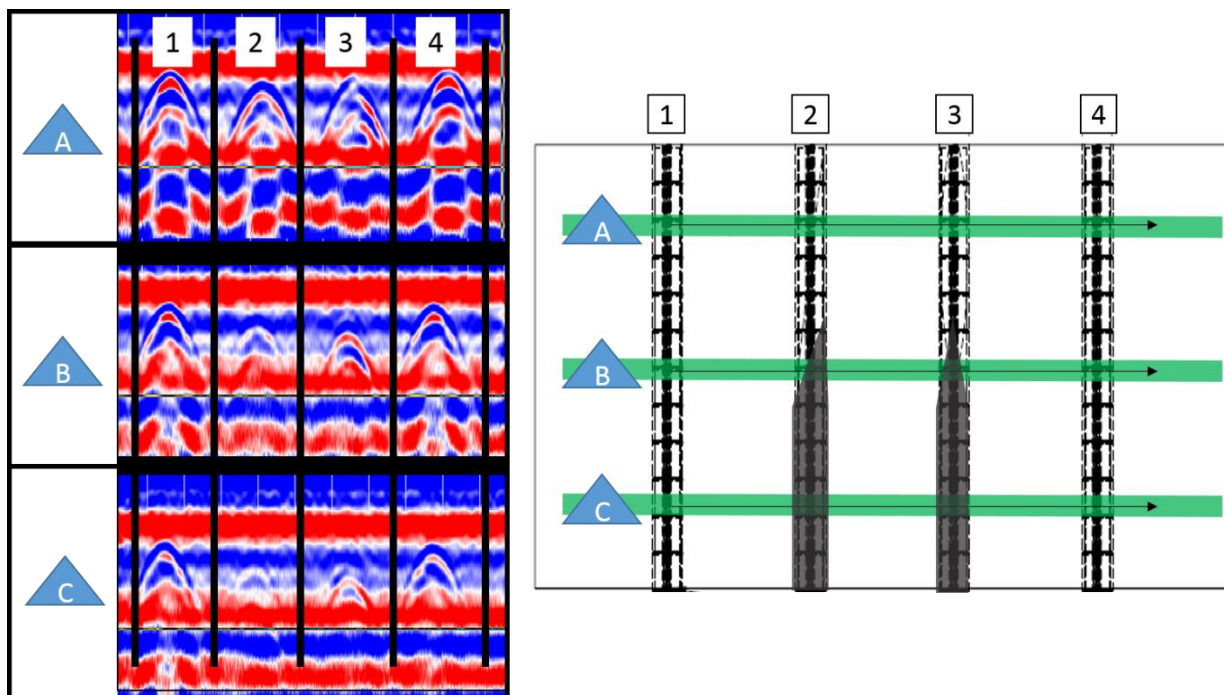


Figure 7-6. Manually performed GPR scans illustrating the effect of air voids in plastic internal PT ducts on GPR reflections.

Additionally, shear wave ultrasound scans were performed using the older operating program, ScannerVoll Wizzard. These data sets were then processed using

simplified, disposable programs built in LabVIEW™. As shown in the data visualization presented in Figure 7-7, dark blue pixels indicate deeper reflections as the stress wave passed through the duct and reflected somewhere within it, either off the tendon itself or the back surface of the duct. Pink reflections indicate the wave reflected off the duct surface, indicating poor grout bonding or a void within the duct.

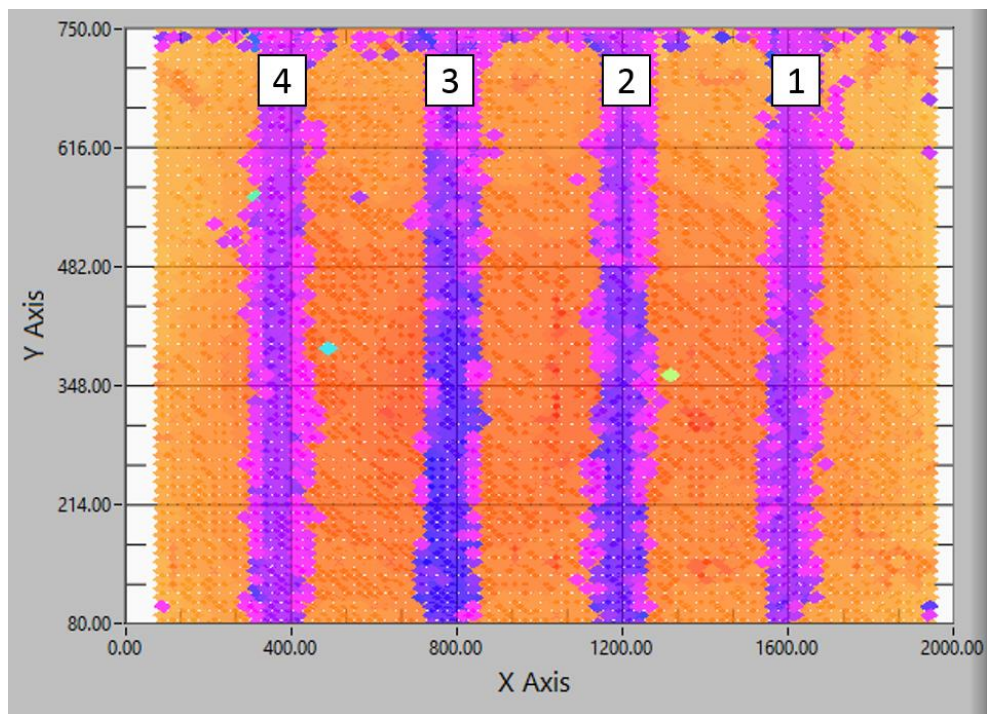


Figure 7-7. View of ultrasound data of dry PT ducts in the XY plane. All units are in mm.

After analyzing this initial ultrasound data, the deeper reflections exhibited in areas of proper grout bonding compared to the shallow reflections of the ungrouted regions of the duct indicated that the shear wave ultrasound method was a promising method for detection of air voids in internal PT ducts. Visualizing the data in this manner, however, would require a significant amount of data points to make accurate inspection possible as an A-Scan waveform at any one point on a PT duct could potentially reflect off the top surface of the duct due to the minor density change or due

to a delamination of insignificant size. Proper inspection of these ducts depended on developing a large data visualization in order to analyze the shape and scale of areas of shallow reflection in order to discern a true defect in the grouted duct system from shallower-than-expected reflections due to other effects. This observation further reinforced the importance of the ANTARES system as an investigation tool capable of collecting spatially dense data sets.

Ultrasound of the Asymmetric Internal PT Duct Block also revealed an unintentional defect: the formwork had deflected significantly during concrete placement, resulting in curved outer surfaces. This defect was clearly visible in the tomograph view shown in Figure 7-8.

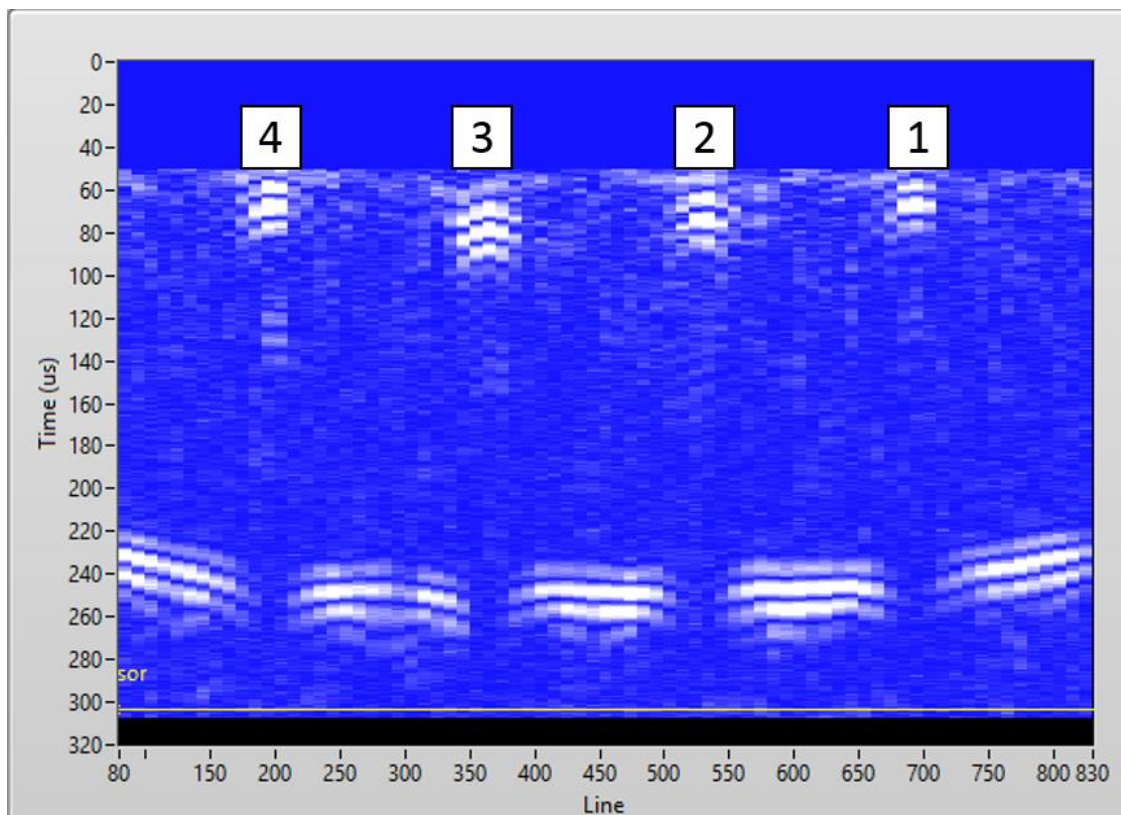


Figure 7-8. View of the Asymmetric Internal PT Duct Block shear wave ultrasound data in the XZ plane. The back wall reflection (bottom, white) shows the curve induced by formwork deflection.

Early scans of the deep cover side of the block revealed a loss of sensitivity to grout defects compared to the shallow cover scans. Though the shear wave ultrasound device could detect the presence and depth of the internal post tensioning ducts, as shown in Figure 7-9 the difference in shear wave reflections from quality grouted duct areas compared to debonded and air-voided duct areas was unclear. Since the stress wave loses energy as it travels through the concrete medium, it is likely that the density, and consequently the shear wave velocity, change from the concrete to the polypropylene medium at the duct surface resulted in a complete reflection of the stress wave back to the source, with no influence from the condition of the grout within the duct.

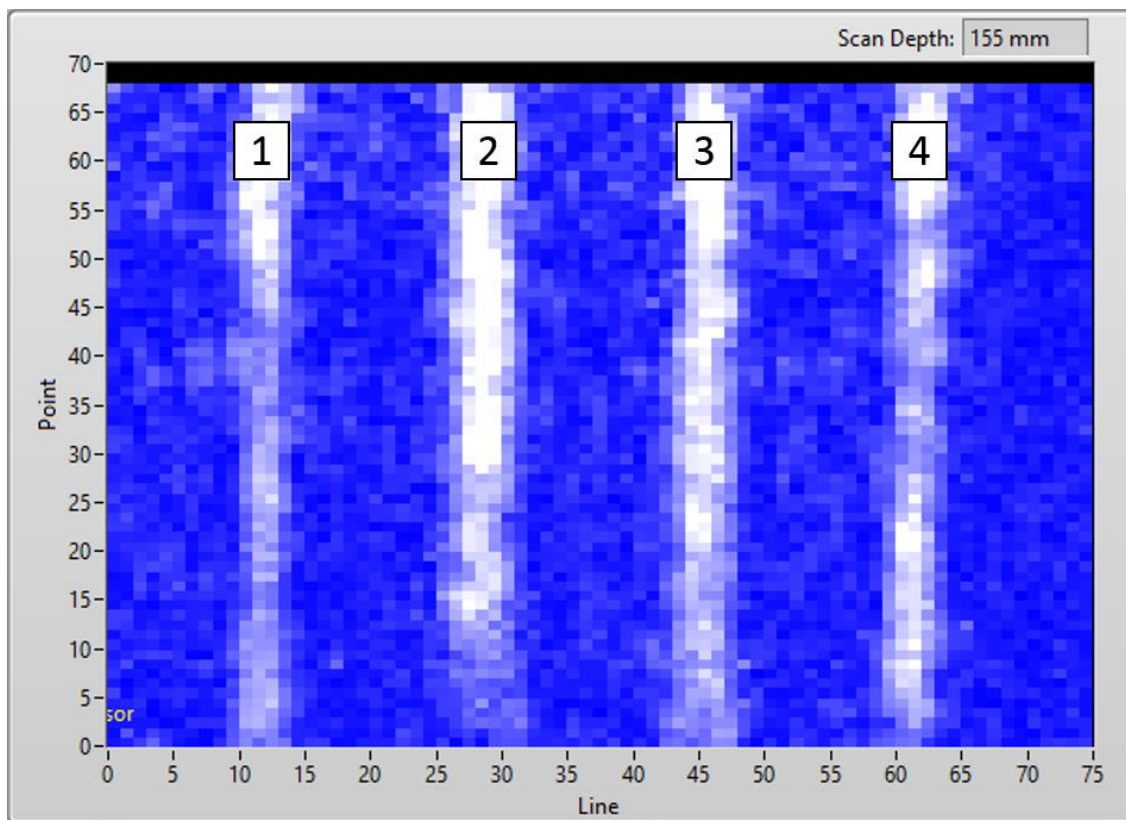


Figure 7-9. Ultrasound scan of deep cover (153mm) side of block showing indistinguishable wave reflections from all four ducts.

Post-grouting NDE scans

Duct #1, the leftmost PT duct when facing the deep cover side of the Asymmetric Internal PT Block, was filled with PT grout 51 days after fabrication of the block (56 days after placement of grout in the middle two ducts). The grout was mixed using a high-shear paddle mixer and pumped directly into the duct from the bottom up using a handheld transfer pump so as to prevent entrapped air. This step was taken to produce an “ideal” duct: one that was grouted undisturbed, in-situ, with a tightly controlled mixing and pumping process. Once the grout hardened, it was used to compare instrument readings with the other ducts both to attempt to better define detection limits on poor grouting and to evaluate the success of the method by which the inclined-void ducts were fabricated. By this time, ANTARES SVW was in its beta version and more advanced data visualizations could be realized.

As shown in Figure 7-10, scans of the block using ultrasound produced mixed results. Careful inspection of the tomograph of the ducts revealed that in-situ grouting (duct 1) produced a better interface for transmission of the ultrasonic shear wave resulting in fewer reflections beyond the duct structure. The more complete reflections of the pre-grouted (ducts 2 and 3) and ungrouted (duct 4) ducts resulted in a continuous series of secondary echoes clearly visible in the tomograph. This difference is, unfortunately, not distinguishable enough for reliable internal PT duct inspection.

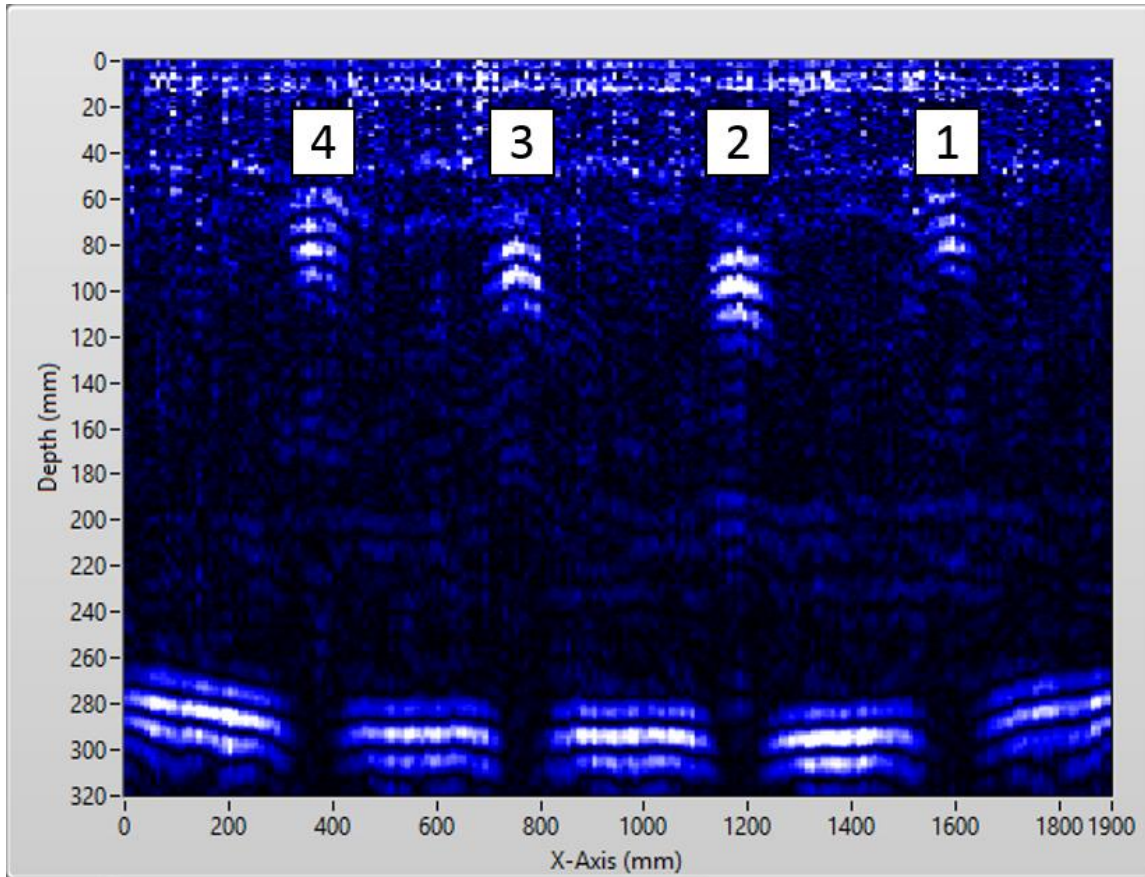


Figure 7-10. Ultrasound XZ plane tomograph of Asymmetric Internal PT Block after *in situ* grouting of duct 1.

A number of other scans were performed on the Asymmetric Internal PT Duct Block during the refinement of the ANTARES SVW software. It was found that with the void spaces in Ducts 2, 3, and 4 filled with water some interesting anomalies were witnessed in GPR scans where the water void directly faced the GPR antennae. Essentially, the water/duct/grout interfaces resulted in refraction of the radar wave and introduced a scattering effect, only visible when all interfaces were presented to the antennae. This scattering effect is visible in Figure 7-11.

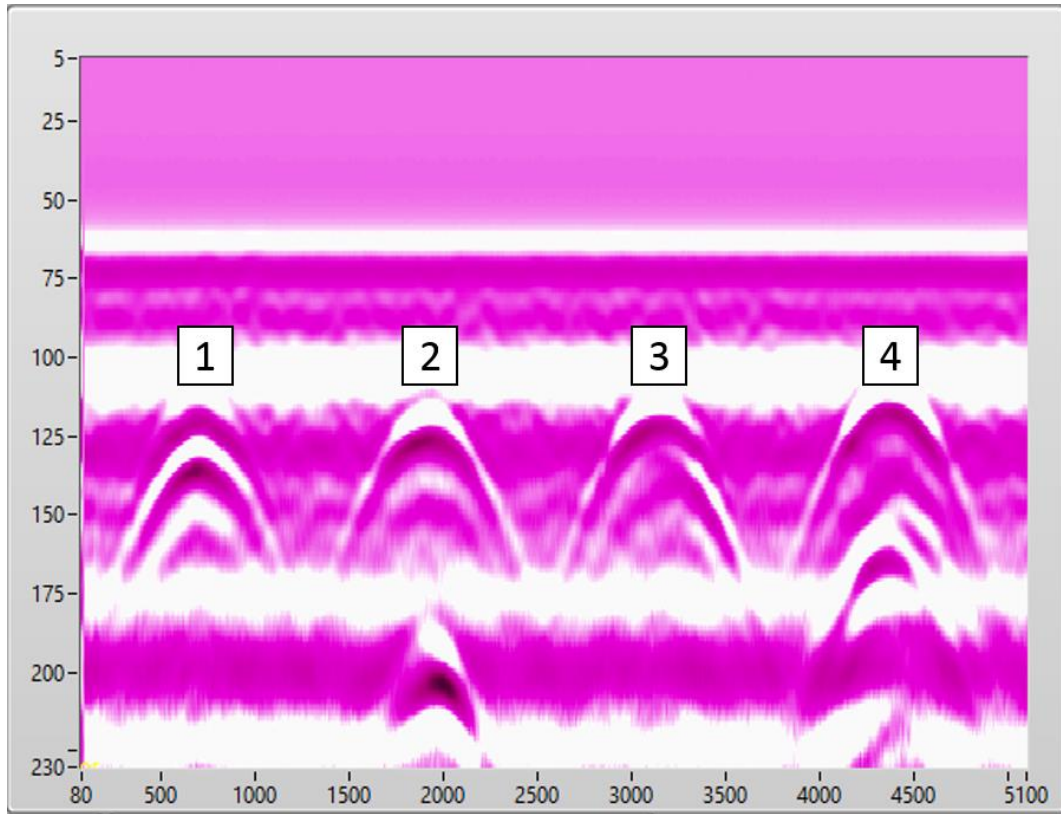


Figure 7-11. GPR trace of Ducts 1-4 showing radar scattering in Ducts 2 and 4 due to duct/water/grout interface refractory effects.

Void and Flaw Detection Block

Design

One of the most common applications for NDE methods in the construction industry is to evaluate the quality of consolidation of concrete within a completed structure. Movement of rebar after initial set, over/under vibration, mix segregation, and development of bleed water pockets can all lead to entrapped voids within a concrete structure and compromise its structural integrity. For these reasons, it was decided that an additional NDE evaluation block needed to be fabricated containing simulated honeycombing, delamination and entrapped air around rebar, and simulated cracking.

The Void and Flaw Detection Block, the sixth and newest ANTARES Laboratory NDE Evaluation Block, was designed to fit in the standard reusable horizontal block

mold. The block would contain three pieces of #6 rebar; one would have plastic tubing affixed to simulate entrapped air, one would be moved horizontally in the mold (X-axis) after initial set of the concrete, and one would be moved vertically in the mold (Z-axis) after initial set. The three rebar lengths would be located in the middle third of the block, while on both ends forced honeycombing and cracking would be put in place. On one end section of the block, three prisms of pervious concrete would be suspended along the central plane of the block. The other end would have an additional prism of pervious concrete placed at surface level during concrete placement along with two simulated angled cracks.

On each end, a small region of the block was reserved for a more realistic but amorphous in shape form of simulated honeycombing. On the end with the embedded features, at the time of concrete placement a measure of the concrete mix wet-sieved to approximately the same volume as the embedded prisms would be placed within the block. A similar procedure would be performed on the end with the surface-visible defects. The overall design for this block is shown in Figure 7-12 and 7-13.

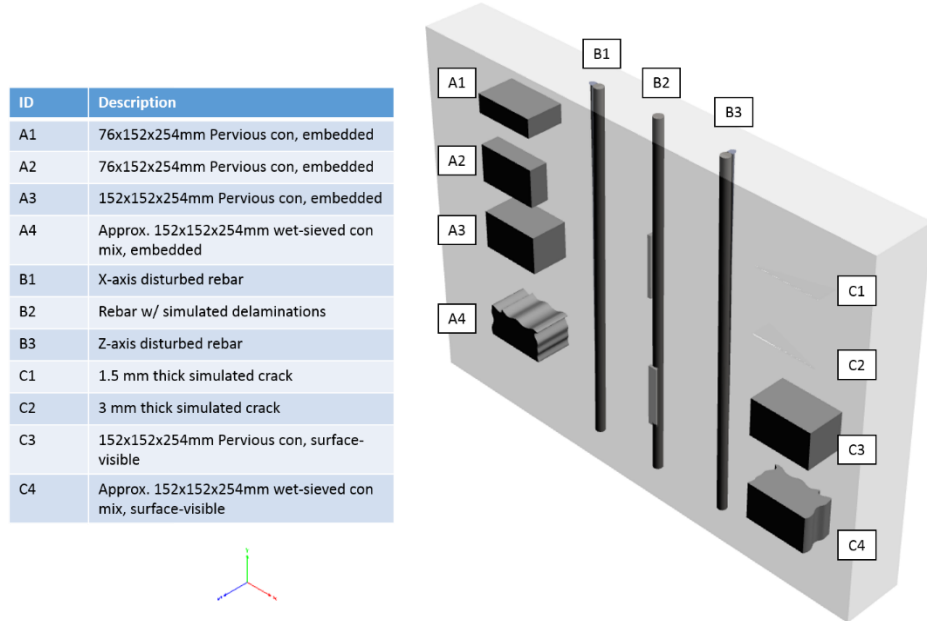


Figure 7-12. 3D render of Void and Flaw Detection Block showing relative location of intentional defects.

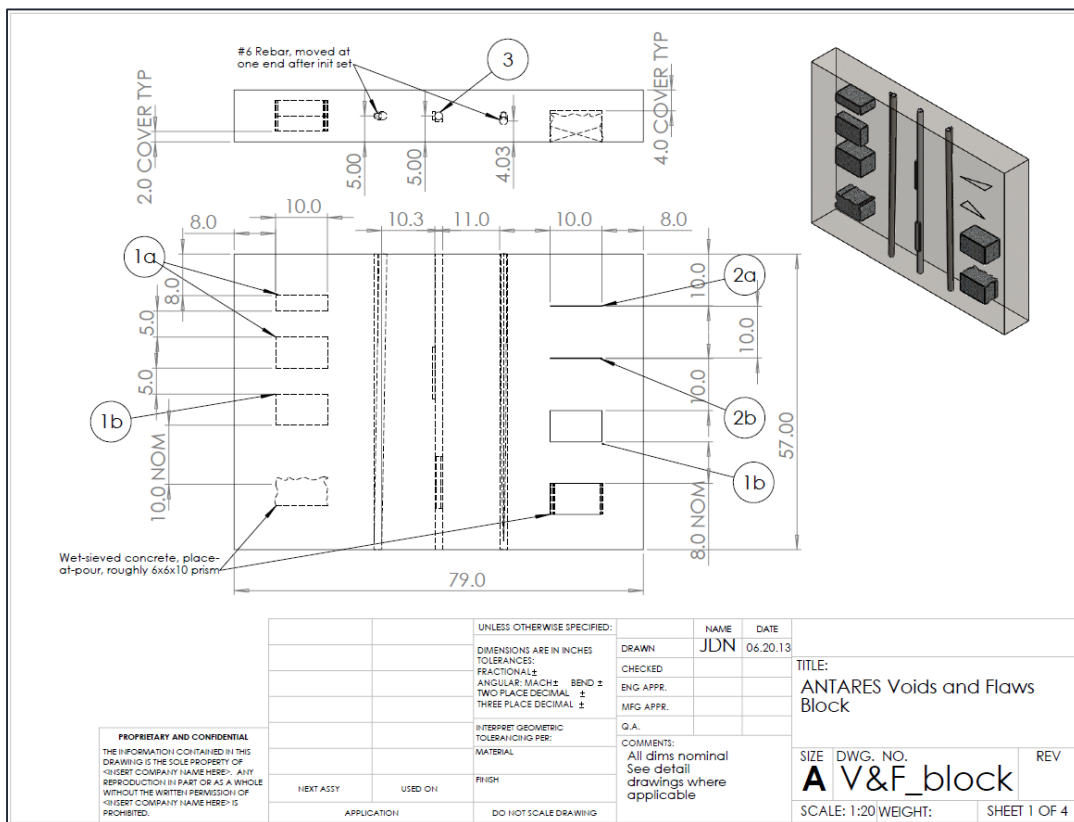


Figure 7-13. Drawing for Void and Flaw Detection Block. Dimensions are in Inches. Complete CAD drawings are available in Appendix B.

Construction

Defects and formwork

The first phase of fabricating the Void and Flaw Detection Block involved fabricating the prisms of pervious concrete used to simulate internal and surface level honeycombing; a common symptom of poor consolidation practices. The prismatic, artificial shape was chosen since its location and volume could be well defined and documented before NDE analyses were performed.

Two prisms measuring 152 x 152 x 254 mm (6 x 6 x 10 in) and two prisms measuring 76 x 152 x 254 mm (3 x 6 x 10 in) were fabricated by compacting a pervious concrete mixture into a standard concrete beam specimen mold. The pervious concrete mixture was fabricated in the laboratory following the mix design submitted to the local concrete plant for delivery, however the fine aggregate and a portion of the cement was removed from the mix to reduce the overall paste quantity and approximate a poorly consolidate region of the delivered mix.

Once the pervious prisms set, they were demolded and saw-cut to length using a wet diamond saw. The prisms to be installed within the finished block were suspended from fiberglass rods designed to support the prisms' weight during formwork construction as shown in Figure 7-14. The fiberglass rods were also stiffened vertically and laterally to hold the prisms down against buoyant force and laterally in place during concrete placement. The fiberglass rods were chosen to be small enough and similar enough in density to not appear on ultrasound scans and were non-metallic so as not to reflect radar waves.

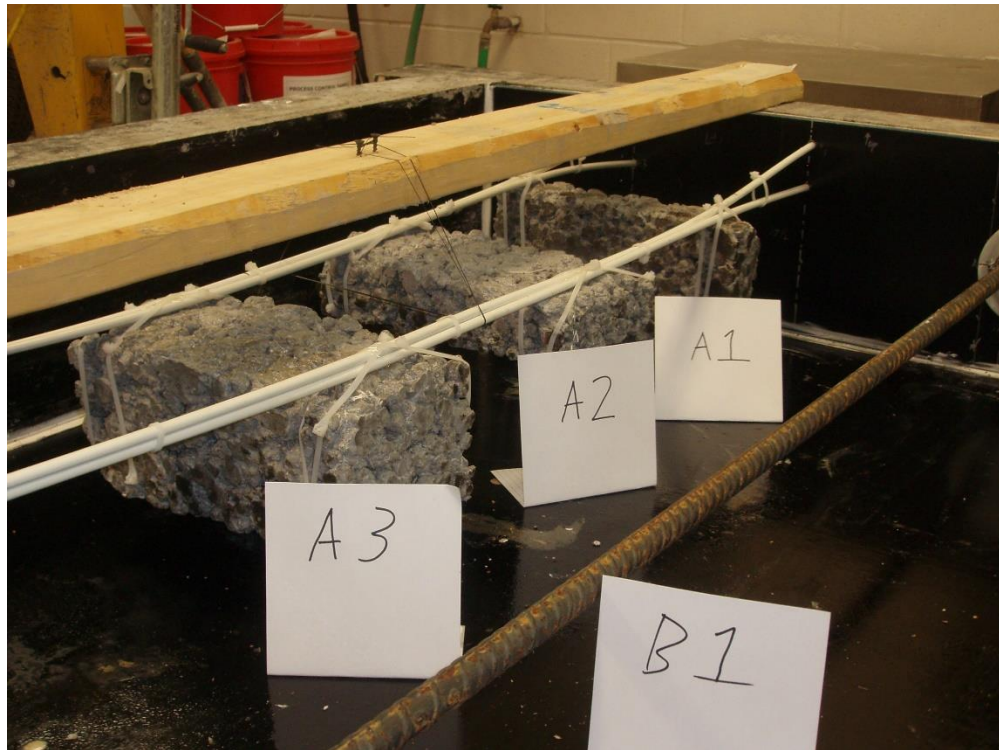


Figure 7-14. Pervious concrete prisms suspended along the middle plane of the formwork for the ANTARES Void and Flaw Detection Block (Photo by J. Nelson).

The remaining pervious concrete prism along with two triangular plates that would be used to form the surface-visible simulated cracks on the other end of the block were to be inserted at the time of fabrication. Each triangular plate was used to form a 254mm (10in) long crack of linearly varying depth from 0 to 76.2mm (3in). The plates were set into a small slot cut into a piece of lumber and epoxied in place to make installation and removal easier.

The three sections of #6 rebar for the middle section were suspended in-place by recessing the last 50mm of their length on either end into a layer of polymer coated form board installed inside the main boards of the reusable formwork as shown in Figure 7-15. The rebar pieces to be moved after initial set of the concrete had one end installed into a slot rather than a hole in the inner form board. In this manner, only one end of the

rebar was moved after concrete placement, allowing for an increasingly severe “trail” of disturbed concrete behind the path of the rebar. The middle rebar was installed with two sections of 12mm ID flexible rubber tubing, each approximately 250mm long, contoured and bonded to the rebar’s surface in two locations in such a way that one presented its entire area to one surface of the block and the other was located transverse to any surface contact instrument’s view.

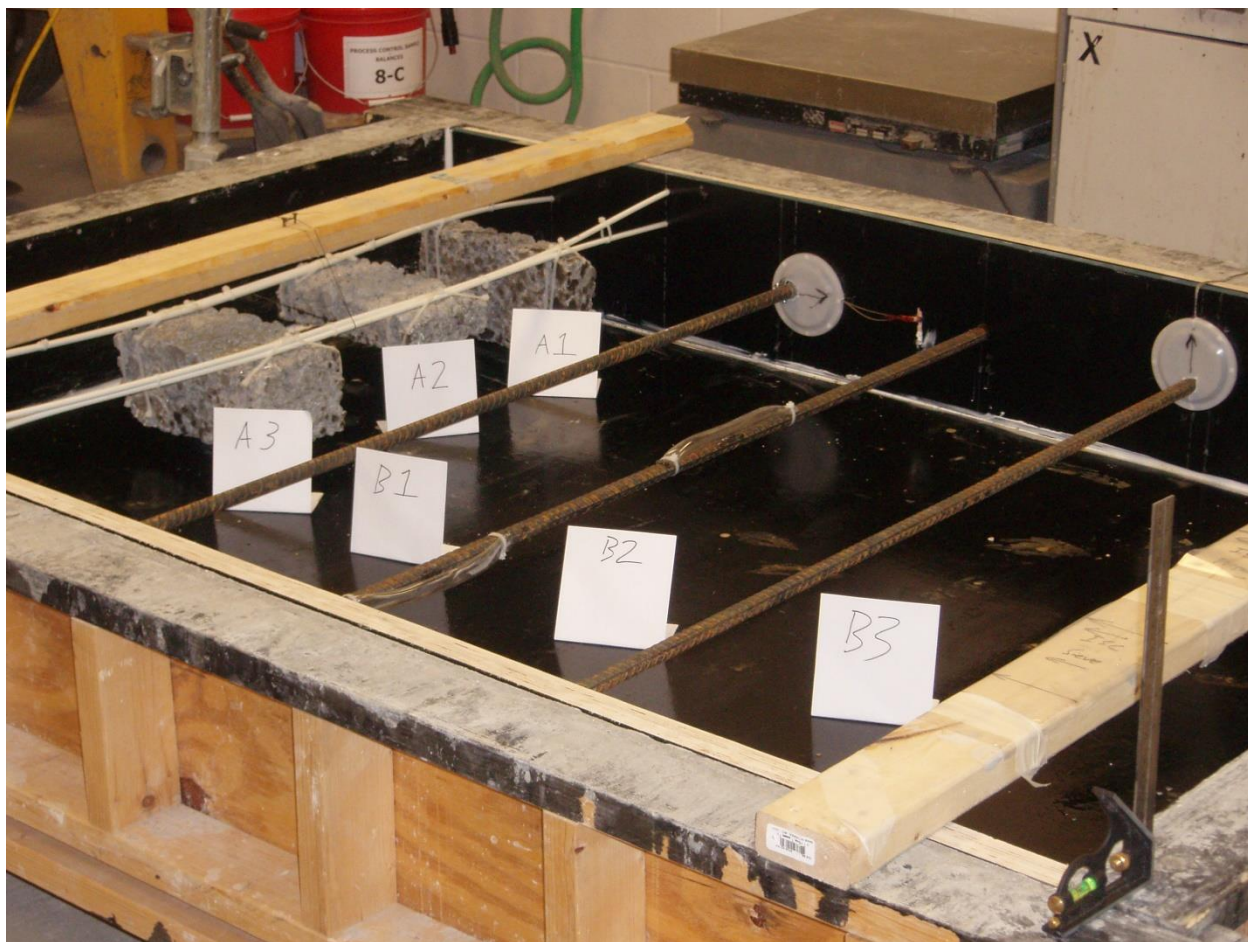


Figure 7-15. Three rebar pieces including the two moving specimens in Void and Flaw Detection Block formwork (Photo by J. Nelson).

Concrete placement

After the formwork was completed, concrete was ordered from a local ready-mix plant. The mix was designed for structural strength but included enough retarding

admixture to allow enough working time to install the surface defects. Concrete was carefully placed around the embedded pervious concrete. Once level with the top of the embedded large pervious concrete prism, a volume of concrete equal to the large prism was removed and wet-sieved through a No. 4 sieve and placed by hand immediately below the fabricated embedded pervious concrete prisms. This area represented a more realistic but more geometrically amorphous area of internal honeycombing.

The formwork was filled and carefully consolidated with an internal vibrator as shown in Figure 7-16, with care taken to avoid disturbing the internal wet-sieved concrete volume. After the formwork was struck off with a long screed as shown in Figure 7-17, the surface defects including the lubricated triangular plates and the pervious prism were embedded in the concrete surface at the desired locations using a guide board shown in Figure 7-18. Using a procedure similar to the first wet-sieved simulated honeycombing area, the surface-visible area of wet-sieved concrete volume was fabricated by removing a volume of concrete with a scoop, sieving it on a vibratory table, and replacing it as shown in Figure 7-19.



Figure 7-16. Consolidating the Void and Flaw Detection Block with an internal vibrator
(Photo courtesy of FDOT State Materials Office).



Figure 7-17. Levelling the Void and Flaw Detection block with a wooden board screed
(Photo courtesy of FDOT State Materials Office).



Figure 7-18. Installing the surface-visible pervious concrete prism in the Void and Flaw Detection Block (Photo courtesy of FDOT State Materials Office).



Figure 7-19. Installing the surface-visible, wet-sieved concrete simulated honeycombing into the Void and Flaw Detection block (Photo courtesy of FDOT State Materials Office).

After initial set of the concrete, the two moving rebar specimens were shifted using their respective installed cables. The rebar piece which moved along the Z-axis direction moved easily as concrete was displaced upwards out of the formwork and allowed to resettle below the block. Its free end was moved the desired 25mm per design. The laterally-moving rebar specimen had a more complicated cable system guided through a lubricated tube into the formwork itself. This system failed to move the rebar as desired and it was confirmed after measurement that this rebar piece moved only 8mm rather than the desired 25mm.

The formwork was removed after 24 hours and the new block was cured under wet burlap with a timer-operated soaker hose to maintain saturation for 7 days. In a carefully-orchestrated forklift operation, the block was flipped vertically using the bottom formwork as a lever and protective shield and wooden support boards to allow a forklift to lift the block from the bottom edge. It was then installed in the scanner frame as shown in Figure 7-20 to begin NDE scans using ANTARES.

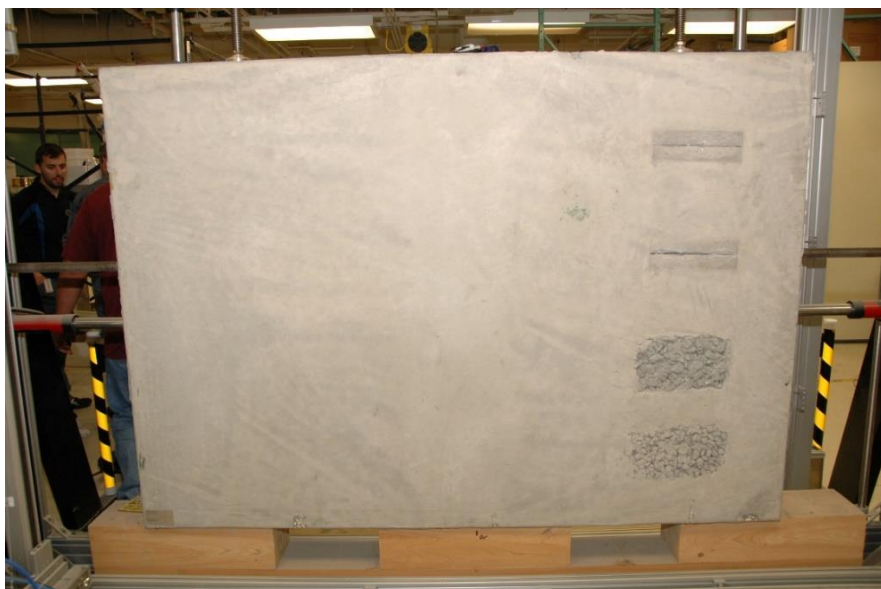


Figure 7-20. ANTARES Void and Flaw Detection Block installed in scanner frame with surface defects visible (Photo by J. Nelson).

Data Collection

For the first time, an NDE laboratory specimen was evaluated entirely by automated techniques using ANTARES and the newly completed ANTARES SVW software package. Where computing power and lack of instrument interference permitted, both scanners operated continuously and simultaneously on both sides of the Void and Flaw Detection Block, quickly producing a mountain of data to be processed.

Laser profilometer

The laser profilometer scan, being a rapid scan operation and not dependent upon time-changing material properties such as elastic modulus, was performed first. Laser scans on the hand-finished surface with surface visible defects (A-side) produced faithful recreations of the surface defects and the marred surfaces around them as shown in Figure 7-21. Laser scans captured the inner contour of a simulated crack for a few data points as shown in Figure 7-22 and 7-23 during a particularly dense scan.

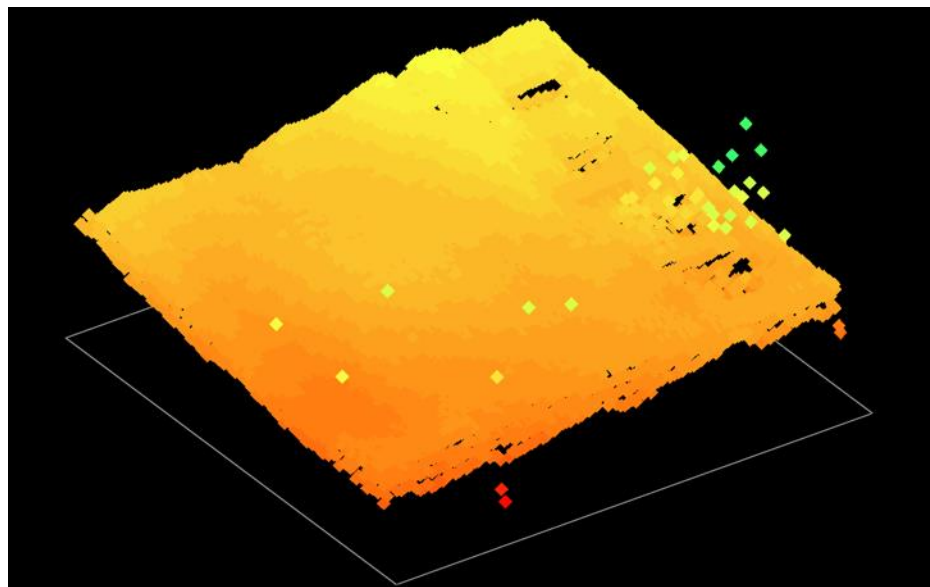


Figure 7-21. Unfiltered 3D trace of defected block surface. Note the scattering above the honeycombed area.

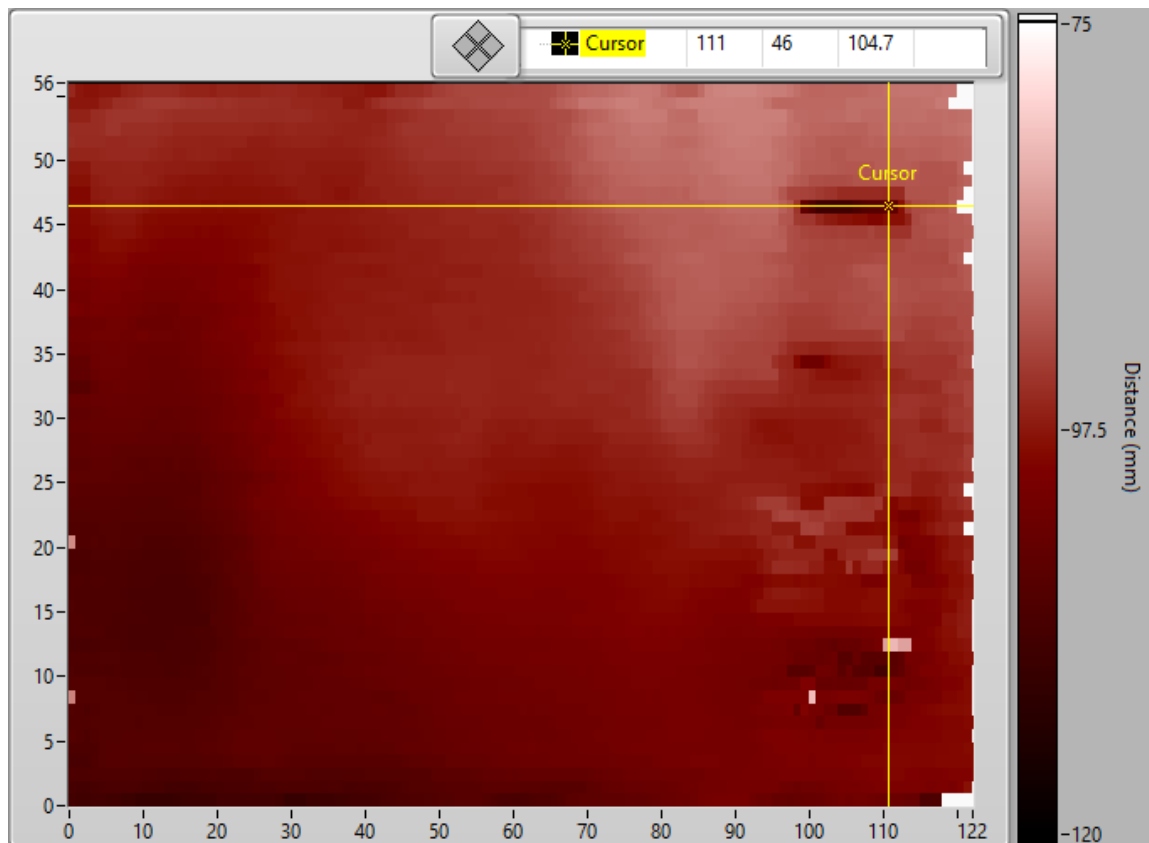


Figure 7-22. Laser C-Scan image of defected block surface with cracks and honeycombing visible.

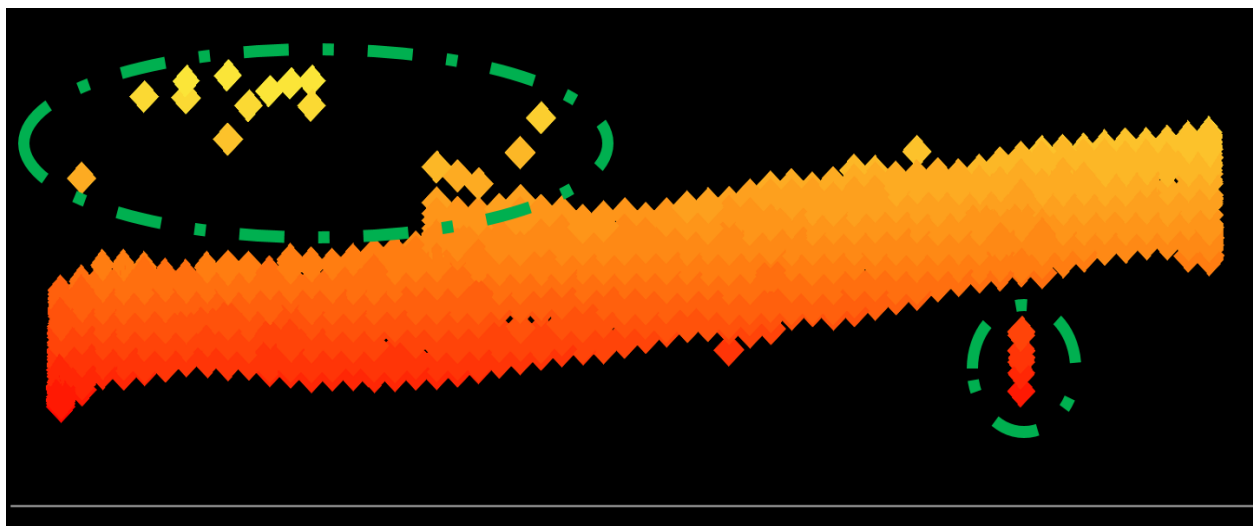


Figure 7-23. 3D laser trace of block surface viewed from defected end in YZ plane. Note the scattering above the honeycombed area (circled upper left) and trace of the inside of a simulated crack (circled lower right).

A laser profilometer scan of the form side (B-side) of the block revealed a very smooth, flat surface as expected, however it also revealed a 22mm change from the depth of the upper left to the lower right corner. This difference is likely due to the block being held slightly off level within the clamping frame, the scanner mounts on the frame being slightly off plane with respect to the specimen, or both.

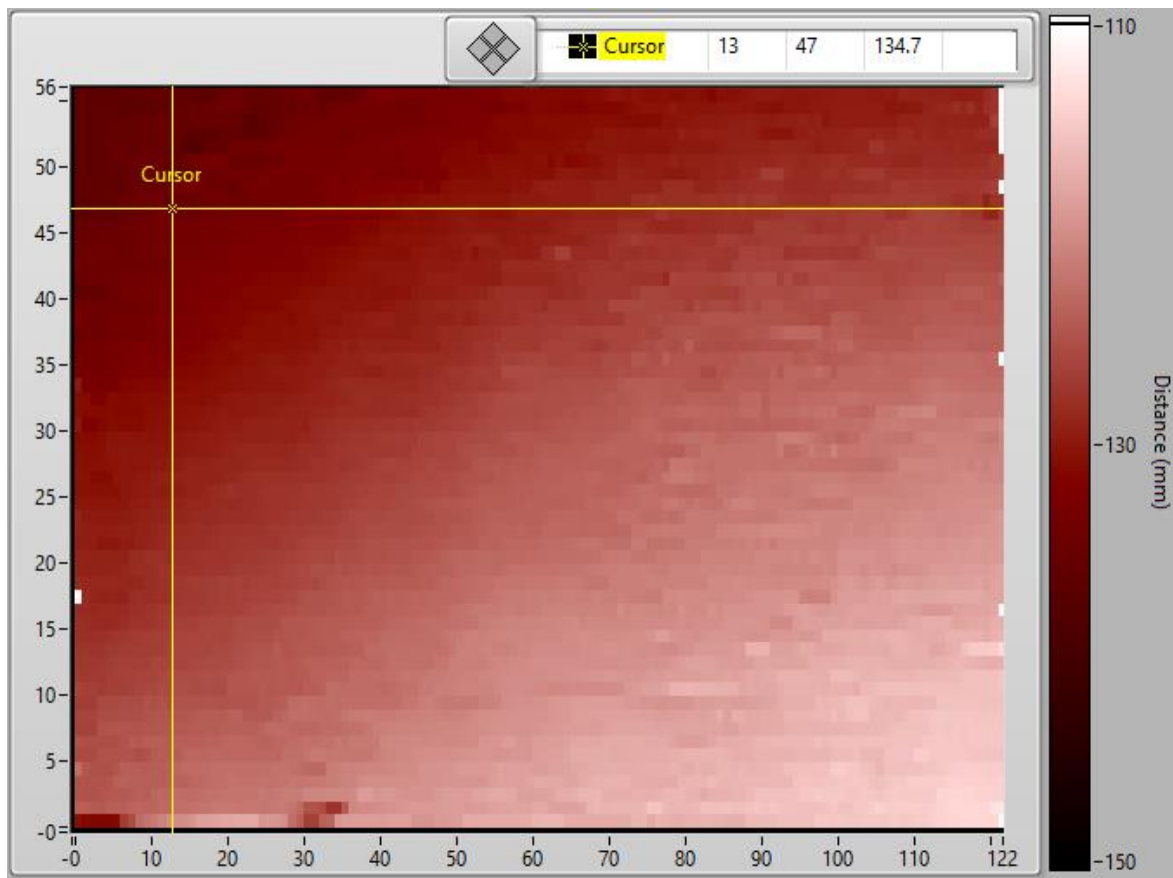


Figure 7-24. Laser C-Scan of B-side of block revealing a smooth—but not flat with respect to the scanner—concrete surface.

GPR

Ground penetrating radar is sensitive to the dielectric constant of the material upon which it impinges. In the case of concrete, if there is a large amount of free water within the capillaries of the specimen an incident radar wave will be almost completely reflected off the surface. This is a well-known phenomenon and GPR manufacturers

recommend applying radar techniques to specimens that are at least moderately dry for investigation purposes.

For this reason, GPR scans were delayed for 28 days until the specimen had chemically absorbed or expressed enough free water to be viable for inspection by GPR. The block was scanned using ANTARES and GPR in a parallel operation manner on the form side (B-side) of the block to attempt to detect the enclosed honeycombing and air-voided steel.

GPR is not usually the NDE method of choice for detection of enclosed air voids due to reasons discussed in Chapter 2, and it takes an experienced operator to discern defects such as honeycombing due to their irregular interfaces and low GPR reflectivity. Nevertheless, it is a common practice in modern field structural NDE to use GPR to evaluate structural integrity in cases where poor consolidation is suspected. For this reason, a detailed GPR scan was conducted on the form side of the Void and Flaw Detection Block.

Initial data visualizations clearly showed the locations of the three rebar specimens within the block as expected. The change in cover on the rebar that was moved upwards in the mold after initial set was very apparent in the C-Scan image as shown in Figure 7-25, which would inform the investigator of a moving reinforcement issue despite the lack of an obvious indication of damaged concrete in the vicinity of the rebar. In a tomograph data view, the entrapped air at the surface of this moved rebar element is visible as a weak, diffused surface reflection as shown in Figure 7-26.

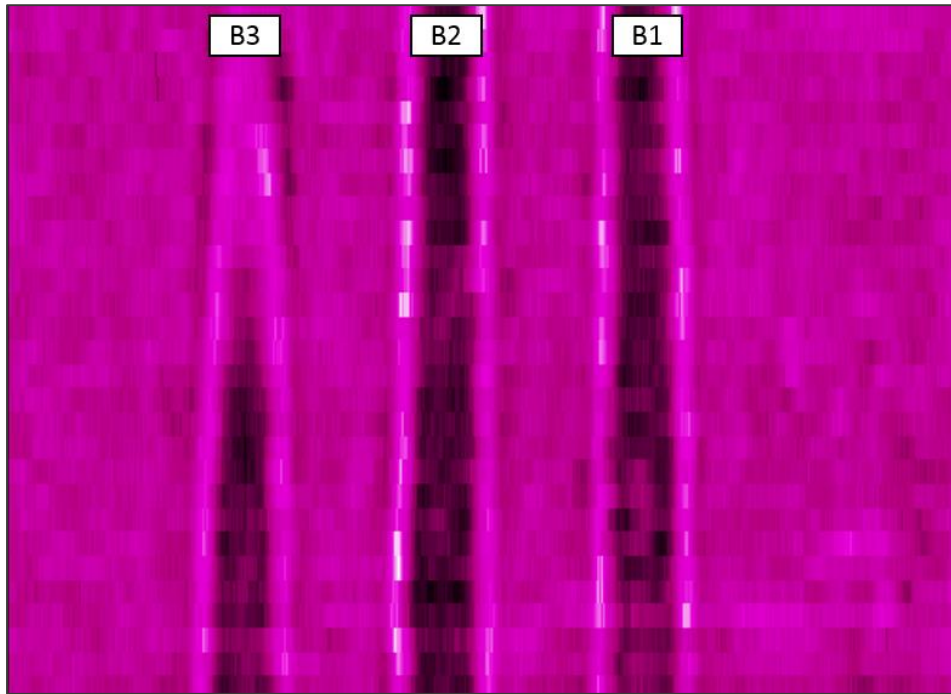


Figure 7-25. GPR C-Scan image of rebar in Void and Flaw Detection block at a depth of 105mm.

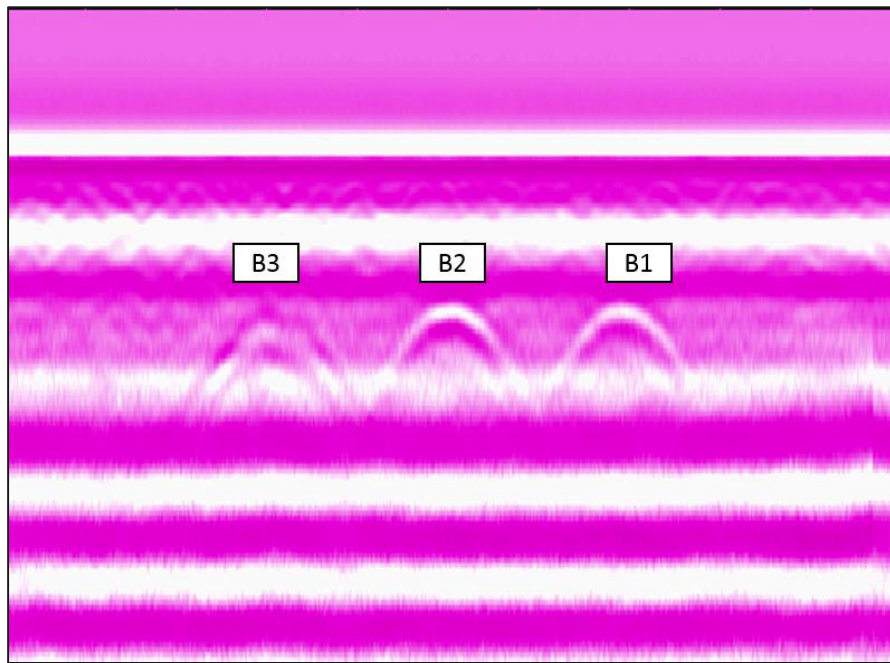


Figure 7-26. XZ Plane GPR tomograph of the Void and Flaw Detection block.

By carefully adjusting the depth of the C-Scan image and fine tuning the contrast of the display, some evidence of the enclosed honeycombing also became visible. It is

clear that while GPR is capable of detecting such flaws, its data needs to be carefully scrutinized to do so successfully and it is still susceptible to missing smaller defects. Indeed the smaller pervious concrete prisms and the surface visible cracks were not apparent in the data visualizations produced by the ANTARES Processing Suite.

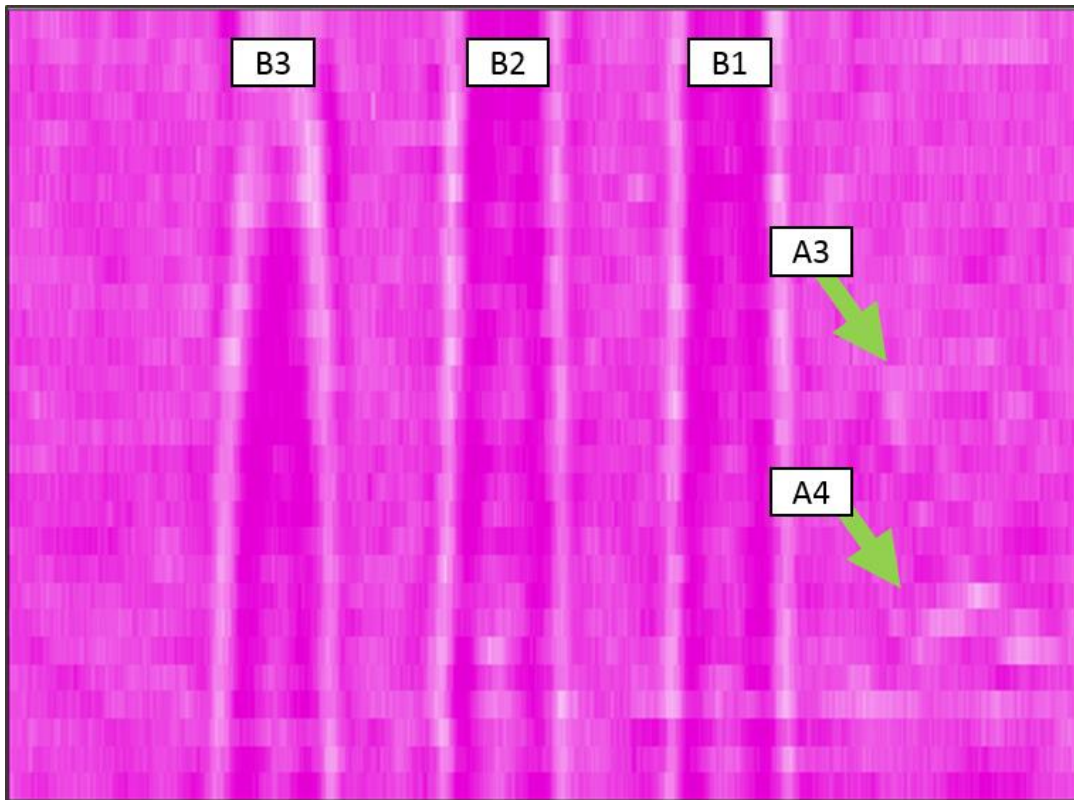


Figure 7-27. GPR C-Scan image of Void and Flaw Detection block.

Shear wave ultrasound

Shear wave ultrasound was the most promising technique used to evaluate the Void and Flaw Detection Block. The technique is sensitive to density changes and has shown great reliability in the detection of entrapped air and water within structural concrete. A series of ultrasound scans were conducted using ANTARES collecting on average around 6000 waveform data points per scan during an approximately 5 hour scan.

Immediately upon processing the ultrasound *.ANTDAT file it was observed that ultrasound had reliably detected all of the most severe defects as shown in Figure 7-27. These defects were visible on the filter settings display, which only displays the depth of maximum reflection and is therefore usually unreliable at displaying all objects of interest within a specimen.

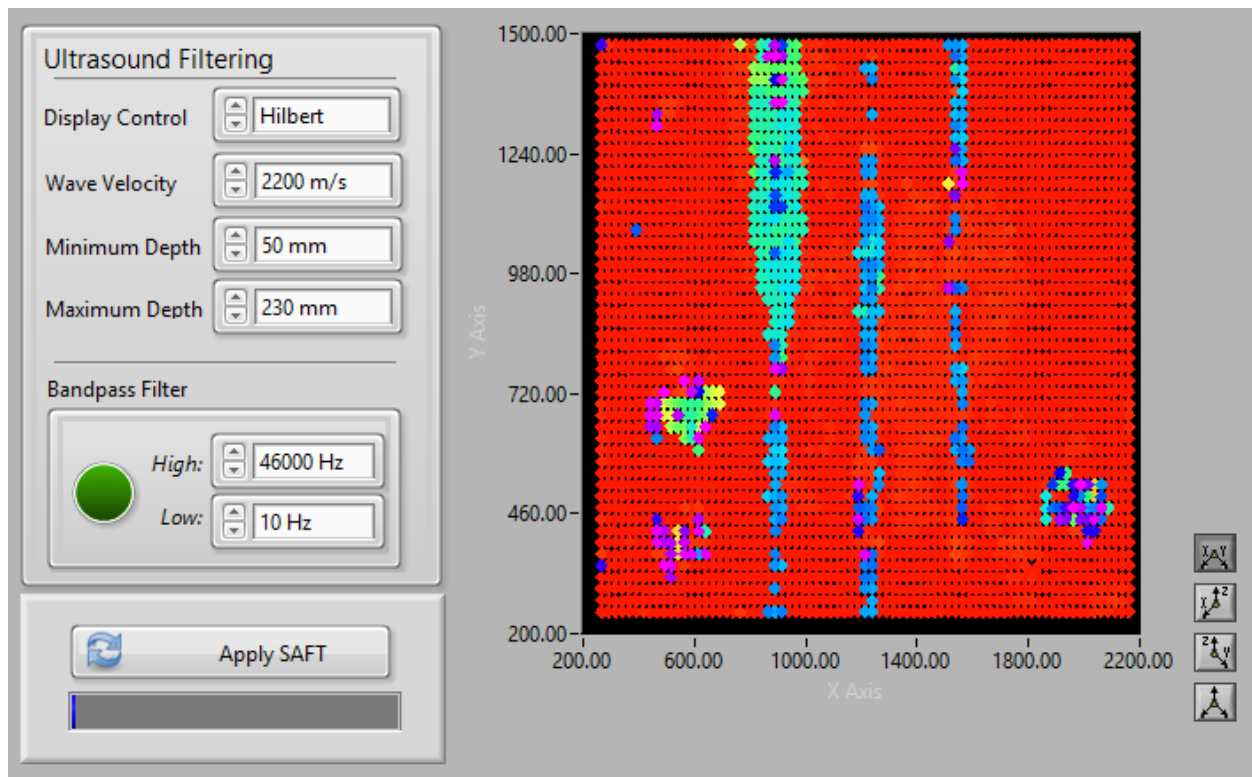


Figure 7-28. Initial ultrasound data processing for Void and Flaw Detection Block.

Focusing on the C-Scan depth display, stepping through the thickness of the specimen first revealed the three embedded pervious concrete prisms and the embedded wet-sieved concrete volume as shown in Figure 7-28. Though their geometries were difficult to define and their outlines were faint, these features could be identified reliably in the ANTARES Processing Suite.

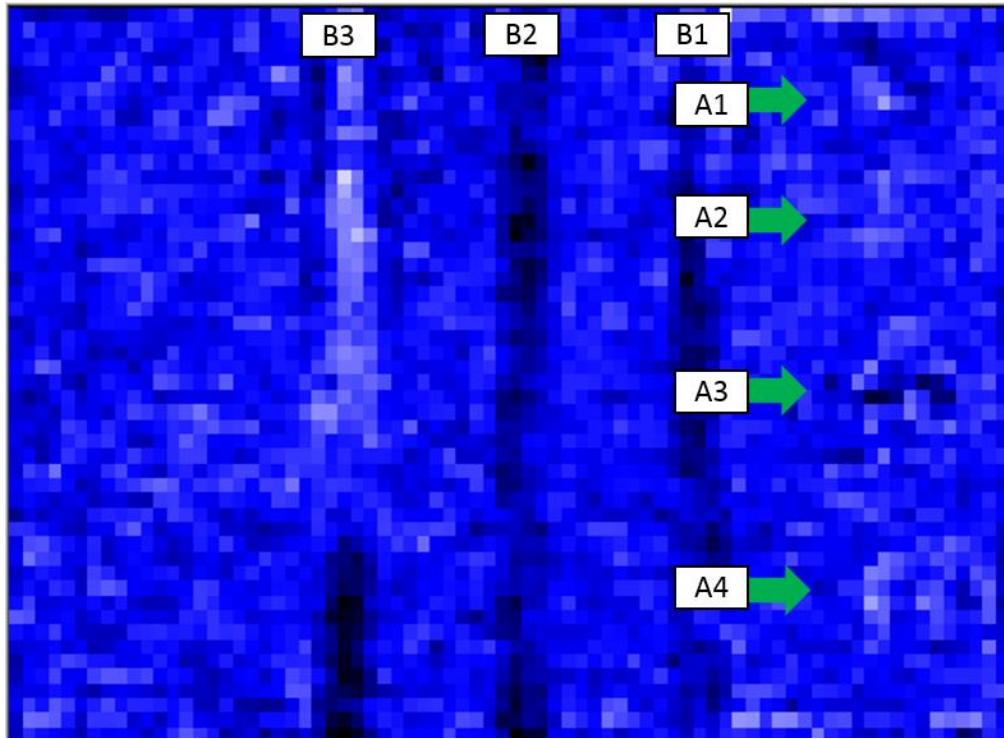


Figure 7-29. Ultrasound C-Scan image with no secondary processing at a depth of 90mm.

It was found that moving the depth control while focusing on regions of the block better allowed the user to discern whether pixel color changes were random or followed an actual defect, suggesting that perhaps video displays of the ANTARES data visualizations would be more effective at communicating the processed data than still images alone.

Continuing through the depth of the block, at a depth of 120mm the traces of the three rebar elements were easy to discern as shown in Figure 7-29. The trace of the Z-axis moving rebar (B3) indicated a significant region of disturbed concrete left behind after the bar's movement. Though the X-axis moving rebar (B1) was not successfully moved the intended 25mm, the C-Scan image indicated some damage to the surrounding concrete near the moved end. The simulated entrapped air located on the middle rebar (B2) was somewhat difficult to discern: after performing an absolute value

transform the tubing located on the side of the rebar from the perspective of the ultrasound transducers became very apparent, though it was difficult to see in other view types. The use of a Hilbert transform visualization shown in Figure 7-30 allowed a very clear image of the other section of tubing located on the middle rebar, despite the defect being behind the rebar and masked from the ultrasound instrument's view.

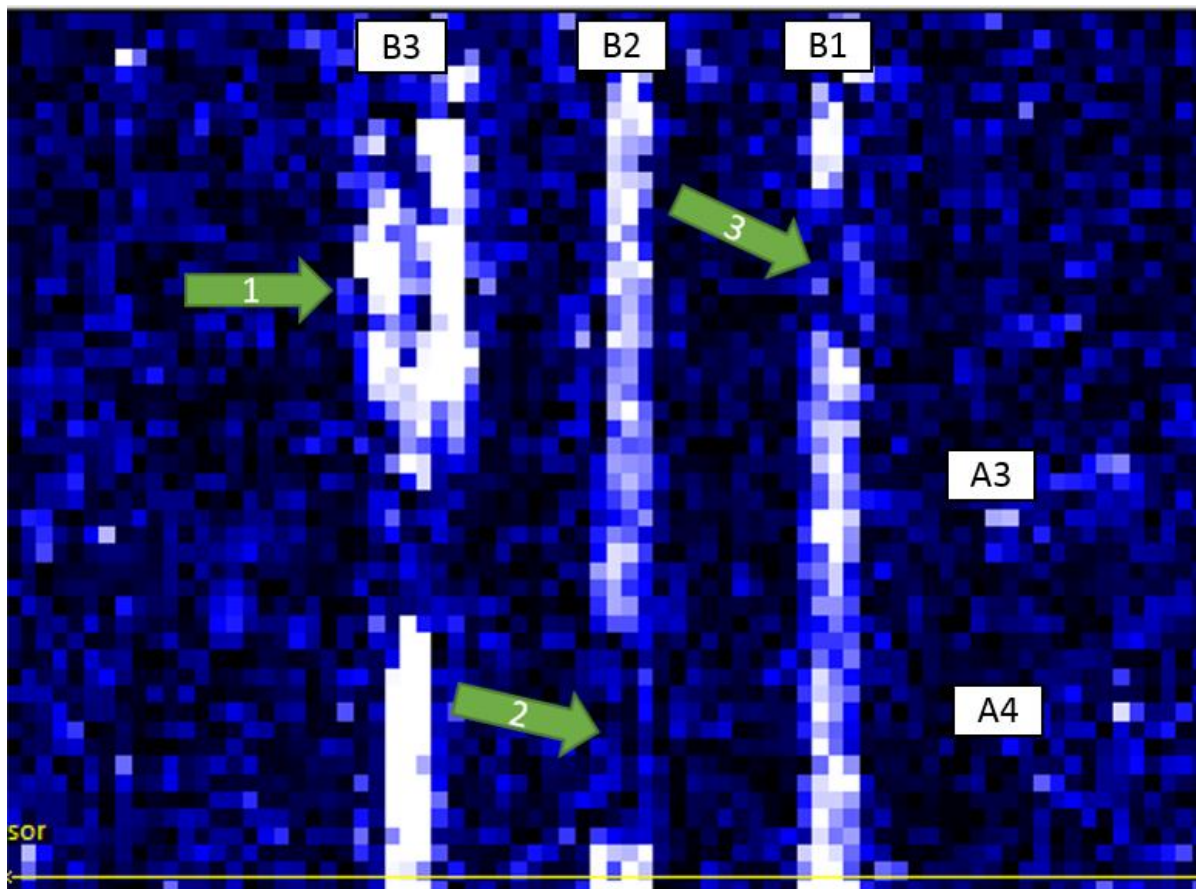


Figure 7-30. Ultrasound C-Scan image of Void and Flaw Detection Block at a depth of 120mm showing damage from depth-moving rebar (1), lack of rebar reflection due to earlier reflection from simulated entrapped air (2), and minor concrete disturbance due to length-moving rebar (3).

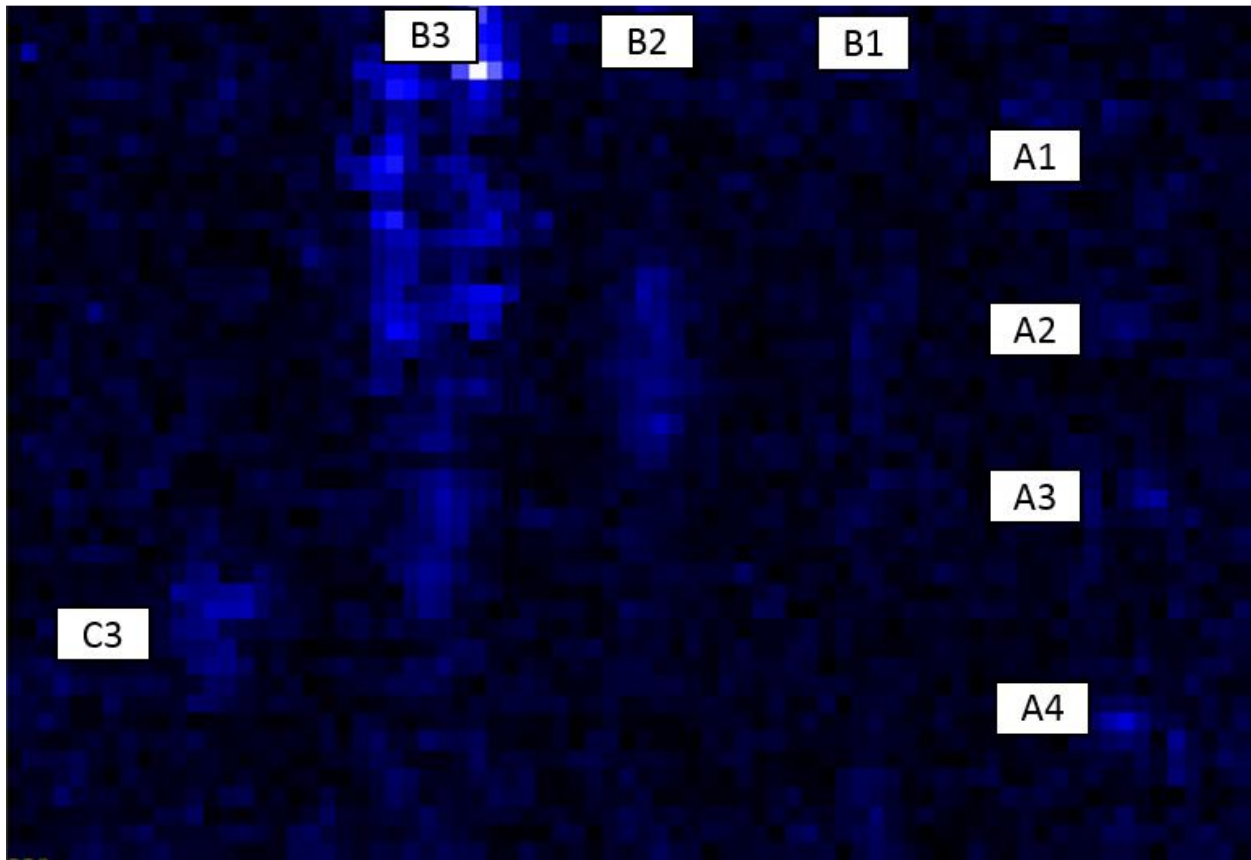


Figure 7-31. Hilbert transform C-Scan ultrasound image of Void and Flaw Detection Block at 120mm depth.

Finally as the depth of the C-scan display reached the back surface of the block (250mm), a continuous plot of similar color would be expected for a monolithic concrete block. In the case of the Void and Flaw Detection Block, however, the enclosed defects meant that the shear stress waves transmitted through the block's thickness at those areas had already reflected back to the source, and so never made it to the back surface of the specimen. A trace of some kind was visible for every defect in the block as shown in Figure 7-31, although these traces did not necessarily adequately reconstruct the defect's geometry and no information on the depth of the defect can be inferred. This effect is known as "shadowing" and can be used to rapidly investigate a specimen of continuous known thickness, such as a slab or bridge deck.

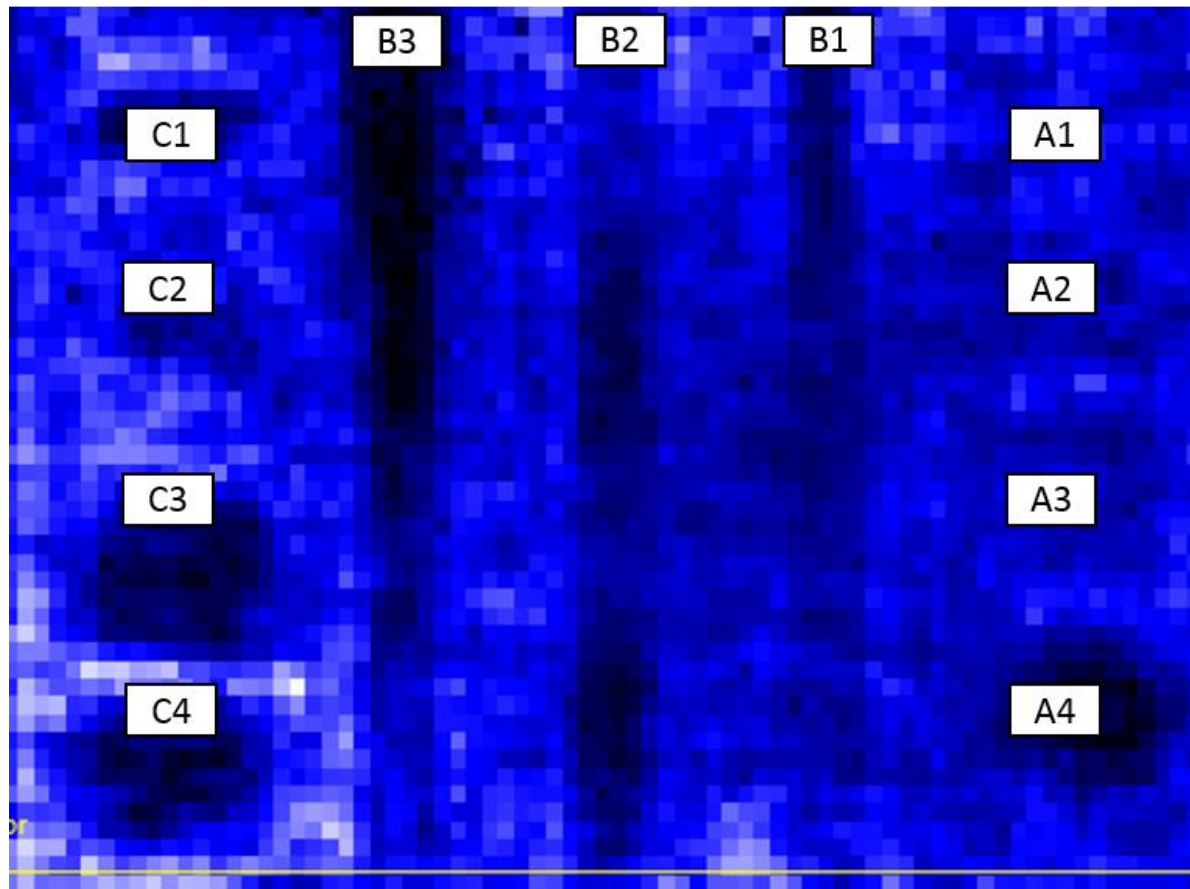


Figure 7-32. Ultrasound C-Scan “shadow” image of the back surface of the Void and Flaw Detection Block.

CHAPTER 8

FIELD DEPLOYMENT AND SYSTEM EVALUATION

Introduction

One of the major milestones in developing the ANTARES system from the Phase I FDOT automated NDE scanner was to be an experimental field deployment to prove the system was ready and viable for use on in-situ structures in the often unpredictable and harsh environment found in the State of Florida. This field deployment would be conducted at a location of the research team's choosing with FDOT support and approval.

The site of the first deployment was chosen to be the FDOT M. H. Ansley Structures Research Center in Tallahassee, Florida. Among many other active research projects, the Ansley center possessed a full scale construction of an experimental bridge that would be a convenient and useful location for both parties for the first ANTARES field deployment.

Since this deployment was a trial of the system and was intended to provide FDOT with an indication of whether or not a more permanent field deployment logistics support system is warranted for the ANTARES system, support for the initial deployment was very limited. The research team needed to invest a serious amount of time in planning and logistics on how to physically transport and deploy the large, heavy scanner frame using readily available equipment.

Once at the Ansley center, the system was deployed and activated and a series of scans were performed. Since the field deployment was limited to a single day, only the most useful NDE instruments were used and the scanned areas were sparse in comparison with the laboratory evaluation block scans.

Despite the aforementioned challenges, once the scanner system was returned safely the data was processed and analyzed and results were sent to the personnel at the Ansley center. The personnel there performed a series of coring operations on the bridge deck to test the validity of the analysis performed using the ANTARES system.

Deployment Site

In one method of Accelerated Bridge Construction (ABC), a bridge is constructed using precast deck elements lowered onto precast concrete girders already in-place as shown in Figure 8-1. The deck elements are levelled using a series of leveling bolts passed through the deck and in contact with the girders upon which they rest. High strength grout is pumped under pressure to fill the interface between each girder and the deck elements it supports. A similar grouting operation bonds the joints between adjacent deck elements together and fills the spaces left when the levelling bolts are removed. This type of bridge construction offers a number of advantages over cast-in-place bridge decks, specifically in reduced time to open the bridge to traffic.



Figure 8-1. Prefabricated bridge deck panels are lowered onto concrete girders during an Accelerated Bridge Construction (ABC) operation (Photo courtesy of STRUCTURE Magazine) [38].

A test element of such a bridge design was fabricated at the FDOT M. H. Ansley Structures Research Center in Tallahassee, Florida as shown in Figure 8-2. This specimen was fabricated at the request of the FDOT Structures Design Office for evaluation of construction practices and feasibility analysis. A major concern of the officials witnessing the placement was the integrity of the grout interface between the bridge deck and girders. Since this interface is levelled before grouting operations by extension of its relationship with the bridge deck roadway surface, it is difficult to guarantee that all entrapped air is displaced and vented by the pressure grouting operation. Air pockets and bleed water pockets in this grout interface present a readily available water infiltration path that can lead to premature corrosion and damage and could be catastrophic in areas prone to freeze-thaw damage.

This test element and its associated concerns presented a unique opportunity for the research team of the ANTARES program to collaborate with the FDOT Structures Design Office to generate mutually beneficial data. Logistically, the test element was conveniently located, supported by local FDOT personnel, contained a multitude of interesting features to investigate, and was relatively easy to deploy the scanner system onto as the bridge element was actually fabricated below ground level, with the bridge roadway surface level with the Ansley center's existing outdoor patio.



Figure 8-2. Location of the test element behind the FDOT M. H. Ansley Structures Research Center in Tallahassee, FL (Photo courtesy of Google Earth).

Transportation of the System

Moving an ANTARES scanner presented a significant logistical challenge. The nearly 4x3m, 180kg scanner was unbolted from its clamping and mounting framed as shown in Figure 8-4, laid down horizontally, and manually carried onto a flatbed trailer as shown in Figure 8-3. The operation is feasible with four people, but much safer with six.



Figure 8-3. ANTARES Scanner 1 fastened to an open frame flatbed trailer outside of the FDOT State Materials Office in Gainesville, FL (Photo by J. Nelson).



Figure 8-4. Laboratory block clamping frame with ANTARES Scanner 1 removed for field transport. Scanner 2 is still attached to the frame and could be operated in the laboratory independently of Scanner 1 (Photo by J. Nelson).

Once the scanner was placed on wooden supports and strapped down to the open frame flatbed trailer, numerous cardboard and plastic elements were used to protect the delicate components of the scanner from road debris. The entire scanner was then wrapped in a waterproof cover for transport.

The field deployment began on Wednesday, July 31, 2013 at 6:00am and the 258km drive to the Ansley center took approximately 3 hours. Ansley center personnel helped move the scanner to its first scan location and set up the required electricity, compressed air, and shade. The scanner was laid directly on the roadway surface as shown in Figure 8-5, and the first scan began at 10:00am.



Figure 8-5. ANTARES system in operation at the Ansley center, performing a laser profilometer scan of the first location on the ABC test element (Photo by J. Nelson).

Scans were conducted until 5:00pm until an encroaching storm forced an end to the field deployment. The system was placed back on the flatbed trailer and transported back to Gainesville.

Deployment Results

Scans using the ANTARES system covered two areas on the ABC test element.

Each location contained a joint running in the Y direction and a girder running in the X direction as shown in Figure 8-6, the intersection of which was clearly visible on the surface and in the NDE data.

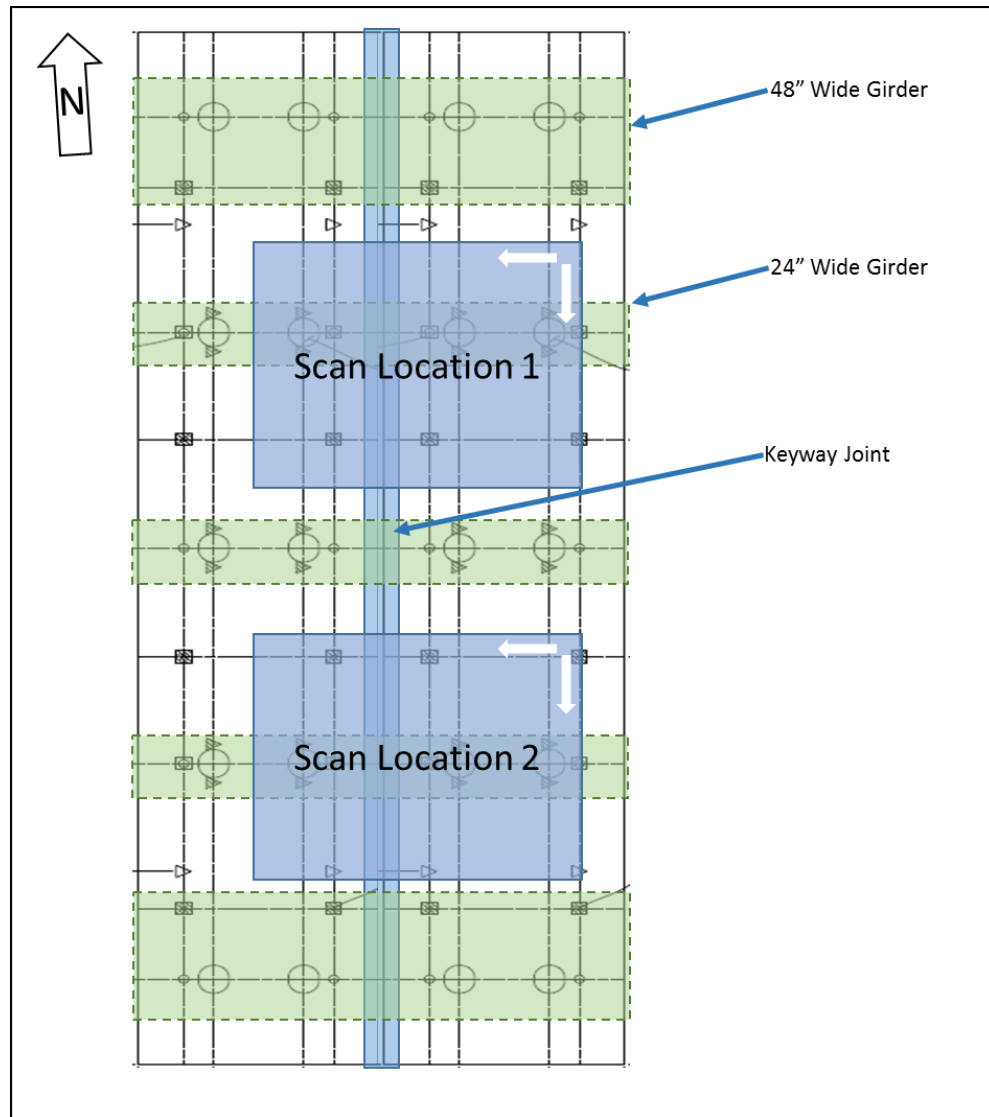


Figure 8-6. ANTARES scan locations on the ABC test element.

The first scan location received a laser profilometer scan and an ultrasound scan.

The second received a GPR scan and an ultrasound scan. All four scans were

performed on a much coarser grid than would have otherwise been used due to time constraints.

The laser profilometer scan showed a very coarse roadway along with residual features from the grouting operations as shown in Figure 8-7. This scan emphasized its value as a supporting instrument; indicating regions where suspect areas determined from contact instruments such as ultrasound may just be artifacts of the surface itself and not an actual structural defect.

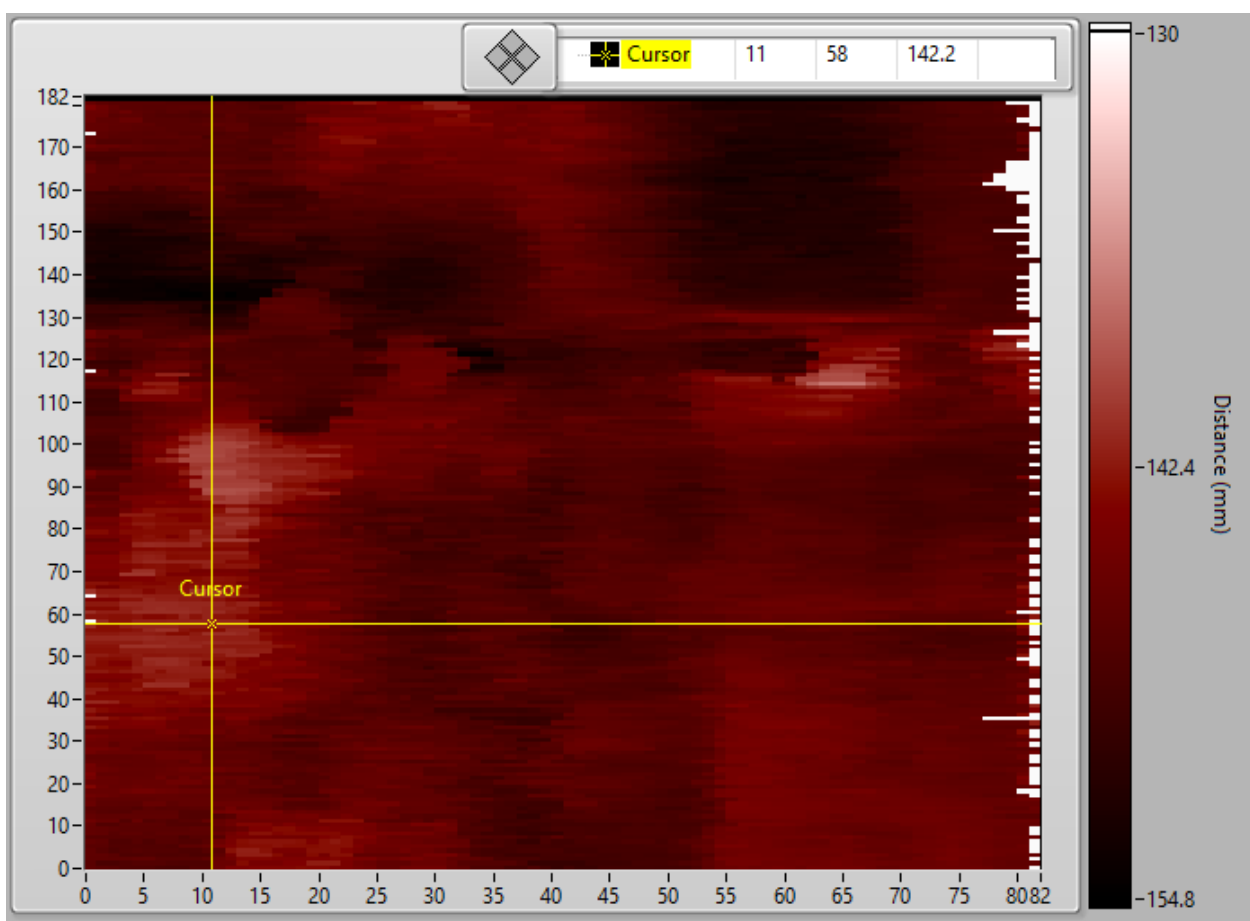


Figure 8-7. Laser profile of the ABC test element surface at location 1. Note the circular artifact at line 120, point 15 resulting from a grout port through the bridge deck.



Figure 8-8. Surface of bridge deck at location 1 as profiled by the laser scan (Photo by J. Nelson).

After analyzing the ultrasound data, some interesting characteristics of the element were noted. The very rough roadway surface had indeed impacted the ultrasound data collection and resulted in a C-Scan image with significantly more noise than a typical image produced from a laboratory specimen. This coupled with an already coarse grid made data interpretation somewhat difficult. Additionally, the back surface of the bridge deck did not produce the kind of strong reflection usually seen in ultrasound C-Scan images when performing the shadowing technique on laboratory specimens. The back wall reflection was weak in the majority of its area with regions of more intense reflection. It was determined that this was due to the fact that the test element was buried in the ground and therefore resting on compacted earth. The shear stress wave was partially reflecting off the bottom edge of the slab, but some of its energy was transmitted into the earth.

To effectively analyze the data at location 1, the depth of the ultrasound C-Scan display was set to 155mm where the interface between the girder and the bridge deck was visible. In Hilbert transform space, two dark traces indicated clearly the intersection between the keyway joint and the girder. Two regions were identified at the grout interface where a significant ultrasound reflection had occurred, which should not occur if the grout layer was complete and properly bonded. An additional suspect area was initially noted, but after comparison with the laser profilometer data it was determined to be a reflection from a grout port and not likely an actual defect. The C-Scan image is presented in Figure 8-9.

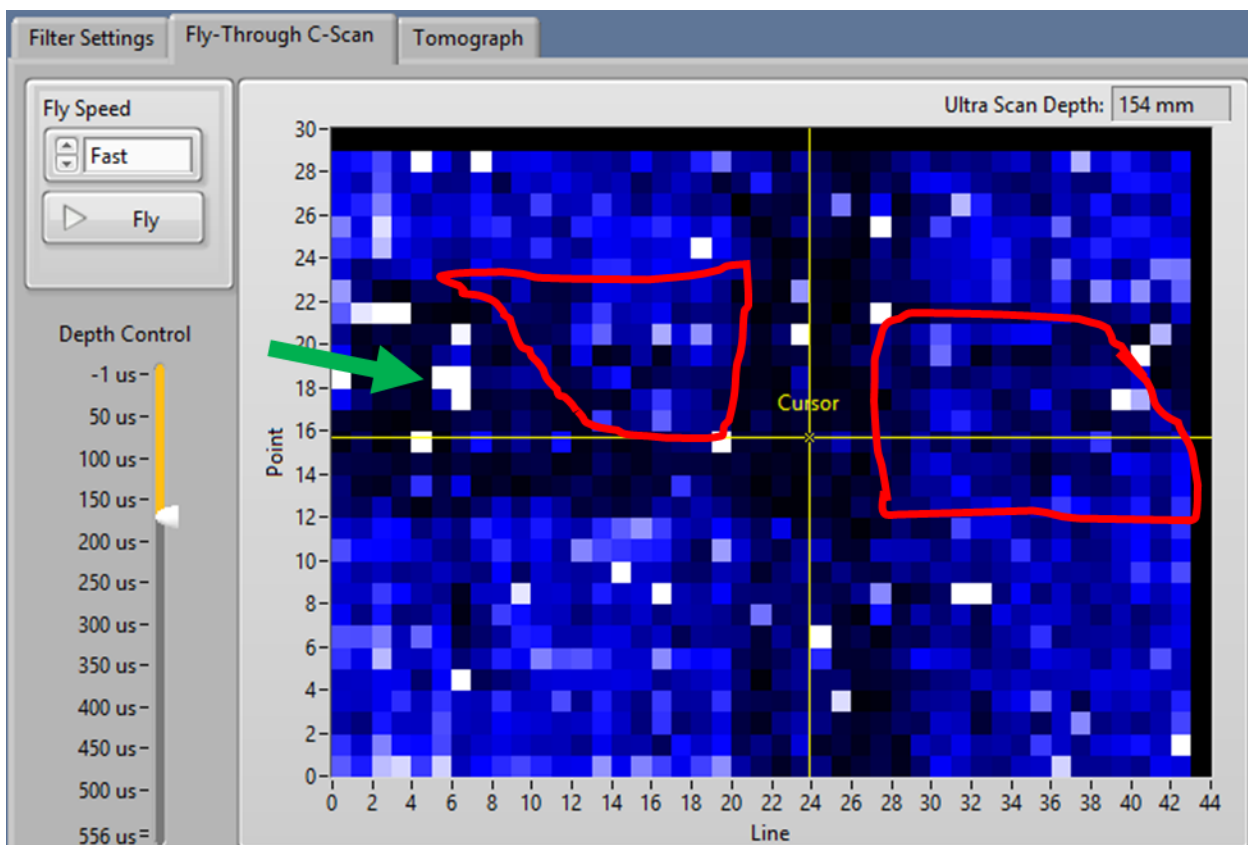


Figure 8-9. Ultrasound C-Scan image at ABC Location 1. The two areas of suspected incomplete grouting are circled in red, while a false defect corresponding to a grout port is indicated with a green arrow.

Scans conducted at location 2 revealed similar results. The ultrasound scan indicated one area of severe delamination on top of the girder and one area that was suspect, but not severe. Interestingly, the adjacent bridge deck element across the keyway joint partially visible in the scan had a much stronger bottom surface reflection than any area previously investigated. It is hypothesized that this section of the bridge deck was not in contact with the earth below the deck elements due to erosion or foundation settlement and therefore exhibited a stronger backwall reflection.

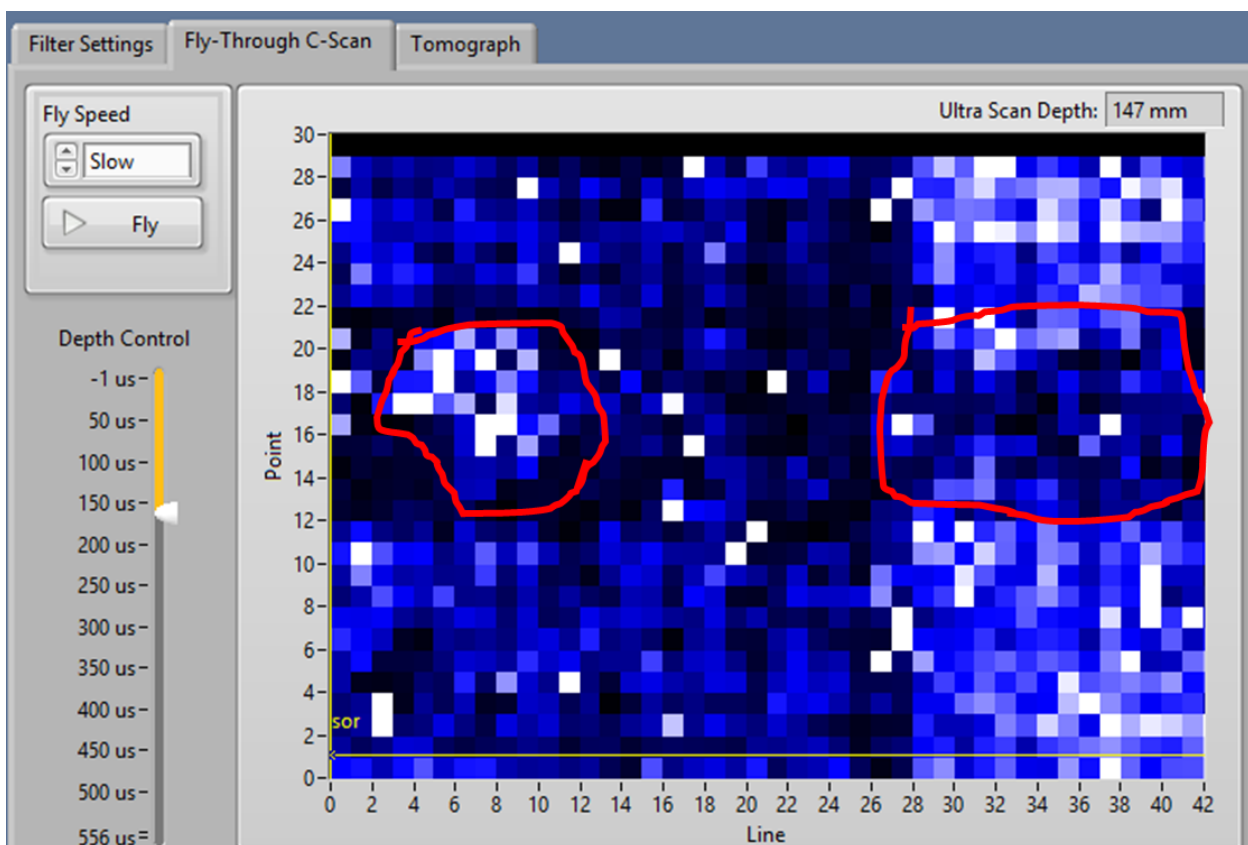


Figure 8-10. Ultrasound C-Scan of location 2 showing severe delamination (circled left) and stronger backwall reflection of adjacent bridge deck due to lack of contact with foundation (right).

A GPR scan was also performed at location 2 to reinforce the findings of the ultrasound scans. The bridge deck was densely reinforced, so the C-Scan image presented in Figure 8-11 contained large areas of steel reflections that occluded any

potential reflections from delaminations within the deck. A closer look at the tomograph view shown in Figure 8-12, however, revealed a strong reflection from the area of suspected severe delamination, further suggesting an area of voided grout.

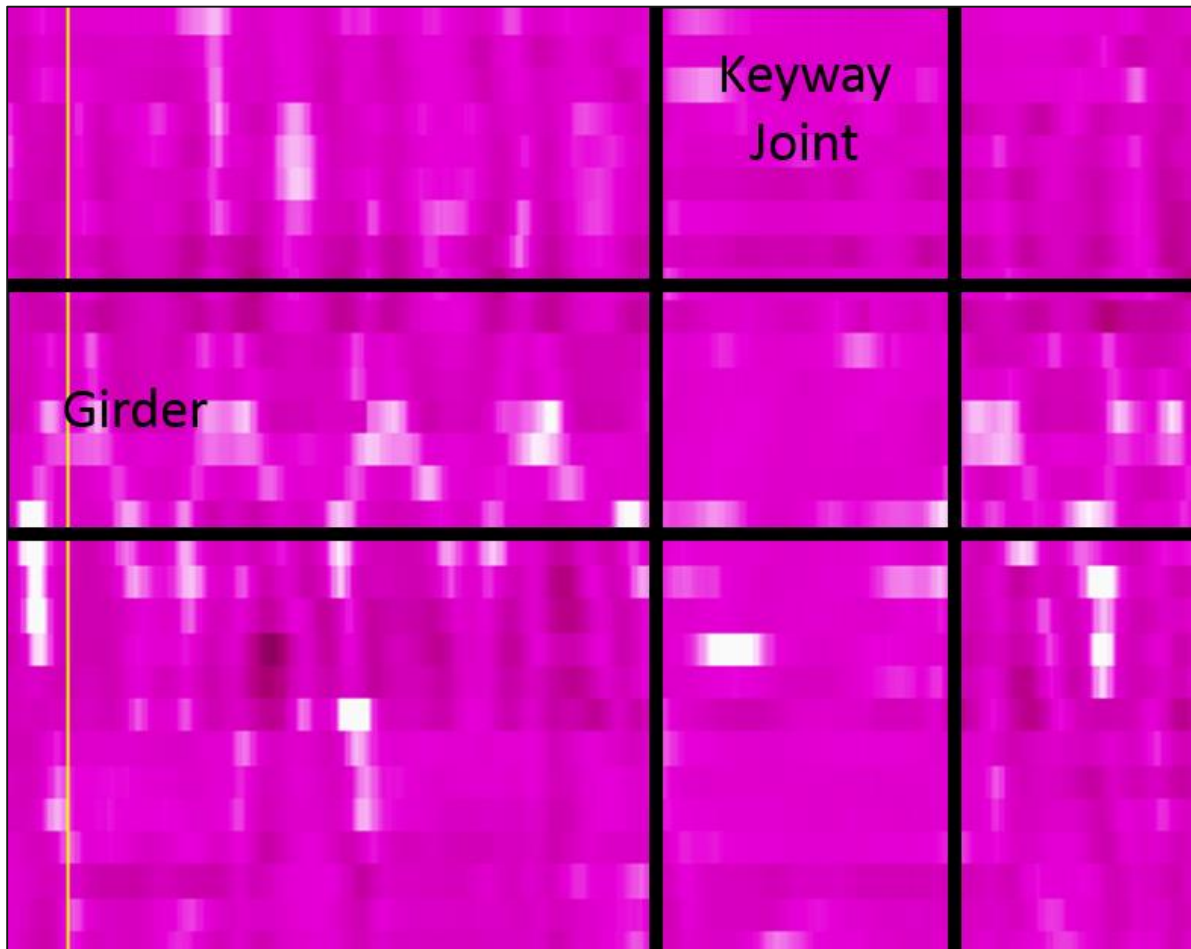


Figure 8-11. GPR C-Scan image at a depth of 120mm showing dense reinforcement on either side of the keyway joint.

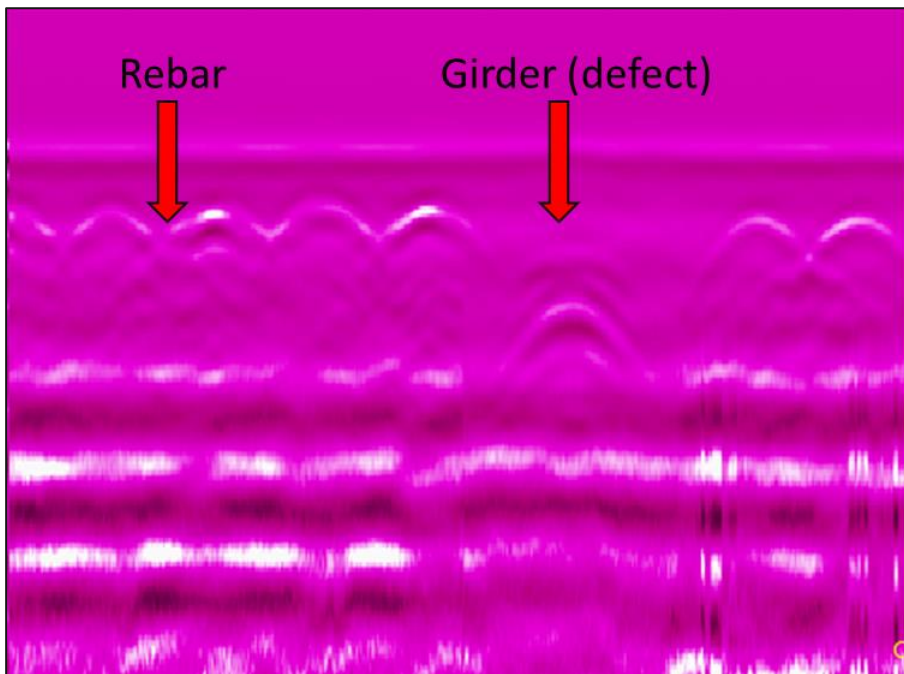


Figure 8-12. GPR B-Scan image of antennae path over the area of suspected severe delamination. The large, faint reflection over the girder indicates a probable air void.

Following the NDE analysis, the personnel at the Ansley center took drilled core specimens from the two suspect locations marked on the test element at Location 1 by the research team with marking paint in order to confirm the findings from ANTARES. In the two locations from the first scan area, the core came out of the barrel bit with a clear space between the concrete bridge deck and the grout layer, falling into two pieces as soon as it was removed. The grout portions of these two cores, with unbounded regions of the grout surface visible, are shown in Figure 8-13. A core was also taken from a non-suspect area on one of the girders and was found to be well bonded and intact as shown in Figure 8-14. Due to time constraints, cores were not taken from ABC Location 2, however the indications of a delaminated area in this regions were far more certain. With these results, it is clear that the ANTARES system performed admirably on its first field trial with despite less than ideal operating conditions.



Figure 8-13. Drilled core specimens from ABC Element Location 1 showing boundaries of regions with grout delamination (Photos courtesy of FDOT M.H. Ansley Structures Research Center).



Figure 8-14. Drilled core of Location 1 in an area predicted by ANTARES to have a proper grout interface (Photos courtesy of FDOT M.H. Ansley Structures Research Center).

CHAPTER 9 CONCLUDING REMARKS

The results of this research and development effort for the sponsoring agency can be thought of as simply a more advanced tool for quality control of concrete structures, investigation of infrastructure components *in situ*, and a platform for evaluating new NDE techniques as they come available. However, it is clear that this project has accomplished much more than that. ANTARES is an expansive and comprehensive analysis system and the beginnings of an entire research program that could potentially advance the industry of concrete NDE and indeed the construction industry as a whole. It is a tool accessible to researcher and technician alike, with unique capabilities and unique applications. It is a powerful, flexible, and expandable software platform owned and operated by non-profit agency.

The ANTARES system has proved itself able to resolve many forms of structural defect and do so in a repeatable and easy to understand manner. The software produces useful, open-format data and easy to understand data displays and is available for use by any agency that wishes to collaborate. The system is certainly not without its limitations, but it is sincerely hoped that future research efforts and collaboration with others in the industry will work for mutual benefit and reduce those limitations systematically.

It is recommended that the potential of the ANTARES system for structural quality control applications be investigated and expanded upon, including statistical analyses of the system's ability to reliably detect defects before a structural element enters service. These capabilities could be further expanded upon by the inclusion of new NDE techniques, including higher energy techniques where applicable

APPENDIX A SELECTED PROGRAMMING EXCERPTS

This Appendix contains a few pieces of code developed in LabVIEW™ that perform critical functions such as reading instruments, moving the scanner servo motors, and reading and writing ANTARES Data Files. Most images are code snippets, and if preserved digitally as a .PNG file can be dragged onto a compatible LabVIEW™ block diagram to generate the code.

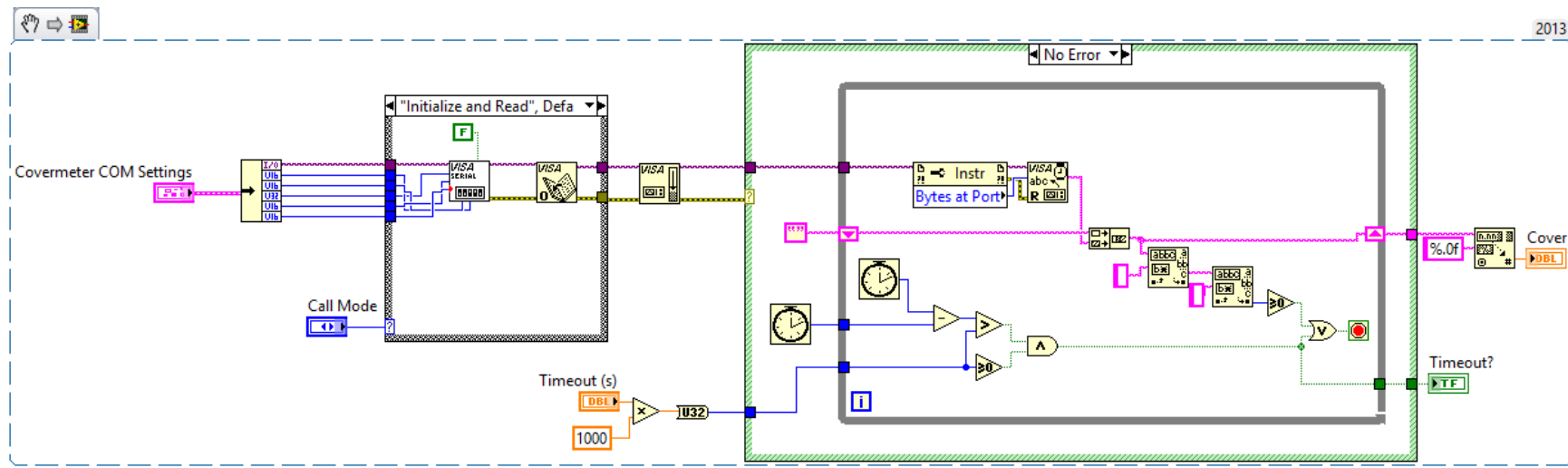


Figure A-1. Covermeter Single Point Acquisition VI.

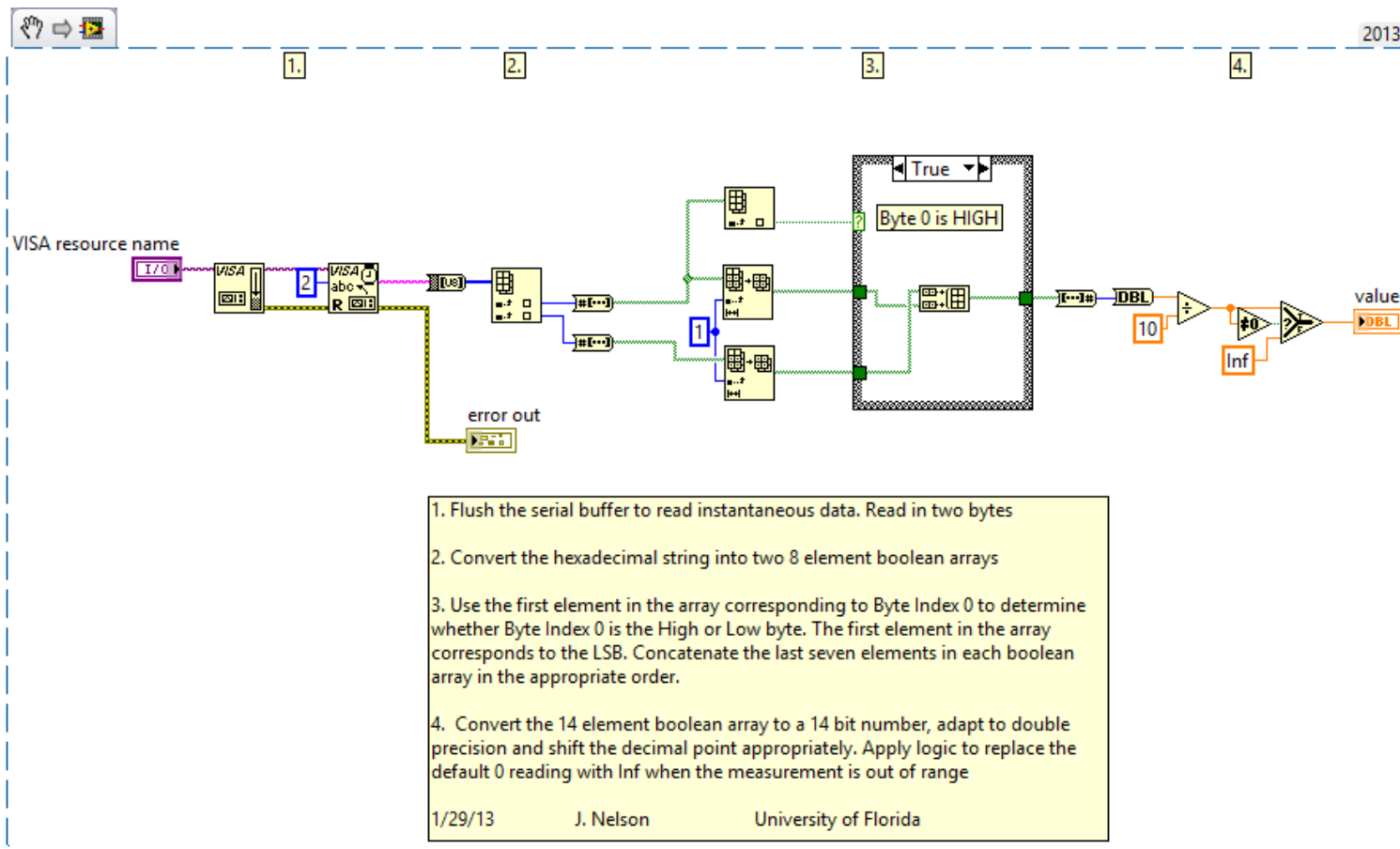


Figure A-2. Laser Single Point Acquisition VI.

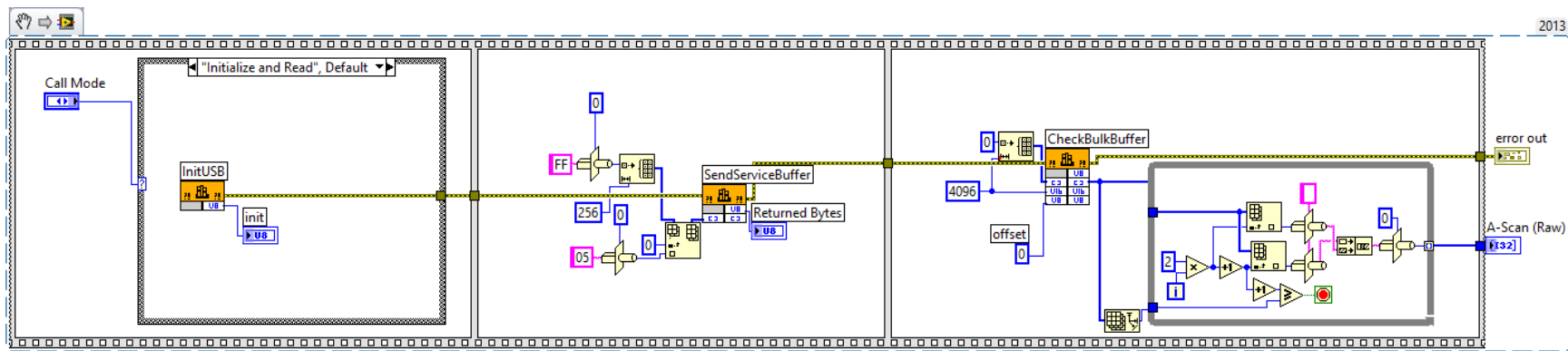


Figure A-3. Ultrasound Single Point Acquisition VI.

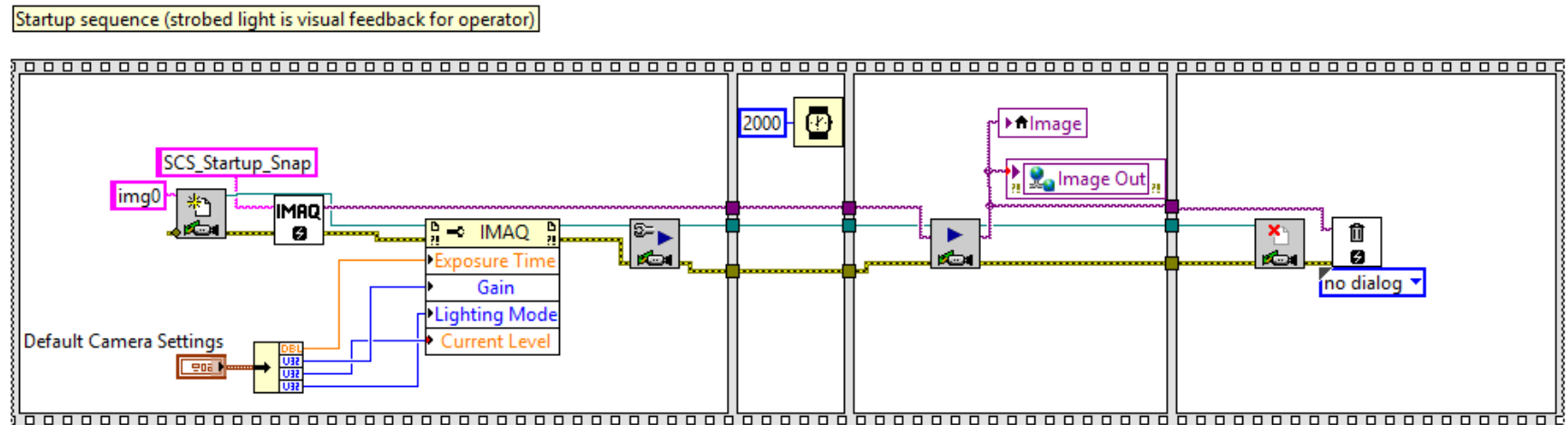


Figure A-4. SCS Startup VI Sequence 0.

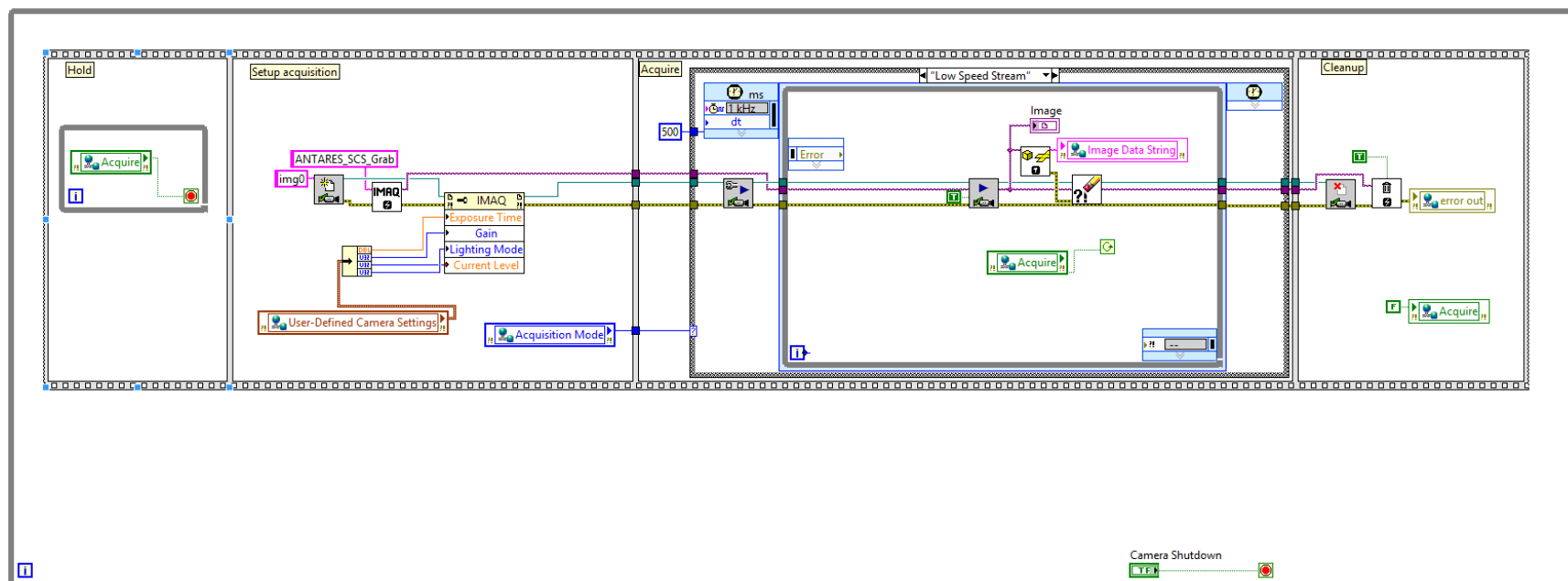


Figure A-5. SCS Startup VI Sequence 1 (main loop).

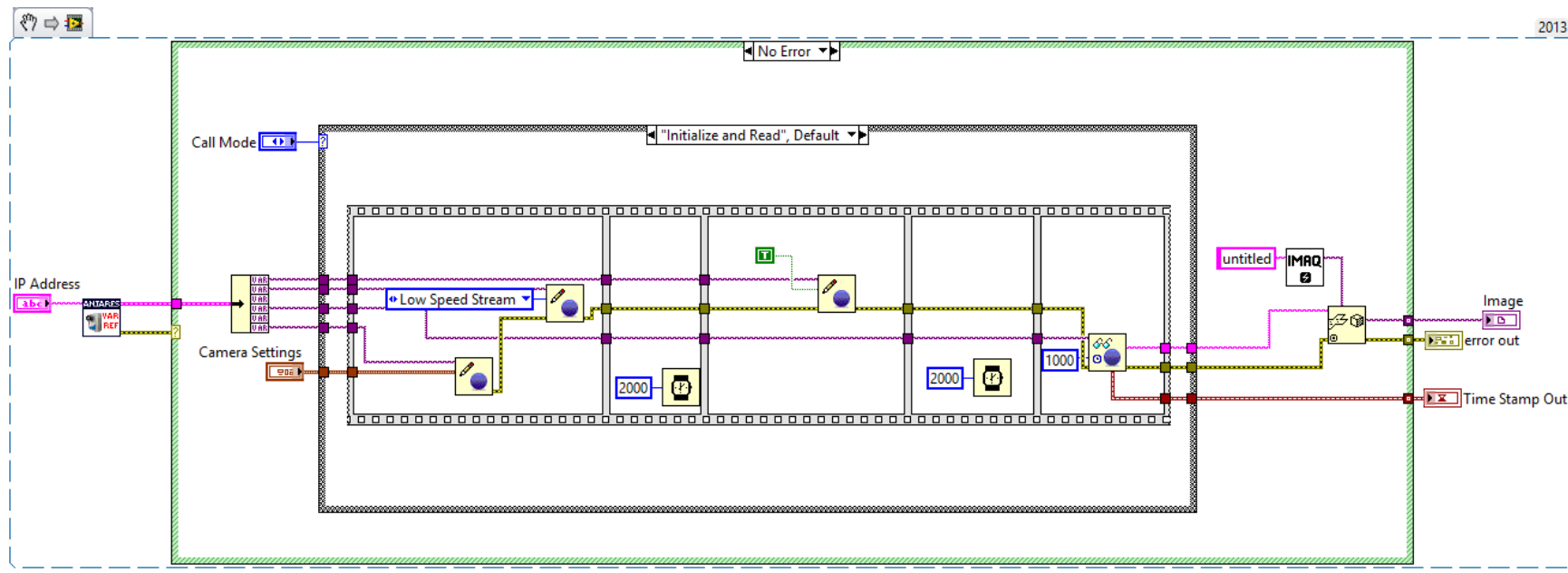


Figure A-6. SCS Image Stream VI.

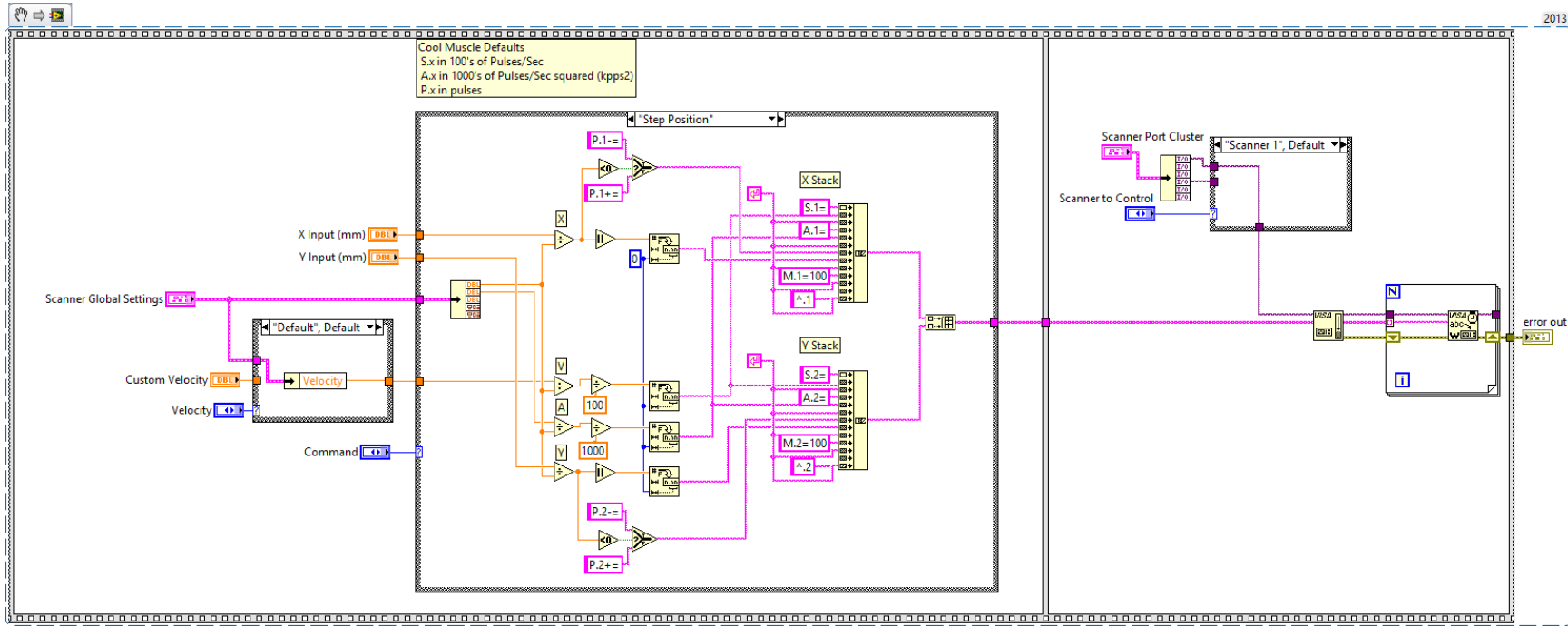


Figure A-7. CML Command VI.

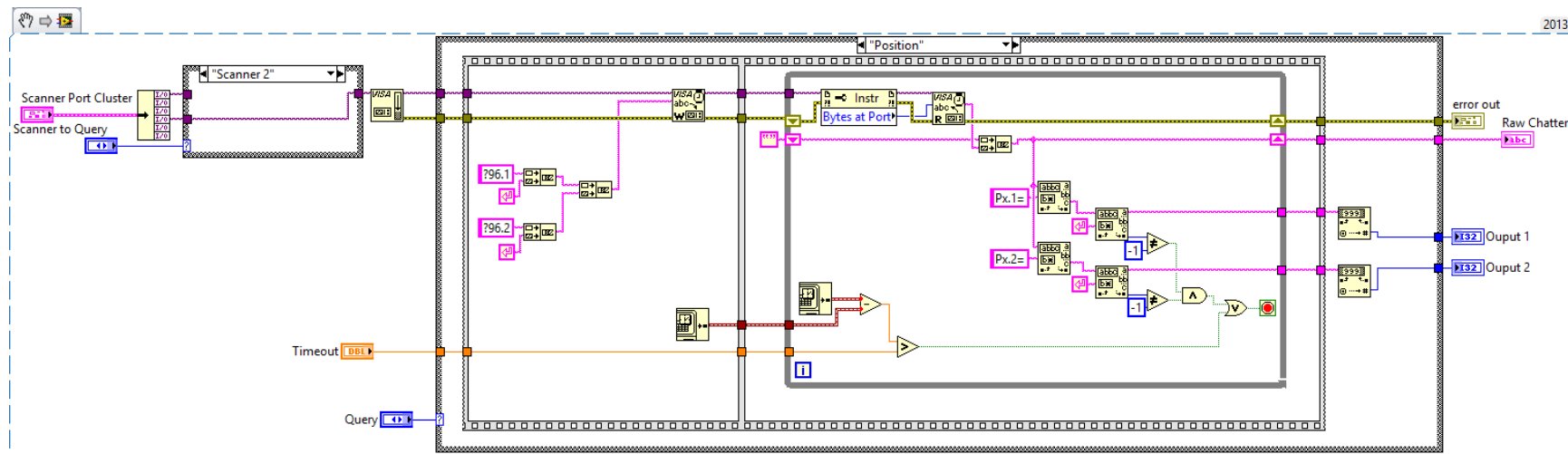


Figure A-8. CML Query VI.

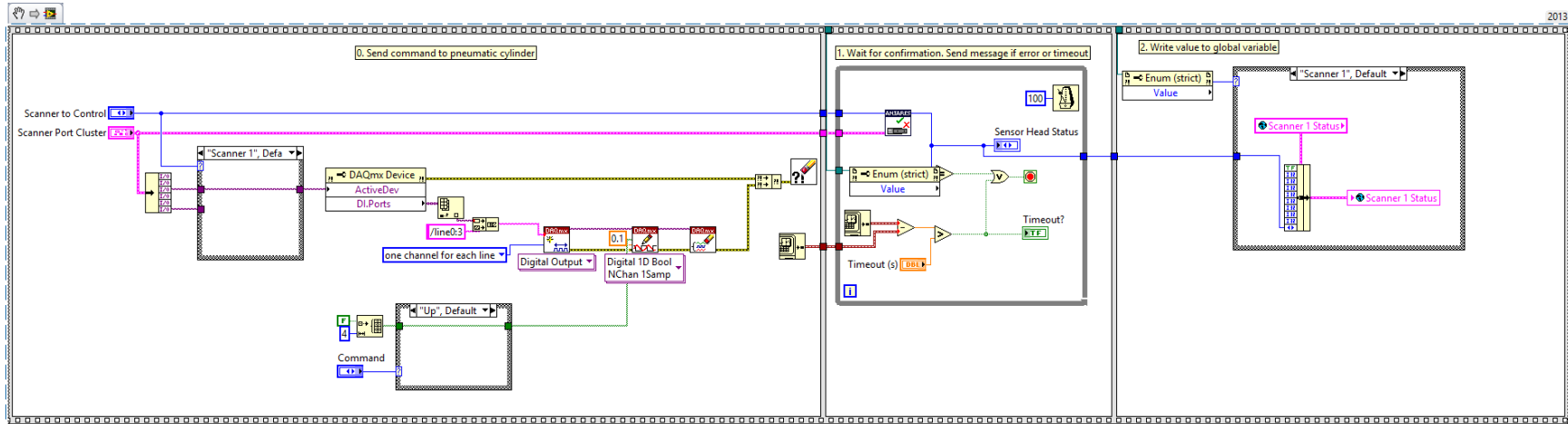


Figure A-9. Pneumatic Head Command VI.

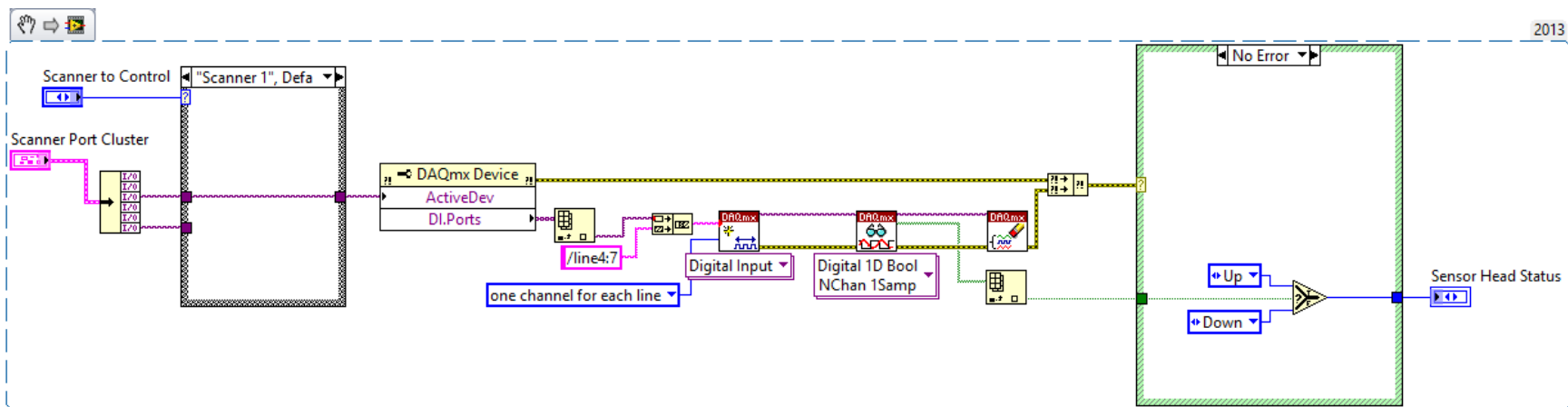


Figure A-10. Pneumatic Head Query VI.

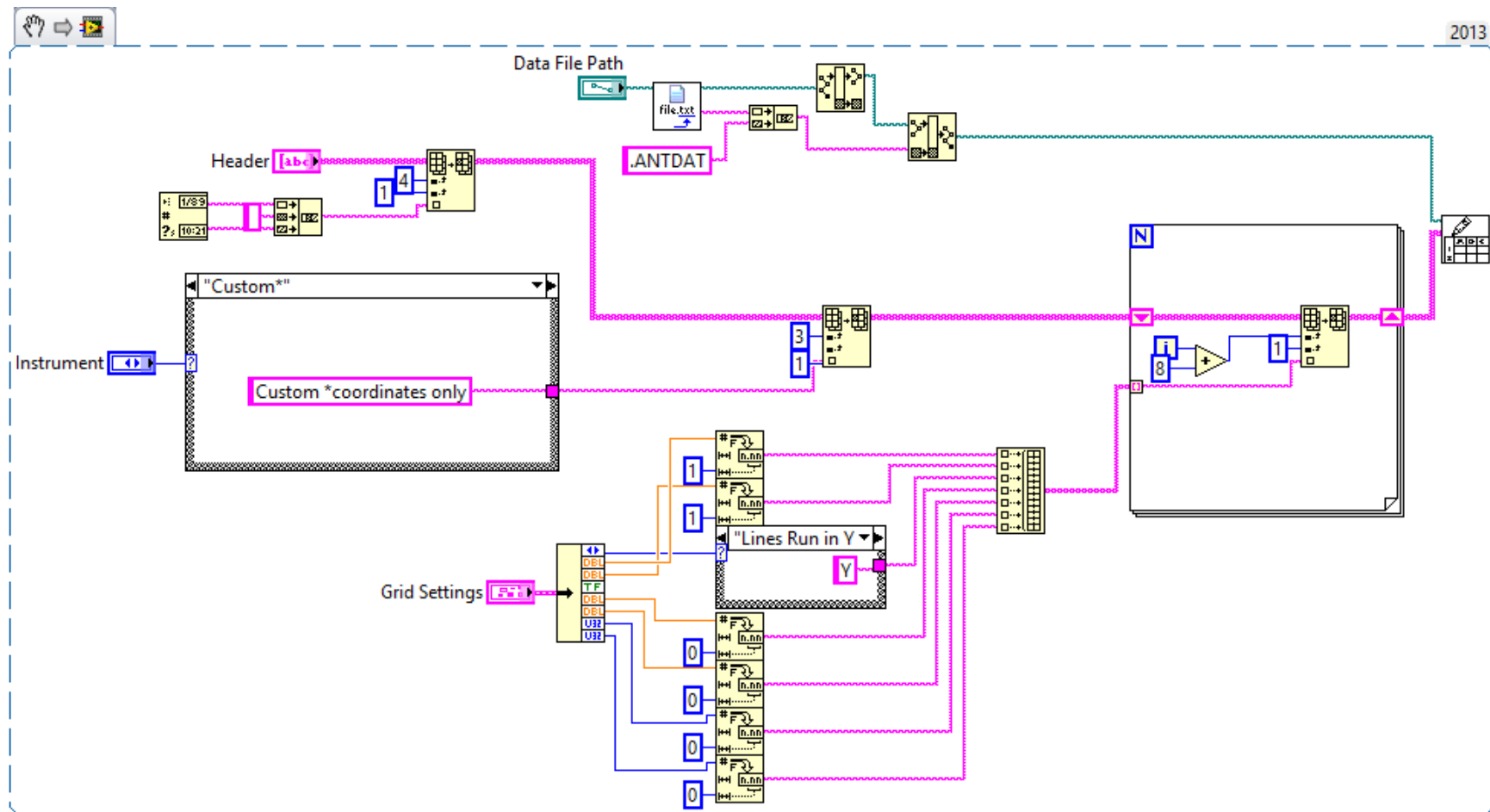


Figure A-11. *.ANTDAT File Creation VI.

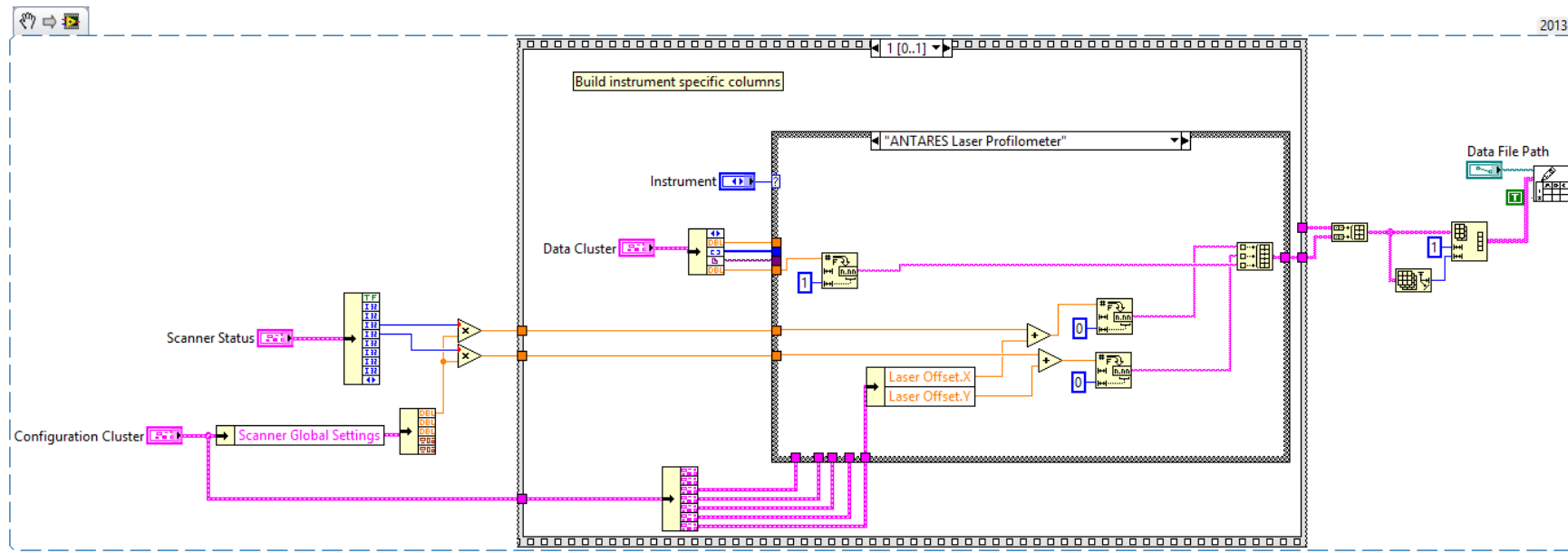


Figure A-12. *.ANTDAT File Append VI.

APPENDIX B SELECTED CAD DRAWINGS

This Appendix contains selected drawings for designed components mentioned in this report. This includes the instrument carrier design, laboratory blocks, and drawings of the ABC test element provided by FDOT

ITEM NO.	PART NUMBER	QTY.
1	11in T-Slot Alum Elem	4
2	8in T-Slot Alum Elem	2
3	2.5in T-Slot Alum Elem	2
4	Corner Bracket	4
5	AlumPlate	1
6	End Feed Fastener	20
7	Corner Fastener	4
8	Thumb Screw	4

UNLESS OTHERWISE SPECIFIED:
DIMENSIONS ARE IN MM
TOLERANCES:
FRACTIONAL: ±
ANGULAR: MACH: ± BEND: ±
ONE PLACE DECIMAL: ±0.5
TWO PLACE DECIMAL: ±0.05

INTERPRET GEOMETRIC
TOLERANCING PER:

DRAWN **JDN** NAME DATE
CHECKED
ENG APPR.
MFG APPR.
Q.A.
COMMENTS:

NEXT ASSY USED ON FINISH
APPLICATION DO NOT SCALE DRAWING

PROPRIETARY AND CONFIDENTIAL
THE INFORMATION CONTAINED IN THIS
DRAWING IS THE SOLE PROPERTY OF
<INSERT COMPANY NAME HERE>. ANY
REPRODUCTION IN PART OR AS A WHOLE
WITHOUT THE WRITTEN PERMISSION OF
<INSERT COMPANY NAME HERE> IS
PROHIBITED.

TITLE:
ANTARES Instrument Carrier Assy

SIZE DWG. NO. REV
A InstCarAssy

SCALE: 1:5 WEIGHT: SHEET 1 OF 1

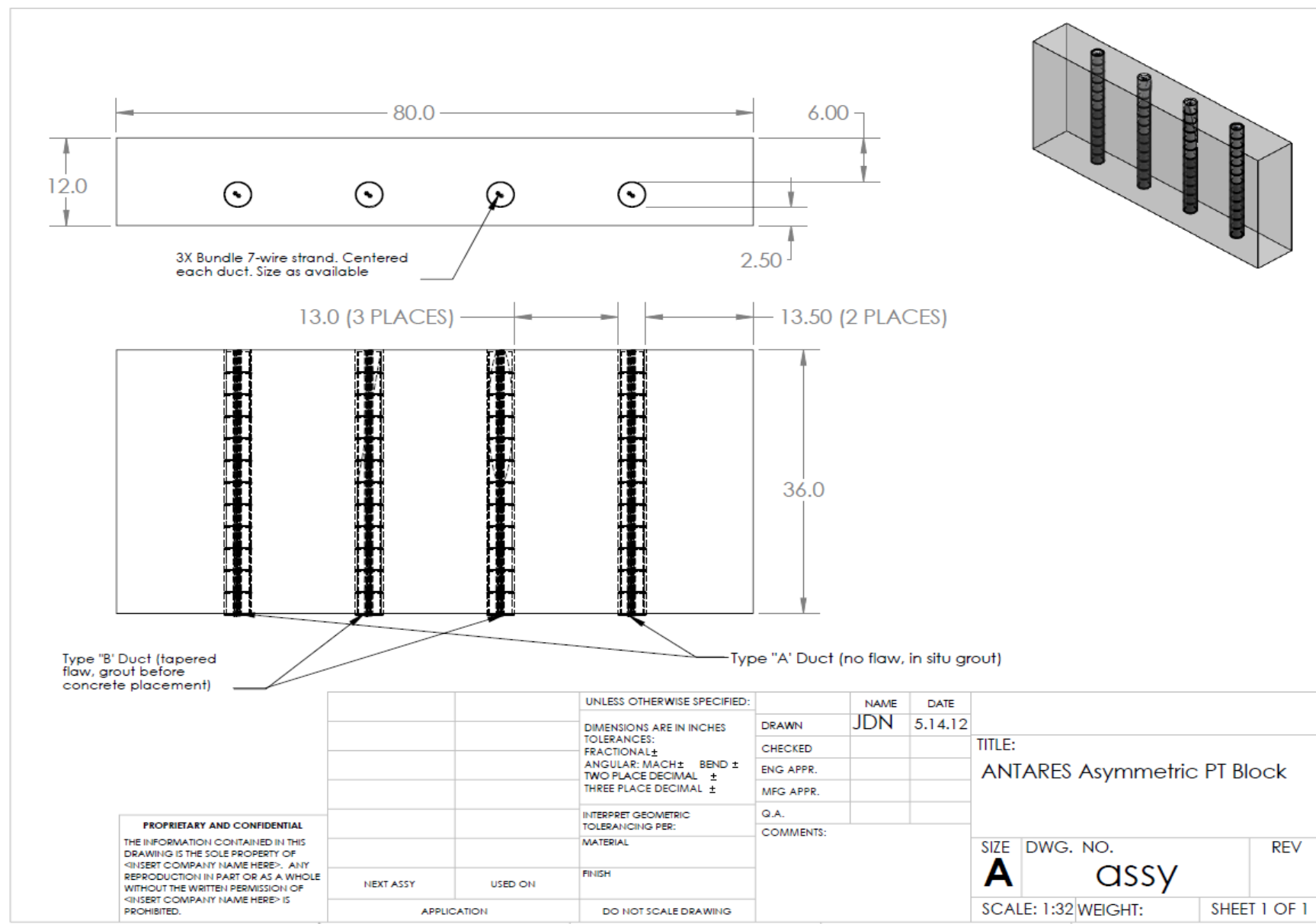
5

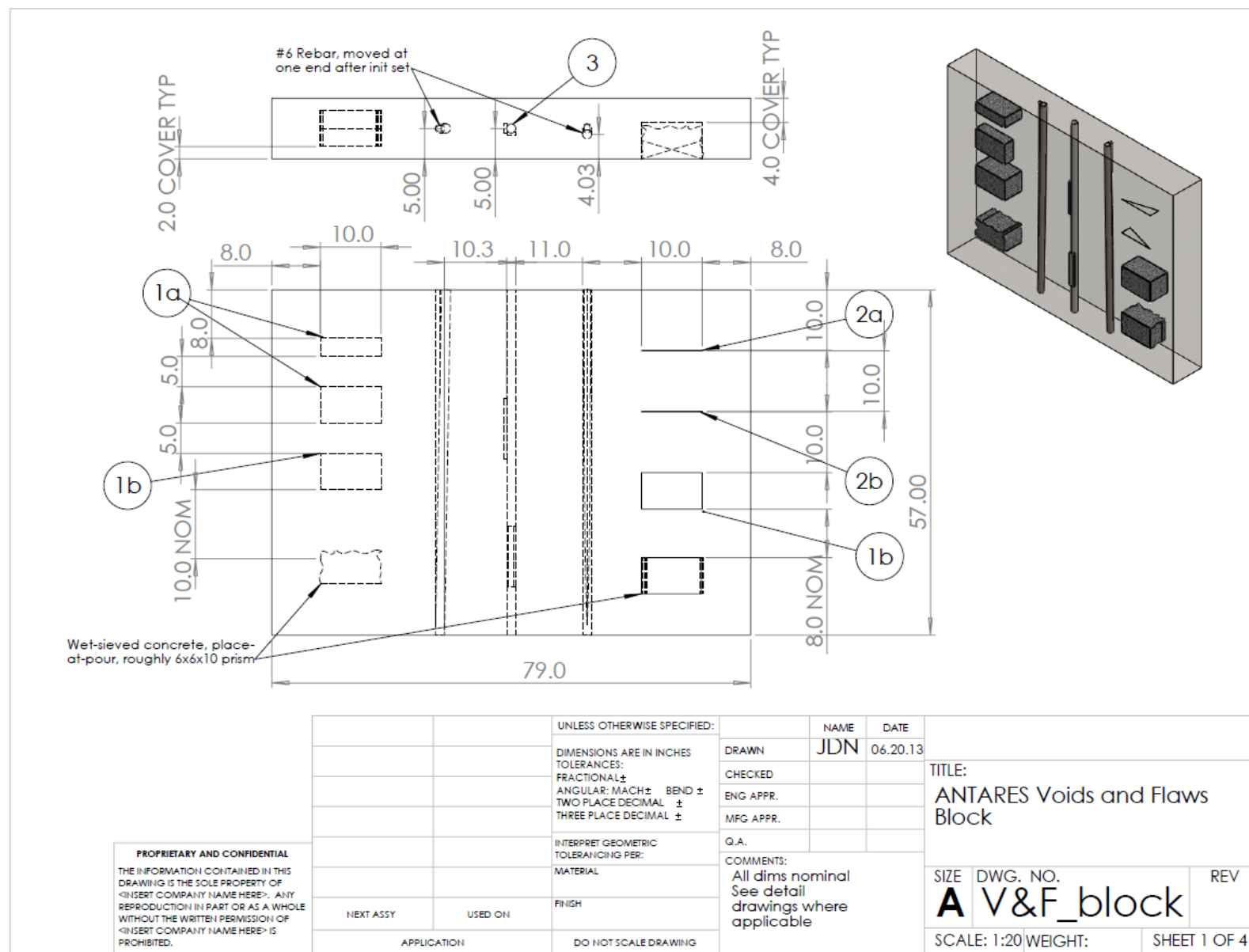
4

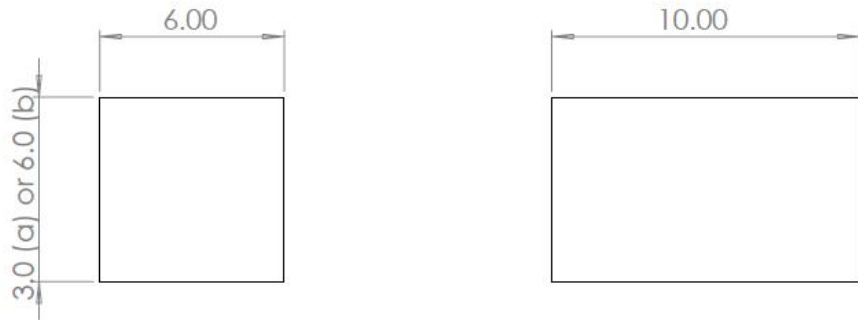
3

2

1







Notes:

Prisms to be constructed by compacting concrete of same mix design with sand removed into 6 inch beam mold and allowing to set before block casting

		UNLESS OTHERWISE SPECIFIED:			NAME	DATE	Detail 1a, 1b	
		DIMENSIONS ARE IN INCHES		DRAWN	JDN	06.20.13		
		TOLERANCES:		CHECKED				
		FRACTIONAL \pm		ENG APPR.				
		ANGULAR: MACH \pm BEND \pm		MFG APPR.				
		TWO PLACE DECIMAL \pm		Q.A.				
		THREE PLACE DECIMAL \pm		COMMENTS:				
		INTERPRET GEOMETRIC TOLERANCING PER:					TITLE:	
		MATERIAL					ISC Prisms, 3 and 6 inch	
		NEXT ASSY		FINISH				
		USED ON		APPLICATION		DO NOT SCALE DRAWING	SIZE DWG. NO. REV	
							A V&F_block	
							SCALE: 1:20 WEIGHT: SHEET 2 OF 4	

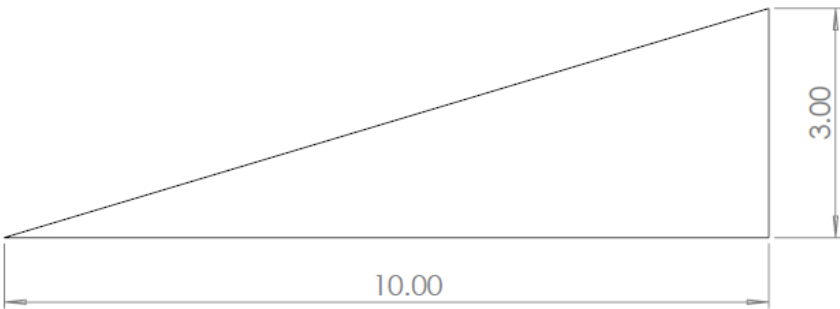
5

4

3

2

1



Notes:

Form triangular wedges from 1/16in thick steel sheet (a) and 1/8 thick polycarbonate sheet (b). Press into block at placement and remove after initial set

		UNLESS OTHERWISE SPECIFIED: DIMENSIONS ARE IN INCHES TOLERANCES: FRACTIONAL \pm ANGULAR: MACH \pm BEND \pm TWO PLACE DECIMAL \pm THREE PLACE DECIMAL \pm	DRAWN CHECKED ENG APPR. MFG APPR. Q.A.	NAME JDN 06.20.13	DATE
		INTERPRET GEOMETRIC TOLERANCING PER: MATERIAL			Detail 2a, 2b
	NEXT ASSY	USED ON	FINISH		TITLE: Crack simulators (1/16 and 1/8 in thicknesses)
		APPLICATION	DO NOT SCALE DRAWING		SIZE DWG. NO. REV A V&F_block
				SCALE: 1:20	WEIGHT: SHEET 3 OF 4

5

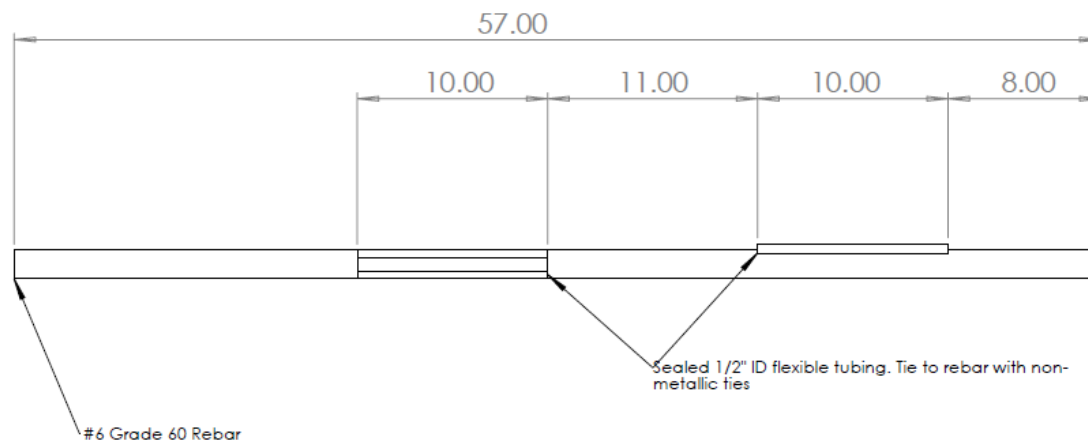
4

3

2

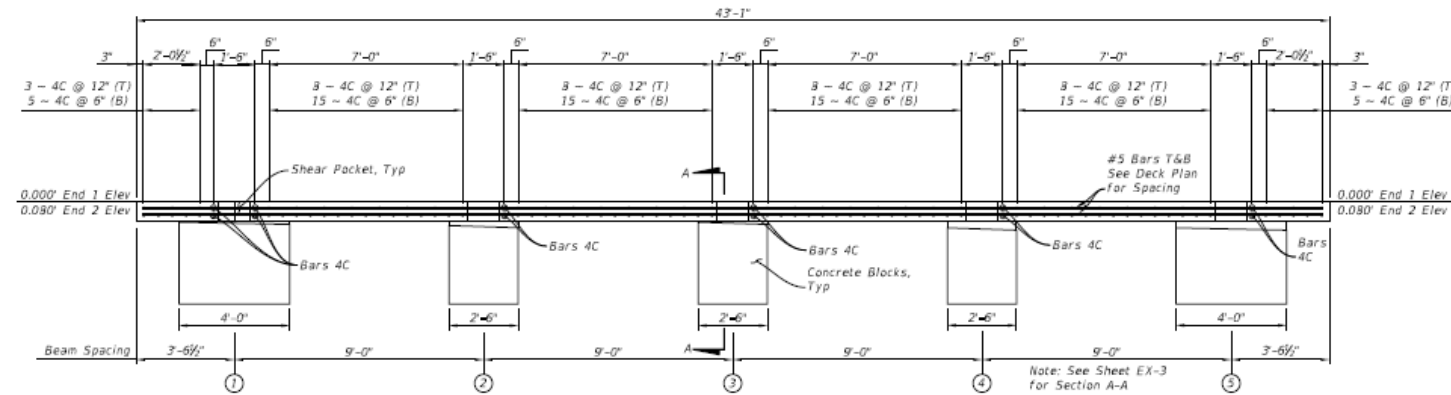
1

PROPRIETARY AND CONFIDENTIAL
THE INFORMATION CONTAINED IN THIS
DRAWING IS THE SOLE PROPERTY OF
<INSERT COMPANY NAME HERE>. ANY
REPRODUCTION IN PART OR AS A WHOLE
WITHOUT THE WRITTEN PERMISSION OF
<INSERT COMPANY NAME HERE> IS
PROHIBITED.

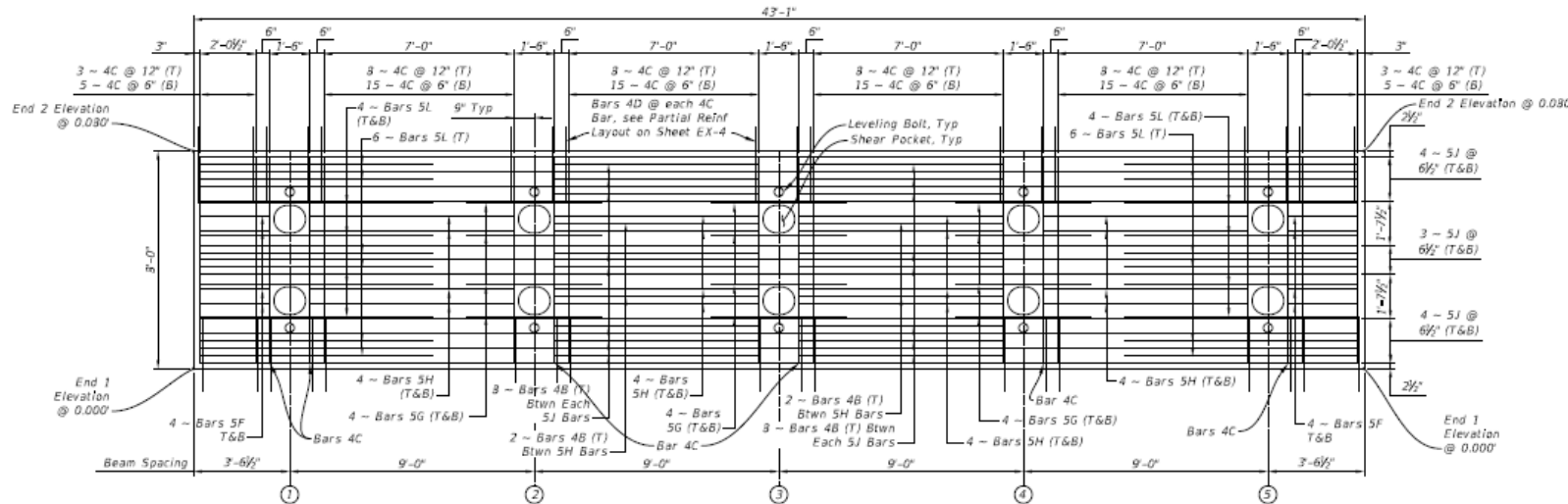


		UNLESS OTHERWISE SPECIFIED:		DRAWN	NAME JDN	DATE 06.20.13	Detail 3							
		DIMENSIONS ARE IN INCHES TOLERANCES: FRACTIONAL ± ANGULAR: MACH ± BEND ± TWO PLACE DECIMAL ± THREE PLACE DECIMAL ±					INTERPRET GEOMETRIC TOLERANCING PER:							
				MATERIAL		COMMENTS:								
NEXT ASSY		USED ON		FINISH										
APPLICATION		DO NOT SCALE DRAWING												
5		4		3		2		1						
PROPRIETARY AND CONFIDENTIAL THE INFORMATION CONTAINED IN THIS DRAWING IS THE SOLE PROPERTY OF <INSERT COMPANY NAME HERE>. ANY REPRODUCTION IN PART OR AS A WHOLE WITHOUT THE WRITTEN PERMISSION OF <INSERT COMPANY NAME HERE> IS PROHIBITED.		SIZE		DWG. NO.		REV								
		A		V&F_block										
		SCALE: 1:20		WEIGHT:		SHEET 4 OF 4								

ABC test element drawings courtesy FDOT Structures Design Office



Precast Deck Elevation



Precast Deck Plan

REVISIONS				DRAWING BY:		STATE OF FLORIDA		DRAWN BY:		REF. DRAW. NO.	
DATE	BY	DESCRIPTION	DATE	BY	DESCRIPTION	04/08/01 VA 08/01	DEPARTMENT OF TRANSPORTATION	04/08/01 VA 08/01	FINANCIAL PROJECT ID:	04/08/01 VA 08/01	
						CHEELED BY: 04/08/01 VA 08/01		RSAD 00	COASTY		SHEET NO. EX-1
						CHECKED BY: 04/08/01 VA 08/01					

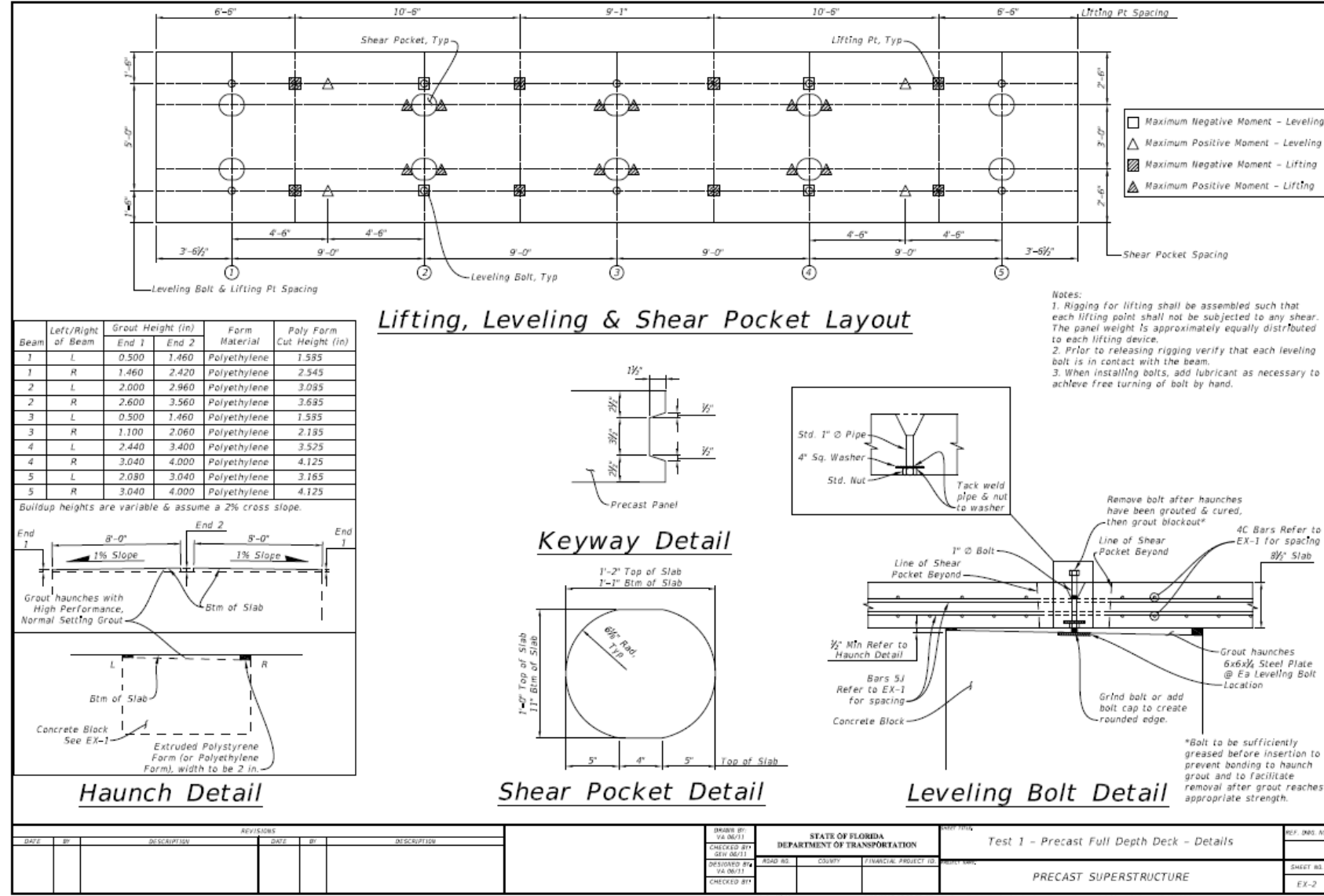
Test 1 - Precast Full Depth Deck - Plan & Elevation

PRECAST SUPERSTRUCTURE

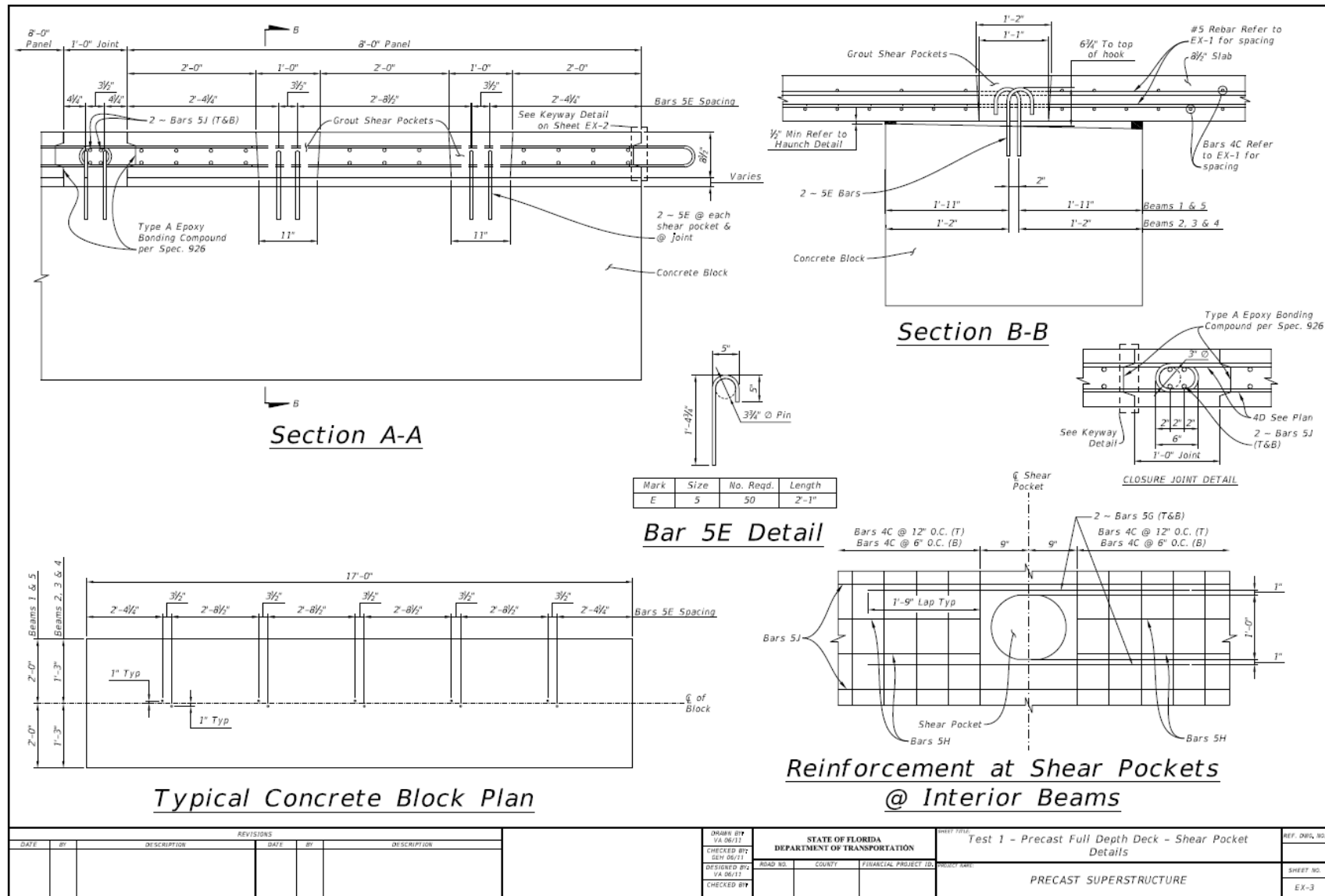
Attn: WWD

2/15/2012 10:31:22 AM C:\Program Files\Standards\Structures\Current\Release_Bridges\013\version2.Dwg

ABC test element drawings courtesy FDOT Structures Design Office



ABC test element drawings courtesy FDOT Structures Design Office



LIST OF REFERENCES

- [1] B. Mitchell, *Concrete Spalling*, Pioneer Masonry Restoration Co., Inc..
- [2] C. C. Ferraro, A. J. Boyd and G. C. Consolazio, "Evaluation of damage to bridge piers using pulse velocity tomography," vol. 38, 2012.
- [3] ACI Committee 201, *ACI 201.1-R08 Guide for Conducting a Visual Inspection of Concrete in Service*, Farmington Hills, MI: American Concrete Institute, 2008.
- [4] FDOT State Materials Office, "Instrumentation of Florida's Accelerated Pavement Testing Facility," Gainesville, FL, 2011.
- [5] "Laser Displacement sensor|LAP LASER," T.J. Solution Co.,Ltd., [Online]. Available: <http://www.tjsolution.com/>. [Accessed 9 June 2013].
- [6] "Laser XVP :: Fugro Roadware," Fugro Roadware, 2013. [Online]. Available: <http://www.roadware.com>. [Accessed 9 June 2013].
- [7] "Cover Meter - Profometer 5+ Covermeter," Proceq USA, Inc., [Online]. Available: <http://www.proceq.com>. [Accessed 6 June 2013].
- [8] P. K. Mehta and P. Monteiro, *Concrete: Microstructure, Properties, and Materials*, New York: McGraw Hill, 1993.
- [9] D. Algernon, D. Hiltunen and C. Ferraro, "Validation of Nondestructive Testing Equipment for Concrete," University of Florida Department of Civil and Coastal Engineering, 2010.
- [10] N. J. Carino, "The Impact-Echo Method: An Overview," *Proceedings of 2001 Structures Congress and Exposition, American Society of Civil Engineers*, 2001.
- [11] M. Sansalone, N. J. Carino and N. N. Hsu, "A Finite Element Study of Transient Wave Propagation in Plates," *Journal of Research of the National Bureau of Standards*, pp. 267-268, 1987.
- [12] J. Krautkrämer and H. Krautkrämer, "Ultrasonic Testing of Materials," *Journal of Sound and Vibration*, pp. 157-158, 1969.
- [13] "Vu-Con System(R) ImpactEcho System For Field Evaluation of Concrete Structures," NDT James, [Online]. Available: <http://www.ndtjames.com>. [Accessed 10 June 2013].

[14] American Society for Testing and Materials, *ASTM C1383-04 Standard Test Method for Measuring the P-Wave Speed and the Thickness of Concrete Plates Using the Impact-Echo Method*, West Conshohocken, PA, 2004.

[15] I. O. Yaman, G. Inci, N. Yesiller and H. M. Aktan, "Ultrasonic Pulse Velocity in Concrete Using Direct and Indirect Transmission," *ACI Materials Journal*, pp. 450-457, 2001.

[16] American Society for Testing and Materials, *ASTM C597-09 Standard Test Method for Pulse Velocity Through Concrete*, West Conshohocken, PA: ASTM International, 2009.

[17] German Instruments, Inc., *EyeCon*, Evanston, IL.

[18] J. Hugenschmidt and J.-P. Balayssac, "Ground Penetrating Radar," in *State-of-the-Art Report of the RILEM Technical Committee 207-INR*, 2012.

[19] "Ground Penetrating Radar Equipment - StructureScan Minis," Geophysical Survey Systems, Inc., [Online]. Available: <http://www.geophysical.com/structurescanmini.htm>. [Accessed 10 June 2013].

[20] I. L. Al-Qadi and S. Lahouar, "Measuring layer thicknesses with GPR - Theory to practice," vol. 19, 2005.

[21] S. Popovics, J. L. Rose and J. S. Popovics, "The Behavior of Ultrasonic Pulses in Concrete," *Cement and Concrete Research*, pp. 259-270, 1990.

[22] T. Voigt, *The Application of Ultrasonic Shear Wave Reflection Method for Nondestructive Testing of Cement-Based Materials at Early Ages - An Experimental and Numerical Analysis*, 2005.

[23] ACI Committee 201, *ACI 2012R-08 Guide to Durable Concrete*, Farmington Hills, MI: American Concrete Institute, 2008.

[24] I. O. Yaman, R. Birgul, H. M. Aktan, N. Hearn and J. F. Staton, "Test Method for Appraising Future Durability of New Concrete Bridge Decks," vol. 1798, 2002.

[25] A. J. Boyd, B. Birgission, C. Ferraro and S. Cumming, "Nondestructive Testing for Advanced Monitoring and Evaluation of Damage in Concrete Materials," University of Florida, Gainesville, FL, 2005.

[26] M. Sargolzahi, S. A. Kodjo, P. Rivard and J. Rhazi, "Effectiveness of Nondestructive Testing for the Evaluation of Alkali–Silica Reaction in Concrete," vol. 24, no. 8, 2010.

[27] R. Beutel, H.-W. Reinhardt, C. U. Grosse, A. Glaubitt, M. Krause, C. Maierhofer, D. Algernon, H. Wiggenhauser and M. Schickert, "Comparitive Performance Tests and Validation of NDT Methods for Concrete Testing," vol. 27, 2008.

[28] M. Scott, A. Rezaizadeh, A. Delahaza, C. G. Santos, M. Moore, B. Graybeal and G. Washer, "A comparison of nondestructive evaluation methods for bridge deck assessment," vol. 36, 2002.

[29] Parsons Transportation Group, *Grouting of Bridge Post-Tensioning Tendons Training Manual*, Tallahassee, FL: State of Florida Department of Transportation, 2002.

[30] M. Krause, "Localization of grouting faults in post tensioned concrete structures," in *Non-Destructive Assessment of Concrete Structres: Reliability and Limites of Single and Combined Techniques*, vol. 1, Springer, 2012.

[31] M. Colombo and R. Felicetti, "New NDT techniques for the assessment of fire-damaged concrete structures," vol. 42, 2007.

[32] J. Heller, "The Day the Skyway Fell," *St. Petersburg Times*, 7 May 2000.

[33] H. Wiggenhauser, D. Streicher and M. Friese, "Automated NDE of PT Concrete Structures," BAM-Federal Institute for Materials Research and Testing, Berlin, Germany.

[34] Leuze electronic, *Optical Distance Sensors ODSL 8 / ODSL 30 / ODS 96*.

[35] J. E. Lucius and M. H. Powers, "GPR Data Processing Computer Software for the PC," U.S. Geological Survey, Denver, CO, 2002.

[36] D. Clayton, C. Smith, C. C. Ferraro, J. Nelson, L. Khazanovich, K. Hoegh, S. Chintakunta, J. Popovics, H. Choi and S. Ham, "Evaluation of Ultrasonic Techniques on Concrete Structures," Oak Ridge National Laboratory, 2013.

[37] D. Clayton and C. Smith, "Summary of Large Concrete Samples," Oak Ridge National Laboratory, 2013.

[38] J. McMinimee and M. L. Ralls, "Accelerated Bridge Construction - Designing for Contractors," *STRUCTURE*, no. 9, p. 5, 2009.

[39] H. Wiggenhauser, D. Streicher and M. Friese, "Automated NDE of PT Concrete Structures," Berlin, Germany.

[40] E. Schmidt, "Method and Apparatus for Testing Hardness of Specimens". United States of America Patent 3,879,982, 8 March 1974.

[41] S. Mindess, J. F. Young and D. Darwin, Concrete 2nd Ed, Upper Saddle River, NJ: Prentice Hall, 2003.

[42] J.-C. Liu, M.-L. Sue and K. Chang-Huan, "Estimating the Strength of Concrete Using Surface Rebound Value and Design Parameters of Concrete Material," *Tamkang Journal of Science and Engineering*, vol. 12, no. 1, pp. 1-7, 2009.

[43] American Concrete Institute, *Structural Building Code (ACI 318-11) and Commentary, Section 8.5 Modulus of Elasticity*, Detroit: American Concrete Institute, 2011.

[44] International Atomic Energy Agency, Guidebook on On-Destructive Testing of Concrete Structures, Vienna, Austria: IAEA, 2002.

[45] American Society for Testing and Materials, *ASTM E1876-09 Standard Test Method for Dynamic Young's Modulus, Shear Modulus, and Poisson's Ratio by Impulse Excitation of Vibration*, West Conshohocken, PA: ASTM International, 2009.

[46] American Society for Testing and Materials, *ASTM C805-13 Standard Test Method for Rebound Number of Hardened Concrete*, West Conshohocken, PA: ASTM International, 2013.

[47] American Society for Testing and Materials, *ASTM C803-03 Standard Test Method for Penetration Resistance of Hardened Concrete*, West Conshohocken, PA: ASTM International, 2003.

[48] American Society for Testing and Materials, *ASTM C469-10 Standard Test Method for Static Modulus of Elasticity and Poisson's Ratio of Concrete in Compression*, West Conshohocken, PA: ASTM International, 2010.

[49] Pioneer Masonry Restoration Comapny, Inc., [Online]. Available: www.pioneer-masonry.com/resources.html. [Accessed 1 June 2013].

BIOGRAPHICAL SKETCH

Jordan Nelson was born in Tallahassee, Florida to parents Clifton Jr. and Susan Nelson. He graduated 10th in his class from Lawton M. Chiles High School there in May 2007 and began pursuing his Bachelor of Science degree in mechanical engineering at the University of Florida in August. After receiving his degree in December 2011 he was accepted to the graduate school and began working on his Master of Engineering degree, with his major in mechanical engineering but his research primarily civil engineering oriented, in July 2012.

A long-time employee of the Florida Department of Transportation, Jordan worked at the FDOT Structures Research Center in Tallahassee before and after his freshman year of college under Marc Ansley, who fostered his early interest in structural testing, fabrication, and mechatronics. Beginning his second year at the University of Florida on Mr. Ansley's recommendation he began work at the FDOT State Materials Office—the sponsoring agency of this research—where he met Christopher Ferraro. After three years of working together at the SMO and at the Civil Engineering Laboratories at the University of Florida, Jordan became Dr. Ferraro's first graduate student. He plans on continuing to work with his friend and employer after graduation as a consultant in civil engineering instrumentation, controls, data acquisition, and nondestructive evaluation.